ResearchOnline@JCU

This file is part of the following reference:

Philippa, Bronson (2014) *Charge transport in organic solar cells.* PhD thesis, James Cook University.

Access to this file is available from:

http://researchonline.jcu.edu.au/40726/

The author has certified to JCU that they have made a reasonable effort to gain permission and acknowledge the owner of any third party copyright material included in this document. If you believe that this is not the case, please contact ResearchOnline@jcu.edu.au and quote **http://researchonline.jcu.edu.au/40726/**

JAMES COOK UNIVERSITY AUSTRALIA

Charge Transport in Organic Solar Cells

Thesis submitted by

Bronson Philippa BEng(Hons) BSc

in December 2014

for the degree of Doctor of Philosophy

in the College of Science, Technology and Engineering

James Cook University

COPYRIGHT © BRONSON PHILIPPA, 2014.

Some rights reserved.

This work is licensed under Creative Commons
Attribution–Noncommercial–No Derivative Works license.

http://creativecommons.org/licenses/by-nc-nd/3.0/au/

Statement of the Contribution of Others

I gratefully acknowledge the contributions detailed below.

Funding support was provided by an Australian Postgraduate Award and the James Cook University Graduate Research Scheme.

Editorial assistance for the overall thesis was provided by Prof. Ronald White of James Cook University. Chapters 4-6 and 8-9 are each based on published papers, and editorial assistance was provided by all of the listed coauthors. A special mention goes to Ronald White, Almantas Pivrikas, Paul Meredith, and Paul Burn for their consistently helpful advice.

Experimental assistance is acknowledged in each respective chapter where the data appear. Notably, Chellappan Vijila provided the photo-CELIV transients for Chapter 4, and Martin Stolterfoht and Almantas Pivrikas obtained experimental data that appears in Chapters 5-7.

Contributions to co-authored publications that form part of this thesis are as follows. Chapters 4-6 are based on co-authored publications, wherein I performed the simulations, analysed the experimental data, prepared the figures, and wrote the text. Experimental data that was collected by others is indicated at the beginning of each respective chapter. I am not the first author on the publications related to Chapter 7, and so the presentation in this thesis is substantially different from that in the submitted manuscripts. The emphasis in Chapter 7 is on my contribution, which was simulations and theoretical analysis. One figure in Chapter 7 was prepared by Martin Stolterhoft, and is reproduced in order to show experimental validation of my work. Chapters 8 and 9 are again based on publications where I am the first author. These are theoretical papers, in which I performed the analysis, prepared the figures, and wrote the text.

Acknowledgements

I am deeply grateful for all of the support that I have received over the course of my PhD. This thesis would not have been possible without the assistance of the people listed below.

To my supervisor Professor Ronald White, I thank you for your endless patience, support, encouragement, and wisdom. You have provided me with so many opportunities for which I am very grateful.

To my de-facto supervisor Almantas Pivrikas, I feel privileged to have benefited from your relentless enthusiasm and creativity. Your regular "what if …" questions continually pushed me to add new features to my software!

Thank you to Martin Stolterfoht, Ardalan Armin, and Chellappan Vijila for sharing your experimental data, your insight, and for allowing me to contribute to your projects. I look forward to continued collaborations with all of you.

Thank you to Rob Robson for your insight, and Mohan Jacob for believing in me. Thank you to all the members of COPE for the time that we shared and the understanding that I gained. A special mention goes to Paul Meredith for allowing me to join your group as an external student.

To my fellow postgrads in "city 17", what times we had! Thank you all, and best of luck with your own theses.

To my family, my parents, and my brother—I will be forever grateful for your encouragement, your wisdom, and for always taking care of me.

Finally, and most importantly, to my dear Zoe, thank you for your love, your liveliness, your trust, and your endless kindnesses.

Abstract

The process of charge transport is fundamental to the operation of all electronic devices. In organic photovoltaics, high efficiencies can only be achieved if charge transport is able to extract charge carriers from the active layer with minimal recombination losses. This work presents new insights into the measurement of charge transport, the underlying physics, as well as new approaches for modelling. Numeric simulation software using a drift-diffusion-recombination model is developed and applied to organic photovoltaic devices. Specifically, this model is used to design and interpret charge transport experiments that are applicable to operational organic solar cells.

Charge carrier mobility is studied using photogenerated charge extraction by linearly increasing voltage (photo-CELIV) and the novel technique of resistance-dependent photovoltage (RPV). These experiments demonstrate the absence of "hot carrier" relaxation effects on the timescales of charge transport in several organic photovoltaic polymer:fullerene blends. This is surprising because it has previously been argued that such relaxation is the cause of the deterimental dispersive transport that affects many organic semiconductor devices. It is argued instead that dispersive transport arises from the loss of carriers to trap states. Next, the techniques are extended to recombination measurements, where the recombination coefficient in a benchmark polymer:fullerene system is found to depend upon the polymer's molecular weight.

Modelling of the steady-state photocurrent produced by a solar cell demonstrates the conditions under which non-geminate recombination may be avoided, and presents a design rule for avoiding non-geminate recombination. Experimental measurements on devices of varying thickness support the conclusion that the space-charge limited current is a fundamental threshold for high-efficiency photocurrent extraction.

Finally, fractional kinetics and generalised diffusion equations are explored. We show that the Poisson summation theorem permits the analytic solution of a fractional diffusion equation to be collapsed into closed form. Subsequently, these techniques are applied to a new type of kinetic model that is capable of unifying normal and dispersive transport within a single framework.

List of Publications

This thesis contains content that has been published in the following journal articles:

[1] B. W. Philippa, R. D. White, and R. E. Robson. Analytic solution of the fractional advection-diffusion equation for the time-of-flight experiment in a finite geometry. *Physical Review E*, **84**, 041138 (2011). doi:10.1103/PhysRevE.84.041138.

[2] Bronson Philippa, Martin Stolterfoht, Ronald D. White, Marrapan Velusamy, Paul L. Burn, Paul Meredith, and Almantas Pivrikas. Molecular weight dependent bimolecular recombination in organic solar cells. *The Journal of Chemical Physics*, **141**, 054903 (2014). doi:10.1063/1.4891369.

[3] Bronson Philippa, Martin Stolterfoht, Paul L Burn, Gytis Juška, Paul Meredith, Ronald D White, and Almantas Pivrikas. The impact of hot charge carrier mobility on photocurrent losses in polymer-based solar cells. *Scientific Reports*, **4**, 5695 (2014). doi:10.1038/srep05695.

[4] Bronson Philippa, R. E. Robson, and R. D. White. Generalized phase-space kinetic and diffusion equations for classical and dispersive transport. *New Journal of Physics*, **16**, 073040 (2014). doi:10.1088/1367-2630/16/7/073040.

[5] Bronson Philippa, Chellappan Vijila, Ronald D. White, Prashant Sonar, Paul L. Burn, Paul Meredith, and Almantas Pivrikas. Time-independent charge carrier mobility in a model polymer:fullerene organic solar cell. *Organic Electronics*, **16**, 205 (2015). doi:10.1016/j.orgel.2014.10.047.

The publications listed below are relevant to this thesis but do not form part of it:

[6] Ardalan Armin, Gytis Juška, Bronson W. Philippa, Paul L. Burn, Paul Meredith, Ronald D. White, and Almantas Pivrikas. Doping-induced screening of the built-in-field in organic solar cells: Effect on charge transport and recombination. *Advanced Energy Materials*, **3**, 321 (2013). doi:10.1002/aenm.201200581.

[7] Chellappan Vijila, Samarendra P Singh, Evan Williams, Prashant Sonar, Almantas Pivrikas, Bronson Philippa, Ronald White, Elumalai Naveen Kumar, S. Gomathy Sandhya, Sergey Gorelik, Jonathan Hobley, Akihiro Furube, Hiroyuki Matsuzaki, and Ryuzi Katoh. Relation between charge carrier mobility and lifetime in organic photovoltaics. *Journal of Applied Physics*, **114**, 184503 (2013). doi:10.1063/1.4829456.

[8] Martin Stolterfoht, Bronson Philippa, Ardalan Armin, Ajay K. Pandey, Ronald D. White, Paul L. Burn, Paul Meredith, and Almantas Pivrikas. Advantage of suppressed non-Langevin recombination in low mobility organic solar cells. *Applied Physics Letters*, **105**, 013302 (2014). doi:10.1063/1.4887316.

[9] Peter W. Stokes, Bronson Philippa, Wayne Read, and Ronald D. White. Efficient numerical solution of the time fractional diffusion equation by mapping from its Brownian counterpart. *Journal of Computational Physics*, **282**, 334 (2015). doi:10.1016/j.jcp.2014.11.023.

Conference Presentations

During my PhD I presented at the following international conferences:

- Bronson Philippa, Ronald White, and Almantas Pivrikas. Numerical Simulation of Electronic Processes in Organic Semiconductors. *International Conference for Young Researchers in Advanced Materials (ICYRAM)*, Singapore, poster presentation (2012).
- Bronson Philippa, Chellappan Vijila, Prashant Sonar, Almantas Pivrikas, Ronald White. Numerical modelling as a technique for characterising temperature dependent charge transport and recombination in bulk heterojunction solar cells. *International Organic Excitonic Solar Cells (IOESC) Conference*, Australia, poster presentation (2012).

Contents

List of Figures

1 Introduction

Semiconductor technology has transformed the world. Integrated circuits, microprocessors, displays, memories, sensors, solar cells, etc. are all ubiquitous in modern society. Yet, most of these technologies are manufactured using the same raw materials, the vast majority being silicon. Silicon is cheap, abundant on the Earth, and well suited to many applications. However, it requires a large energy input due to its reliance on high temperature manufacturing processes, and is generally used in the form of a brittle crystal that cannot be bent or twisted.

A new class of semiconductors has emerged that might be able to fill a niche that silicon cannot. These are polymers, or in casual terms, "plastics". Most polymers are insulating, but there are a special class of polymers that are able to conduct charges very effectively. The key is conjugation, which is a sequence of alternating single and double bonds. Conjugation is not limited to polymers; it can also be found in many other organic molecules. All together, these materials are called organic semiconductors [10].

Organic semiconductors have attracted tremendous scientific attention because of their promise of extremely low-cost fabrication, chemical tunability, and mechanical flexibility [11–17]. These features would especially benefit solar cells, because organic semiconductors make it possible to literally "print" a solar module onto a roll of plastic [18]. However, the power conversion efficiency of even the best organic solar cells is still far below that achieved using other technologies [19]. The performance of organic photovoltaics needs to be improved if they are to be commercially successful and obtain market penetration.

The poor performance of organic electronics is partly due to their poor charge transport properties. (Charge transport is the mechanism by which electric charges

are conducted through the device.) To work towards improving charge transport performance, it is first necessary to have robust tools for *measuring* that performance. As will be described in the next chapter, classical measurement techniques are not well suited to organic photovoltaics.

The objective of this thesis is to develop novel approaches for characterising charge transport in organic semiconductor devices, and especially organic solar cells. This is achieved through joint theoretical-experimental studies. The theoretical work is based on two major types of model. Firstly, a drift and diffusion numerical simulation, which is a well-known modelling approach with a long history of success [20–22]. The second modelling approach is the so-called fractional kinetic theory [23, 24]. The experimental work is the measurement of charge transport properties in a variety of organic photovoltaic systems using the techniques that are developed in this thesis.

The structure of this document is as follows. Chapter 2 is a literature review with a focus on organic photovoltaics, measurement techniques, and modelling approaches. Chapter 3 describes the numerical simulation model. Chapter 4 applies the model to a classical measurement technique (photo-CELIV) and addresses some of the limitations of that technique. Chapters 5 and 6 report on novel experimental approaches developed as part of this study for measuring mobility (speed of charge transport) and recombination (between electrons and holes, and hence energy loss during transport), respectively. Chapter 7 applies the model to a very common measurement (photocurrent as a function of light intensity), and reports on new insights that were gained. Next, the focus shifts towards the second class of modelling that was addressed in this work. Chapter 8 presents mathematical advances regarding the analytic solution of a certain type of fractional differential equation for charge transport. Then, Chapter 9 applies these mathematical techniques to a novel kinetic model that unifies different types of charge transport under a common framework. Finally, Chapter 10 concludes and makes recommendations for the future.

2 Fundamentals

This chapter presents a literature review. We begin with some background on the characteristics of solar cells in general, before moving onto the history and current status of organic solar cells. The next topic is charge transport, starting with some fundamental concepts and a discussion of the important physical processes. Key techniques for measuring charge transport properties are reviewed, and then various modelling approaches are discussed. Some gaps in the current knowledge or weaknesses with current methods are highlighted in order to motivate the rest of the thesis.

2.1 Solar Cell Fundamentals

A solar cell is a device that converts light into electric power [25]. The electrical behaviour of a solar cell is defined by its current-voltage curve [25, 26], called an IV curve or a JV curve, where the symbol I or i refers to current, J or j refers to current density (current per unit area), and V or v refers to voltage. Often current density is used (instead of current) because it allows a more direct comparison between solar cells with different surface areas. A solar cell has an asymmetric IV curve, as shown in Figure 2.1. Considering first the "dark" curve (when light is not applied), the solar cell behaves as a diode. In reverse bias, no charge is injected and no current will flow; whereas in forward bias, charge will be injected and current will flow once the voltage exceeds the diode threshold voltage. The distinction between reverse bias and forward bias is important in charge transport experiments, to prevent (or induce) the electrical injection of charges, respectively.

When light is applied, the solar cell produces current, as shown by the light curve in Figure 2.1. Useful electrical power $P = iv$ is generated in the region indicated

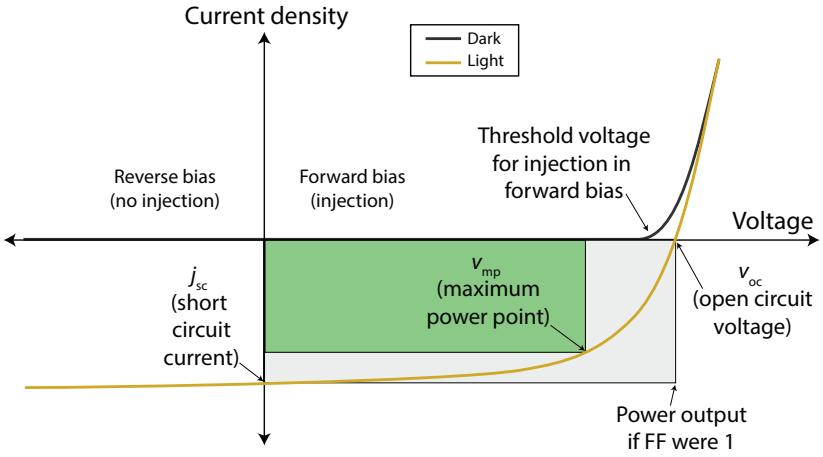

Figure 2.1: A current-voltage curve for a solar cell. The power generated is indicated schematically by the area of the green rectangle.

by the grey box. Three key points on the IV curve are the short-circuit current (i_{sc} or j_{sc}, when the voltage is zero), the maximum power point (v_{mp}, when the power output is maximised), and the open-circuit voltage (v_{oc}, when the current is zero). The maximum power point is illustrated schematically in Figure 2.1 by area enclosed in the green rectangle. The ratio between the actual power produced (the green rectangle) and the product $i_{sc}v_{oc}$ is called the fill factor (FF). Specifically,

$$\mathrm{FF} = \frac{P_{\max}}{i_{sc}v_{oc}}, \tag{2.1}$$

where $P_{\max}$ is the power produced at the maximum power point. A fill factor of unity would indicate a perfectly rectangular IV curve.

The "headline" performance number for a solar cell is its power conversion efficiency (PCE), defined as [27]

$$\mathrm{PCE} = \frac{P_{out}}{P_{in}}, \tag{2.2}$$

where P_{out} is the electrical power generated and P_{in} is the light power incident on the solar cell. To ensure that PCE measurements are reproducible, it is necessary to define a standard reference solar spectrum. Natural sunlight is too variable because it depends upon the position on the Earth, the time of day, etc [25]. The most commonly used standard is the "AM1.5" spectrum defined by the American Society for Testing and Materials (ASTM) [28], which is plotted in Figure 2.2. Three spectra are shown. The extraterrestrial spectrum is that observed from outside the Earth's atmosphere; it is also called the "AM0" spectrum because it has been attenuated by zero air masses, where an "air mass" is the thickness of the atmosphere. The AM1.5 spectra represent the solar energy remaining after the sunlight has passed through 1.5 air masses, which is considered to be a standard reference that accounts for the fact that the sun is not always perfectly overhead. There are two AM1.5 spectra: the Direct spectrum contains only that light originating from a small solid angle surrounding the sun, whereas the AM1.5 Global spectrum additionally includes the typical diffuse irradiance caused by

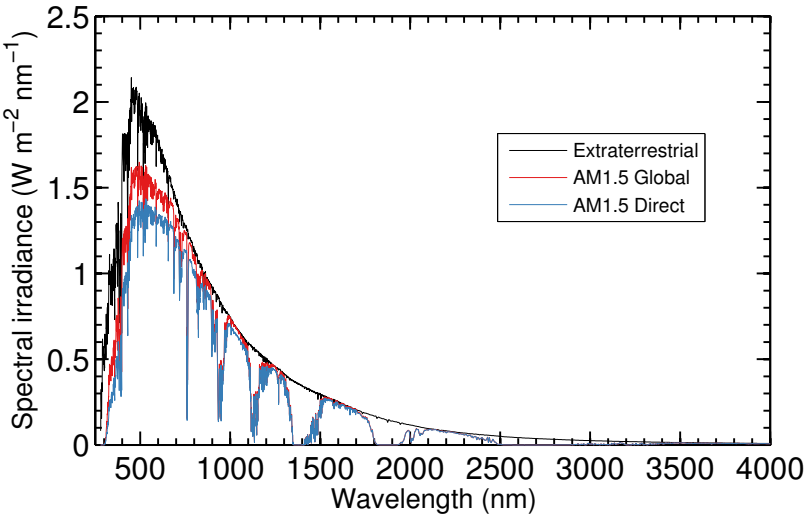

Figure 2.2: Standard benchmark solar spectra. The two AM1.5 spectra demonstrate the typical attenuation caused by the atmosphere.

the rest of the sky. For flat solar panels, the AM1.5 Global spectrum is the standard benchmark.

Not every photon is successfully converted into an electron-hole pair, and not every electron-hole pair is successfully transported to their respective electrodes. The combined efficiency of the photon-to-extracted-charge-carrier process is called the quantum efficiency of the solar cell. There are two separate quantum efficiencies that are commonly reported: the Internal Quantum Efficiency (IQE) represents the proportion of *absorbed* photons that result in fully extracted electron-hole pairs; conversely, the External Quantum Efficiency (EQE) represents the proportion of *incident* photons that result in fully extracted electron-hole pairs [27]. The IQE represents the efficiency of charge generation and collection in isolation from the optical properties, whereas the EQE also includes the optical reflectance and transmittance of the device. Calculating the IQE requires precise optical modelling in order to determine the proportion of incident photons that are actually absorbed in the active layer [29].

This thesis will examine a new class of emerging solar cells, made from organic semiconductors. These are discussed next.

2.2 Organic Solar Cells

Organic semiconductors are carbon-rich materials that exhibit semiconducting properties [30]. Interest in these materials often arises because of the belief that they will deliver substantially reduced costs when compared to conventional, inorganic semiconductors [11–14,31,32]. Organic semiconductors also attract attention because they permit novel form factors such as lightweight, flexible and transparent electronics [15–17].

The chemical structures of some commonly studied organic semiconducting materials are shown in Figure 2.3. These materials are conjugated, that is, they have chains of alternating single and double bonds. The conjugation causes π orbitals to

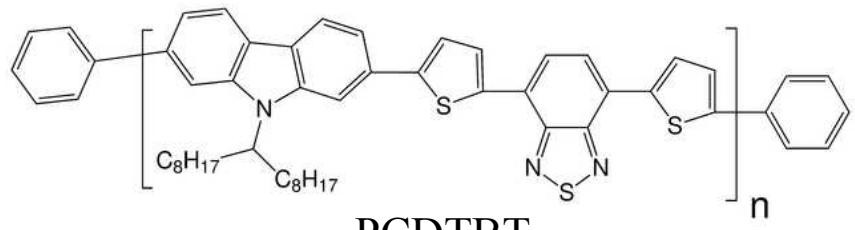

PCDTBT

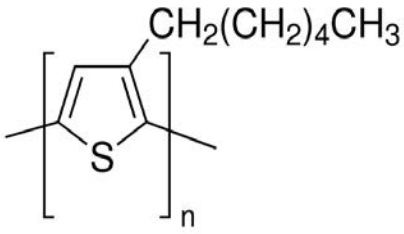

P3HT

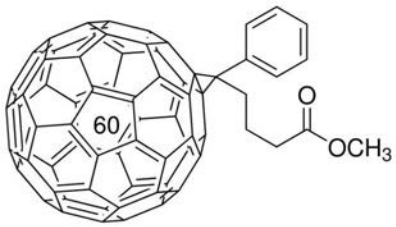

PCBM

Figure 2.3: Some common organic semiconducting materials. Poly[N-9 -heptadecanyl-2,7-carbazole-alt-5,5-(4 ,7 -di-2-thienyl-2 ,1 ,3 -benzothiadiazole)] (PCDTBT) and Poly(3-hexylthiophene-2,5-diyl) (P3HT) are electron donors, while [6,6]-phenyl-C61-butyric acid methyl ester (PCBM) is an electron acceptor. Images from Sigma-Aldrich.

be delocalised over the conjugated segment, allowing ready charge transport along a molecule and giving rise to interesting electronic properties [10].

There are many applications of organic semiconductors. These include solar cells [33,34], light emitting diodes [35], optically pumped lasers [36,37], thin film transistors [38–41], thin-film memory devices [42], and biosensors [43]. This thesis will focus on organic solar cells.

The earliest organic solar cells were made using a single active layer [44]. Photovoltaic effects were observed, but device performance was extremely disappointing ($\ll$ 1% power conversion efficiency).

The first major development was the bilayer organic solar cell published by Tang in 1986 [45]. It improved upon earlier devices by utilising two dissimilar organic semiconductors that act as electron accepting and electron donating materials. This concept is the foundation of modern organic solar cells. The original bilayer device had a power conversion efficiency (PCE) of approximately 1%, and was notable because of its greatly improved fill factor, demonstrating the benefits of having separate donor and acceptor materials.

The next major development came in 1992 with the report of ultrafast photoinduced electron transfer from a polymer to a fullerene by Sariciftci, *et al* [46]. That article established C_{60} fullerenes as the prototypical electron acceptor. Nevertheless,

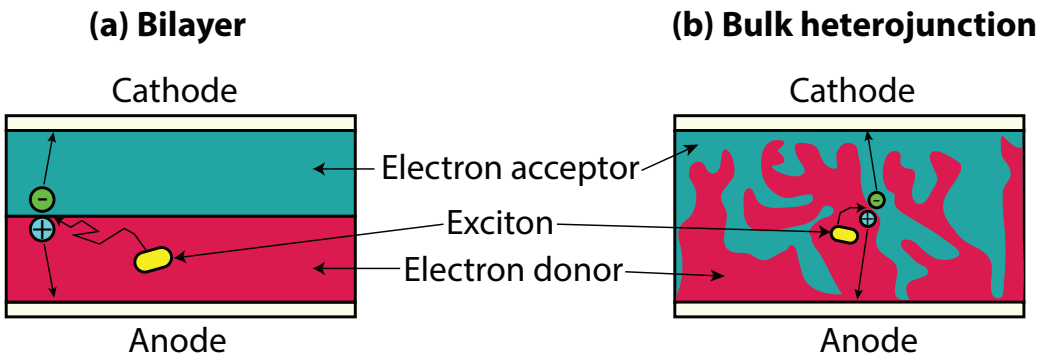

Figure 2.4: Two architectures of organic solar cell. **(a)** A bilayer structure can be manufactured by sequential deposition of two distinct layers. **(b)** A bulk heterojunction structure can be manufactured by deposition of a mixed solution. The advantage of the bulk heterojunction structure is that the interfacial surface area is greatly increased, improving the overall exciton separation efficiency at the expense of potential charge transport problems if there are isolated "islands" that are not connected to their respective electrode. (The anode and cathode naming convention in solar cells refers to the forward bias diode behaviour, even though the desirable photocurrent is in the opposite direction.)

a substantial architectural problem remained. Photogenerated excitations, called "excitons", will only separate with high efficiency if they are able to reach the donor-acceptor interface within their short lifetime (typically 10^{-10} to 10^{-9} seconds [47–49]). The original devices had a bilayer structure, as shown in Figure 2.4 (a). Only those excitons that were generated near to the interface could contribute to the photocurrent. Bilayer devices are therefore fundamentally limited.

A substantial improvement to the early bilayer devices came with the invention of the bulk heterojunction structure, which is a continuous intermixed network of donor and acceptor phases, as shown in Figure 2.4 (b). The idea of this structure is that an exciton should not need to diffuse far before it reaches an interface and can separate. However, the bulk heterojunction introduces new challenges because the domain sizes must be large enough to ensure that most domains are continuously connected to their respective electrode for rapid charge extraction, yet the domains must also be small enough that excitons can reach the heterojunction. A successful method to form such a structure was reported in 1995 by Yu *et al* [50]. The manufacturing process was tantalisingly simple: the two materials were simply mixed in solution and spin cast. This was made possible by the development of the soluble fullerene derivative [6,6]-phenyl-C61-butyric acid methyl ester (PCBM) [51], the structure of which is shown in Figure 2.3. PCBM is still very commonly used to this day [52].

Since these pioneering early publications, the field of organic solar cells has grown enormously. The current PCE record for a single junction organic solar cell is 10.7% [19]. This remains substantially below the record for crystalline silicon cells of 25% [19], and even further behind the GaAs thin film record of 28.8% [19]. However, organic photovoltaics (OPV) still attract interest because of their potential low cost

and innovative form factors. It has been predicted that OPV efficiencies of 20% or more should be achievable [53].

Some perspective on the modern state of the field can be obtained from a meta-analysis published by Jørgensen, *et al* [52] in 2013. These authors analysed the status of OPV by an exhaustive literature survey. Their literature search located 8962 relevant journal papers, which they claim was the complete record of all OPV publications at that time. From these papers they compiled data on 10533 individual organic solar cells. Overall, the vast majority of devices exhibited performance well below the record-holding "hero" cells that are commonly cited in performance benchmarks. They concluded that the headline performance numbers are unrepresentative of the majority of actual devices being produced in laboratories around the world. Consequently, despite the steady improvements in PCE world records, it's clear that much progress still needs to be made.

To understand the operational principles of organic solar cells, it's helpful to follow the sequence of events as a photon is absorbed [54]. As mentioned above, the absorption of light creates an excited state called an exciton [49] that may move by diffusion until it reaches the interface between the donor and acceptor phases. At this interface, it is energetically favourable for the electron to cross from the donor into the acceptor. The result is a "charge transfer" (CT) state [49] that consists of a Coulombically bound electron-hole pair, with the electron in the acceptor and the hole in the donor material. Finally, the charges in the CT state move away from each other, to yield free charge carriers.

The specifics within the above sequence of events are still under debate [55–61]. For a CT state to dissociate into free charges it must overcome a binding energy that is estimated to be an order of magnitude larger than k_BT at room temperature [49, 55]. (Here, k_B is the Boltzmann constant and T the temperature.) Given the apparently strong binding energy, it's somewhat surprising that charge separation occurs at all, let alone with high efficiency.

It has been proposed that above-bandgap light might contribute additional energy to assist with the separation of the CT state [58]. An exciton created by above-bandgap light is considered to be "hot." According to this theory, the resulting "hot" CT states dissociate more readily, using their additional energy to overcome the Coulombic binding energy. However, this theory has been disputed [29, 59, 62]. Quantum yields of extracted charges have been shown to be independent of the photon energy [59], suggesting that "hot" excitons are not actually important for efficient charge generation. Additionally, when optical effects are properly accounted for, some internal quantum efficiency (IQE) spectra are flat [29, 62], further questioning the hot exciton theory. We will return to the question of "hot" carriers in Chapter 5.

It has also been proposed that CT dissociation is assisted by the delocalisation of charge [63], which would assist charge separation by increasing the effective size of the CT state and thus weakening the binding energy. Another possibility is that dissociated charges have higher entropy because a free carrier may sample from a

wider range of possible states, and therefore CT dissociation is assisted by an entropic contribution [49, 64]. Whatever the mechanism, it is effective, because there exist organic materials with nearly 100% conversion of photons to charge carriers [59, 65].

Once free charge carriers have been created, they must be extracted to the appropriate electrodes in order to provide useful energy. This is the process of *charge transport*, and it is the main focus of this thesis. Optimal charge transport would move the charges through the device as quickly as possible, while simultaneously avoiding the loss of energy through recombination. These steps are discussed below.

2.3 Charge Transport

2.3.1 Semiconducting properties

Conventional semiconductor theory describes transport using a band model [66, 67], with a conduction band and a valence band that are separated in energy. Electrons can be conducted through the material once they are excited from the valence band into the conduction band. Similar energetic states exist in organic semiconductors, but due to their chemical structure, the terminology is *Highest Occupied Molecular Orbital* (HOMO) and *Lowest Unoccupied Molecular Orbital* (LUMO). The HOMO is the analogue of the valence band, while the LUMO is the analogue of the conduction band [10, 68]. The absorption of a photon can excite an electron from the HOMO into the LUMO.

The chemical structure of organic semiconductors is such that charge carriers are substantially delocalised over conjugated segments of the molecule [69]. This allows charge to travel very quickly along conjugated segments. However, charge cannot travel so rapidly *between* conjugated segments [57]. Such a charge transfer will be strongly dependent upon the local spatial and energetic configurations of the respective sites.

An intuitive picture of charge transport in organic materials is that of localised charge hopping between sites. A network of sites is distributed in space and energy, as shown in Figure 2.5. Charges move from one site to another by tunnelling or by thermally activated hopping [12, 70, 71]. If there is an applied electric field, then hops in the direction of that field will be favourable because the work done by the field effectively lowers the energy of the sites in that direction.

In classical semiconductor theory of ideal systems, there are no energetic states between the conduction band and the valence band. This means that a carrier in the conduction band cannot thermalise any lower than the conduction band, and will therefore continue to be able to be conducted for an arbitrarily long period of time. However, defects in the material may result in energetic states between the two bands. These are called “traps”. A carrier that is captured by a trap has dropped out of the conduction band and is no longer able to move. Eventually, thermal fluctuations will impart enough energy to that carrier that it can be released from the trap and return to the conduction band. An equivalent situation occurs in the hopping model of Figure

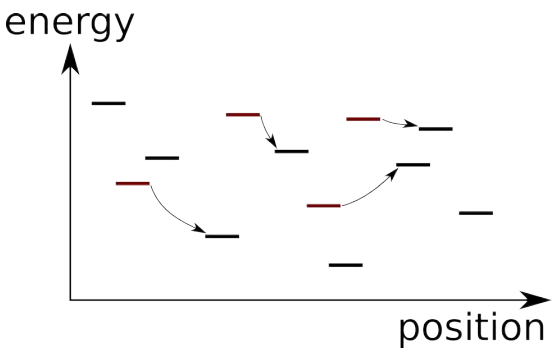

Figure 2.5: The hopping model of charge transport. Carriers occupy sites which are distributed in energy and position. Movement of charge occurs by hopping events in which a carrier rapidly transitions from one site to another.

2.5, where a trap would be a state low enough in energy such that its release time is much longer than normal.

The effectiveness of charge transport is often quantified by a parameter called the carrier mobility. The mobility is the constant of proportionality between the drift velocity and the electric field, i.e. the velocity is $\mu\mathbf{E}$ where μ is the mobility and $\mathbf{E}$ is the field. A higher mobility is desirable for electronics, since higher-performance electronics results from faster-moving carriers. Typical mobilities in organic solar cell materials are $\sim 10^{-5}$ to 10^{-3} $\mathrm{cm^2V^{-1}s^{-1}}$ [72–75].

2.3.2 Normal transport vs dispersive transport

The hopping model suggests that charge transport results from the chaotic movement of charges throughout a complex spatial and energetic landscape. At the microscopic level of individual carriers, some may follow a fortunate sequence of jumps and make rapid motion through the film, while others might take substantially longer [76]. Consequently, the classical notion of a carrier mobility is not precisely defined. There's no single velocity that applies to all carriers, because some carriers effectively move faster than others at any given moment.

More precisely, charge carrier mobility can no longer be thought of as a invariant material property [77, 78]. The mobility must be subject to a distribution, which might be time, position, or temperature dependent [79, 80]. This complicates the measurement and the modelling of charge transport.

Experimentally, it is not possible to observe the instantaneous velocity distribution because the observable conduction current measures only the average motion of all the charge carriers that are present. The best that can be done is to measure the instantaneous average velocity. Surprisingly, in some systems, even the average velocity is not always well defined [78], because it is time-dependent and therefore influenced by the geometry of the sample. This is called dispersive transport.

Dispersive transport occurs when the photocurrent reduces with time even before any charge carriers have been extracted. The photocurrent results from the average motion of all carriers, so this implies that the average *velocity* is decreasing and/or the

number of carriers is decreasing. This apparent time-dependent mobility makes it difficult to extract a representative value, resulting in an apparent thickness-dependence, where thicker devices have longer transit times and consequently allow more time for the photocurrent to decay [78]. These issues will be discussed below in relation to the experimental methods that are commonly applied.

2.3.3 Recombination

Recombination occurs when oppositely charged carriers annihilate [67, 81]. It is the operational mechanism of light emitting diodes, where radiative recombination events generate photons. Conversely, recombination is a loss mechanism in solar cells.

Recombination is classified as geminate or non-geminate [82–84]. Geminate recombination occurs when the recombining electron and hole both originated from the same photon. It is not necessary that the recombination event occur at exactly the same location as where the photon was absorbed, because the exciton may diffuse some distance before recombining. Such movement of excitons cannot contribute to the electrical current because the exciton is not charged.

Non-geminate recombination occurs when the recombining electron and hole have originated from different photons. The electron and hole must physically meet and then interact. There are various mechanisms by which this can occur, but the simplest is "band-to-band" recombination where two mobile (untrapped) carriers are drawn together in each other's electrostatic field. This process is called bimolecular recombination and it is described by the rate equation [67, 85–87]

$$\left.\frac{\partial p}{\partial t}\right|_{\text{bimolecular recomb.}} = \left.\frac{\partial n}{\partial t}\right|_{\text{bimolecular recomb.}} = -\beta np, \tag{2.3}$$

where n and p are the number density of electrons and holes, respectively. (The number density is the number of charges that are present per unit of volume.)

The prefactor β is the called the bimolecular recombination coefficient. It has units of volume per time, and typical values in organic solar cells are 10^{-13} to 10^{-11} cm^3s^{-1} [88–91].

A simple physical model that aids in understanding the meaning of β is a charge carrier undergoing random Brownian motion. As it moves, that carrier continuously samples the surrounding volume looking for a recombination target. Once it crosses into the sphere of influence of an opposite charge, it is likely to recombine. The recombination coefficient β gives the rate at which each carrier samples its surrounding volume, i.e., volume per time. According to this model, the recombination coefficient is a volume swept per unit time, i.e. $\beta = Sv_{th}$, where the S is the cross-section for recombination and v_{th} is the velocity due to thermal motion.

The rate equation (2.3) can be re-written as

$$\left.\frac{\partial p}{\partial t}\right|_{\text{bimolecular recomb.}} = -\frac{p}{\tau_\beta}, \tag{2.4}$$

where $\tau_\beta \equiv (\beta n)^{-1}$ is the bimolecular lifetime. The lifetime gives an approximate length of time that a carrier is expected to survive before recombination.

Many published organic photovoltaic materials exhibit Langevin recombination [12,92,93], which specifies that the bimolecular recombination coefficient is

$$\beta_L = \frac{e\,(\mu_p + \mu_n)}{\epsilon\epsilon_0}, \tag{2.5}$$

where e is the charge of an electron, μ_p and μ_n are the mobilities of holes and electrons, respectively, and $\epsilon\epsilon_0$ is the dielectric permittivity. Langevin recombination is derived based on the assumption that *transport* is the rate limiting step. Charges cannot possibly recombine faster than they can physically meet, and hence Langevin recombination represents an upper limit on the bimolecular recombination rate.

Some organic photovoltaic devices display recombination coefficients less than the Langevin rate [94–97]. These are called "non-Langevin" materials, and are highly desirable for efficient photovoltaics.

The derivation of the Langevin rate is usually presented in terms of the Coulomb radius [98]. The Coulomb radius (r_c) is the distance at which the electrostatic attractive potential energy of two charges equals the thermal energy,

$$V(r_c) = \frac{e^2}{4\pi\epsilon\epsilon_0 r_c} = kT$$

or

$$r_c = \frac{e^2}{4\pi\epsilon\epsilon_0 kT}. \tag{2.6}$$

The typical argument for the use of the Coulomb radius is as follows. If a charge passes within a distance r_c of another charge, then the mutual attraction of the two charges will dominate over any tendency for the charges to escape each other (e.g. by diffusion or an external electric field). It is often suggested [94,99–104] that Langevin recombination applies if the mean free path is less than the Coulomb radius.

The discussion of the Coulomb capture radius presents a compelling physical picture, but it is not actually necessary in the mathematical derivation. Mathematically, it suffices to take any *arbitrary* radius and calculate the flux of recombination targets crossing such a sphere. Consider a frame of reference attached to an electron. In this moving reference frame, holes have an effective mobility $\mu_n + \mu_p$. We consider a sphere of radius r centred at this electron, and calculate the flux of holes crossing the sphere due to electrostatic attraction. The physical assumption is that any hole that crosses this sphere is certain to recombine, i.e. no escape is possible. The holes crossing the sphere move with a velocity $(\mu_n + \mu_p)E$, where E is the electric field. At a distance r from the electron at the origin, the field is given by $E = e/4\pi\epsilon\epsilon_0 r^2$. Combining these,

$$\text{flux density per electron} = p\,(\mu_n + \mu_p)\,E = p\,(\mu_n + \mu_p)\,\frac{e}{4\pi\epsilon\epsilon_0 r^2}.$$

Integrating across the surface of the sphere to obtain the total flux, the radius cancels:

$$\text{recombination flux per electron} = \frac{ep\left(\mu_n + \mu_p\right)}{\epsilon\epsilon_0}.$$

This is the recombination flux due to a single electron. The total recombination rate is obtained by multiplying by the electron number density n,

$$\text{recombination rate} = \left[\frac{e\left(\mu_n + \mu_p\right)}{\epsilon\epsilon_0}\right] np,$$

which from Eq. (2.3) allows the Langevin recombination coefficient to be identified:

$$\beta_L = \frac{e\left(\mu_n + \mu_p\right)}{\epsilon\epsilon_0}. \tag{2.7}$$

This derivation is independent of the assumed radius r. It is necessary to assume that the electric field near the electron is given by the electrostatic attraction of that electron alone, and this is an approximation that improves with decreasing radius.

The Langevin derivation requires that charges be treated as continuous number densities, so that the flux crossing the sphere is density times velocity. It also requires that charges be free to move towards each other so that their velocity is μE in the vicinity of the recombination target.

Another recombination mechanism that must be considered is recombination via trap states [105]. In this mechanism, a charge is first captured into a trap where it becomes immobilised. At some later time, an oppositely charged carrier may approach and recombine with it. This may be described as "monomolecular" recombination with a first order rate [106, 107]

$$\left.\frac{\partial p}{\partial t}\right|_{\text{monomolecular recomb.}} = -\frac{p}{\tau}, \tag{2.8}$$

where τ is the monomolecular lifetime. The lifetime τ is controlled by the density of trapped charges. However, this model is too simple for our needs because it does not balance the recombination rates of both types of charges. According to Eq. (2.8), the hole density p will continue to decay regardless of whether there are any electrons left in the trap states. This violates the conservation of charge.

The problem of trap-assisted recombination was first solved by Shockley and Read [108] and Hall [109]. The so-called Shockley-Read-Hall (SRH) recombination via electron traps is described by the equations

$$\left.\frac{\partial p}{\partial t}\right|_{\text{SRH recomb.}} = \left.\frac{\partial n}{\partial t}\right|_{\text{SRH recomb.}} = \beta_{SRH}(np - n_1 p_1) \tag{2.9}$$

$$\beta_{SRH} = \frac{C_n C_p N_t}{C_n\left(n + n_1\right) + C_p\left(p + p_1\right)}, \tag{2.10}$$

where n_1 (p_1) is the equilibrium concentration of electrons (holes), C_n is the probability per unit time that an electron will be captured by an empty trap, C_p is the probability

per unit time that a hole will be captured by a trapped electron, and N_t is the density of electron traps. SRH recombination is derived from the principle of detailed balance for a system in thermal equilibrium.

Instead of the SRH expression, which inherently incorporates the trap capture time, one might prefer to decouple the recombination model from the trapping model so that these can be specified in isolation. To achieve this, there are three possible mechanisms which must be considered [110]:

1. A free electron recombining with a free hole;
2. A free electron recombining with a trapped hole; and
3. A trapped electron recombining with a free hole.

Each mechanism will be second order, proportional to the number density of each respective species, i.e., of the form βnp for some recombination coefficient β. It has been shown that the coefficient β may be estimated from the Langevin rate with the corresponding mobility set to zero [105]. This makes physical sense, because in systems with near-to-Langevin recombination, the limiting process is likely to be charge transport. We will return to this issue in the following chapter, when we introduce recombination terms into our numerical model.

2.4 Experimental Methods for Characterising Charge Transport

Characterisation of charge transport in organic semiconductors is challenging because of complex dependencies on device geometry, film morphology, electric field, and charge carrier concentration; consequently, a variety of techniques have been developed [92, 111–115]. This review focusses specifically on those that apply to solar cell geometries, because measurements taken on other geometries (such as transistors) can differ dramatically [116] and are not necessarily representative of photovoltaic performance due to a concentration-dependence in the carrier mobility [117].

2.4.1 Current-voltage curves

Carrier injection (in the dark) can be used to probe charge transport. For the case of injection into an ideal undoped, unipolar semiconductor, the Mott-Gurney square law describes the current density as a function of voltage [118]

$$j = \frac{9}{8}\frac{\epsilon\epsilon_0\mu V^2}{d^3}, \tag{2.11}$$

where $\epsilon\epsilon_0$ is the permittivity, μ is the mobility, V is the effective voltage (applied plus built-in), and d is the thickness of the semiconductor. If a JV curve has a regime where the slope is proportional to V^2, then the mobility can be extracted by fitting

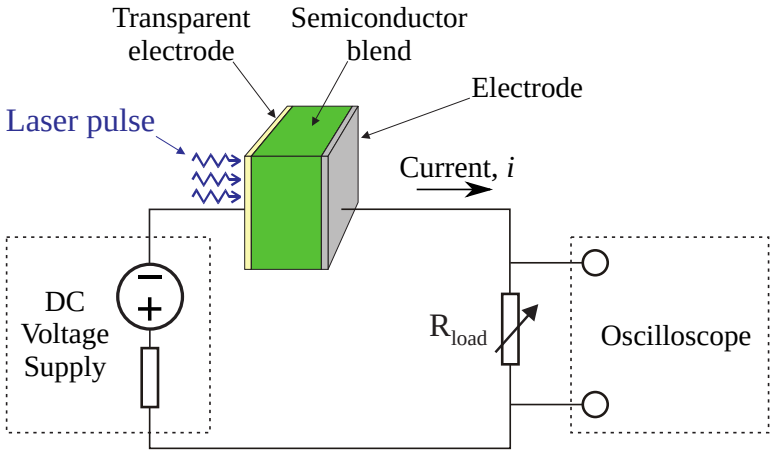

Figure 2.6: Typical experimental setup for time-of-flight. The laser pulse photogenerates carriers that subsequently move under the influence of the DC voltage. The resulting electric current is measured by the oscilloscope and the load resistance R_{load}.

Eq. (2.11) to the data. When applying this technique, care must be taken to ensure that the current is not limited by injection barriers or series resistances. Furthermore, a major weakness of this approach is that the presence of charge trapping will modify the slope of the JV curve [119]. It is possible to calculate $j(V)$ for certain types of trapping distribution [118, 120], but this requires assumptions or knowledge about the types of traps.

Solar cells blends are bipolar conductors, and the Mott-Gurney law does not apply if both types of carrier are present. Nevertheless, it can be used as an approximation if special "hole only" or "electron only" devices are fabricated by using a poorly matched electrode that prevents injection of the corresponding type of carrier [104, 121]. Changing the electrode material may modify the film morphology, and consequently it is desirable to measure the mobilities in actual operational devices.

"Double" injection (of both types of carrier) into bipolar devices can also be used to characterise charge transport [106, 122, 123]. However, the double injection current depends upon the mobilities of both carriers, the bimolecular recombination coefficient, and the distribution of traps. Consequently, care must be taken when interpreting double injection experiments that all of these dependencies are properly accounted for. The interpretation is much simpler when the transport of a single type of carrier can be studied in isolation, as is possible with time-of-flight.

2.4.2 Time-of-Flight

The time-of-flight (TOF) technique is a well established method that has been used for many years [124, 125]. The experimental setup is shown in Figure 2.6. A DC voltage is applied to the sample in reverse bias. It is necessary that the sample has a very low conductivity so that the resulting "dark" conduction current in reverse bias is negligible. A packet of charge carriers is generated near one of the electrodes, typically with a nanosecond laser pulse. The DC voltage causes the charge packet to move through the semiconductor, and the time of the charge carriers' "flight" is observed by

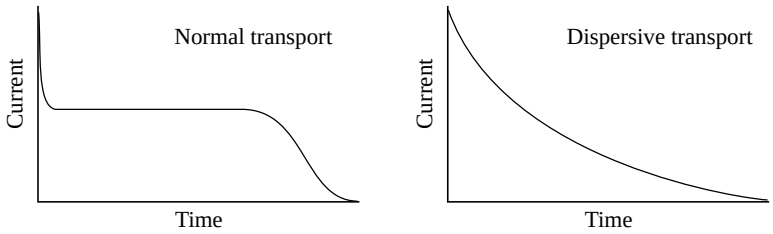

Figure 2.7: Typical current transients measured in time-of-flight experiments, when the light intensity is low such that the electric field is not disturbed by space charge effects. In the case of normal transport, the plateau reveals the constant velocity of the carriers, whereas in the case of dispersive transport, the carrier mobility is poorly-defined.

measuring the electrical current. The velocity of the charges, and hence their mobility, can be calculated with knowledge of the geometry of the sample.

Classical time-of-flight as just described depends upon the smooth and constant motion of the packet of charge carriers. For this to occur, the electric field inside the device must be undisturbed by space charge effects, and so it's necessary to use a light intensity low enough that the amount of photogenerated charge is much less than the charge on the electrodes, CU, where C is the capacitance of the device and U is the voltage. Note that time-of-flight can also be conducted at high light intensities, in which case it provides a measure of charge carrier recombination [89, 102].

Schematic representations of typical low-light intensity time-of-flight transients are shown in Figure 2.7. Normal transport—in which charges move in a coherent packet—is shown on the left side, whereas dispersive transport—in which the photocurrent continuously decays—is shown on the right side. The flat plateau in the case of normal transport indicates a packet of charge moving with a constant velocity. Conversely, in the case of dispersive transport, no such plateau is visible.

The apparently featureless dispersive transient usually demonstrates some structure when plotted on logarithmic axes, as shown in Figure 2.8. Often there are two power law regimes with slopes $-1+\alpha$ and $-1-\alpha$, respectively, where $0 < \alpha < 1$ [77, 78]. The dimensionless parameter α describes the severity of the dispersion, with smaller values of α indicating more severe dispersion. The transition between the two regimes occurs when the slope changes, and this is often interpreted as a representative transit time, from which mobilities are determined.

The two power law slopes of $-1 \pm \alpha$ were predicted by an influential model due to Scher and Montroll called the continuous-time random walk [77]. The details of this model will be described in more detail below, but for analysing time-of-flight data it is important to recognise that the two slopes sum to -2, independent of the value of α. Therefore, the "sum of slopes" is a test that determines whether the transport can be described by a Scher-Montroll continuous-time random walk.

To obtain meaningful time-of-flight transients like Figures 2.7 and 2.8, it is necessary to photogenerate carriers in only a very thin section of the device near to the

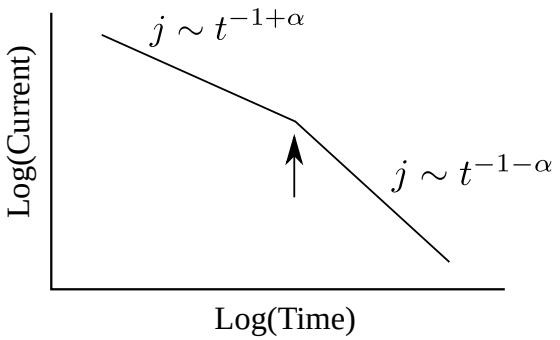

Figure 2.8: Typical dispersive current transits plotted on double logarithmic axes. The two regions are labelled with the asymptotic behaviour of the current density (j) as a function of time (t). The coefficient α describes the degree of dispersion. The change in slope, which is marked by an arrow, is often interpreted as a transit time.

surface. This ensures that all charges travel approximately the same distance, and consequently their velocities can be calculated on the basis of the sample's geometry. A highly efficient solar cell will always have a thickness similar to the optical penetration depth, because otherwise a substantial portion of the device will not receive light and therefore will not contribute photocurrent. Even more detrimentally, the additional thickness beyond the optical penetration depth would serve to delay charge extraction and weaken the electric field by spreading the built-in voltage over a larger thickness. The reduced built-in field would cause charges to "pile up" inside the device, increasing recombination losses. Consequently, good solar cells are necessarily too thin for classical time-of-flight. If the devices are made thicker, then the film morphology or microstructure may change [126, 127], and so time-of-flight is not well suited here.

2.4.3 CELIV

Charge extraction by linearly increasing voltage (CELIV) addresses some of the difficulties associated with the standard time-of-flight technique. It was originally used in the dark to measure mobilities in doped semiconductors [128], and was later extended to use laser photogeneration [129] or LED photogeneration [72]. When photogeneration is used, the technique is called photo-CELIV. Conversely, the name dark-CELIV is sometimes used to explicitly indicate the absence of photogeneration. As shown in Figure 2.9, the experimental setup is similar to time-of-flight, except that the charges are linearly accelerated by a rising voltage.

A CELIV or photo-CELIV transient contains several features, which are shown in Figure 2.9. There is a displacement current i_0 and corresponding current density j_0 caused by capacitive charging with a linearly increasing voltage. The displacement current $i_0 = AC$, where A is the slope of the applied voltage and C is the capacitance of the device. Superposed with the displacement current "step" is the conduction current density Δj. The conduction current displays a maximum j_{max} at a time t_{max}. The maximum j_{max} is the total current at the maximum, whereas Δj_{max} refers to the conduction current only, i.e. $\Delta j_{max} = j_{max} - j_0$. The mobility is evaluated from

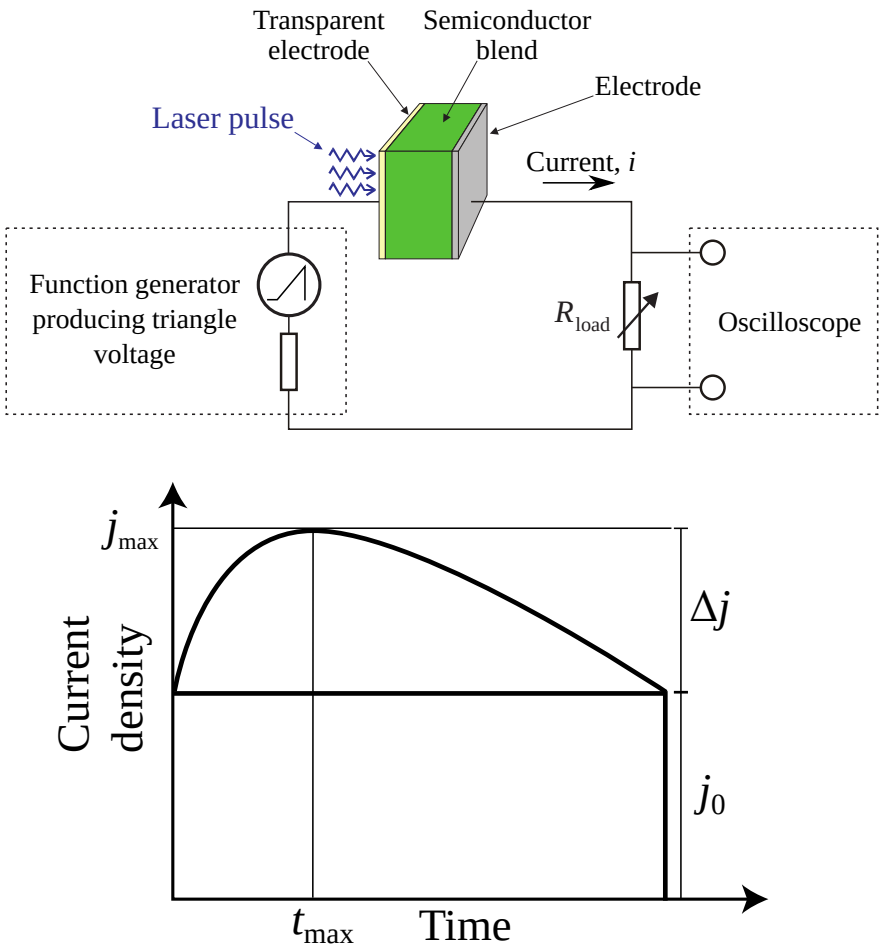

Figure 2.9: Typical experimental setup for photo-CELIV (top), and a schematic current transient (bottom).

the time t_{max}. The original dark-CELIV theory specified that the mobility should be calculated with [128]

$$\mu = \frac{2}{3}\frac{d^2}{At_{max}^2}, \tag{2.12}$$

whereas for photo-CELIV [130]

$$\mu = \frac{2d^2}{3At_{max}^2\left[1 + 0.36\frac{\Delta j_{max}}{j_0}\right]}. \tag{2.13}$$

Other forms of the mobility equation have been proposed [131], and more recently it has become apparent that proper interpretation of photo-CELIV requires correction factors computed via numerical simulations [132, 133].

A strong advantage of photo-CELIV is that it can be applied to thin films [92]. It works well in the case of volume photogeneration, as occurs in operational solar cells. Additionally, photo-CELIV can conveniently estimate the bimolecular recombination coefficient with [100]

$$\frac{\beta}{\beta_L} \approx \frac{j_0}{\Delta j_{sat}}, \tag{2.14}$$

where Δj_{sat} is Δj_{max} at a high enough light intensity that it is saturated. Overall, photo-CELIV has proven itself to be a powerful tool in the study of charge transport in organic semiconductors [6, 134–136]. It has been widely used to elucidate the fundamental mechanisms of time-, field-, and carrier concentration-dependence in various systems [94, 103, 137–143].

The impact of dispersion on photo-CELIV is unclear. In time-of-flight, there is a qualitative distinction between non-dispersive and dispersive transients. Photo-CELIV does not appear to display such a sharp transition. Intuitively, this may be because photo-CELIV measurements are performed on much thinner films than time-of-flight, so charge carriers will have less time to relax before they are extracted from the film. Nevertheless, the impact of dispersion deserves further attention, and we will return to this question in Chapter 4.

A weakness of photo-CELIV is that the widely used formulae (2.12)-(2.14) are believed to be inaccurate under certain important operating conditions [21, 22, 131, 132, 144]. For example, even in the ideal case of uniform photo-generation, a general expression for the mobility cannot be found unless approximations are made [131]. Non-uniform light absorption requires numerical correction factors that have been published only for the special case of Langevin recombination and Beer-Lambert absorption [133]. In the case of thin films—those having an absorption coefficient-thickness product (αd) of 2 or less—the correction factor in the equation to calculate the mobility varies by approximately a factor of 50 across the range of $\Delta j/j_0$ [133]. If thick films are also included, the variation is as much as 100 times. Real devices display more complex optical absorption patterns [29], and calculation of the correction factor is therefore more difficult, but the Beer-Lambert case provides an estimate of the size of the uncertainty. These correction factors need to be adjusted if the system exhibits non-Langevin recombination, and so the uncertainly may be even larger in the case of strongly suppressed recombination. Charge trapping is another problem for photo-CELIV. A study by Hanfland *et al* [144] concluded that CELIV mobilities for "typical organic solar cells" are only accurate to within one or two orders of magnitude. Overall, it should be expected that photo-CELIV mobilities have an uncertainty of at least an order of magnitude, and probably more if numeric simulations are not used to supply correction factors.

A further problem with photo-CELIV is the unintended extracted of charge by the built-in field during the delay time between photo-generation and the beginning of the applied voltage ramp [145]. This has been addressed via improvements in the experimental methodology. A nanosecond switch can be used to hold the device at open circuit during the delay time [88, 146]. Alternatively, the open-circuit voltage transient can be prerecorded and then "played back" during the delay time to simulate open circuit conditions [72]. However, even if the electric field were perfectly compensated, there will still be diffusion and recombination during that time, which will influence the shape of the extraction transient, and hence the measured mobility. This issue

will be addressed in Chapter 4. The weaknesses of the photo-CELIV technique have inspired the development of the RPV technique (Chapters 5 and 6).

2.4.4 Transient PhotoVoltage (TPV)

The transient photovoltage (TPV) technique measures the lifetime of charge carriers via a decay in voltage [147]. Typically, a white-light bias is applied to generate an open-circuit voltage v_{oc}, then a small optical perturbation (typically with a pulsed laser) temporarily increases v_{oc}. The decay of this open-circuit voltage v_{oc} is recorded using an oscilloscope with a large input impedance. It is commonly believed that the measured decay in voltage corresponds to the recombination of the additional charges that were photogenerated by the optical perturbation [147]. The measured lifetime depends upon the concentration of charge carriers that are present according to $\tau_\beta = (\beta n)^{-1}$, and so the lifetime alone (without analysis of the charge carrier concentration) is insufficient to quantify the nature of the recombination or to compare distinct systems, despite some attempts to do so [148]. It is necessary to obtain the carrier concentration by other means in order to compare TPV lifetimes between systems [149].

The TPV measurement is conducted under open-circuit conditions, where charge carriers are spatially separated and recombination is suppressed. More importantly, however, the number density n in the lifetime equation $\tau_\beta = (\beta n)^{-1}$ is likely to be strongly non-uniform, as indicated by simulations of open circuit conditions [20]. Consequently, the spatially-varying lifetime at open circuit greatly complicates the interpretation of lifetime measurements [150].

2.5 Models of Charge Transport

Microscopic models of charge transport in organic semiconductors are typically based on the hopping of charge carriers between localised sites (see, for example, references [76, 77, 93, 151–158]). These models are remarkably successful in explaining and predicting charge transport fundamentals, however, they suffer from several problems. Firstly, the model inputs are in terms of microscopic parameters, such as the characteristics of the site-to-site hopping mechanisms, and these are difficult to measure. Secondly, these models are computationally expensive, especially since each chargeable site—and often each individual carrier—is accounted for individually. It is thus difficult to scale these models to a realistic number of sites or a realistic number of carriers. Some transport effects (such as space charge limitations) only appear at high concentrations of charge, and therefore these are difficult to model using a microscopic approach.

An alternative is a drift-diffusion model [20–22]. These models consider a *continuum* of charge densities, rather than discrete chargeable sites, and are described by partial differential equations (PDEs) rather than probabilistic hopping rates. The continuum model's input parameters are all macroscopically important quantities, such as

carrier mobilities and recombination coefficients. Additionally, there are strong computational advantages because large devices with high charge densities can be simulated in seconds on a typical computer. A weakness of the continuum models is that any temperature-, field- or density-dependence must be assumed *a priori* and inserted as an input parameter [159], whereas microscopic models can often make *ab initio* predictions of any such dependencies [151]. Additionally, dispersive transport often arises naturally in microscopic models, in contrast to standard drift-diffusion models where dispersive mechanisms must be explicitly included in the model.

2.5.1 Gaussian Disorder Model

Perhaps the most commonly used hopping framework is the Gaussian Disorder Model (GDM) [76, 160–162]. According to this model, the energy levels of the sites follow a Gaussian distribution, perhaps because of the central limit theorem where the energy of the sites results from the interaction of a large number of random variables. The density of states is written

$$g(E) = \frac{1}{\sqrt{2\pi\sigma^2}} \exp\left(\frac{-E^2}{2\sigma^2}\right), \tag{2.15}$$

where E is the energy with respect to the mean of the density of states, and σ is the width of the distribution and indicates the level of disorder that is present. The value of σ is called the *diagonal disorder*. This model may be simulated with Monte Carlo techniques. A typical implementation will place the sites on a three-dimensional grid, populate some sites with carriers, and then simulate the hopping motion by random sampling from the probability distribution of allowable hops. To implement such a procedure, the probability of each possible hop must be calculated. These are usually obtained first in terms of the hopping *rates*, i.e. the number of carriers that would be expected to make such a hop in a given unit of time.

The most commonly used hopping rates are due to Miller and Abrahams [163]. According to the Miller-Abrahams rate, hops *upward* in energy are penalised by a Boltzmann factor, whereas hops *downward* in energy receive no additional contribution. Hops are always accompanied by the absorption or emission of phonons. The jump rate is [163]

$$\nu_{ij} = \begin{cases} \nu_0 e^{-2\alpha R_{ij}} \exp\left(-\frac{E_j - E_i}{k_B T}\right), & E_j > E_i \\ \nu_0 e^{-2\alpha R_{ij}}, & E_j < E_i, \end{cases} \tag{2.16}$$

where ν_{ij} is the hopping rate from site i (which has energy E_i) to site j (which has energy E_j), ν_0 is an attempt to hop frequency, α is the reciprocal of the decay length of the localised wavefunctions, and R_{ij} is the distance between the two sites.

Monte Carlo simulations are performed by calculating the hop rates ν_{ij}. Long hops have vanishing probabilities, and therefore it is only necessary to consider some set of nearest neighbours as candidate destinations j. At any given instant, an individual carrier will have many allowable destination sites. We introduce the label n to stand for

a particular combination of source and destination indices, i and j respectively. Then, to calculate the hop which is actually taken, we consider the following distribution [164]:

$P(\tau, n)d\tau = P(\text{the next hop is type } n \text{ AND it occurs within a time interval } \tau \text{ to } \tau{+}d\tau).$

This distribution can rewritten as the product of two factors:

$$\begin{aligned} P(\tau, n)d\tau = P(&\text{no hops of any type occuring before time } \tau) \\ &\times P(\text{hop of type } n \text{ occuring in the interval } \tau \text{ to } \tau + d\tau). \end{aligned}$$

The second factor can be immediately written down. The probability of a hop n in the differential time interval $d\tau$ is $\nu_n d\tau$, where ν_n is the rate constant for the hop of type n.

To calculate the first factor, we consider the probability that the hop *does not occur* in the (arbitrarily large) length of time τ by dividing this interval into K segments of width τ/K. In each such segment, the probability of the hop *not occurring* is $1 - \nu_n\tau/K$, to first order in K^{-1}. Then the probability that the hop does not occur in the entire interval of length τ is the product of all these probabilities, in the limit of large K:

$$\begin{aligned} P(\text{hop } n \text{ not occurring in } t \text{ to } t+\tau) &= \lim_{K\to\infty}\left[1 - \frac{\nu_n\tau}{K}\right]^K \\ &= \exp\left(-\nu_n\tau\right). \end{aligned}$$

It follows that the probably that *no hop at all* occurs is the product over all possible types

$$\begin{aligned} P(\text{no hops of any type occurring in } t \text{ to } t+\tau) &= \prod_m \exp\left(-\nu_m\tau\right) \\ &= \exp\left(-\sum_m \nu_m\tau\right). \end{aligned}$$

This gives the distribution $P(\tau, n)d\tau$ as

$$P(\tau, n)d\tau = \exp\left(-\sum_m \nu_m\tau\right)\nu_n d\tau. \tag{2.17}$$

This distribution is not normalised because it is not certain that the next hop is in fact of type n. Summing over all n yields a normalised distribution.

A Monte Carlo simulation will sample from Eq. (2.17) to evaluate the hop taken by each carrier. As the number of carriers increases, the conduction current will converge to the macroscopic average. The macroscopic conduction current resulting from this simple model contains surprisingly rich behaviour [165, 166]. The charge carrier mobility varies with the energetic configuration of the sites, the electric field, and the temperature [76, 167, 168]. The results are sensitive to short-range correlations

between site energies, which might be expected to arise in practice because nearby sites will be influenced by similar features of the molecular-scale morphology [151]. A further complication is the impact of the charge carrier concentration, because higher concentrations force the carriers to occupy higher energy states in order to comply with the Pauli exclusion principle [169–171].

A fundamental weakness of hopping models is their computational complexity. The need to track individual carriers and individual charge sites makes large-scale models rather challenging. An alternative approach is to apply a macroscopic continuum model, such as a continuity equation.

2.5.2 Continuity equations

Continuity equations describe the macroscopic processes that influence the charge carrier number density $n(\mathbf{x}, t)$. The carrier number density gives the number of particles per unit volume, and it varies with position $\mathbf{x}$ and time t. A typical continuity equation would be

$$\frac{\partial n}{\partial t} + \nabla \cdot \mathbf{j} = G(\mathbf{x}, t) - R(\mathbf{x}, t),$$

where $\mathbf{j}$ is the flux of particles (i.e. the conduction current), G is the rate of carrier generation, and R is the rate of carrier loss (or recombination). This partial differential equation can be solved analytically in simple cases, but in general numerical solutions are needed. Fortunately, numerical solutions of this form are computationally efficient, and modern computers can solve such systems in a matter of seconds. This thesis primarily utilises continuity equations. A full continuity equation model will be developed in the next chapter.

2.5.3 Drift and diffusion

A very widely used model for normal transport writes the conduction current as the sum of drift and diffusion terms [67]. For example, the conduction current of holes would be

$$\mathbf{j}_p(\mathbf{x}, t) = e\mu_p(\mathbf{E}, p)\mathbf{E}(\mathbf{x}, t)p(\mathbf{x}, t) - \mu_p(\mathbf{E}, p)k_B T \nabla p, \tag{2.18}$$

where e is the fundamental charge, μ_p is the carrier mobility, $\mathbf{E}$ is the electric field, p is the number density of holes, k_B is the Boltzmann constant, and T is the temperature. The first term in Eq. (2.18) is the drift current, which is caused by the electric field. The second term is the diffusion current, which is caused by a gradient in concentration. Carriers in regions of high concentration tend to diffuse towards regions of lower concentration.

We note that in certain organic semiconductors, the carrier mobility μ_p may be dependent upon the electric field and/or the density of charge carriers [153,169]. Equation (2.18) displays these dependencies explicitly. Furthermore, Eq. (2.18) also assumes the Einstein relation, $D = \mu k_B T/e$, where D is the diffusion coefficient. The Einstein relation allows the diffusion coefficient to be calculated from the carrier mobility and the temperature, however, the applicability of this equation to organic semiconductors

has been disputed [172]. Nevertheless, the Einstein relation does appear to be valid under conditions near to thermal quasi-equilibrium [173], as would occur in operational solar cells. For this reason we have written Eq. (2.18) with the Einstein relation included. However, if the Einstein relation does not apply, then the variation can be modelled by simply inserting a prefactor into the diffusion term [174].

To apply this model, the conduction current (2.18) forms the transport term in a continuity equation. It is coupled with a similar continuity equation for electrons, and then the electric field is calculated using the Poisson equation. A complete description of such a model and its software implementation is provided in the following chapter.

These models are very widely used [105,159,174–182]. They are simple and computationally efficient. Nevertheless, they do not account for dispersive transport, which is often present in organic materials, unless further terms are added. One mechanism to implement dispersive transport is the multiple trapping model.

2.5.4 Multiple trapping

The multiple trapping model makes a distinction between free and trapped charge [183]. Free charges are considered to be propagating according to standard drift and diffusion, but there exists a mechanism whereby a free charge can become trapped. Trapped charges are immobile, until they are released by some physical process (typically thermal activation), whereupon they continue their motion as before.

Multiple trapping models can be formulated in terms of a discrete set of trap levels [184]

$$\frac{\partial n}{\partial t} + \nabla \cdot \mathbf{j} = \sum_i -\frac{n}{\tau_{c,i}} + \frac{n_i}{\tau_{r,i}} \tag{2.19}$$

$$\frac{\partial n_i}{\partial t} = \frac{n}{\tau_{c,i}} - \frac{n_i}{\tau_{r,i}}, \tag{2.20}$$

where n is the number density of free carriers, $\mathbf{j}$ is the flux of carriers, n_i is the number density of carriers in the i^{th} trap state, $\tau_{c,i}$ is the capture time for the i^{th} trap, and $\tau_{r,i}$ is the release time for the i^{th} trap.

Multiple trapping models can also be formulated in terms of a continuum of trap levels [185]

$$\frac{\partial n}{\partial t} + \nabla \cdot \mathbf{j} = \int_{-\infty}^{0} -\nu_c g(\epsilon) n + \nu_r e^{\epsilon/k_B T} n_t(\epsilon)\, d\epsilon \tag{2.21}$$

$$\frac{\partial n_t(\epsilon)}{\partial t} = \nu_c g(\epsilon) n - \nu_r e^{\epsilon/k_B T} n_t(\epsilon), \tag{2.22}$$

where $g(\epsilon)$ is the density of trap sites, ν_c is a capture rate, ν_r is a release rate, and $n_t(\epsilon)$ is the number density of trapped sites at energy ϵ. Here, energies are measured with respect to the conduction band, i.e. $\epsilon = 0$ is the edge of the conduction band and more negative energies represent states lower in energy. Carriers are thermally excited out of their localised states, and deeper traps have concomitantly slower release rates.

The above formulations implicitly assume that the charge concentration is low compared with the number of trap sites, because the rate of trapping does not consider the amount of charge already trapped. If the number of charges becomes comparable with the number of trap sites, then "trap filling" effects need to be included. Trap filling can be modelling by introducing a factor of the form $1 - f$, where f is the fractional occupancy of the trap site [185]. This causes the equations to become nonlinear.

Multiple trapping can model dispersive transport if the density of states $g(\epsilon)$ is chosen correctly. Carriers relaxing within an *exponential* density of states exhibit dispersive transport with a temperature dependent dispersion parameter $\alpha = T/T_c$, where T_c represents the width of the exponential density of states [184,186,187]. Other density of states distributions may give rise to alternative behaviour. Further details of multiple trapping and its implementation are discussed in the following chapter.

2.5.5 Continuous time random walks

The continuous time random walk (CTRW) was an early model for dispersive transport that has been particularly influential [77,188–190]. This is a microscopic scheme where carriers make random hops in space. Crucially, the time between hops is also random. The scheme is described by a probability density function (pdf) $\psi(\mathbf{z}, t)$, where $\psi(\mathbf{z}, t)d\mathbf{z}dt$ is the probability of a jump of length $\mathbf{z}$ to $\mathbf{z} + d\mathbf{z}$ occurring after a delay of duration t to $t + dt$.

To analyse a CTRW, we define the waiting time (or hopping time) pdf $\phi(t)$ and jump length pdf $\lambda(\mathbf{z})$ as:

$$\phi(t) = \int \psi(z, t)d^3\mathbf{z}, \qquad \lambda(\mathbf{z}) = \int_0^\infty \psi(\mathbf{z}, t)dt, \tag{2.23}$$

where the integration with respect to $\mathbf{z}$ is taken over the full extent of all spatial coordinates in the relevant coordinate system.

It is possible to solve this scheme analytically [191]. To do this, we introduce the pdf $\eta(\mathbf{z}, t)$, which is the probability of *just* having arrived at a point $\mathbf{z}$. The probability of arriving at a point $\mathbf{z}$ at time t is the combined probabilities of all the jumps that could terminate there. This is the integral over all possible jump lengths and times,

$$\eta(\mathbf{z}, t) = \delta(t)p_0(\mathbf{z}) + \int \int_0^t \eta(\mathbf{z}', t')\psi(\mathbf{z} - \mathbf{z}', t - t')dt'd^3\mathbf{z}', \tag{2.24}$$

where $p_0(\mathbf{z})$ is the initial condition, that is, the probability of finding a carrier at position $\mathbf{z}$ at time $t = 0$. As above, the integral over $\mathbf{z}'$ is taken over the full extent of all the spatial coordinates. Recognising that the integrals are convolutions, we are

motivated to take a Laplace-Fourier transform[1] to algebraically solve for η:

$$\begin{aligned} \eta(\mathbf{k},s) &= p_0(\mathbf{k}) + \eta(\mathbf{k},s)\psi(\mathbf{k},s) \\ \eta(\mathbf{k},s) &= \frac{p_0(\mathbf{k})}{1-\psi(\mathbf{k},s)}. \end{aligned} \tag{2.25}$$

The probability that a carrier is still located at a position $\mathbf{z}$ some time after it initially arrived there depends upon the survival probability. The survival probability is the probability of not hopping away:

$$\Phi(t) = 1 - \int_0^t \phi(t')dt'. \tag{2.26}$$

Combining these, the overall probability density function for a carrier being at a position $\mathbf{z}$ at time t is

$$p(\mathbf{z},t) = \int_0^t \eta(\mathbf{z}, t-t')\Phi(t')dt'. \tag{2.27}$$

In Fourier-Laplace space,

$$\begin{aligned} p(\mathbf{k},s) &= \eta(\mathbf{k},s)\Phi(s) \\ &= \eta(\mathbf{k},s)\left[\frac{1}{s} - \frac{\phi(s)}{s}\right] \\ &= \frac{p_0(\mathbf{k})}{1-\psi(\mathbf{k},s)}\frac{1-\phi(s)}{s}. \end{aligned} \tag{2.28}$$

Equation (2.28) gives an analytic solution to any CTRW defined by a probability density function $\psi(\mathbf{z},t)$, where $\psi(\mathbf{z},t)$ is the probability of making a hop with displacement $\mathbf{z}$ after a time t, and where $\phi(t) = \int \psi(z,t)d^3\mathbf{z}$ is the waiting time distribution. The behaviour of this solution depends strongly upon the moments of ψ. For the purposes of illustration, we now simplify the problem to one spatial dimension. The characteristic waiting time T and the jump length variance Σ^2 are

$$\phi(t) = \int_{-\infty}^{\infty} \psi(z,t)dz \qquad \lambda(z) = \int_0^{\infty} \psi(z,t)dt \tag{2.29}$$

$$T = \int_0^{\infty} t\phi(t)dt, \qquad \Sigma^2 = \int_{-\infty}^{\infty} z^2\lambda(z)dz. \tag{2.30}$$

Various types of CTRW scheme can be classified according to whether T and Σ^2 are finite or divergent. Classical transport occurs when both T and Σ^2 are finite. An example of such a system is charge carriers in crystalline semiconductors. The fact that T and Σ^2 are finite implies that the pdf $\psi(k,s)$ has the power series expansion in Laplace-Fourier space

$$\psi(k,s) = 1 - sT - iM_1k - \frac{\Sigma^2k^2}{2} + ..., \tag{2.31}$$

[1]Transformed functions are denoted by explicit dependence on the Laplace variable s and Fourier variable $\mathbf{k}$. The combined transformation is $f(\mathbf{k},s) = \int\int_0^t f(\mathbf{z},t)\exp(-st)\exp(-i\mathbf{k}\cdot\mathbf{z})dtd\mathbf{z}$.

where M_1 is the first moment of $\lambda(z)$. We substitute this distribution into the CTRW solution (2.28), discarding the higher order terms:

$$n(k,s) = \frac{n_0(k)}{iM_1k/T + \Sigma^2k^2/2T + s}.$$

Rearranging,

$$sn(k,s) - n_0(k) + \frac{iM_1k}{T}n(k,s) + \frac{\Sigma^2k^2}{2T}n(k,s) = 0$$

and inverting the Laplace and Fourier transforms yields

$$\frac{\partial n}{\partial t} + \frac{M_1}{T}\frac{\partial n}{\partial z} - \frac{\Sigma^2}{2T}\frac{\partial^2 n}{\partial z^2} = 0.$$

This is the classical advection-diffusion equation with normal drift and diffusion terms. Consequently, a CTRW with finite moments T and Σ^2 obeys a diffusion equation.

Conversely, if T is divergent but Σ^2 remains finite, the CTRW describes dispersive transport [192]. Early development of this model [77, 193, 194] introduced an *ad hoc* waiting time distribution $\phi(t) \sim t^{-\alpha-1}$ with $0 < \alpha < 1$. This model predicts time-of-flight current transients of the form [77],

$$i(t) \sim \begin{cases} t^{-1+\alpha}, & t \leq t_{tr} \\ t^{-1-\alpha}, & t \geq t_{tr}, \end{cases} \tag{2.32}$$

where t_{tr} is the transit time of the carriers. Recall that these are exactly as observed in many dispersive systems, complete with a "sum of slopes" of -2. This model was successfully applied to dispersive transport in a variety of materials [78].

Since the regular diffusion equation cannot describe dispersive transport, it is interesting to solve the dispersive CTRW to see what kind of *generalised diffusion equation* results. To illustrate, we shall use the following power series expansion with a divergent first moment in time [191, 195]

$$\psi(k,s) = 1 - (s\tau)^\alpha - iM_1k - \frac{\Sigma^2k^2}{2} + ..., \tag{2.33}$$

where $0 < \alpha < 1$ and τ is a time scale parameter. Using this distribution in the CTRW solution (2.28),

$$n(k,s) = \frac{s^{\alpha-1}n_0(k)}{iM_1k/\tau^\alpha + \Sigma^2k^2/2\tau^\alpha + s^\alpha}.$$

Rearranging,

$$s^\alpha n(k,s) - s^{\alpha-1}n_0(k) + \frac{iM_1k}{\tau^\alpha}n(k,s) + \frac{\Sigma^2k^2}{2\tau^\alpha}n(k,s) = 0. \tag{2.34}$$

The first two terms are reminiscent of a Laplace-transformed derivative. Indeed, if we put $\alpha = 1$, then we have the first derivative. However, we previously specified

α to be strictly less than one. We can use *fractional calculus* to invert this Laplace transform and obtain a diffusion equation for dispersive transport. We shall introduce fractional calculus next, and then return to Eq. (2.34).

2.5.6 Fractional Calculus

A brief aside: the Leibniz notation for a derivative of order n, $\frac{d^n y}{dx^n}$, is suggestive. The notation itself tempts thoughts about how this expression could be interpreted for *arbitrary* values of n. One could consider a "half-derivative", $n = \frac{1}{2}$. Applying the "half-derivative" twice should be equivalent to an ordinary derivative. Indeed, *arbitrary* orders could be defined.

Modern mathematical tools allow the development of fractional calculus quite succinctly [196, 197]. It is easiest to first consider arbitrary orders of integration.

Fractional Integration

We begin by considering the integration identity of the Laplace transform:

$$\mathcal{L}\left\{\int_0^t f(t)dt\right\} = \frac{\mathcal{L}\{f(t)\}}{s} \equiv \frac{F(s)}{s}, \tag{2.35}$$

where $\mathcal{L}\{\cdot\}$ is the Laplace transform, and the Laplace transform of $f(t)$ is written $F(s)$. By repeated application of this identity, one can generalise this expression to the n-fold integral

$$\mathcal{L}\left\{\underbrace{\int_0^t \int_0^t \cdots \int_0^t}_{n \text{ times}} f(t) \; \underbrace{dt\, dt \cdots dt}_{n \text{ times}}\right\} = \frac{F(s)}{s^n}. \tag{2.36}$$

For clarity of notation, we introduce the integral operator

$$I_t^n f(t) \equiv \underbrace{\int_0^t \int_0^t \cdots \int_0^t}_{n \text{ times}} f(t) \; \underbrace{dt\, dt \cdots dt}_{n \text{ times}}, \qquad n \in \mathbb{N}^+, \tag{2.37}$$

where $\mathbb{N}^+ = \{1, 2, 3, \cdots\}$. The Laplace transform of the integral operator is then

$$\mathcal{L}\{I_t^n f(t)\} = \frac{F(s)}{s^n}. \tag{2.38}$$

The expression on the right hand side could be interpreted as the product of two functions, $F(s)$ and s^{-n}. A product in Laplace space is a convolution in the time domain. Noting that the inverse Laplace transform of s^{-n} is $t^{n-1}/(n-1)!$, we have:

$$I_t^n f(t) = \frac{1}{(n-1)!} \int_0^t (t-\tau)^{n-1} f(\tau) d\tau. \tag{2.39}$$

This is the Cauchy formula for repeated integration.

The operator I^n in Eq. (2.39) was defined for natural numbers n, but one could envisage the formal replacement of n by some arbitrary number α. To achieve this, it is necessary to exchange the factorial with the Gamma function. Consequently, we arrive at

$$I_t^\alpha f(t) \equiv \frac{1}{\Gamma(\alpha)} \int_0^t (t-\tau)^{\alpha-1} f(\tau) d\tau, \qquad \Re(\alpha) > 0, \tag{2.40}$$

which defines the fractional integral. It is necessary that $\Re(\alpha) > 0$ for this integral to converge.

The Laplace space representation is straightforward:

$$\mathcal{L}\{I_t^\alpha f(t)\} = \frac{F(s)}{s^\alpha}. \tag{2.41}$$

Equation (2.40) and its Laplace transform (2.41) define *fractional integration*. For example, a "half-integral" is obtained for $\alpha = \frac{1}{2}$. The Laplace representation (2.41) makes it clear that applying the "half-integral" twice is equivalent to an ordinary integral of the first order.

Fractional Derivatives

Fractional integration is elegantly defined by the generalisation of the repeated integration formula (2.39). Unfortunately, there is no corresponding formula for "repeated differentiation." So how to form a fractional derivative?

The solution is to combine ordinary derivatives and fractional integration. To form a derivative of order α, we differentiate m times (where m is the next integer larger than α), and integrate $m - \alpha$ times. However, the order of application is significant. Integration and differentiation operators do not commute, so we immediately arrive at two alternative definitions [198],

$$\text{Riemann-Liouville derivative, } {}^{RL}D_t^\alpha \equiv \frac{d^m}{dt^m} I_t^{m-\alpha} \tag{2.42}$$

$$\text{Caputo derivative, } {}^{C}D_t^\alpha \equiv I_t^{m-\alpha} \frac{d^m}{dt^m}. \tag{2.43}$$

In general, these two derivatives are different operators. When α becomes an integer, then both types of derivative reduce to the standard operator $\frac{d^m}{dt^m}$, because I_t^0 is the identity operator[2].

For the case where $0 < \alpha \leq 1$, these two forms of derivative have the Laplace transforms

$$\mathcal{L}\left\{{}^{RL}D_t^\alpha f(t)\right\} = s^\alpha F(s) - \lim_{t\to 0^+} I_t^{1-\alpha} f(t) \tag{2.44}$$

$$\mathcal{L}\left\{{}^{C}D_t^\alpha f(t)\right\} = s^\alpha F(s) - s^{\alpha-1} f(0). \tag{2.45}$$

Notice that the Riemann-Liouville derivative has a *fractional* initial condition, whereas the Caputo derivative has the usual initial condition. It is not always clear how this

[2]This can be easily seen from the Laplace space definition Eq. (2.41).

fractional initial condition can be obtained from physical measurement, although some models do admit such a physical interpretation [199]. Nevertheless, the additional work required to define the initial condition is a weakness of Riemann-Liouville formulations.

2.5.7 Fractional diffusion

We are now able to return to the equation in Section 2.5.5 that contained a Laplace transformed "derivative" that we could not invert. Recall that we were considering the analytic solution in Fourier-Laplace space of a continuous time random walk describing dispersive transport, which is repeated here for clarity:

$$s^{\alpha}n(k,s) - s^{\alpha-1}n_0(k) + iM_1kn(k,s) + \frac{\Sigma^2k^2}{2\tau^{\alpha}}n(k,s) = 0.$$

We now recognise the first two terms on the left hand side as a Caputo fractional derivative. Consequently, we can invert the transforms, and obtain a *fractional diffusion equation*

$$ {}_0^C D_t^{\alpha} n + \frac{M_1}{\tau^{\alpha}}\frac{\partial n}{\partial z} - \frac{\Sigma^2}{2\tau^{\alpha}}\frac{\partial^2 n}{\partial z^2} = 0. \tag{2.46}$$

Here, M_1/τ^{α} is a generalised drift velocity with units $(\text{length})\,(\text{time})^{-\alpha}$, and $\Sigma^2/2\tau^{\alpha}$ is a generalised diffusion coefficient with units $(\text{length})^2\,(\text{time})^{-\alpha}$. In the limit $\alpha \to 1$, the classical diffusion equation is recovered.

Equation (2.46) is one of many fraction diffusion equations that have been proposed [23]. The various models can be separated into two main categories, depending upon whether they model the *total* charge in the system or only the *untrapped* charge.

The example above began with a CTRW framework, describing total charge. The result is Eq. (2.46), or equivalently [200, 201]

$$ {}_0^C D_t^{\alpha} n(x,t) + W_{\gamma}\frac{\partial n}{\partial x} - D_{L,\gamma}\frac{\partial^2 n}{\partial x^2} = 0. \tag{2.47}$$

We will return to Eq. (2.47) in Chapter 8, where we will present mathematical advances related to its efficient analytic solution. This model can also be cast into the form of a Riemann-Liouville derivative and a source term [24]

$$ {}_0^{RL} D_t^{\alpha} n(x,t) + W_{\gamma}\frac{\partial n}{\partial x} - D_{L,\gamma}\frac{\partial^2 n}{\partial x^2} = \frac{n(x,0)t^{-\alpha}}{\Gamma(1-\alpha)}. \tag{2.48}$$

Alternatively, if one begins with a multiple trapping framework—describing untrapped charge—the result is a fractional diffusion equation with a Riemann-Liouville derivative but *no* source term [185, 202]

$$ {}_0^{RL} D_t^{\alpha} + W_{\gamma}\frac{\partial n}{\partial x} - D_{L,\gamma}\frac{\partial^2 n}{\partial x^2} = 0. \tag{2.49}$$

This equation has a peculiar feature: it does not conserve number density. This is understood to represent the permanent loss of charges to deep trap states from which they will not be released [203].

Fractional diffusion equations such as these can be solved analytically, often by utilising the Laplace transform or by invoking special functions [204–206].

2.5.8 Kinetic theory

Diffusion equations are extremely popular transport models, however, they are necessarily a special case of a more fundamental system. For example, the standard diffusion equation is an approximation to kinetic theory [207]. Kinetic theory describes particle distributions as a function of position *and velocity*, and is consequently able to capture more of the underlying physics. The relationship between kinetic theory and the diffusion equation is well established. Diffusion equations are valid in the limit of long times and small gradients [207]. They are useful because these assumptions are often well met, and their simplicity outweighs their small inaccuracy.

On the other hand, *fractional* diffusion equation is typically developed from a probabilistic, random-walk model rather than a kinetic theory. For example, Eq. (2.46) results from the truncation of a power series [Eq. (2.33)]. The type of kinetic model that would give rise to a fractional diffusion equation has not been widely studied. Such a model is developed and studied in Chapter 9.

2.6 Conclusion

Organic semiconductors are promising and exciting materials, but they are hampered by poor performance and complex physics. Experimental characterisation of transport physics is challenging. Consequently, modelling plays a key role in understanding experimental results. There are two board categories of model which are used for this purpose: microscopic models (such as the Gaussian Disorder Model), which track individual charges as they hop between sites; and macroscopic models (such as the drift-diffusion equation), which describe the evolution of the number density. Drift-diffusion models are advantageous due to their computational efficiency and the macroscopic nature of their input parameters. The development and implementation of a drift-diffusion model will be described in the following chapter.

3

Device Modelling and Numerical Methods

This chapter describes the development and implementation of a numerical simulation program. The model is a one-dimensional generalised drift-diffusion-recombination solver that is implemented in MATLAB. Its development begins with specification of equations that describe drift, diffusion, charge generation, and recombination. Next, we discuss non-dimensionalisation, in which the physical quantities are scaled into dimensionless units, yielding physical insights into the true degrees of freedom of the model. Finally, the implementation details are presented.

3.1 The One-Dimensional Drift-Diffusion Model

We are developing a model for thin film devices where the film thickness (d) is much less than the width or height of the electrodes. As a consequence, almost all of the spatial variation will be confined to the direction normal to the electrodes, which we define as x, and consequently a one-dimensional model is a useful approximation. We specify that the semiconductor occupies the region $0 \leq x \leq d$.

The drift-diffusion model [67] asserts that the conduction current density consists of a drift component and a diffusive component:

$$j_p(x,t) = e\mu_p E(x,t)p(x,t) - \mu_p k_B T \frac{\partial p}{\partial x} \tag{3.1}$$

$$j_n(x,t) = e\mu_n E(x,t)n(x,t) + \mu_n k_B T \frac{\partial n}{\partial x}, \tag{3.2}$$

where j_p (j_n) is the conduction current density due to holes (electrons), e is the elementary charge, μ_p (μ_n) is the mobility of holes (electrons), E is the electric field, p (n) is the number density of holes (electrons), k_B is the Boltzmann constant, and T is the temperature.

We utilised the Einstein relation for the diffusion coefficient, $D = \mu k_B T/e$, to represent the diffusion coefficient in terms of the mobility and temperature. The validity of the Einstein relation in organic semiconductors is sometimes disputed [172], but is generally supported [173]. We note that variations from the Einstein relation could be incorporated by introducing a prefactor to the diffusion terms in Eqs. (3.1) and (3.2) [174].

Applying the principle of conservation of charge, we write continuity equations for electrons and holes:

$$\frac{\partial p}{\partial t} + \frac{1}{e}\frac{\partial j_p}{\partial x} = g(x,t) - r(x,t) \tag{3.3}$$

$$\frac{\partial n}{\partial t} - \frac{1}{e}\frac{\partial j_n}{\partial x} = g(x,t) - r(x,t), \tag{3.4}$$

where the source-sink terms on the right hand side represent the generation rate g and recombination rate r.

The electric field E will be specified using Poisson's equation

$$\frac{\partial^2 V}{\partial x^2} = \frac{e(n-p)}{\epsilon\epsilon_0} \tag{3.5}$$

$$E = -\frac{\partial V}{\partial x}, \tag{3.6}$$

where $V(x,t)$ is the electric potential, and $\epsilon\epsilon_0$ is the permittivity of the semiconductor. As a voltage reference, we choose $V(d)$, where d is the thickness of the semiconductor:

$$V(d) = 0. \tag{3.7}$$

For notational convenience, we define $U(t)$ as the voltage across the semiconductor:

$$U(t) = V(0,t) - V(d,t) = \int_0^d E(x,t)dx. \tag{3.8}$$

3.1.1 Measurement Circuit

A typical measurement circuit is shown in Figure 3.1. Here, the sample under test is placed in series with a load resistor, and a function generator is used to apply a voltage. The quantity of interest is the current $i(t)$, measured using the load resistor and an oscilloscope. As mentioned above and shown in Figure 3.1, the voltage ground reference is taken to be one of the electrodes.

By applying Kirchhoff's voltage law to the circuit, we find

$$V_{psu}(t) = U(t) + i(t)R, \tag{3.9}$$

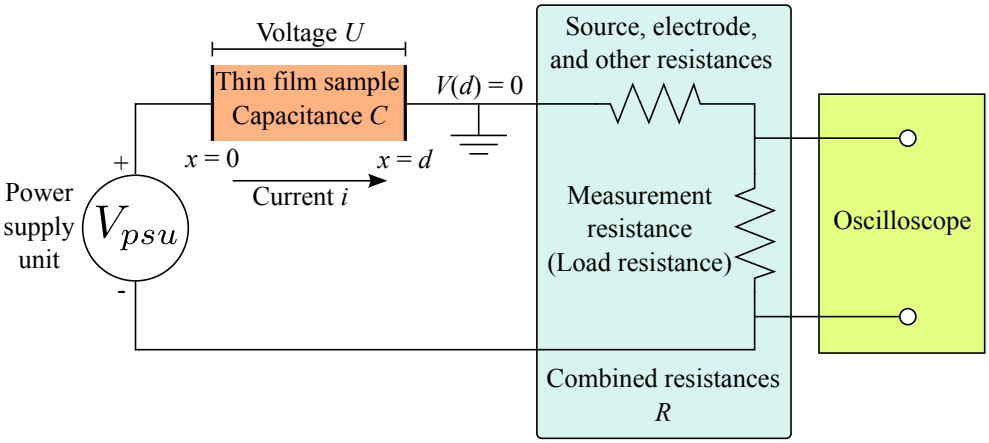

Figure 3.1: A typical measurement circuit for transient measurements. All circuit resistances are lumped together as R, while the capacitance of the thin film sample is C. A power supply unit generates a waveform $V_{psu}(t)$, which is applied to the RC circuit. The resulting current is measured using a load resistance and an oscilloscope.

where the symbols are defined in Figure 3.1. The voltage across the thin film sample $U(t)$ arises due to the charge accumulating on the capacitive plates. The current i must be same everywhere in the circuit, due to Kirchhoff's current law. It will consist of both a conduction current i_c and a displacement current i_d

$$\begin{aligned} i(t) &= i_c(t) + i_d(t) \\ &= S\left[j_n\left(x_1,t\right) + j_p\left(x_1,t\right) + \epsilon\epsilon_0\frac{\partial E(x_1,t)}{\partial t}\right], \end{aligned} \tag{3.10}$$

where S is the surface area of the device, $j_n(x)$ and $j_p(x)$ are the conduction current densities for electrons and holes, respectively; and x_1 is any point inside the sample. The current must be the same everywhere, so x_1 is arbitrary within the range $0 < x_1 < d$. Defining the total conduction current density $j_c = j_p + j_n$, and integrating across the thickness of the film:

$$\begin{aligned} \int_0^d i(x,t)dx &= S\int_0^d j_c(x,t)dx + S\epsilon\epsilon_0\frac{\partial}{\partial t}\int_0^d E(x,t)dx \\ \Rightarrow\ i(t) &= S\left\langle j_c(t)\right\rangle + C\frac{\partial U}{\partial t}, \end{aligned} \tag{3.11}$$

where $C = S\epsilon\epsilon_0/d$ is the geometric capacitance of the device, and the angle brackets denote a spatial average.

Combining Eqs. (3.9) to (3.11), we obtain

$$RC\,\frac{dU}{dt} = V_{psu}(t) - U(t) - i_c(t)R, \tag{3.12}$$

where the conduction current $i_c(t) = S\left\langle j_c(t)\right\rangle$. Equation (3.12) is the form we will use to incorporate the measurement circuit in the model. In the limit of $R \to 0$, we find $V_{psu} = U$. Therefore, in the model, we can "turn off" the effects of the external circuit by setting the parameter R to zero.

3.1.2 Photogeneration of carriers

Most experiments involve the photogeneration of carriers. Often, a brief flash of light is used at the beginning of the experiment. We will model this behaviour by setting the initial values of n and p according to an optical absorption model [133, 208]. The initial condition will be

$$n(x,0) = p(x,0) = Q_{ph}Q_1(x), \tag{3.13}$$

where Q_{ph} is a scaling prefactor that indicates the quantity of photogenerated charge, and $Q_1(x)$ is the photogeneration profile normalised such that $\int_0^d Q_1(x)dx = 1$. Note that Q_{ph} implicitly includes the quantum efficiency for free carrier generation. The spatial profile $Q_1(x)$ will be determined by a photogeneration model. For example, the Beer-Lambert law would give

$$Q_1(x) = \frac{\alpha}{1 - e^{-\alpha d}} e^{-\alpha x} \tag{3.14}$$

if the photogeneration is from the $x = 0$ side, or

$$Q_1(x) = \frac{\alpha}{1 - e^{-\alpha d}} e^{-\alpha(d-x)}, \tag{3.15}$$

if the photogeneration is from the $x = d$ side. Here, α is the absorption coefficient. We should highlight that the numerical solver that implements this model will permit arbitrary specification of the photogeneration profile $Q_1(x)$.

Another possible setup is continuous illumination. This will be modelled using a generation term in the continuity equation:

$$\left.\frac{\partial p}{\partial t}\right|_{\text{photogeneration}} = \left.\frac{\partial n}{\partial t}\right|_{\text{photogeneration}} = G(t)Q_1(x), \tag{3.16}$$

where $G(t)$ gives the light intensity in units of generated charge carriers per unit area per unit time.

3.1.3 Recombination

There are two types of recombination that need to be considered: geminate and non-geminate [82–84]. Geminate recombination occurs when the recombining carriers originated from the same photon. Any movement of these carriers cannot contribute to the electrical current, because the net movement of one carrier is perfectly compensated by the identical net movement of the other. Consequently, from an electrical perspective, the geminate recombination rate can be incorporated into the quantum efficiency for charge generation (i.e., through Q_{ph}). That is the approach that we will take for this model.

Non-geminate recombination includes both band-to-band recombination and trap-assisted recombination. The relevant equations are (Section 2.3.3 and ref. [105])

$$\left.\frac{\partial p}{\partial t}\right|_{\text{recomb.}} = -\frac{\beta}{\beta_L}\frac{e\left(\mu_n+\mu_p\right)}{\epsilon\epsilon_0}np - \frac{\beta}{\beta_L}\frac{e\mu_p}{\epsilon\epsilon_0}n_t p \tag{3.17}$$

$$\left.\frac{\partial n}{\partial t}\right|_{\text{recomb.}} = -\frac{\beta}{\beta_L}\frac{e\left(\mu_n+\mu_p\right)}{\epsilon\epsilon_0}np - \frac{\beta}{\beta_L}\frac{e\mu_n}{\epsilon\epsilon_0}np_t \tag{3.18}$$

$$\left.\frac{\partial p_t}{\partial t}\right|_{\text{recomb.}} = -\frac{\beta}{\beta_L}\frac{e\mu_n}{\epsilon\epsilon_0}np_t \tag{3.19}$$

$$\left.\frac{\partial n_t}{\partial t}\right|_{\text{recomb.}} = -\frac{\beta}{\beta_L}\frac{e\mu_p}{\epsilon\epsilon_0}n_t p, \tag{3.20}$$

where n and p are the number densities of free electrons and holes, respectively; n_t and p_t are the number densities of trapped electrons and holes, respectively; β/β_L is a prefactor to account for non-Langevin recombination; and $e\left(\mu_n+\mu_p\right)/\epsilon\epsilon_0$ is the Langevin coefficient.

Note that we have assumed that band-to-band recombination and trap-assisted recombination are both described by the same reduction factor β/β_L. This simplifying assumption is made on the basis of experimental evidence that trap-assisted recombination in certain systems is described by a Langevin-like expression with one of the mobilities set to zero [105]. Additionally, this assumption is physically reasonable in near-to-Langevin systems such as most organic solar cells, because the limiting step is likely to be charge transport. However, the model could be easily extended to cover the case where trap-assisted recombination is governed by a different reduction factor.

3.1.4 Boundary Conditions

Precise modelling of the interface between a metallic electrode and an organic semiconductor is difficult, primarily because of challenges in quantifying the exact nature of the interface, and fabricating reproducible samples [209, 210]. Consequently, we will consider simplified boundary conditions that represent *ideal* behaviour. Our intent is to model the bulk transport without the influence of non-ideal boundaries.

For the continuity equations (3.1)-(3.2), there are four boundary conditions that need to be specified: two species of charged particle each interacting with two electrodes. For each species of charged particle, we can categorise one electrode as the "injecting" boundary and the other electrode as the "extracting" boundary. For example, holes inject at the boundary where the electric field points into the device, whereas electrons inject at the boundary where the electric field points out of the device. With this terminology, we can define several boundary conditions:

Outflow boundary condition—This is the default boundary condition for reverse bias experiments such as photo-CELIV (Chapter 4) and RPV (Chapters 5 and 6). This boundary condition allows unimpeded charge extraction, and guarantees that charges will escape into the electrode provided that there is an electric field to drive them. At the extracting boundaries, the current is given by the drift term $j_p = e\mu_p Ep$,

and similarly for electrons. This is an ideal boundary condition in the sense that the presence of the boundary does not interfere with the charge carrier density other than to provide a sink for extracted charges. This boundary condition has been used for ideal extracting electrodes in analytic solutions and numerical simulations [122, 133]. At the *injecting* boundaries, the current is set to zero ($j_p = 0$ and $j_n = 0$), because that is the ideal case for reverse bias.

Ohmic boundary condition (zero field)—This is the default boundary condition for forward bias experiments that involve the injection of charge carriers. This boundary condition represents perfect charge injection by specifying that the electric field at the injecting electrode is zero, because if it were non-zero there would be a current that injects more carriers until the field is completely screened. Numerically, the implementation calculates the number density needed just inside the semiconductor so that the field at the semiconductor-electrode interface satisfies $|E| < \epsilon$ where ϵ is a small threshold. This boundary condition was used by Lampert and Mark [118] for their analytic solutions of various carrier injection problems. These analytic solutions are valuable because they can be used to benchmark the accuracy of the numeric solver. The extracting boundaries are the same as for the *Outflow* case, which matches the analytic solutions that are available [118].

Ohmic boundary condition (Boltzmann statistics)—As an alternative mechanism to implement Ohmic injection, the number density at the boundaries can be held fixed, to simulate Boltzmann statistics where the semiconductor edge is in thermal equilibrium with the reservoir of charges in the metal [20]. According to this boundary condition, the injecting electrode has the fixed number density

$$n(0) = N_c, \tag{3.21}$$

while the extracting electrode has

$$p(0) = N_c \exp\left(\frac{-E_{gap}}{kT}\right),$$

where N_c is an effective density of states and E_{gap} is the bandgap energy (i.e. the difference between the LUMO of the acceptor and the HOMO of the donor). In this boundary condition, the effective density of states N_c becomes a free parameter that must be fit from experimental data (such as JV curves).

Blocking boundary condition—The blocking boundary condition is relevant when an insulating layer contacts the semiconductor, rather than a metal. Blocking boundary conditions set the current to zero.

Some boundary conditions specify the conduction current, and others specify the number density. A combination of these could be specified (e.g. Ohmic injection at one side of the device and a blocking boundary at the other side), or the system could transition from one to another (e.g. when charges are injected and then later extracted). The dynamic switching between boundary conditions of different types requires careful implementation in the code.

The boundary conditions for Poisson's equation are

$$\begin{aligned} V(0) &= U(t) \\ V(d) &= 0, \end{aligned}$$

where $U(t)$ is the voltage across the semiconductor that is determined via solution of Eq. (3.12).

3.1.5 Summary of Model

The basic one-dimensional semiconductor model developed in this section can be summarised by the following system of equations:

$$j_p(x,t) = e\mu_p E(x,t)p(x,t) - \mu_p k_B T \frac{\partial p}{\partial x} \tag{3.22}$$

$$j_n(x,t) = e\mu_n E(x,t)n(x,t) + \mu_n k_B T \frac{\partial n}{\partial x} \tag{3.23}$$

$$i_c = \langle j_p + j_n \rangle S \tag{3.24}$$

$$\frac{\partial p}{\partial t} + \frac{1}{e}\frac{\partial j_p}{\partial x} = g(x,t) - r(x,t) \tag{3.25}$$

$$\frac{\partial n}{\partial t} - \frac{1}{e}\frac{\partial j_n}{\partial x} = g(x,t) - r(x,t) \tag{3.26}$$

$$g(x,t) = Q_{gen}(t)Q_1(x) \tag{3.27}$$

$$r(x,t) = \beta np \tag{3.28}$$

$$\frac{\partial^2 V}{\partial x^2} = \frac{n-p}{\epsilon\epsilon_0} \tag{3.29}$$

$$E = -\frac{\partial V}{\partial x} \tag{3.30}$$

$$U(t) = \int_0^d E(x,t)dx \tag{3.31}$$

$$RC\,\frac{dU}{dt} = V_{psu}(t) - U(t) - i_c R. \tag{3.32}$$

3.2 Non-Dimensionalisation

Non-dimensionalisation means that the model equations are converted into a dimensionless system of units. Ideally, the parameters should be scaled such that physically reasonable values have magnitudes not too far from unity, because such a scaling will make the numerics easier and more accurate. (Differential equation solvers—especially implicit solvers—work best when all variables are approximately the same order of magnitude.) Normalising the model has the added benefit of eliminating redundant degrees of freedom in the parameter space, and thereby identifying the relationships between variables.

To perform the normalisation, we need to select reference scales for physical units such as time, voltage, and length. Here, we start with an elegant scaling published by

Juška [106,122], and then extend it. In this section, we denote dimensionless quantities with a prime.

Voltage scale—The obvious voltage scale for normalisation is the maximum voltage for CELIV and the applied voltage for TOF and other experiments. However, we would like to retain the freedom to vary the applied voltage without rescaling other parameters, if it should be necessary. Therefore, we define a *reference voltage* U_{ref} as the voltage scale. We normalise the maximum voltage (for CELIV), or applied voltage (for ToF) in terms of this reference

$$U'_{max} = \frac{U_{max}}{U_{ref}}.$$

Almost always we take $U'_{ref} = 1$, which corresponds to choosing U_{max} as the voltage reference. We normalise all voltages to the reference voltage

$$U' = \frac{U}{U_{ref}}$$

such that $0 \leq U' \leq U'_{ref}$ is the range of applied voltages for CELIV models and $U' = U'_{ref}$ is the applied voltage for ToF models.

Length scale—The natural length scale is the width of the sample (d), and we normalise the position coordinate as $x' = x/d$.

Time scale—While the natural time scale is the transit time of carriers, in the case of CELIV experiments we will instead use the pulse duration, t_{pulse}. This choice of units makes it easier to reason about the impact of changing the voltage slope. By normalising to t_{pulse}, we can vary the voltage slope without changing the entire system of units for measuring time. Consequently, we normalise the time coordinate as

$$\begin{aligned} t' &= \frac{t}{t_{scale}} \\ t_{scale} &= \begin{cases} t_{pulse}, & \text{(CELIV experiment)} \\ \frac{d^2}{\mu_p U_{ref}}, & \text{(other experiments).} \end{cases} \end{aligned}$$

Charge scale—We use the charge on the electrodes at the reference voltage, $Q_{ref} = CU_{ref}/Sd$ to scale units of charge.

3.2.1 Consequences of this system of units

The above system of units requires the normalised electric field to be

$$E' = \frac{Ed}{U_{ref}}.$$

The CELIV voltage slope $A = U_{max}/t_{scale}$ has normalised value $A' = U'_{max}$. As mentioned above, we will almost always take $A' = 1$.

We normalise the number densities to the charge scale

$$\begin{aligned} n' &= \frac{enSd}{CU_{ref}} = \frac{end^2}{\epsilon_0 \epsilon_r U_{ref}} \\ p' &= \frac{epSd}{CU_{ref}} = \frac{epd^2}{\epsilon_0 \epsilon_r U_{ref}}, \end{aligned}$$

such that $n' = 1$ everywhere in the device would correspond to a charge of CU_{ref} distributed evenly.

We also normalise the mobility in terms of the above voltage, time and length scales:

$$\mu' = \frac{U_{ref} t_{scale}}{d^2} \mu.$$

For time-of-flight and other experiments where $t_{scale} = t_{tr}$, this system of units requires $\mu' = 1$. (More precisely, the faster carrier mobility is 1.) For CELIV experiments, the case of $t_{pulse} = t_{tr}$ corresponds to $\mu' = 2$, and therefore realistic CELIV transients will have $\mu' \geq 2$.

We normalise the circuit resistance to the time scale selected above:

$$R' = \frac{RC}{t_{scale}}.$$

This scaling is such that the time-of-flight experiment (where $t_{scale} = t_{tr}$) operates in differential mode when $R' \ll 1$ and in integral mode with $R' \gg 1$. Differential mode is required for classical time-of-flight, in which the measurement circuit does not substantially interfere with the measured current. Conversely, in integral mode, the measurement circuit acts as an analog integrator, and the measured signal is the integral of the TOF transient.

The above normalisations require the dimensionless current to be

$$i' = \frac{t_{scale}}{CU_{ref}} i,$$

while the dimensionless current density is

$$j' = \frac{t_{scale}}{CU_{ref}} Sj = \frac{t_{scale}}{CU_{ref}} i.$$

This implies $i' = j'$, i.e. the normalised current and current density are equal.

We normalise the recombination rate β to the Langevin rate, that is,

$$\beta' = \frac{\beta}{\beta_L},$$

such that a Langevin material will have $\beta' = 1$, while non-Langevin materials will have $\beta' < 1$.

Finally, we define the dimensionless temperature as

$$T' = \frac{k_B T}{eU_{ref}}.$$

3.2.2 CELIV specifics

In the CELIV experiment, the current can be separated into two components: the displacement current caused by the charging of a capacitor with a linearly increasing voltage, and the conduction current. As discussed in Chapter 2, the displacement current is given by

$$i_0 = \frac{dU}{dt}C = AC$$

where A is the slope of the applied triangle voltage. In normalised units, $i'_0 = U'_{max}$, and almost always $U'_{max} = 1$ such that the normalised displacement current is equal to unity. This is why t_{pulse} (rather than t_{tr}) is the preferred time scale for the CELIV experiment, because if t_{tr} were the time scale then the displacement current i'_0 would depend upon the mobility!

Since current and current density are equivalent in this system of units, we also have $j'_0 = U'_{max}$.

3.2.3 Normalised system of equations

The normalised system of equations are

$$\begin{aligned}
j'_p(x',t') &= \mu'_p E'(x',t')p'(x',t') - \mu'_p T' \frac{\partial p'}{\partial x'} && (3.33)\\
j'_n(x',t') &= \mu'_n E'(x',t')n'(x',t') + \mu'_n T' \frac{\partial n'}{\partial x'} && (3.34)\\
i'_c &= \left\langle j'_p + j'_n \right\rangle && (3.35)\\
\frac{\partial p'}{\partial t'} + \frac{\partial j'_p}{\partial x'} &= g'(x',t') - r'(x',t') && (3.36)\\
\frac{\partial n'}{\partial t'} - \frac{\partial j'_n}{\partial x'} &= g'(x',t') - r'(x',t') && (3.37)\\
g'(x',t') &= Q'_{gen}(t')Q'_1(x') && (3.38)\\
r'(x',t') &= \beta'(\mu'_p + \mu'_n)n'p' && (3.39)\\
\frac{\partial^2 V'}{\partial (x')^2} &= n' - p' && (3.40)\\
E' &= -\frac{\partial V'}{\partial x'} && (3.41)\\
U'(t) &= \int_0^1 E'(x',t')dx' && (3.42)\\
R' \frac{dU'}{dt'} &= V'_{psu}(t) - U'(t) - i'_c R'. && (3.43)
\end{aligned}$$

For the remainder of this chapter, we will drop the primes and write directly in normalised units unless otherwise specified.

3.3 Modelling Trapping and Dispersion

From a modelling perspective, we can treat both trapping and dispersion effects through a unified framework. The key insight that makes this possible is that number density can be "partitioned" into distributions *that have different mobilities*. A "mobility partition" is a partial number density, i.e.

$$n(x,t) = \sum_i n^i(x,t), \tag{3.44}$$

where n^i is the number density of particles in the i^{th} mobility partition.

Traps are simply mobility partitions with zero mobility, whereas non-trap partitions will have a nonzero mobility assigned to them. A mix of shallow and deep traps (with fast and slow release rates, respectively) can be modelled using multiple partitions, since the release rates of each partition can be specified independently. Similarly, a distribution of mobilities can be modelled by assigning different mobilities to each partition. Consequently, "mobility partitions" are a general framework that can implement a variety of physical effects.

To numerically implement mobility partitions, we recognise that they effectively introduce a new dimension to the number density distribution. Number density will be a function of position, time, and *mobility*. Discretisation along the mobility axis results in Eq. (3.44).

It is straightforward to extend the charge transport terms in the continuity equation,

$$j_p^i = \mu_p^i E p^i + \mu_p^i T \frac{\partial p^i}{\partial x} \tag{3.45}$$

$$\frac{\partial p^i}{\partial t} + \frac{\partial j_p^i}{\partial x} = g^i - r_p^i, \tag{3.46}$$

and similarly for electrons. (All equations in this section and for rest of this chapter are written in normalised units.)

The recombination term must be considered carefully, because recombination events could occur between any oppositely charged pair of mobility partitions with a rate proportional to the sum of their respectively mobilities. Generalising the trap-assisted recombination model given by Eqs. (3.17)-(3.20), we write a sum over all possible recombination targets:

$$\left.\frac{dp^i}{dt}\right|_{\text{recomb.}} = -\sum_j \left(\mu_p^i + \mu_n^j\right) \beta' p^i n^j. \tag{3.47}$$

A key assumption here is that the reduction factor $\beta' \equiv \beta/\beta_L$ is the same for all partitions. There is an experimental justification for this assumption in the case of trap-assisted recombination, where it has been shown that the recombination rate due to traps is related to the recombination rate due to free carriers, where the trap-assisted

case simply has the appropriate mobility set to zero [105]. In the absence of contrary evidence, we therefore keep the number of free parameters low by assuming the same reduction factor across all partitions.

New terms in the continuity equation are needed to model the movement of charges from one mobility partition to another, for example, the rates of trapping and de-trapping. In general, there might be a net movement of charge between any two mobility partitions i and j,

$$\left.\frac{\partial n^i}{\partial t}\right|_{\text{due to partition } j} = \nu_{ij}^{(n)} = -\nu_{ji}^{(n)} \tag{3.48}$$

where $\nu_{ij}^{(n)}$ is the net rate of movement of electrons from partition i to partition j, with the superscripts $^{(n)}$ used for electrons and $^{(p)}$ used for holes. This rate may be time and position dependent. For example, if n^0 represents free electrons and n^1 represents trapped electrons, then $\nu_{01}^{(n)}(x,t)$ is the *net* rate of trapping.

The inter-partition rate coefficients $\nu_{ij}^{(n)}$ (for electrons) and $\nu_{ij}^{(p)}$ (for holes) are calculated by one of the models discussed below. Any one of these models can be turned on for a given simulation, in which case the corresponding portion of code will be invoked to calculate $\nu_{ij}^{(n)}(x,t)$, $\nu_{ij}^{(p)}(x,t)$ and the mobilities of each partition $\mu_n^i(x,t)$ and $\mu_p^i(x,t)$.

3.3.1 Simple trapping

The simple trapping model includes one free mobility partition and one trapped mobility partition with fixed capture and release times. It is the simplest trapping model, and it is described by the equations [211]

$$\frac{\partial n_f}{\partial t} = -\frac{n_f}{\tau_c} + \frac{n_t}{\tau_r} \tag{3.49}$$

$$\frac{\partial n_t}{\partial t} = \frac{n_f}{\tau_c} - \frac{n_t}{\tau_r}, \tag{3.50}$$

where n_f is the free distribution, n_t is the trapped distribution, τ_c is the capture time, and τ_r is the release time. Separate capture and release times are specified for each type of carrier.

In the notation of mobility partitions, if n^0 represents free electrons and n^1 represents trapped electrons, then

$$\left.\frac{\partial n^0}{\partial t}\right|_{\text{due to partition } 1} = \nu_{01}^{(n)}(x,t) = -\frac{n^0}{\tau_c} + \frac{n^1}{\tau_r}. \tag{3.51}$$

3.3.2 Simple trapping with trap filling

The simple trapping with trap filling model introduces a blocking term to describe the filling up of trap states. The simple trapping model is modified by introducing a

"blocking factor" proportional to the number of unoccupied trap states that remain [185]

$$\frac{\partial n_f}{\partial t} = -\frac{n_f}{\tau_c}\left(\frac{N_t - n_t}{N_t}\right) + \frac{n_t}{\tau_r} \tag{3.52}$$

$$\frac{\partial n_t}{\partial t} = \frac{n_f}{\tau_c}\left(\frac{N_t - n_t}{N_t}\right) - \frac{n_t}{\tau_r}, \tag{3.53}$$

where N_t is the number of available trap states, n_f is the free distribution, n_t is the trapped distribution, τ_c is the capture time, and τ_r is the release time. Separate parameters (N_t, τ_c, τ_r) are again specified for each type of carrier.

Expressed as transition rates between mobility partitions,

$$\left.\frac{\partial n^0}{\partial t}\right|_{\text{due to partition 1}} = \nu_{01}^{(n)}(x,t) = -\frac{n^0}{\tau_c}\left(\frac{N_t - n^1}{N_t}\right) + \frac{n^1}{\tau_r}. \tag{3.54}$$

3.3.3 Multiple trapping

As described in Section 2.5.4, the multiple trapping model [212–215] considers traps to be distributed in energy space. The trapped distribution is $n_t(x,t,\epsilon)$ where ϵ is the energy below the conduction band. Then, the trapping and de-trapping terms in the continuity equation are:

$$\frac{\partial n_f}{\partial t} = \int_{-\infty}^{0} \frac{e^{\epsilon/k_B T} n_t(\epsilon)}{\tau_r} - \frac{g(\epsilon) n_f}{\tau_c}\, d\epsilon \tag{3.55}$$

$$\frac{\partial n_t(\epsilon)}{\partial t} = -\frac{e^{\epsilon/k_B T} n_t(\epsilon)}{\tau_r} + \frac{g(\epsilon) n_f}{\tau_c}, \tag{3.56}$$

where k_B is the Boltzmann constant, T is temperature, τ_r is a release time, τ_c is a capture time, and $g(\epsilon)$ is the density of trap states. Usually, to model typical dispersive transport [77] we use an exponential density of states,

$$g(\epsilon) = \frac{e^{\epsilon/\epsilon_{\text{trap}}}}{\epsilon_{\text{trap}}}, \tag{3.57}$$

where ϵ_{trap} is an energy scale representing the width of the distribution.

The numerical implementation requires that this system be discretised in energy space, each discrete energetic level forming one number density partition. Firstly, it is necessary to truncate the infinite space to a depth $\epsilon_{\min}$ at which the density of states $g(\epsilon)$ is sufficiently small. Next, energy space is discretised into the linearly spaced values $\{\epsilon_1, \epsilon_2, \cdots, \epsilon_N\}$ separated by a width $\Delta\epsilon$, resulting in the transition rates

$$\nu_{0j} = \frac{e^{\epsilon_j/k_B T} n^j}{\tau_r}\Delta\epsilon - \frac{g(\epsilon_j) n^0}{\tau_c}\Delta\epsilon, \tag{3.58}$$

where n^0 is the number density of free carriers, and n^j ($j \geq 1$) is the number density of trapped carriers at energy depth ϵ_j. The numerical discretisation width $\Delta\epsilon$ is chosen

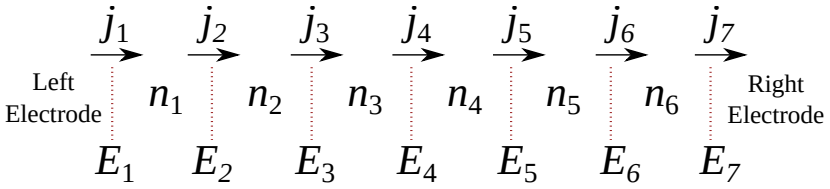

Figure 3.2: Spatial discretisation scheme in the case of six cells. Number densities (n) are defined at cell midpoints, whereas the electric field (E) and current (j) are defined at cell boundaries.

to be sufficiently small that the simulation output is independent of it, i.e. the result does not change as $\Delta\epsilon$ is reduced.

3.4 Numerical Implementation of Model

3.4.1 Spatial discretisation

Spatial discretisation is done using a finite volume method [216], as shown in Figure 3.2. Number densities are defined at cell midpoints, whereas fluxes and related quantities are defined at cell boundaries. The finite volume method was selected because it exactly preserves the conservation of mass [216]. Additionally, the boundary conditions can be easily specified in terms of current densities, which as discussed previously are often physically relevant.

Using the finite volume method, continuity equations are written for each cell. These take the form of ordinary differential equations rather than partial differential equations:

$$\frac{dn_i}{dt} = \frac{j_i - j_{i+1}}{\Delta x} + g_i - r_i, \tag{3.59}$$

where n_i is the number density in the i^{th} cell, j_i is the current density between cells n_{i-1} and n_i, g_i is the generation rate and r_i is the recombination rate or loss rate. The generation and loss terms also include effects such as trapping and release.

Electric fields are defined at cell boundaries, rather than cell midpoints, because the finite volume method requires the current densities to be specified at the boundaries. We use a first order upwind scheme [216], where the advective contribution to the current is calculated from the number density of the neighbouring "upstream" cell. The "upstream" cell is the one that charge carriers are leaving, as determined by the direction of the electric field. The advantage of defining the electric field at the boundary is that it makes it easy to identify the "upstream" cell in regions where the electric field changes sign.

3.4.2 Time integration

Spatial discretisation results in a large system of ordinary differential equations (ODEs) of the form

$$M\frac{\partial \mathbf{y}}{\partial t} = f(\mathbf{y}, t), \tag{3.60}$$

where M is a constant matrix and $f(\mathbf{y},\mathrm{t})$ is a function of the state vector

$$\mathbf{y} = \begin{bmatrix} n^0(x_0) \\ n^0(x_1) \\ \vdots \\ n^0(x_N) \\ p^0(x_0) \\ p^0(x_1) \\ \vdots \\ p^0(x_N) \\ U \end{bmatrix}, \tag{3.61}$$

where U is the voltage across the sample. We have written $\mathbf{y}$ for the case of a single mobility partition. If multiple mobility partitions are present, they are inserted into the state vector underneath n^0 and p^0. The Poisson equation and the electric field are not part of the ODE state $\mathbf{y}$; they are simply evaluated at every time step, i.e. they form part of the right-hand-side function $f(\mathbf{y}, t)$.

The system of equations (3.60) is numerically solved by using the ODE solvers built into MATLAB. The implicit scheme *ode15s* generally achieved the highest performance. This solver operates by numerically approximating the Jacobian matrix, i.e. all possible partial derivatives $\partial f(y_i)/\partial y_j$ in the ODE system given by Eq. (3.60). For some problems, the solver would occasionally "stall," and continuously recalculate the Jacobian with very tiny step sizes. The cost of recalculating the Jacobian is proportional to the square of the number of ODEs, and therefore this operation is costly. Consequently, the following optimisation was implemented.

The solver's speed is continuously monitored. We define the speed as the amount of ODE time advanced in a given window of real time, i.e. simulated time per second. If the solver's speed drops below a critical threshold, and certain other heuristics are met, then the program temporarily switches away from the *ode15s* solver and onto one of the explicit solvers. Explicit solvers do not require the use of a Jacobian matrix. Once the explicit solver has advanced the problem past the troublesome point, use of *ode15s* is resumed. This approach of dynamically switching ODE solvers has turned out to be tremendously useful in reliably achieving high performance simulations.

To implement solver switching, it was necessary to modify the Application Programming Interface (API) of the ODE solver. Consequently, custom implementations of *ode15s, ode23*, and *ode23s* were produced. Additionally, the Jacobian finder—which uses finite differences to numerically approximate the matrix—was reimplemented as a parallel algorithm.

3.5 Conclusion

This chapter introduced a model for charge transport in disordered semiconductors. Physical effects including advection, diffusion, space charge, recombination, and trapping were introduced and a system of equations was developed. Finally, the numerical implementation of this system of equations was described. The following four chapters go on to apply the numerical solver that was described here.

4

Charge Extraction by Linearly Increasing Voltage (CELIV)

This chapter contains material that has been published in the following journal article:

[5] Bronson Philippa, Chellappan Vijila, Ronald D. White, Prashant Sonar, Paul L. Burn, Paul Meredith, and Almantas Pivrikas. Time-independent charge carrier mobility in a model polymer:fullerene organic solar cell. *Organic Electronics*, **16**, 205 (2015). doi:10.1016/j.orgel.2014.10.047.

This chapter includes experimental data that was measured by Chellappan Vijila. The experimental method is summarised here, and full details are found in the cited publications. The analysis of the data was performed by me. All other work described in this chapter is my own.

4.1 Introduction

As discussed in Chapter 2, photo-CELIV is an attractive tool to study charge transport because it uses a diode geometry that is representative of the architectures used in organic solar cells. However, a key weakness of photo-CELIV is that the experimental settings such as the light intensity, applied voltage, or delay time can affect the shape of the transient and thus the apparent mobility. Variations in the delay time have previously been used as evidence of a time-dependent mobility [137, 138]. However, changing the delay time will change the charge carrier concentration and therefore the

shape of the transient may change [133]. It remains unclear whether the apparent time-dependent mobility that has been observed is a genuine effect or whether the photo-CELIV technique has been misleading due to transport and recombination during the delay time.

Dispersive transport and in particular charge trapping can also affect the analysis of the photo-CELIV experiment. It has been reported that the CELIV mobility in the presence of traps is only accurate to within one or two orders of magnitude [144]. Dispersive transport, where the photocurrent reduces with time even before charge extraction, is commonly observed in organic semiconductors with time-of-flight experiments [75,217–219]. However, it is not clear how to interpret dispersive photo-CELIV transients, nor is the impact of dispersion on charge carrier extraction necessarily understood.

This chapter will address these questions through a combined theoretical and experimental study. We will apply the numeric simulation software that was described in the previous chapter. We explore the impact of the time delay as well as the role of traps and dispersive transport on the analysis of photo-CELIV experiments and the extraction of the charge mobility. Our study is based on the organic solar cell blend poly[3,6-dithiophene-2-yl-2,5-di(2-octyldodecyl)-pyrrolo[3,4-c]pyrrole-1,4-dione-*alt*-naphthalene] (PDPP-TNT) and [6,6] phenyl-C71-butyric-acid-methyl-ester (PC70BM) [220]. Optimised solar cells made made from this blend exhibit power conversion efficiencies in the range of ~ 5% [221]. We will show that the photo-CELIV technique is potentially misleading and demonstrate how to avoid these issues.

4.1.1 Summary of solar cell fabrication and experimental methods

Solar cell fabrication followed a previously described procedure [7]. PDPP-TNT (33 wt. %) and PC70BM (American Dye Source, 67 wt. %) were dissolved at a total concentration of 15 mg/mL in a mixture of chloroform and o-dichlorobenzene (4:1 by volume), then spin coated onto a cleaned ITO-patterned glass substrate. Next, the sample was heated on a hot plate at 60 °C for 10 minutes to drive off excess solvent. The device was finished with a 100 nm thick aluminium electrode that was deposited by thermal evaporation under a pressure of 10^{-5} mbar. The thickness of the active layer was 170 nm as measured with a KLA-Tencor P10 surface profiler. The active area of the device was 0.04 cm^2.

Photo-CELIV measurements were conducted with a pulsed Nd:YAG laser pumped OPO (Ekspla). The pulse width was < 4 ns, and the repetition rate was 1 Hz. The sample was excited through the ITO side of the device at a wavelength of 740 nm and an intensity of ~ 0.06 mJ/cm^2. Neutral optical density filters were used to attenuate the light for the intensity dependent measurements. The temperature of the device was controlled with a closed cycle helium cryostat. We reported on the temperature dependences of these devices in a previous publication [7]. All the measurements reported here were obtained at 120 K, because the reduced temperature enhances the

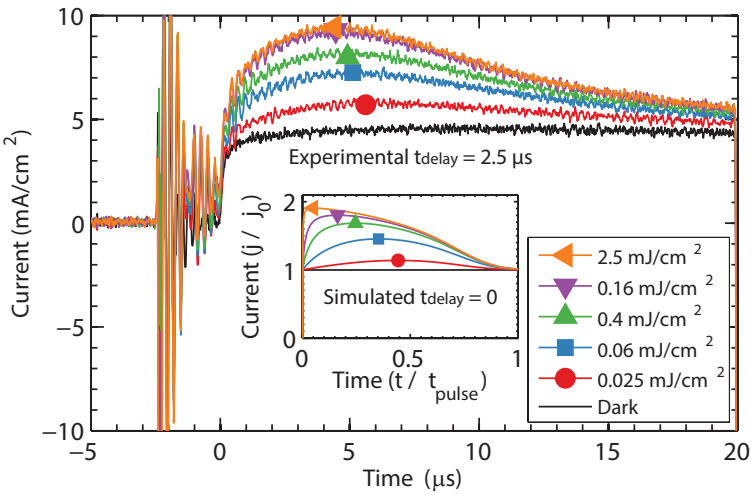

Figure 4.1: Photo-CELIV transients experimentally recorded at various light intensities. The current maxima (which are marked with symbols) only display a small shift as the light intensity is increased. This is in contrast with the simulation results shown in the inset, where the maximum position shifts to extremely short times. Note that the legend refers to the experimental data only. The simulation results neglect the delay time, as is common in numerical and analytic treatments of CELIV. The clear qualitative differences between the experimental and numerically calculated transients raise the question of whether the shift in $t_{\max}$ originates from the photophysics of charge transport or whether it is an artefact of the photo-CELIV technique. This difference is important and must be accounted for when calculating the carrier mobility using the photo-CELIV technique.

dispersive effects that we aimed to study. The locations of the maxima were obtained from the noisy data by smoothing the transients with an adjacent averaging filter.

Simulations were performed using the software described in the previous chapter. We assumed a Langevin bimolecular recombination rate, in accordance with our previous study of these devices [7]. We assumed a carrier mobility ratio of $\mu_{\text{faster}}\mu_{\text{slower}} = 50$, although the results are insensitive to this ratio because the faster carrier mobility dominates in the case of Langevin recombination. Since the devices are thin (170 nm active layer), we applied volume photogeneration (i.e. a homogeneous initial photocarrier distribution). Additionally, we assumed that the built-in field is perfectly compensated by the applied constant offset voltage of 0.5 V during the delay time.

4.2 Effect of the delay time and laser intensity

Two related factors that can affect the photo-CELIV transient are the laser pulse intensity and the delay time. Both parameters influence the concentration of charge carriers during the CELIV extraction. The light intensity controls the quantity of photogenerated charges, whereas the delay time controls how many of these recombine before initiation of the CELIV triangular voltage pulse. Carrier mobility has been shown to depend upon concentration [169], so the photo-CELIV response is likely to change as the light intensity and/or delay time are varied. However, a more insidious

problem is that the shape of the photo-CELIV transient varies with concentration *even if the mobility is constant* [133].

Experimentally measured photo-CELIV transients at varying light intensities are shown in Figure 4.1 and the corresponding simulated transients are shown in the inset. The extraction maxima ($t_{\max}$) are marked by the symbols, and it can be seen that there is a qualitative difference between the experiment and the simulation. Numerical simulations and analytic results both predict that the time of the extraction maximum $t_{\max}$ should become smaller as the light intensity (or the height of the extraction peak) increases [100, 131–133]. Our simulations demonstrate this effect in the inset, where the maxima move into the far top-left corner of the plot. In contrast, the experimental results in Figure 4.1 show that $t_{\max}$ decreases (shifts to the left) only slightly before saturation is reached. One reason for the difference between the simulations and experiment is that the simulations neglect the delay time between photo-generation and the initiation of the ramp voltage. We note that the delay time is commonly neglected in theoretical treatments of photo-CELIV [100, 132, 133], presumably because increasing the delay time acts to reduce the concentration, which is equivalent to varying the light intensity in simple models.

The delay time is typically used in the experiment to prevent the extraction transient from being obscured by the voltage oscillations that are caused by the laser excitation. These oscillations are visible in Figure 4.1. Crucially, the system is not "frozen" during the delay period, that is, photo-generated charges will diffuse and recombine, and the subsequent loss of carrier concentration will affect the extraction transient. Consequently, changing the delay time should lead to a change in the maxima, and indeed this effect was observed, as shown in Figure 4.2. The locations of the maxima were found to shift by a factor of approximately two over the range of delay times that were measured, despite an unchanging light intensity. This would correspond to a change in mobility by a factor of approximately four if the basic dark-CELIV equation $\mu = 2d^2/3At_{\max}^2$ was used [128], where d is the device thickness and A is the rate of change of the triangular voltage.

To determine the origin of the delay dependence of $t_{\max}$ observed in Figure 4.2, we simulated $t_{\max}$ as a function of t_{delay}, as shown in Figure 4.3. If the delay time is set to zero (as in Figure 4.3a and the inset of Fig. 4.1), the position of $t_{\max}$ shifts to the left of the dark-CELIV predicted position, with the largest shift at the highest light intensities. When experimentally relevant delay times are included (as in Figures 4.3b and 4.3c), the shift of $t_{\max}$ is reduced particularly at higher light intensities, and the simulations more closely resemble the experimental results. Thus when comparing photo-CELIV transients it is important to ensure that there are identical delay times and excitation intensities used if a valid comparison of trends is to be made.

From Figure 4.3 it can be predicted that the shift in $t_{\max}$ will be most prominent at high light intensities and short delay times. This can be understood by considering the bimolecular recombination that occurs during the delay time. At high light intensities, the bimolecular recombination is very rapid, so a small change in the delay time results

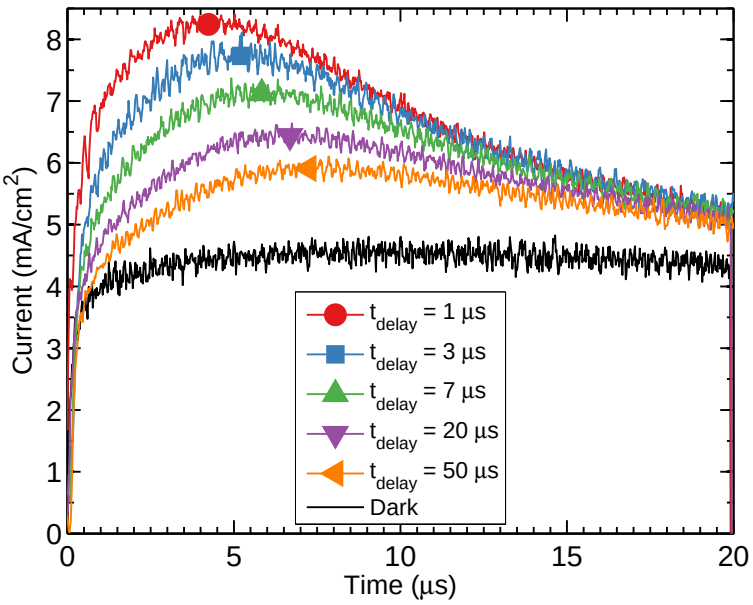

Figure 4.2: Measured photo-CELIV transients with varying laser delay times and a light intensity of 0.06 mJ/cm^2. The maxima, which are marked by the symbols, move to the right with increasing delay time. This could be interpreted as a time-dependent mobility, although we will show in Figure 4.7 that this shift actually originates from charge recombination during the delay time.

in a large change in the surviving concentration (Figure 4.4a). Similarly, at long delay times, the bimolecular recombination has had sufficient time to eliminate the differences between light intensities, especially when the initial concentration is high (Figure 4.4b). Overall, accurate mobility estimation requires that the carrier concentration be approximately constant at the start of extraction, which can be achieved via low light intensities and/or longer delay times.

4.3 Effect of traps on the transient shape

There are three general regimes for transport in organic semiconductors, which include deep traps, shallow traps, and no traps. Previous reports have shown that localized trap states influence the shape of CELIV transients, and hence the interpretation of results and calculation of transport parameters [144, 222]. The case of no traps has already been examined in Figure 4.3. Next, we consider the case of long-lived traps (deep traps), which we define as traps whose average release time exceeds the transit time of carriers. (The transit time in a CELIV experiment is $t_{tr} = d\sqrt{2/\mu A}$, where d is the film thickness, μ is the mobility, and A is the slope of the triangle voltage.) In the presence of these long-lived traps, charges may remain within the film after the transient has concluded. If the traps are sufficiently deep, then trapped carriers may still be present when the next laser shot is fired. We call this effect "film charging", because the extracted charges leave behind uncompensated trapped charges. Although such trapped charges do not contribute to the current, they do disturb the electric

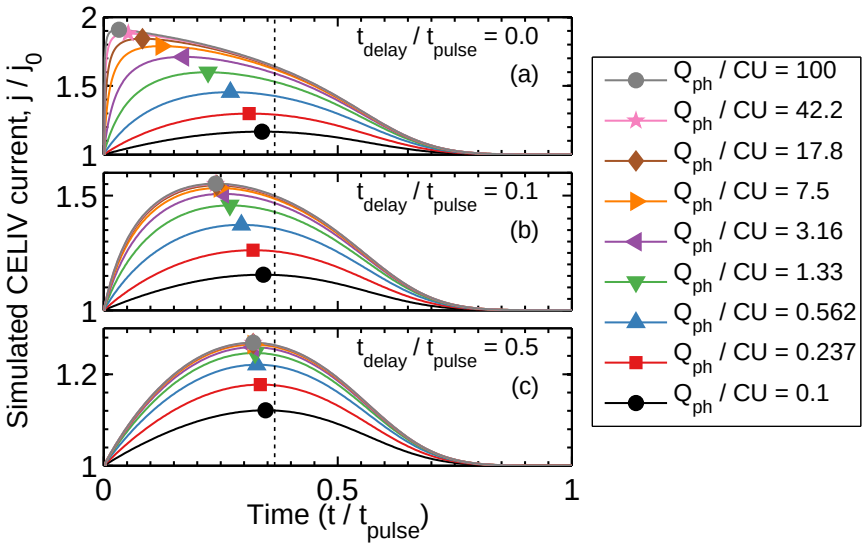

Figure 4.3: Simulated photo-CELIV transients at varying light intensities and at three different laser delay times, showing the impact of the delay time. The light intensity is represented as the photogenerated charge (Q_{ph}) normalised to the charge on the electrodes at the end of the voltage ramp (CU). The vertical dotted lines indicate $d\sqrt{2/3\mu A}$, which is the location of the maximum according to the low concentration dark-CELIV theory [128]. **(a)** When the delay time is neglected, the location of t_{max} (as marked by the symbols) is predicted to shift very strongly with increasing light intensity. **(b, c)** In contrast, introducing a small delay time greatly reduces the shift in the maxima, which is in agreement with experimental transients such as those shown in Figure 4.1. These data demonstrate that correct estimations of the carrier mobility require that the technique-induced shift in t_{max} be avoided, by using low light intensities or increasing the delay time.

field and also provide recombination targets for untrapped carriers, thus influencing the shape of the transient.

To investigate these effects, we simulated the scenario of a perfectly unipolar conductor. We set the slower carrier mobility to zero to represent strongest possible trapping of one type of carrier. We used a delay time of zero to more clearly demonstrate the impact of the traps. Next, we populated the traps by simulating ten photo-CELIV experiments in sequence, with the trapped carriers remaining in the film between experiments. This is similar to how measurements are conducted with a repetitive pulsed laser. We applied bimolecular recombination with the Langevin coefficient adjusted to have one mobility set to zero. This ensured that trapped carriers were able to recombine with mobile carriers. After the traps were populated, we simulated the experiment at varying light intensities, as is shown in Figure 4.5.

The results in Figure 4.5 demonstrate that deep traps reduce the shift in t_{max} that would otherwise occur at high light intensities. The underlying mechanism explaining this behaviour is that a larger voltage is required to overcome the space charge created by the trapped carriers. This space charge opposes extraction, resulting in the temporarily negative currents at the very beginning of the transient. Note that these simulations neglected the *RC* rise time of the measurement circuit. In practice,

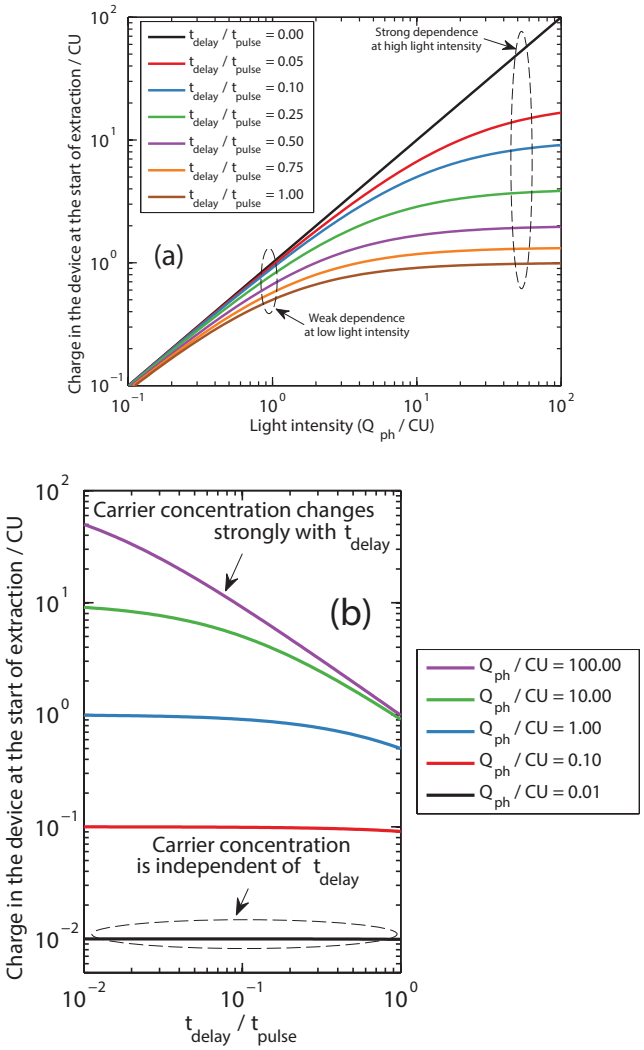

Figure 4.4: The amount of charge remaining in the device after the delay time, calculated from the solution of the bimolecular recombination equation $dn/dt = -\beta_L n^2$, where n is the carrier concentration and β_L is the Langevin recombination coefficient. Light intensity is shown in units of photogenerated charge (Q_{ph}) per CU, where CU is the charge on the electrodes at the end of the CELIV triangle voltage. **(a)** and **(b)** show two different presentations of the same data.

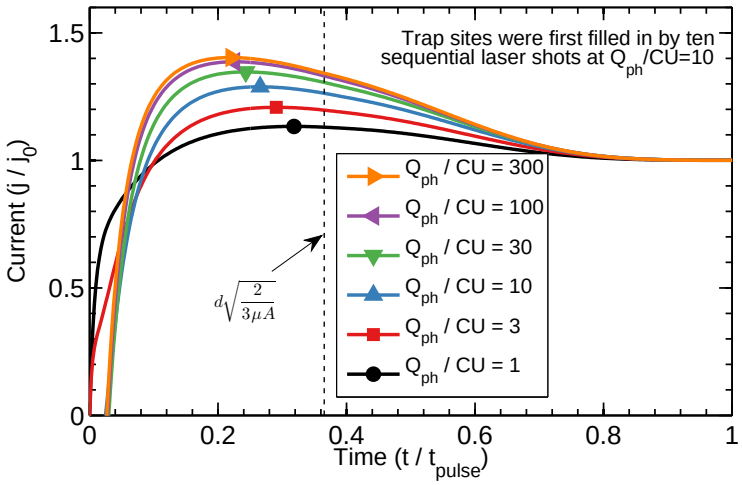

Figure 4.5: Simulated photo-CELIV transients in the case of a unipolar conductor with trap sites pre-populated by immobile carriers whose release time from traps is much longer that the transit time of mobile carriers. The vertical dotted lines indicate $d\sqrt{2/3\mu A}$, which is the location of the maximum according to the low concentration dark-CELIV theory [128]. The electric field due to the trapped charges opposes the extraction of the photogenerated charges, eliminating the strong shift in $t_{\max}$ that occurs without traps (Figure 4.3a). Consequently, the technique-induced shift in $t_{\max}$ is not so significant if long-lived traps are present. These simulations neglected *RC* effects, and there was no delay time applied.

the very early transients arising due to any trapped charge are not likely to be visible because of the *RC* rise time and/or the voltage oscillations coincident with the laser pulse.

The trend in Figure 4.5 is reminiscent of that in Figure 4.3b,c in which a time was introduced. This might explain why some systems display a trend of shifting $t_{\max}$ while others do not. Devices with sufficient quantities of deep traps will show only a minimal change with light intensity. Thus it is important to quantify the trapping and charging inside a film, which can be done using methods such as resistance dependent photovoltage (RPV) [3]. RPV is described in the following chapter.

The final regime to be examined is that of shallow traps that lead to dispersive transport. While the signature of dispersive transport is often observed in time-of-flight experiments [77] it is less clear how dispersive transport will influence photo-CELIV transients. To address this question, we applied a multiple trapping and release model with an exponential density of shallow localised states [212–214]. This model extends the drift-diffusion equations by including repeated trapping and de-trapping of carriers as they transit through the film. Its advantage is that the dispersive results can be directly compared with the non-dispersive results because both are implemented in the same way. Dispersion arises because of the statistical distribution of trap release times. The severity of the dispersion is controlled by the average depth of the traps, which is quantified by an energy level E_{trap}/kT, where k is the Boltzmann constant

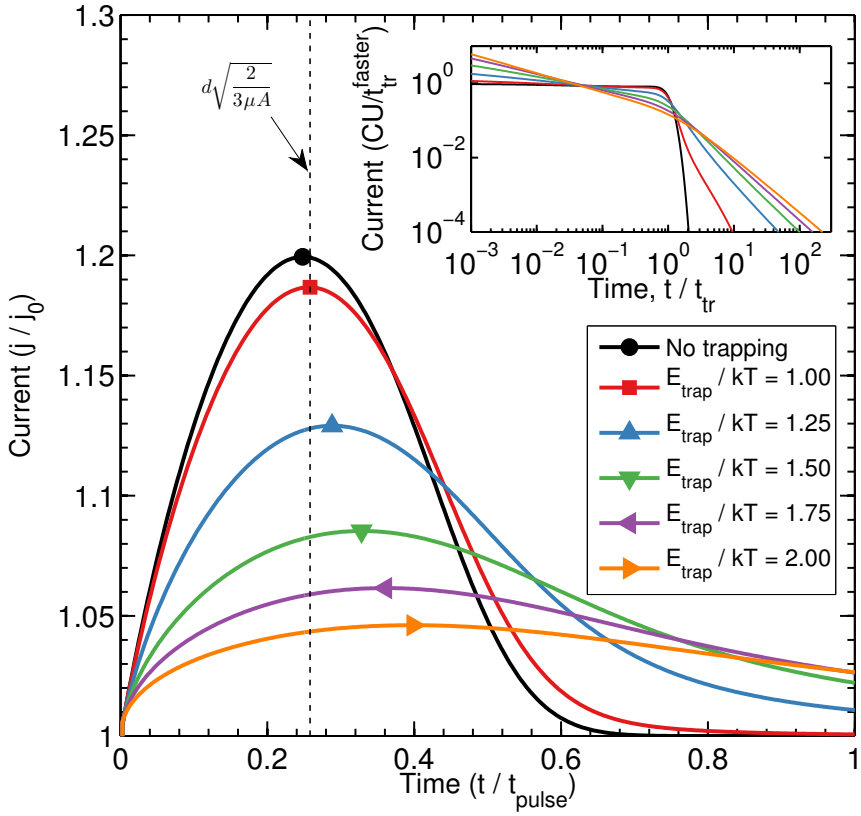

Figure 4.6: A non-dispersive to dispersive transition in simulated photo-CELIV transients. Increasing the dispersion broadens the pulse and slightly increases $t_{\max}$. The inset shows surface generation time-of-flight for the same trap settings, to give a visual indication of how dispersive each setting is. This graph demonstrates that temperature-dependent studies will need to account for the dispersion effect because the shift in $t_{\max}$ with increasing dispersion will hinder estimations of the activation energy.

and T is the temperature. The full list of equations used in the model were given in the previous chapter.

Figure 4.6 shows simulated dispersive photo-CELIV transients. The carrier transit time was kept constant, as is shown by the surface-generation time-of-flight transients in the inset. Dispersion broadens the transient while also shifting the position of the maximum to the right. This shift is due to the distribution of mobilities that results from the dispersion. We note that a similar shift has been reported as a function of trap density [144]. The most characteristic feature of the dispersive transients is that the current does not reduce to the capacitive charging current j_0 before the end of the pulse. Experimental transients (such as Figure 4.1) often demonstrate this effect [75, 138]. The shift of the maximum with increasing dispersion will complicate temperature-dependent studies. For example, if the amount of dispersion depends upon temperature – as is predicted by multiple trapping models – then decreasing temperature will artificially shift the extraction peak to the right, as shown in Figure 4.6. This will hinder studies of temperature-dependent mobilities and activation energies, and so other techniques should be used for these measurements.

4.4 Time-dependent photocarrier mobility

With the effects of time delay, light intensity and traps now understood, the question remains as to how to analyse the photo-CELIV data for the PDPP-TNT:PC70BM blend. The measurements plotted in Figure 4.1 and Figure 4.2 show that t_{max} moves to shorter times with increasing laser power or decreasing delay time. We can reasonably assume that the impact of deep traps is minimal because the solar cells are of high efficiency, and the transients more closely resemble the shallow trapping case (Figure 4.6) rather than the deep trapping case (Figure 4.5). Since the temperature is constant, the amount of dispersion will remain constant, and so we assume that shallow traps are unlikely to contribute a time dependence. To justify this assumption, we will show that recombination during the delay time can entirely predict the observed t_{max} shift, so it is not necessary to introduce other time dependencies (e.g. due to trapping or relaxation). We ran simulations across the entire range of delay times that were measured, and plotted the resulting t_{max} values in Figure 4.7a. There is an excellent agreement between the experimental and numerical data, from which we conclude that the observed variation can be entirely explained by charge carrier recombination during the delay time. Consequently, the measured trend of an increasing t_{max} with delay time is an artefact of the photo-CELIV measurement and is not caused by a changing charge mobility within these devices.

Figure 4.7b compares mobilities calculated directly from t_{max} with those obtained from fits to simulations. The fitting procedure was to adjust the simulated mobility until the predicted t_{max} equalled the actual t_{max}. The crucial difference between the two approaches is that simulation includes recombination during the delay time, whereas the simple mobility equation neglects this effect. We find that there is no evidence of carrier relaxation on transport timescales, in agreement with our previous studies of charge transport in different organic solar cell blends [3]. The resultant average mobility was 2.3×10^{-5} cm^2/Vs, which is similar to our previous report of 5×10^{-5} cm^2/Vs at this temperature (120 K) [7].

4.5 Conclusion

Variations in light intensity and delay time can cause substantial shifts in the position of the CELIV t_{max}, resulting in apparent changes in mobility. Since the shape of the CELIV transient is sensitive to the concentration of carriers [133], we propose that the shift is caused by recombination during the delay time. In the organic photovoltaic blend studied in this work, we demonstrate that the photocarrier mobility is constant on the time scale of charge extraction, despite a large change in t_{max}. This suggests that photocarrier relaxation effects are insignificant, with any excess energy being lost on much shorter time scales. In addition, we studied the impact of shallow traps (causing dispersive transport), and determined that changing amounts of dispersion – as are very likely to occur with changing temperature – will artificially shift the

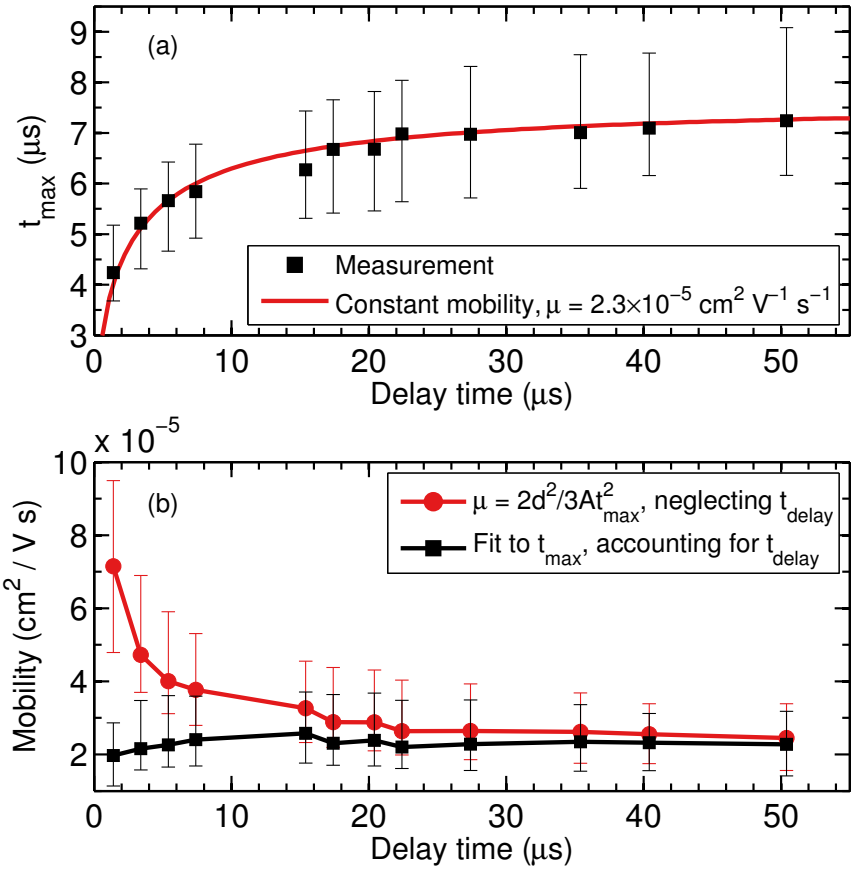

Figure 4.7: **(a)** Delay time dependence in the photo-CELIV extraction maximum ($t_{\max}$). The error bars indicate the time taken for the transients to change by 0.05 mA/cm^2. **(b)** Carrier mobilities calculated directly from $t_{\max}$ (red circles), versus mobilities obtained by fitting simulations to $t_{\max}$ (black squares). The shift in $t_{\max}$ with delay time (panel **a**) results in an apparent time-dependent mobility, but this time dependence is an artefact of the measurement technique, and it disappears when recombination during the delay time is properly accounted for (panel **b**).

position of the CELIV maximum, complicating temperature-dependent studies. In conclusion, photophysical parameters measured from photo-CELIV, and their trends when external parameters are changed, should be estimated with the help of numerical predictions and simulations.

5

Resistance-dependent PhotoVoltage (RPV)

This chapter contains material that has been published in the following journal article:

[3] Bronson Philippa, Martin Stolterfoht, Paul L Burn, Gytis Juška, Paul Meredith, Ronald D White, and Almantas Pivrikas. The impact of hot charge carrier mobility on photocurrent losses in polymer-based solar cells. *Scientific Reports*, **4**, 5695 (2014). doi:10.1038/srep05695.

The solar cells studied in this chapter were fabricated by Martin Stolterfoht. Unless otherwise specified, experimental measurements were conducted by Martin Stolterfoht and Almantas Pivrikas. The analysis of the data was performed by me. All other work described in this chapter is my own.

5.1 Introduction

The previous chapter reported a study of charge carrier mobility and thermalization using the photogenerated charge extraction by linearly increasing voltage (photo-CELIV) technique. As was discussed in that chapter, the photo-CELIV technique suffers from various limitations, most notably that numerical simulations are required for accurate interpretation because of the influence of non-uniform photogeneration [133], charge trapping [144], and a non-uniform electric field [145].

Other measurement techniques also have issues. For instance, the current-voltage methodology is strongly influenced by trapping [119, 120], while time-of-flight usually requires films that are much thicker than typical high-efficiency operational devices [82,

223]. These issues inspired the development of the Resistance-dependent PhotoVoltage (RPV) technique that is presented here.

In this chapter, we develop and apply the RPV technique to address the origin of dispersive transport and the impact of above-bandgap photon energy on the charge extraction process. Above-bandgap photons create "hot" excitons, the impact of which on charge generation has been extensively studied [58, 224, 225]. However, this level of attention has not extended to studies of the *extraction* of hot charge carriers, despite the fact that efficient charge extraction is crucial for device performance [226].

It is important to understand the origin of dispersive transport because it harms device performance by lowering the average photocarrier mobility [227]. Consequently, the vast majority of novel organic semiconductors remain inapplicable for efficient devices. Moreover, the detrimental effects of dispersion are exacerbated by the inhomogeneities in film thicknesses caused by the targeted low cost deposition methodologies, because the transit time distributions become dramatically longer and more dispersed in regions of increased thickness.

Dispersive transport in organic semiconductors is usually thought to be caused by the energetic relaxation of hot charge carriers within their density of states [76]. Spectroscopic measurements and Monte Carlo simulations have revealed energetic relaxation extending even to the microsecond timescales, where it could be relevant to bulk charge transport [228, 229]. Even if the bulk of the energetic relaxation were to occur on very fast timescales, there is still the question of whether residual thermalization might continue to long, microsecond timescales. This energetic relaxation is often understood to cause a time-dependent mobility and therefore explain dispersive current transients [217, 230], yet we will show in this chapter that this commonly-used model is inconsistent with our observations in high efficiency organic solar cell materials. Instead, there is an alternative mechanism for the creation of a distribution of carrier velocities, namely, via trapping. This observation has a very direct impact on the numerous models, theories and experimental results describing dispersive charge transport in disordered organic semiconductors. Furthermore, it points to a new strategy for improving charge transport "management" in devices such as organic solar cells.

The classic signature of dispersive transport is a time-of-flight photocurrent signal that decays with time even before the carriers have transited through the film [77]. This decay in photocurrent can occur due to two mechanisms, a reduction in carrier mobility, and/or a reduction in the number (or concentration) of moving carriers. The former, a time-dependent hot carrier mobility, is presently commonly believed to be the cause of dispersion in organic semiconductors [76, 217, 230] and it is usually understood to originate from a loss of energy as carriers thermalize within their density of states [231–233]. Higher energy carriers are expected to have a higher hopping probability, and hence a higher velocity [151, 169, 234], so the thermalization within the density of states causes the carrier mobility to decline. Recent studies have reported mobility thermalization times on the order of microseconds [228, 229]. However, an

alternative explanation for the decaying transient photocurrent, which is less commonly accepted in organic semiconductors, is a time dependent concentration that can arise if carriers are gradually lost to traps [141, 212, 213]. The photocurrent signal will continue to reduce as long as the net concentration of moving carriers continues to decrease. If that physical process prevails, there can be decaying photocurrent despite the moving carriers having a constant drift velocity. Additionally, if the cause of dispersion is trapping, then it will influence all devices, even those which operate in the dark [73, 235].

In this chapter, we demonstrate that a time-dependent hot carrier mobility cannot explain the dispersive transport in our studied bulk heterojunction solar cells. We address this issue by performing transient photoconductivity experiments in which we vary the transit time by changing the electric field and/or device thickness. The expectation is that if the dominant cause of dispersive transport is mobility relaxation, then the average mobility and the amount of dispersion should vary with the electric field and/or film thickness, because longer transit times will allow for more relaxation to occur. Conversely, if the dominant effect is trapping, then it is the concentration of carriers which is changing in time rather than their mobility, and consequently, the average mobility and the dispersion range should not vary with film thickness or electric field. This transit time dependence allows these two dispersive mechanisms to be experimentally distinguished.

5.2 Experimental Design

Our experiments were made possible by the development of a new transient photoconductivity technique that we call Resistance dependent PhotoVoltage (RPV). The experimental measurement circuit for RPV is shown in Figure 5.1. This setup is similar to time-of-flight, where charge carriers are photogenerated by a short low-intensity laser pulse. A low light intensity is necessary so that the electric field inside the device is undisturbed. The transient photosignal is determined by the competition between two simultaneous processes: the transport of charge carriers inside the film, and the response of the external RC circuit. Unique to the RPV approach, and in contrast with time-of-flight, the entire measurement is repeated at many different load resistances spanning the range from differential mode (small R) to integral mode (large R). The resistance is varied for two reasons: firstly, to visualize the transit times, as will be shown below; and secondly, to reveal the slower carrier mobility by amplifying the slower carrier's conduction current. The slower carriers produce a much smaller current than the faster carriers, and their transit would be buried in the noise at resistances that are optimized for the faster carriers. Slower carriers have much longer transit times, allowing the use of larger resistances, and consequently allowing for their weaker electrical signal to be amplified. In this way, RPV bridges the gap between differential mode and integral mode time-of-flight, and allows measurement of the transport of both types of charge carriers.

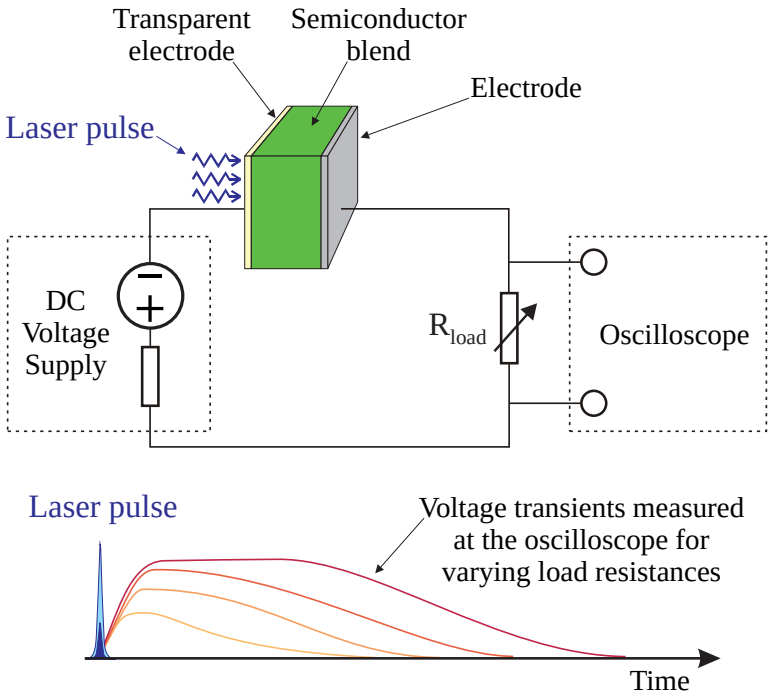

Figure 5.1: Experimental setup for Resistance dependent PhotoVoltage (RPV). A low light intensity nanosecond laser pulse is used to photogenerate charge carriers inside the semiconductor junction of an organic solar cell. Low light intensity is critical in the RPV experiment to ensure operation within the "small charge extraction mode" where the internal electric field distribution in the film is not altered by transported charges. After photogeneration, the charge carrier transport through the film is driven by the built-in or the applied external electric field, and the resulting transient photosignal is recorded by an oscilloscope. The transient photosignals are measured at various load resistances R_{load}.

The combination of the RC circuit dynamics, dispersive transport, and optical interference effects prevent analytic analysis of the transients. To study highly dispersive systems, such as organic solar cells, the simultaneous impact of all these effects must be understood. We applied numerical simulations to develop this understanding, using the simulation software that was described in Chapter 3.

5.2.1 Ideal case

Figure 5.2 shows typical transients for the ideal case of no trapping and no dispersion, where the voltage across the load resistance is plotted as a function of time. We use the notation that V is the voltage on the load resistor and U is the effective voltage across the semiconductor (which is the sum of the built-in voltage and the applied voltage). The results are shown in normalised units, with the load resistance R expressed as $RC/t_{\text{tr(faster)}}$, where C is the device capacitance and $t_{\text{tr(faster)}}$ is the transit time of the faster carriers. The transients show two distinct extraction "shoulders," as indicated by the arrows. The positions of these arrows correspond to the exact transit times required for the faster and slower carriers to cross the entire thickness of the film. In Figure 5.2, carriers were generated uniformly throughout the film, so there is a spread

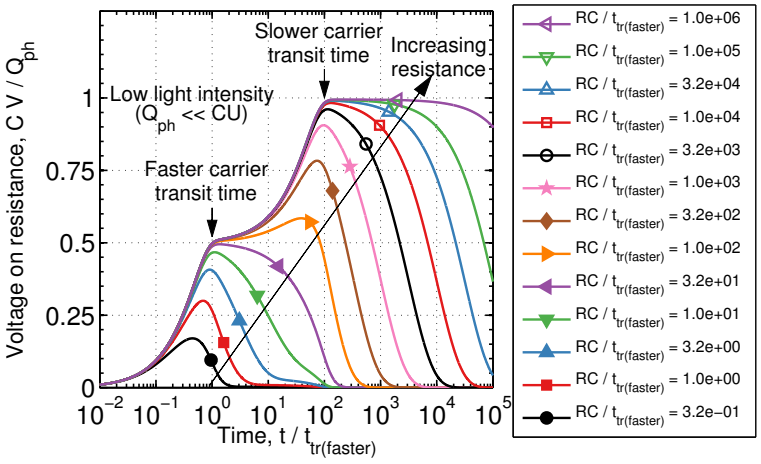

Figure 5.2: Simulated non-dispersive RPV transients demonstrating how the gradually increasing resistance assists in revealing the two transit times. The arrows indicate the exact transit times.

of arrival times as different carriers travel different distances. Gradually increasing the load resistance assists in revealing these arrival times by lengthening the time scale of the measurement to incorporate those carriers that have to travel further. With a large enough resistance, the peak location saturates, indicating complete extraction of the corresponding type of carrier. In this way, the final saturated peak location reveals the transit time of those carriers that transited the entire film. Saturation of the peak voltage is thus an important indicator of complete carrier extraction, and failure to observe this saturation could result in an underestimation of the transit time. The mobility is then calculated from the transit time using the equation $t_{tr} = d^2\mu^{-1}U^{-1}$, where d is the film thickness, μ is the mobility, and U is the sum of the built-in voltage and the applied voltage. Experimentally, the amount of photogenerated charge (Q_{ph}) needs to be kept small, such that $Q_{ph} < CU$, in order to avoid the space charge effects that would redistribute the electric field and disturb the transit time. This condition is easily checked experimentally by confirming that the maximum photovoltage is at least 10 times smaller than U.

5.2.2 Optical interference

While Figure 5.2 was calculated using the simplified case of uniform volume generation, the extension to non-uniform photogeneration does not affect the technique. The case of Beer-Lambert absorption is shown in Figure 5.3. The heights of the peaks vary, but their positions are mostly undisturbed. Since the transit times are obtained from the positions of the peaks, the RPV technique is a robust tool for measurement of carrier mobilities.

The Beer-Lambert case is an idealisation that neglects optical cavity effects [29]. Real photogeneration profiles are considerably more complex. Figure 5.4 (a) shows typical absorption profiles at varying wavelengths of light for one of the solar cells studied in the Results (Section 5.3) below. These profiles were calculated using the

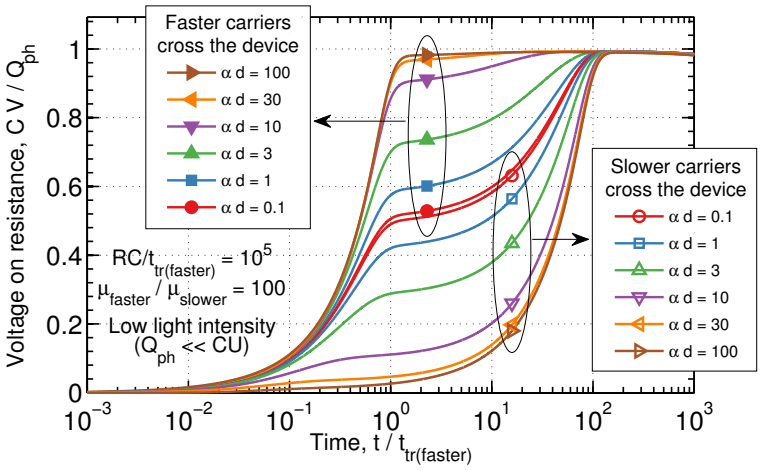

Figure 5.3: The robustness of the RPV technique against varying photogeneration profiles. Shown here are simulated transients at large resistances. Photogeneration profiles follow the Beer-Lambert law, i.e. the initial distribution of charges is proportional to $e^{-\alpha x}$, where α is the absorption coefficient and x is distance into the film. For thin films ($\alpha d \leq 3$), the heights of the peaks vary but their locations do not, demonstrating the robustness of the RPV technique.

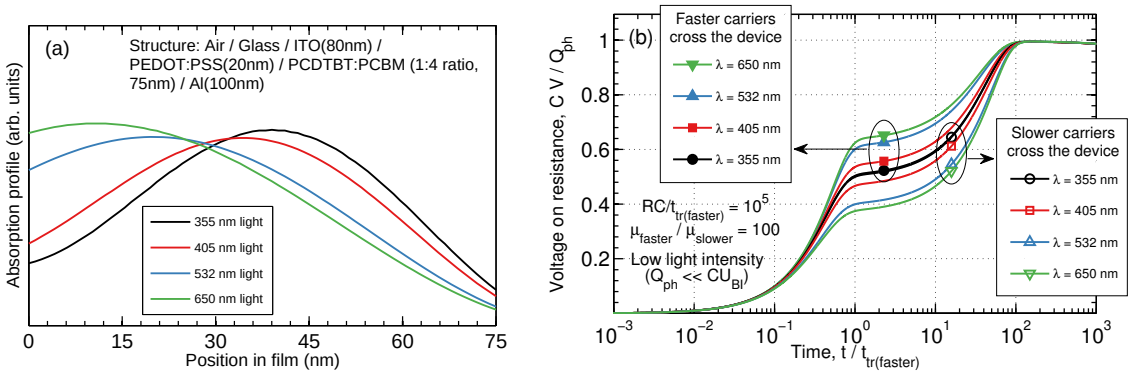

Figure 5.4: The robustness of the RPV technique to optical interference. **(a)** Light absorption profiles calculated for the organic solar cell structure written at the top of the plot. Material abbreviations are defined in the Results section below. **(b)** RPV transients for each light absorption profile, for both polarities of applied voltage. In all cases, both transit time shoulders are visible, demonstrating that the RPV technique can be applied to thin film operational devices without concern for optical interference.

transfer matrix method [208]. The corresponding simulated RPV transients are shown in Figure 5.4 (b). The transit time shoulders are clearly visible, independent of the wavelength of light or the applied voltage polarity. We consider that the RPV technique is insensitive to light interference effects, and can be applied to operational devices with or without optical cavities.

5.2.3 Charge trapping and dispersion

Typical simulated transients for an organic solar cell with dispersive transport are shown in Figure 5.5. The positions of these arrows correspond to the mean transit times required for the faster and slower carriers to cross the entire thickness of the film.

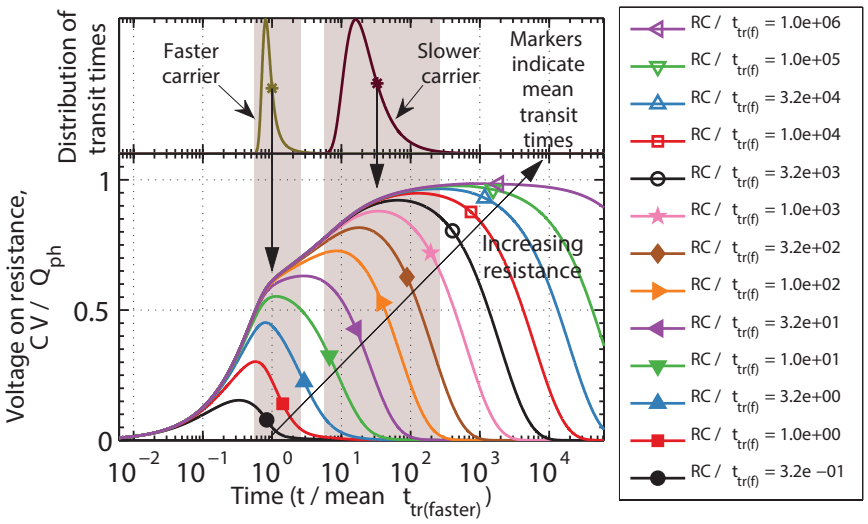

Figure 5.5: Simulated RPV transients in the case of dispersive transport caused by shallow traps. The extraction "shoulders" approximately correspond to the mean carrier mobility, allowing a good estimation of carrier mobility even in the presence of strong dispersion.

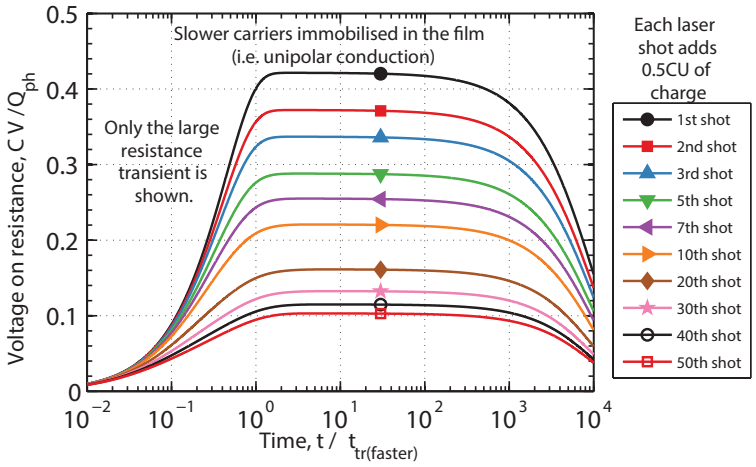

Figure 5.6: Simulated RPV transients in the case of film charging caused by deep traps. The magnitude of the RPV transit is reduced in subsequent shots of the laser, but the transit "shoulder" remains unhindered, which allows for reliable mobility estimation.

In this simulation, carriers are repeatedly trapped and de-trapped, creating dispersion because the total time spent in traps is different for different carriers. The resulting distribution of transit times is shown at the top of Figure 5.5, and its approximate width is indicated by the shaded background. It can be seen that the RPV technique allows the mean charge carrier mobility to be obtained even in the presence of strong dispersion.

In addition to shallow traps that cause dispersion, we also considered deep traps that immobilize carriers for times much longer than the transit time of either carrier. Long lived trapping is typical in disordered organic semiconductors [119, 141], because many organic materials behave as unipolar conductors, and solar cells often have strongly imbalanced mobilities [236]. In these cases, repeated photogeneration

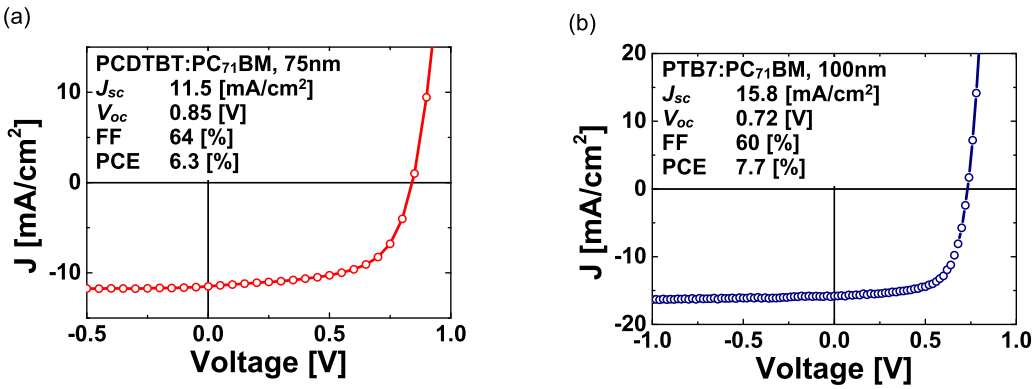

Figure 5.7: Current-voltage curves under AM1.5G illumination for the solar cells studied in this chapter.

adds more trapped charge in the form of the immobilized charge carriers, which might accumulate with every repetitive laser shot, redistributing the electric field and distorting the measurement. Figure 5.6 shows simulations of this film charging for the case of fast Langevin-type recombination under repeated laser shots, as would arise from the presence of deep trap states far inside the forbidden energy gap [118]. These are large resistance transients, in other words, the measurement circuit has integrated the photocurrent such that the peak voltage is proportional to the extracted charge. If the extracted charge is decreasing and the extraction time remains constant, then carriers must be lost to recombination and not due to field screening, and hence we conclude that the trapped charges act as recombination sites for the mobile carriers. However, the mobility of the charge carriers can be determined independently of the trapping effects, because the rapid Langevin recombination prevents the build-up of large amounts of trapped charge that would disturb the transit time.

5.3 Results

We chose to study the well-known photovoltaic blend [65] of poly[N-9”-hepta-decanyl-2,7-carbazole-*alt*-5,5-(4’,7’-di-2-thienyl-2’,1’,3’-benzothiadiazole)] (PCDTBT) and [6,6]-phenyl-C_{70}-butyric acid methyl ester (PC70BM) in an optimized blend ratio of 1:4 by weight [72]. This blend is ideally suited to this study because its amorphous nature allows the elimination of any film thickness dependent morphology [237]. In order to see the generality of observed effects, we have also done the same experiments on poly[[4,8-bis[(2-ethylhexyl)oxy]benzo[1,2-b:4,5-b’]dithiophene-2,6-diyl][3-fluoro-2-[(2-ethylhexyl)-carbonyl]thieno[3,4-b]thiophenediyl]] (PTB7):PC70BM blends. The thin film (active layer thickness of 75 nm) PCDTBT:PC70BM solar cell exhibited a power conversion efficiency of 6.3% under standard AM1.5G illumination, while the PTB7:PC70BM blends reached 7.7%. Current-voltage curves for both devices are shown in Figure 5.7. None of the optimized PCDTBT or PTB7 based devices demonstrated any significant film morphology inconsistencies in the range of studied film thickness. The presence of dispersive transport was confirmed by time-of-flight experiments on thick films (Figure

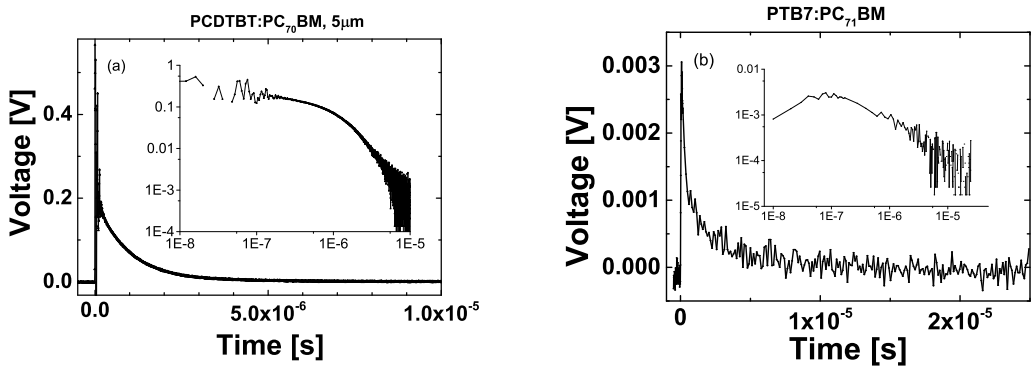

Figure 5.8: Dispersive time-of-flight transients measured in thick film devices of (a) PCDTBT:PC70BM and (b) PTB7:PC70BM. The insets show the same data plotted on logarithmic axes. Both devices show highly dispersive transients.

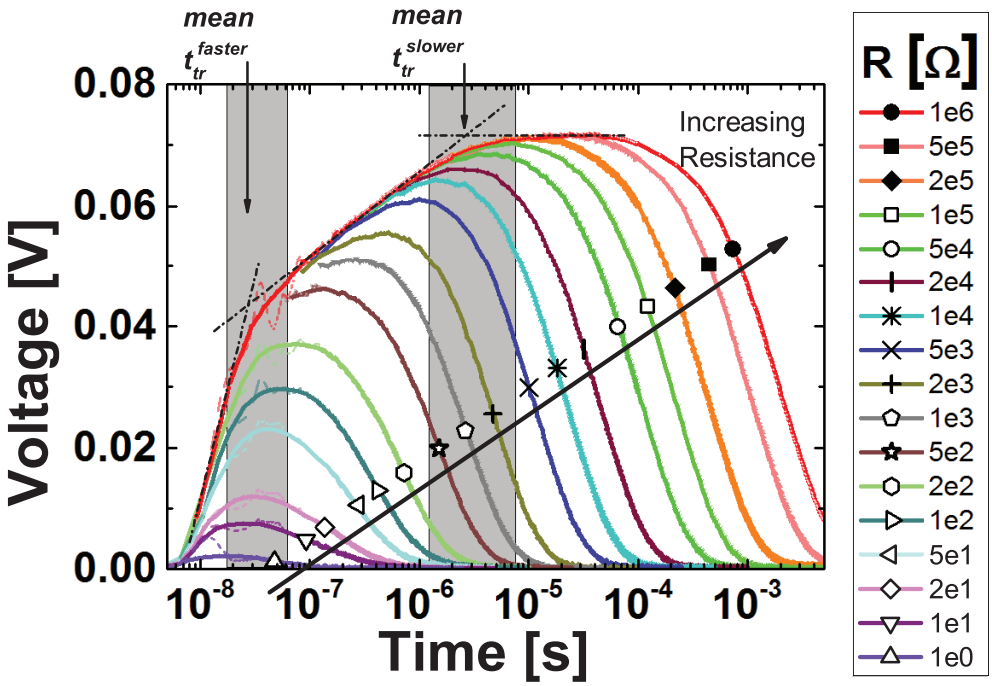

Figure 5.9: Measured RPV transients for an optimised PCDTBT:PC70BM solar cell. Mean electron (faster) and hole (slower) transit times are marked, from which the respective mean mobilities are estimated. The dispersive nature of charge transport in the studied solar cells is highlighted by shaded boxes that mark the range of carrier arrival times. Thin curves show recorded data, while bold show show data smoothed by adjacent averaging. The short timescales for large resistances were omitted for clarity.

5.8). As can be seen, there are no photocurrent plateaus. The transients decrease with time as is typical of dispersive systems.

Figure 5.9 shows the recorded RPV transient signals for a PCDTBT:PC70BM solar cell. All transients were recorded at near to short-circuit conditions. This remains true even at large resistances, because the maximum photovoltage occurring during the transient is substantially less than the built-in voltage. The first shoulder marks the arrival time of faster carriers (27 ns), which is attributed to electron transport because

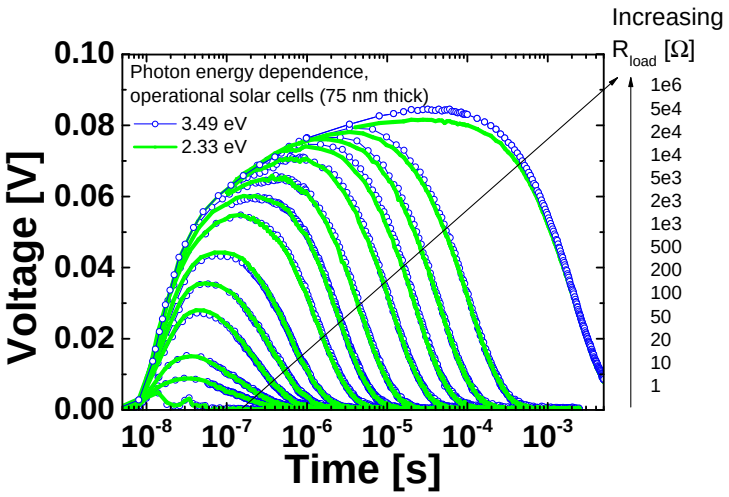

Figure 5.10: RPV transients measured on a 75 nm PCDTBT:PC70BM solar cell using two different laser wavelengths: 355 nm (3.49 eV) and 532 nm (2.33 eV). The nearly identical transient responses directly demonstrate the absence of hot carrier effects in this system.

its time scale is similar to that measured for PC70BM. The second shoulder is less well defined due to the strongly dispersive nature of the hole transport in this system, but marks the arrival of the slower carriers (2.59 µs). Mean electron and hole mobilities were determined from the shoulders in the transients, as indicated by arrows in Figure 5.9, with the approximate spread of arrival times indicated by the shaded boxes (corresponding to the regions where the transients deviate from the dotted lines). The edges of these shaded boxes give the "fastest" and "slowest" case transit times, from which we obtained the dispersion range in the mobilities for each species. This range is an essential feature of the dispersive transport exhibited by this system, because a single mobility value does not correctly quantify the transport when the system is dispersive. We measured the mean electron mobility to be 2.9×10^{-3} cm^2 V^{-1} s^{-1} with a dispersion range from 1.1×10^{-3} cm^2 V^{-1} s^{-1} to 4.5×10^{-3} cm^2 V^{-1} s^{-1}, and the mean hole mobility to be 3×10^{-5} cm^2 V^{-1} s^{-1} with a dispersion range from 9.2×10^{-6} cm^2 V^{-1} s^{-1} to 7.4×10^{-5} cm^2 V^{-1} s^{-1}. Despite the high level of dispersion observed here (the hole dispersion range covers nearly an order of magnitude), the OPV device still maintains good performance. However, further work is necessary to identify the impact of the dispersion range on the performance of solar cells.

Next, we studied the impact of photon energy on the hot charge carrier transport, because any relaxation effects are likely to be dependent upon the initial energy. This is important because of recent suggestions that excess above-bandgap energy may assist excitonic dissociation [58], although the methodology of that observation has been challenged [62]. We note that quantum yields have been shown to be independent of the energy level of the excited state, suggesting that hot excitons are indeed not beneficial for exciton separation [59]. Nevertheless, hot charge carriers – rather than excitons – might also possess excess energy and shape the internal quantum efficiency spectra; therefore, it is important to clarify these effects, aiming for improvement

in the charge extraction of typical low mobility organic materials. In the past the absence of hot charge carrier effects has been observed indirectly [238]. Numerical simulations predict that RPV is independent of optical interference effects (Figures 5.3 and 5.4), allowing direct and unambiguous measurement of any hot charge carrier effects that may be present. RPV transients were measured at two different photon energies, 3.49 eV (355 nm) and 2.33 eV (532 nm). The results are plotted in Figure 5.10, showing nearly identical transients resulting from laser excitation at the two different wavelengths. The photon energy independent mobility suggests that excess energy plays a minimal role in dispersive transport, since carrier thermalization (if it is present) must happen in time scales much shorter than the transit time.

To further confirm that the dispersion in hot carrier mobilities is not caused by the thermalization of carriers, we studied the electric field and film thickness dependence. Longer transit times should allow more time for thermalization, thus influencing the result if the dispersion is due to carrier relaxation. The results are shown in Figure 5.11. The mobilities and dispersion ranges are completely independent of electric field and photon energy [Figure 5.11 (a)], suggesting that trapping mechanisms are more significant than relaxation mechanisms. The lack of electric field dependence is in contrast with the Poole-Frenkel dependence reported in pristine PCDTBT [239]. This is an unexpected result, because in disordered organic systems significant electric field dependence is typically observed, even at relatively low values of electric fields [239], which is thought to originate from hopping-type charge transport. Further studies of the temperature dependence, and measurements on other systems, have to be performed in order to clarify the origin of this observation. Additionally, we observe that the mean mobilities and dispersion ranges are nearly independent of the film thickness [Figure 5.11 (b)]. We attribute the small changes in mobility to device-to-device variations that result from the fabrication process. The thickness independence of the mean mobilities and dispersion ranges further support the claim that the dispersion is caused by traps instead of relaxation. A charge carrier density dependence in the mobility even at low concentrations has been observed in P3HT:PCBM blends [73], and we note that a concentration dependence might cause dispersion as carriers gradually become trapped and the density decreases. We do not exclude the possibility of a density dependence here. However, in our measurements, increasing thickness corresponds to lower densities because the amount of photogenerated charge was always less than CU, which is inversely proportional to thickness. Consequently, the thickness independence in the mobility implies that there is negligible density dependence at the concentrations probed here.

Further measurements were also performed on solar cells made with PTB7 blends. Typical transients are shown in Figure 5.12. Only a single transit time is visible, which we attribute to the fact that charge transport is more balanced in PTB7 blends than in PCDTBT blends. Nevertheless, the electric field and thickness dependencies show the same conclusions as the PCDTBT blends: the mean mobility and dispersion ranges are independent of both of these parameters (Figure 5.13). Consequently, the same

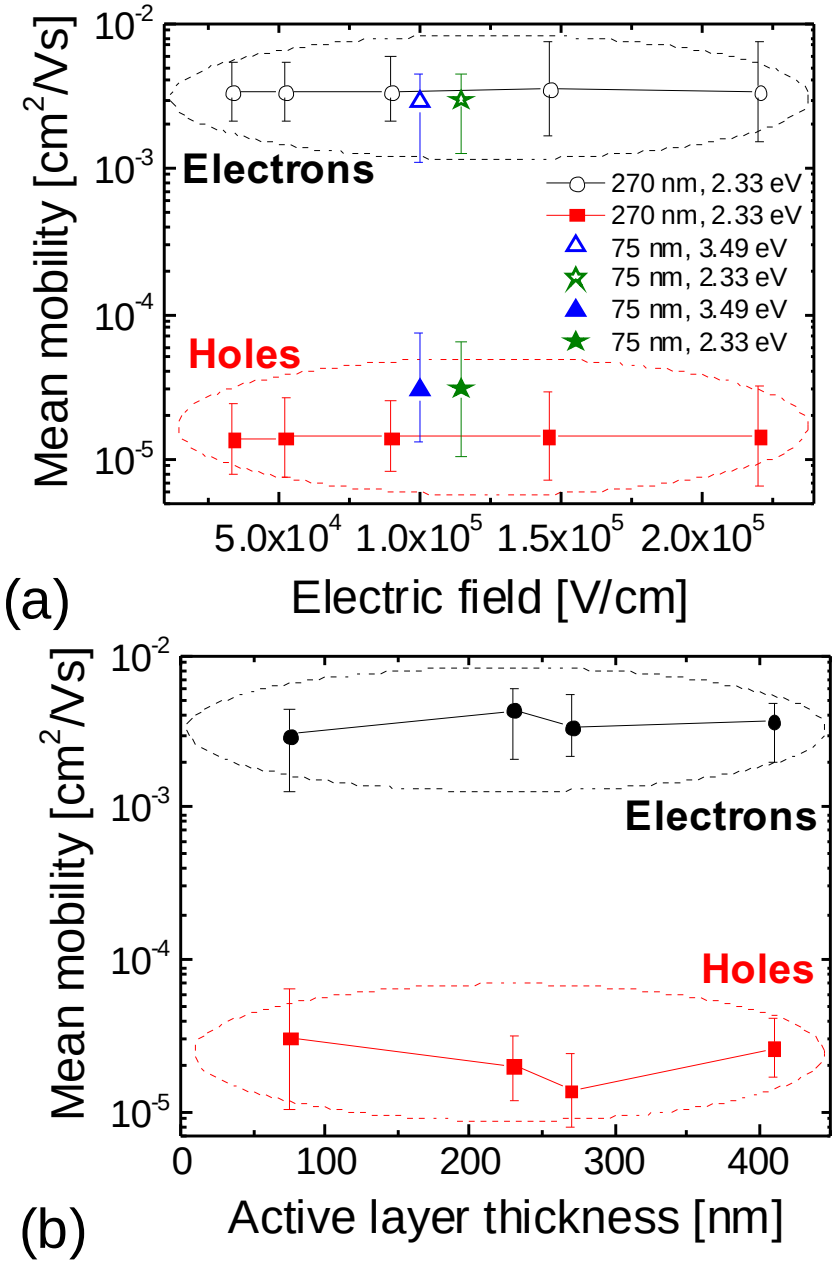

Figure 5.11: Electron and hole mobilities measured in PCDTBT:PC70BM solar cells. The error bars show the dispersion ranges. Carrier mobilities and dispersion ranges are independent of electric field and photon energy [panel (a)], and nearly independent of film thickness [panel (b)], demonstrating that carrier thermalization cannot account for the dispersive transport in this system. Consequently, dispersion is caused by trapping.

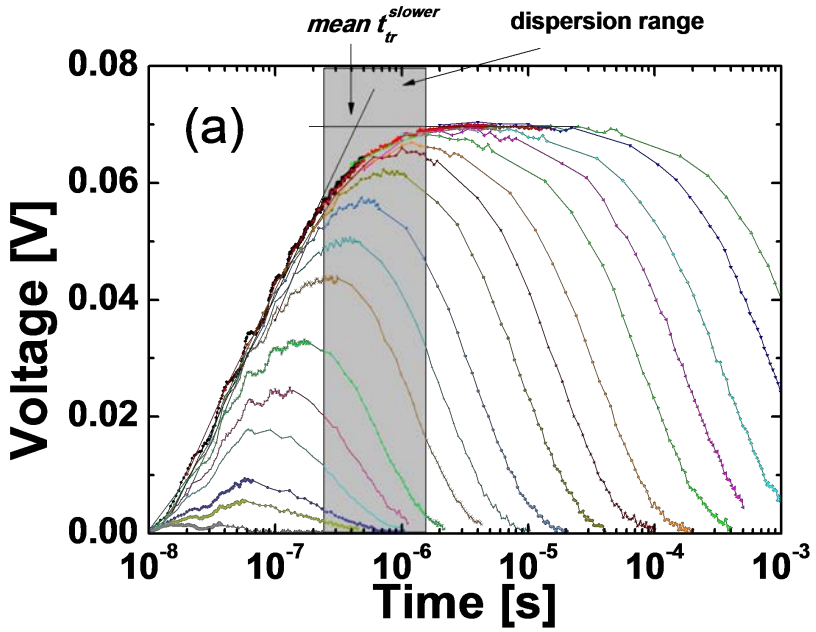

Figure 5.12: RPV measurements conducted on PTB7:PC70BM solar cells. Only the slower carrier transit time is visible, possibly because the transport in PTB7 blends is more balanced than in PCDTBT blends.

arguments apply, and these results appear to be generally applicable and are certainly not specific to PCDTBT blends.

5.4 Discussion

Charge transport in the studied operational OPV blends is strongly dispersive, as demonstrated by the decaying time-of-flight photocurrent transients in thick devices (Figure 5.8). These time-of-flight transients were recorded in a regime where drift dominates over diffusion, so the current density is described by $j = eE(n\mu_n + p\mu_p)$, where e is the charge of an electron, μ_n and μ_p are the electron and hole mobilities, n and p are the carrier concentrations, and E is the electric field. The observation of a decaying photocurrent density j can be explained by two mechanisms: thermalisation (a time dependent mobility, μ), and/or trapping (a time dependent concentration of moving charge carriers, n). These mechanisms are schematically illustrated in Figure 5.14, from which it can be seen that either model would result in dispersive photocurrent transients. We found no evidence of thermalisation-type effects on the timescales comparable with those involved in charge transport. Figure 5.10 directly demonstrates that that excess energy of hot carriers has essentially no contribution to mobility or dispersion. In Figure 5.11, we demonstrate that the dispersion range is essentially independent of the applied electric field and changes very little with thickness, over the ranges that were tested. If thermalisation on transport time scales were the cause of the dispersion, then modifications to the transit time should change the mean mobility and/or dispersion range by varying the time available for relaxation. Such a

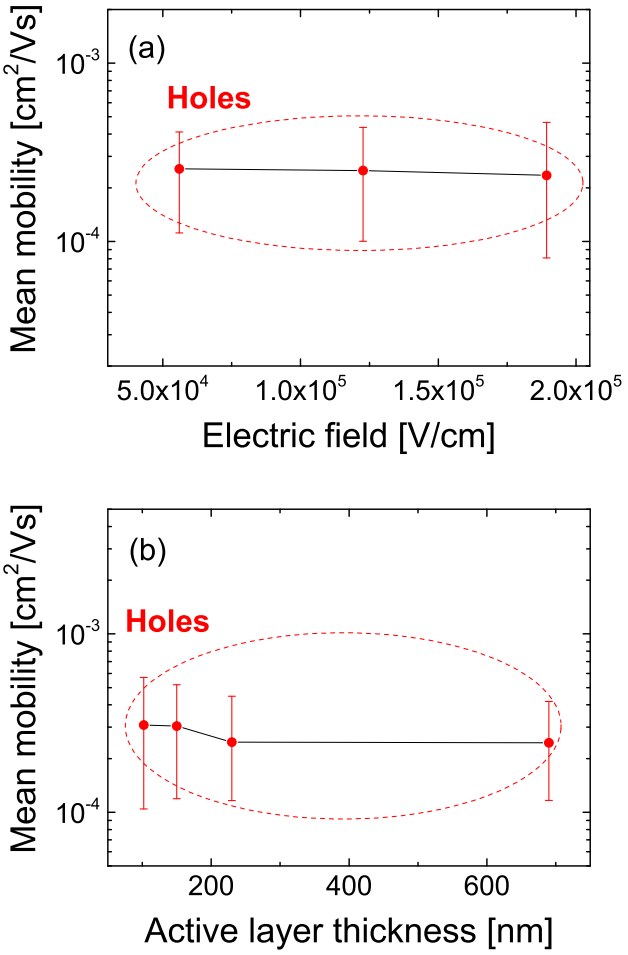

Figure 5.13: Mobilities measured in PTB7:PC70BM solar cells, as a function of (a) electric field and (b) film thickness. The mobilities are independent of electric field and thickness, as observed above for the PCDTBT blends, suggesting that carrier thermalisation is not the cause of the dispersion in this system.

variation was not observed, and hence we exclude thermalisation as the mechanism of the dispersive transport. Any relaxation processes must be much faster than charge transport, so that the distance covered by charges as they relax is insignificant compared with the film thickness, and hence the relaxation has negligible contribution to the overall dispersion.

With relaxation excluded, the only remaining mechanism is a reduction in the concentration of moving carriers, therefore, we conclude that trapping is the primary cause of the dispersion in these systems. This challenges the widely-used model of hot carrier relaxation within the density of states. Consequently, dispersive transport potentially impacts on the many different devices that employ films made from disordered semiconductors, including those that operate in the dark or at steady-state conditions.

We cannot exclude the possibility that excess photon energy is not transferred to the charge carrier at all, i.e. that it is dissipated earlier in the photogeneration process. Nevertheless, the central conclusion that thermalisation effects are insignificant

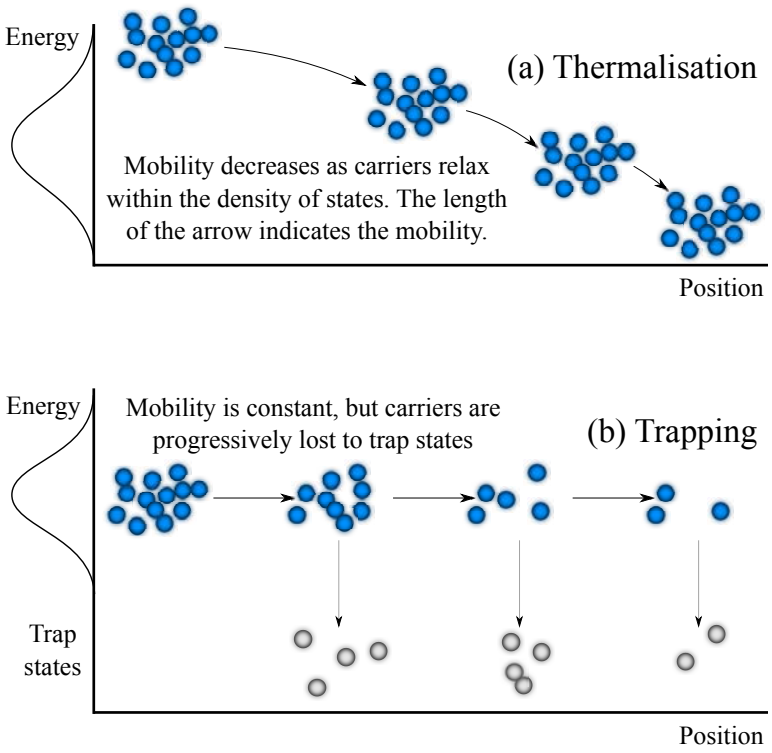

Figure 5.14: . Schematic illustration of the two pathways to dispersive transport. **(a)** Thermalisation causes the mobility to decrease with time, whereas **(b)** trapping causes the loss of carrier density. We have shown here that the latter case (trapping) is the dominant effect in the studied solar cells.

is supported by the observation that the mobility is independent of the transit time (Figure 5.11). Even if hot carriers are not formed by high energy photons, dispersive transport must be caused by trapping rather than energetic relaxation.

5.5 Conclusion

Electron and hole mobilities and their dispersion ranges were measured simultaneously using the RPV technique in a high efficiency narrow optical gap polymer/fullerene system (PCDTBT:PC70BM). We found that the transport of electrons and holes are both strongly dispersive in these thin, efficient solar cells. We introduced the dispersion range as a parameter to quantify charge transport, since a single mobility value is insufficient to properly characterize a dispersive material.

We directly observed the absence of "hot carrier" effects on time scales relevant to charge extraction, and furthermore found that the dispersion is caused by trapping rather than thermal relaxation. We have found that the widely-used model of hot carrier relaxation within a density of states is not the dominant process causing the dispersion in the studied solar cells. Furthermore, in contrast with the Poole-Frenkel dependence previously reported in pristine PCDTBT and other disordered systems, the studied solar cell blends exhibit an unexpected negligible electric field dependence. While further work is needed to clarify this observation, electric field independence

may assist in maintaining a good fill factor by keeping the mobility higher near the maximum power point. The absence of hot carrier effects and an electric field independent mobility were also observed in PTB7:PC70BM solar cells, suggesting that these conclusions may be more generally applicable.

This work signifies the importance of localized trap states as opposed to thermalization and hot carrier effects in efficient polymer-based solar cells. Since dispersion arises from trapping, it is also important for other types of devices, such as organic field effect transistors and diodes. Trap states are relevant whether the carriers were injected or photogenerated, and whether the device is in transient or equilibrium conditions. Our results suggest that further scientific research should be directed towards reducing the density of trap states rather that utilizing above-bandgap energy for improving electronic device performance.

6

High Intensity RPV (HI-RPV)

This chapter contains material that has been published in the following journal article:

[2] Bronson Philippa, Martin Stolterfoht, Ronald D. White, Marrapan Velusamy, Paul L. Burn, Paul Meredith, and Almantas Pivrikas. Molecular weight dependent bimolecular recombination in organic solar cells. *The Journal of Chemical Physics*, **141**, 054903 (2014). doi:10.1063/1.4891369.

The low molecular weight polymer studied here was fabricated by Marrapan Velusamy. Solar cells were manufactured and measured by Martin Stolterfoht, Anton Bavdek, and Almantas Pivrikas. The analysis of this data that is presented here was performed by me. All other work described in this chapter is my own.

6.1 Introduction

The previous chapter presented results of applying the RPV technique at low light intensities in order to study mobility. It was shown that RPV was a robust tool, and that it is applicable to operational solar cell devices. In this chapter, the RPV technique is extended to high light intensities in order to probe carrier recombination. Recombination is important because it is one of the key loss mechanisms in organic bulk heterojunction solar cells, especially those with thicker junctions or those made from materials which do not possess a sufficiently high carrier mobility [12, 82, 240].

Recombination coefficients are commonly compared with the prediction of Langevin [12, 89, 92], which is $\beta_{\mathrm{L}} = e\left(\mu_{\mathrm{p}} + \mu_{\mathrm{n}}\right)/\epsilon\epsilon_0$, where e is the charge of an electron, μ_{p} (μ_{n}) is the mobility of holes (electrons), and $\epsilon\epsilon_0$ is the dielectric permittivity. A suppressed, non-Langevin recombination coefficient (with $\beta < \beta_L$) has been reported in organic photovoltaic blends that exhibit high performance [94, 95, 103, 241, 242]. Suppressed

recombination is desirable to ensure efficient charge extraction. The reduction factor β/β_L is a useful "figure of merit" for screening candidate photovoltaic blends to rapidly identify those which are likely to be highly performing [89].

A variety of techniques are available to study recombination dynamics. Techniques that operate on fully operational devices (i.e. those without blocking layers or other modifications [104]) include transient photovoltage (TPV) [147, 149], photogenerated charge extraction by linearly increasing voltage (photo-CELIV) [128, 129], and time-of-flight (TOF) [124, 125].

TPV studies often show an apparent reaction order higher than the expected value of two [150]. It has been suggested that this is due to a concentration dependence in the recombination coefficient [243], recombination through trap states [244], or the spatial separation of the carriers under open circuit conditions [150]. The spatial separation at open-circuit conditions can be reduced by studying the solar cell nearer to short-circuit conditions [20], as in the photo-CELIV or TOF experiments.

Photo-CELIV can be used to study charge carrier mobility and also the bimolecular recombination coefficient [7, 245–249]. The recombination coefficient can be estimated from the maximum extraction current in the photo-CELIV transient [100, 133]. However, this transient is influenced by experimental factors that are not fully accounted for in the theory, such as the spatial distribution of light absorption [133], the circuit resistance [21], and the voltage slope [131]. Additionally, premature escape of charge from the film [250] contributes to the charge redistribution during the delay time [145], which results in a false position of the extraction maximum and makes the measurement unreliable. While some attention has been directed to minimizing this issue [72], a full compensation of carrier redistribution is impossible due to Fermi level pinning, an inhomogeneous electric field inside the film and strong diffusion near the electrode where carriers are photogenerated.

Another well known technique to characterise recombination is high intensity time-of-flight (TOF) [75, 112, 113]. The recombination coefficient can be estimated from the amount of charge extracted during a TOF experiment [89, 102, 223]. However, the external circuit resistance influences the extracted charge [95], making the measurement unreliable due to its dependence on the experimental conditions. Previous works have neglected the impact of the *RC* circuit [89]. Here, we resolve this issue by extending the previous work to achieve more reliable experimental results.

In this chapter, we study recombination in the benchmark organic photovoltaic system PCDTBT:PC70BM (see the experimental section for details of the materials). We quantify the recombination in this system, and compare solar cells made with low molecular weight PCDTBT to those made with high molecular weight PCDTBT. Our recombination study will be conducted using a variant of time-of-flight that we call High Intensity Resistance dependent PhotoVoltage (HI-RPV). An exact analytic solution of the relevant differential equations is not known, so we apply numerical simulations to show the applicability of the technique to a variety of experimental

conditions. After demonstrating the generality of the technique, we go on to apply it to operational bulk heterojunction solar cells.

Our simulations take an effective medium approach to model device-scale behaviour, an approach which is commonly used for organic solar cell simulation [20–22, 144, 251, 252]. We consider the situation where the films are not doped and there is no film charging due to deep traps whose release times are longer than the transit time. These assumptions are typically met in high efficiency devices. The details of our numerical solver were described in Chapter 3.

6.2 Experimental Setup

The experimental setup is shown in Figure 6.1. Similarly with time-of-flight, charges are photogenerated using a high intensity laser, and the voltage across the load resistor is measured with an oscilloscope. However, in contrast with traditional time-of-flight, the measurement is repeated many times across a wide range of load resistances. Furthermore, volume photogeneration is desirable, and consequently operational thin-film solar cells can be studied.

The experiment begins with the photogeneration of a large quantity ($\gg CU$) of charge carriers using an intense laser pulse. These carriers induce a photocurrent that charges the electrodes, which act as capacitive plates. The electrodes rapidly acquire a charge of CU, where C is the capacitance and U is the solar cell's built-in field (or the applied voltage). Next, two processes occur simultaneously. The first is the recombination of the photogenerated charges, and the second is the discharge of the capacitor through the external RC circuit. If the RC time is large, then the photocarriers will completely recombine before the capacitor can discharge, and the total extracted charge will be limited to CU. Conversely, if the RC time is small, then the capacitor will discharge before the carriers completely recombine, more photocurrent will flow, and the extracted charge will exceed CU. In the intermediate regime, there is an interplay between the bimolecular lifetime and the RC time. We exploit this relationship in order to quantify the carrier recombination.

6.3 Device Thickness and Light Absorption Profile

It has been shown in the past that the light absorption profile strongly affects CELIV transients [133], so it is important to clarify the impact that the light absorption has on HI-RPV. We apply the Beer-Lambert law to represent the photogeneration profile,

$$n_0 = p_0 = L\alpha e^{-\alpha x}, \tag{6.1}$$

where n_0 (p_0) is the initial concentration of electrons (holes), L is the light intensity in photons per unit area, α is the absorption coefficient at the laser wavelength, and x is

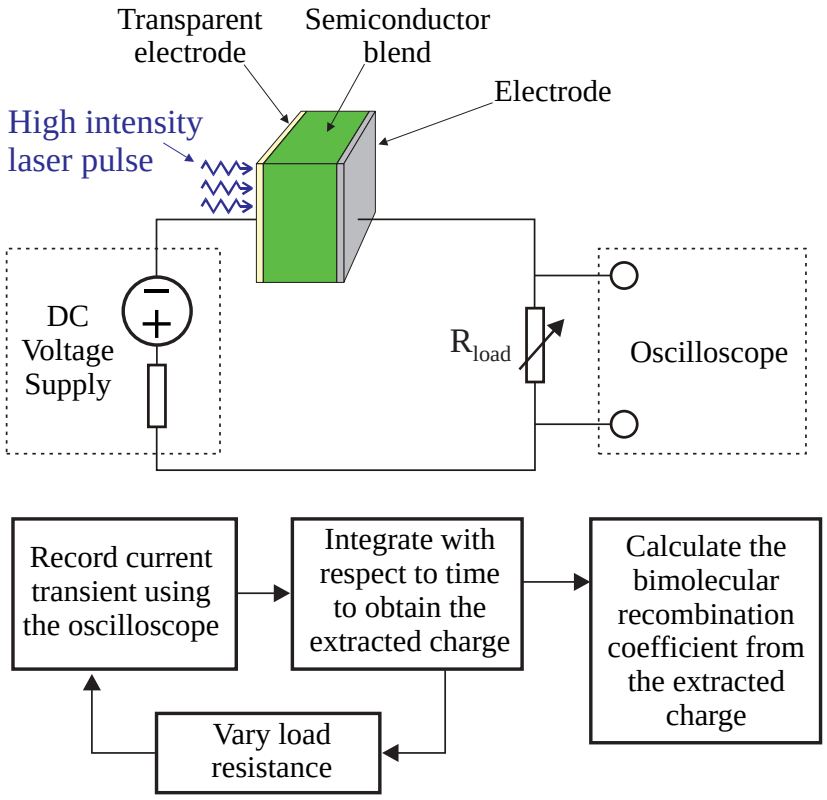

Figure 6.1: Circuit schematic for the High Intensity Resistance dependent Photo-Voltage (HI-RPV) experiment. Current transients are recorded across a range of load resistances, and then integrated to obtain the extracted charge, Q_e. The variation in the extracted charge with resistance is used to quantify the recombination processes and determine the bimolecular recombination coefficient. If the device under test is an operational solar cell, then the DC voltage supply is optional and the experiment can be done under the solar cell's built-in field.

the spatial coordinate. Normalising the absorption coefficient α to the film thickness d, the shape of the initial distribution is described by the dimensionless quantity αd.

We performed numerical simulations at varying values of αd and for varying light intensities. The light intensity is represented by the quantity of photogenerated charge carriers $Q_{\mathrm{ph}} = L\left(1 - e^{-\alpha d}\right)$, which is the integral of Eq. (6.1) over the device. We selected a fixed circuit resistance, $RC/t_{\mathrm{tr(sum)}} = 0.05$, where R is the resistance of the circuit external to the device, C is the device capacitance, and $t_{\mathrm{tr(sum)}} \equiv d^2 \left(\mu_{\mathrm{p}} + \mu_{\mathrm{n}}\right)^{-1} U^{-1}$ is an effective transit time calculated from the sum of carrier mobilities crossing a film of thickness d under a voltage U. The use of $\mu_{\mathrm{p}} + \mu_{\mathrm{n}}$ in the normalisation scale will be justified below. The bimolecular recombination was given by the Langevin rate ($\beta/\beta_L = 1$).

The light intensity dependence in the amount of extracted charge is plotted in Figure 6.2. The simulations were conducted with equal electron and hole mobilities; however, the results are essentially unchanged if the mobilities are not equal (as shown in Figure 6.3). We observe that the extracted charge Q_e/CU becomes essentially independent of αd when αd is less than 1. The inset of Figure 6.2 shows the αd dependence at high light intensity, demonstrating that Q_e/CU is essentially insensitive

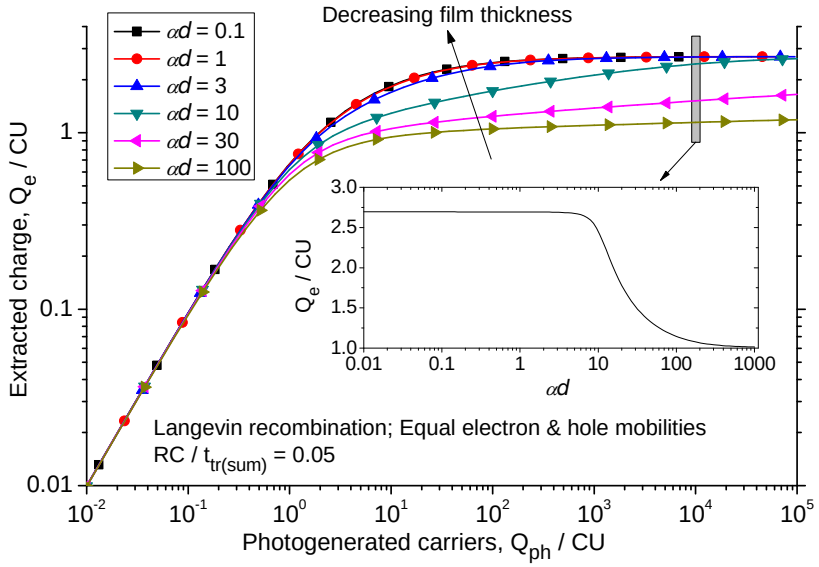

Figure 6.2: The impact of the film thickness and light absorption profile on the extracted charge. The film thickness is incorporated within the absorption-thickness product αd (where α is the absorption coefficient and d the thickness). The inset shows the αd dependence in the region indicated by the thin grey box ($Q_{\rm ph}/CU = 10^4$), and demonstrates that the extracted charge is independent of the initial carrier distribution for thin films ($\alpha d < 1$). The extracted charge readily saturates with high light intensity. This graph shows that a general theory for thin film devices can be developed, without detailed optical modelling, and without regard for the precise quantity of photogenerated carriers in the saturation regime.

to the initial carrier spatial distribution, in the case of volume generation. For example, in the case of $\alpha d = 3$ (see Figure 6.2), the light intensity at the back of the device is approximately 5% of the light intensity at the front of the device. Such a strong inhomogeneity in the spatial distribution does not meaningfully affect the extracted charge.

Physically, the insensitivity to the initial spatial distribution is caused by bimolecular recombination. The bimolecular recombination process will be more rapid in regions of higher light intensity, and slower in regions of lower light intensity. This will, in effect, "smooth" the carrier distribution across the device, erasing the initial spatial distribution. More precisely, the carrier concentration at early times is given by $n(t) = \left(n_0^{-1} + \beta t\right)^{-1}$, where n_0 is the initial carrier concentration [118]. In the limit of very large n_0, the dependence on the initial condition vanishes [$n(t) \approx (\beta t)^{-1}$]. This explains why the absorption profile is irrelevant at high light intensities.

In summary, to first order, detailed optical modelling to account for exact carrier distribution in operational solar cells is not necessary, since the precise spatial distribution of carriers is rapidly erased by bimolecular recombination. Therefore, the HI-RPV technique can be applied to thin film devices ($\alpha d \leq 1$) without concern for optical interference.

Since the technique is insensitive to the light absorption profile, we will remove αd from the set of parameters being tested, and approximate the initial condition by

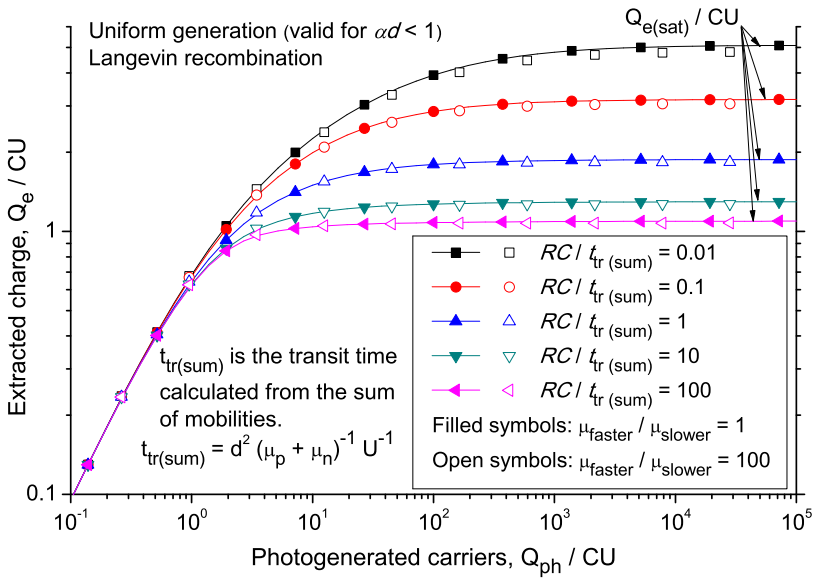

Figure 6.3: The impact of the circuit resistance on the extracted charge from simulated resistance dependent photovoltage experiments. Filled symbols with lines show balanced mobilities ($\mu_{\text{faster}}/\mu_{\text{slower}} = 1$); open symbols without lines show strongly unbalanced mobilities ($\mu_{\text{faster}}/\mu_{\text{slower}} = 100$). The two are very similar, because the normalisation scale for the circuit RC time minimises the effect of the mobility ratio. The saturation value $Q_{\text{e(sat)}}/CU$ depends almost entirely upon the normalised resistance. These results demonstrate that the load resistance needs to be accounted for to correctly measure the recombination coefficient.

perfectly uniform carrier generation. All subsequent numerical calculations are performed with this simplified uniform initial condition, rather than the Beer-Lambert law. Using this approximation, the simulation parameters are reduced to light intensity (expressed as Q_{ph}/CU), recombination coefficient (expressed as β/β_L), mobility ratio $\mu_{\text{faster}}/\mu_{\text{slower}}$, and the circuit resistance (expressed as $RC/t_{\text{tr(sum)}}$). The circuit resistance, which we will address next, is a crucial parameter that may have been overlooked in the past [95].

6.4 Circuit Resistance

In a HI-RPV experiment, the circuit resistance is varied over many orders of magnitude in order to observe the dynamical interaction between the known circuit RC time and the unknown bimolecular lifetime.

We examined the impact of the circuit resistance using our simulations, as shown in Figure 6.3. Importantly, we observe that more charge can be extracted at lower resistances. A smaller resistance allows the charge extraction to complete in a shorter time, so that less recombination occurs, and the overall extracted charge is higher.

The faster carrier mobility is normalised out of the simulation by the system of units (as described in Chapter 3). However, it is necessary to specify the ratio of carrier mobilities $\mu_{\text{faster}}/\mu_{\text{slower}}$. To confirm that variation in this ratio will not interfere with the measurement, Figure 6.3 shows the case of balanced mobilities ($\mu_{\text{faster}}/\mu_{\text{slower}} = 1$)

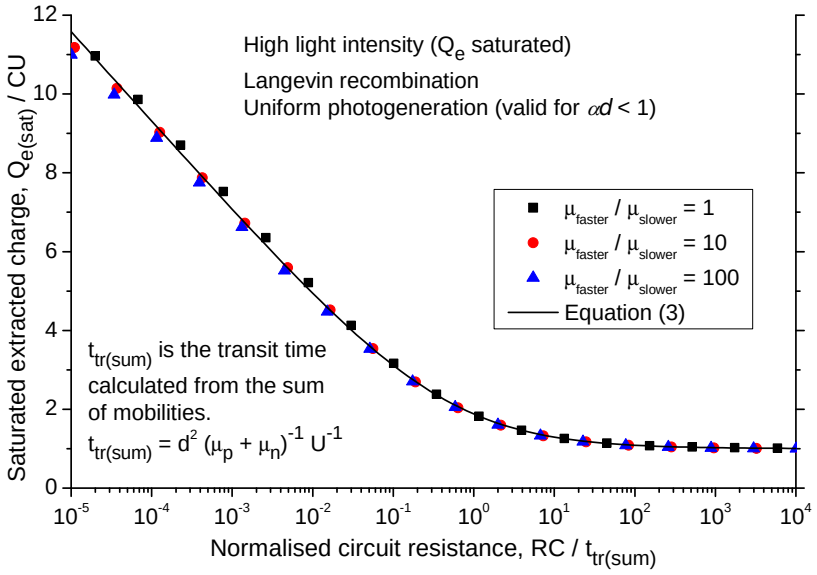

Figure 6.4: Simulations of the impact of load resistance on the extracted charge from thin film devices with Langevin recombination at varying mobility ratios. Points are calculated from simulations at high light intensity ($Q_{\mathrm{ph}}/CU = 10^6$, although the precise value is unimportant because of the saturation in the extracted charge Q_{e}, as shown in Figure 6.3). The ratio of carrier mobilities does not affect the extracted charge, so HI-RPV measurements can be applied equally to systems with balanced mobilities and systems with strongly unbalanced mobilities.

with filled symbols and lines and strongly unbalanced mobilities ($\mu_{\mathrm{faster}}/\mu_{\mathrm{slower}} = 100$) with open symbols and no lines. This covers a wide range of mobility ratios to examine the variation that might be expected to occur in practice. The two cases (balanced mobilities and strongly unbalanced mobilities) are essentially indistinguishable, as shown in Figure 6.3. We explain this insensitivity as follows. The amount of extracted charge Q_{e} is primarily controlled by the recombination. The Langevin recombination rate is proportional to the *sum* of carrier mobilities. The relevant time scale for this process is $t_{\mathrm{tr(sum)}} \equiv d^2/(\mu_{\mathrm{p}} + \mu_{\mathrm{n}})\,U$.

Figure 6.3 shows that the extracted charge saturates at high light intensities to a value that we call $Q_{e(\mathrm{sat})}/CU$, as indicated by the arrows. Therefore, if the HI-RPV experiment is operated in this saturation regime, the amount of extracted charge does not depend on the laser power which is applied. The extracted charge is also independent of the carrier mobility ratio (Figure 6.3) and the light absorption profile (Figure 6.2). Consequently, the only parameters remaining to be quantified are the circuit resistance and the bimolecular recombination coefficient.

The impact of the circuit resistance is shown in Figure 6.4. If the normalised resistance is small, the extracted charge $Q_{\mathrm{e(sat)}}$ can exceed the charge on the electrodes CU by an order of magnitude or more, even in the presence of Langevin recombination. The TOF experiment under these circumstances is therefore misleading, especially if comparing two systems with different values of the normalised resistance, $RC/t_{\mathrm{tr(sum)}}$. We resolve this problem by introducing the HI-RPV technique. We firstly develop

predictions for Langevin systems, and then in the following section extend this to the general case.

Figure 6.4 shows a single universal curve that all Langevin systems should obey. We developed an empirical equation to describe this curve by arbitrarily choosing an appropriate functional form that would give a logarithmic dependence at small R (as shown in Figure 6.4), and would saturate to 1 at large R (as also shown in Figure 6.4),

$$\frac{Q_{\mathrm{e(sat)}}}{CU} = 1 + p_1 \log\left[1 + p_2 \left(\frac{t_{\mathrm{tr(sum)}}}{RC}\right)^{p_3}\right]. \tag{6.2}$$

We used non-linear least squares regression to calculate the coefficients p_i from the simulation results in Figure 6.4. The result is:

$$\frac{Q_{e(\mathrm{sat})}}{CU} = 1 + 1.8 \log\left[1 + 0.63 \left(\frac{t_{\mathrm{tr(sum)}}}{RC}\right)^{0.55}\right], \tag{6.3}$$

which is valid for Langevin recombination and thin films. Equation (6.3) is plotted against the simulation results in Figure 6.4, demonstrating excellent agreement.

The purpose of Eq. (6.3) is to determine the type of recombination present in a thin film device; for example, one could plot this equation alongside measured data in order to determine whether the recombination is of the Langevin type. This is important, since recombination orders higher than two have been experimentally observed [150], and it is necessary to identify the type of recombination dynamics that might apply to the system being studied. A plot of extracted charge versus resistance (Figure 6.4) will follow the form of Eq. (6.3) if Langevin recombination is dominant. In contrast, if there is a higher order of recombination, then the carrier concentration will decay according to a different time dependence, and the functional form of the extracted charge versus resistance will change. If the recombination is stronger than Langevin, the experimental data will lie *below* the line. On the other hand, if the dominant form of recombination is slower than Langevin, then less recombination will occur and the experimental data will lie *above* the line.

We will show below that our experimental data can be described by a bimolecular recombination process with a Langevin reduction prefactor. We do not exclude the possibility of higher-order effects such as a concentration-dependent recombination coefficient [243], but these are not necessary to explain our data. Therefore, in the following section, we extend our theory to systems with suppressed (non-Langevin) recombination of purely second order.

6.5 Bimolecular Recombination Coefficient

In order to develop a tool for convenient experimental quantification of the recombination coefficient (β/β_L), we applied numerical simulations to predict the amount of extracted charge as a function of β/β_L. These simulations are plotted in Figure

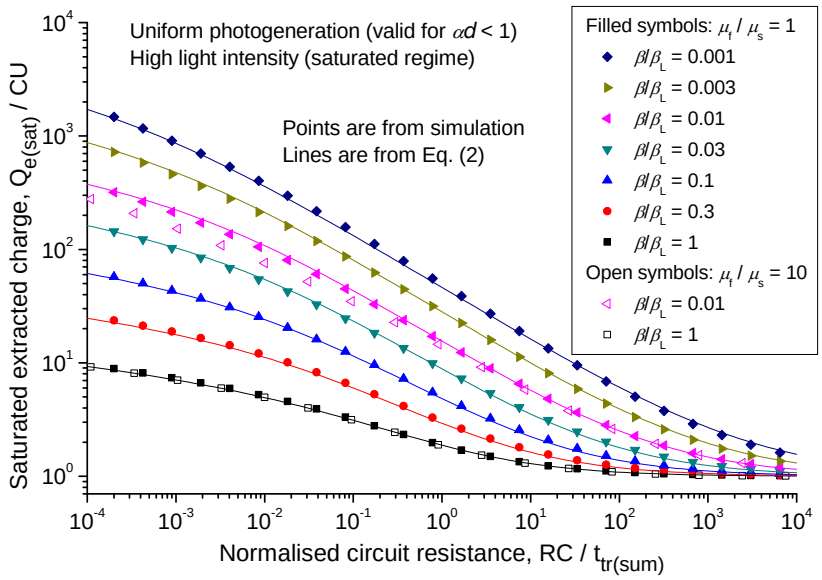

Figure 6.5: Numerically predicted extracted charge as a function of load resistance in High Intensity Resistance dependent PhotoVoltage (HI-RPV) experiments for different recombination coefficients β/β_{L}. The extracted charge shown in this figure is calculated at the highest light intensities where the extracted charge saturates, as shown in Fig. 6.2. The points are from simulations, whereas the lines are Eq. (6.2) evaluated for each respective value of β/β_{L}. This graph presents numerical predictions to be used when measuring the recombination coefficient β/β_L experimentally from HI-RPV in systems without deep traps.

6.5. As expected, the amount of extracted charge increases dramatically in the presence of non-Langevin recombination. To confirm that our technique remains valid, we checked that non-Langevin devices also exhibit saturation at high light intensity, and that the extracted charge is independent of the optical absorption profile for thin films ($\alpha d < 1$). We found that systems with strongly suppressed recombination ($\beta \ll \beta_{\mathrm{L}}$) exhibit a stronger dependence on the mobility ratio than Langevin systems. The more unbalanced the mobilities, the less charge can be extracted. A representative example ($\mu_{\mathrm{faster}}/\mu_{\mathrm{slower}} = 10$) is plotted in Figure 6.5 with open symbols.

We are now ready to specify how the HI-RPV technique can be applied. The recombination coefficient can be determined by comparing measurements of the extracted charge against the simulation results in Figure 6.5. This approach is valid for any thin film ($\alpha d < 1$) device. Importantly, this technique is not hindered by the RC-dependence that affects traditional high intensity TOF [89,95], because the impact of the RC time constant on the extracted charge is accounted for on the horizontal axis of Figure 6.5. However, for accurate measurements, it is necessary to reach the regime where $RC/t_{\mathrm{tr(sum)}} \ll 1$. This may not be possible in extremely high mobility materials, especially when the series resistances are included in R. Ideally, R should be varied over many orders of magnitude.

As an alternative to visual inspection of the graph, we can also specify an empirical equation that describes the data in Figure 6.5. We started with the general functional form [Eq. (6.2)] and applied a procedure similar to that described earlier for the

Langevin case. We performed simulations across a physically realistic parameter space in both $RC/t_{\mathrm{tr(sum)}}$ and β/β_{L}. The simulations were performed with balanced mobilities, because that corresponds to the maximum extracted charge. With least squares regression, we found the parameters p_i as a function of β/β_{L}. Finally, we parametrised the p_i values as follows, choosing an arbitrary functional form that best described the data:

$$p_1 = 1.829\left(\frac{\beta}{\beta_{\mathrm{L}}} + 0.0159\sqrt{\frac{\beta}{\beta_{\mathrm{L}}}}\right)^{-1} \tag{6.4}$$

$$p_2 = 0.63\left(\frac{\beta}{\beta_{\mathrm{L}}}\right)^{0.407} \tag{6.5}$$

$$p_3 = 0.55\left(\frac{\beta}{\beta_{\mathrm{L}}}\right)^{0.0203}. \tag{6.6}$$

These functional forms were found to obtain the best fit to the simulated results.

Figure 6.5 shows the simulation results compared with Eq. (6.2) with the parameters (6.4)-(6.6). A good agreement is demonstrated for balanced mobilities; if the mobilities are unbalanced then Eq. (6.2) will slightly overestimate the extracted charge.

These equations are a convenient tool to analyse experimental data. For example, to determine the recombination coefficients for the data presented below, we set up a spreadsheet table to compare the model with experimental data and thereby estimate the bimolecular recombination coefficient.

In order to confirm the validity of the newly presented HI-RPV technique, we have compared its results in various systems with other techniques including photo-CELIV [129], double injection transients [253] and plasma extraction [254]. The results are in agreement, given the limitations of each technique. These limitations must be carefully considered when comparing measurements, which is why we have developed the present HI-RPV approach.

6.6 Experimental Measurements

We manufactured bulk heterojunction organic solar cells with the donor:acceptor blend poly[N-9”-hepta-decanyl-2,7-carbazole-*alt*-5,5-(4’,7’-di-2-thienyl-2’,1’,3’-benzothiadiazole)] (PCDTBT) and [6,6]-phenyl-C_{71}-butyric acid methyl ester (PC70BM). This blend, PCDTBT:PC70BM, has previously been reported to exhibit near to Langevin recombination [75]. Two sources of PCDTBT were used. A low molecular weight batch ($\overline{\mathrm{M}}_{\mathrm{n}}$ = 4.3 kDa, $\overline{\mathrm{M}}_{\mathrm{w}}$ = 12.1 kDa, PDI = 2.8, dissolved in 1,2,4-trichlorobenzene at 140 °C) was synthesized in our laboratory following the Suzuki cross-coupling protocols previously described [255]. A high molecular weight batch ($\overline{\mathrm{M}}_{\mathrm{n}}$ = 22.7 kDa, $\overline{\mathrm{M}}_{\mathrm{w}}$ = 122.2 kDa, PDI = 5.4) was purchased from the SJPC Group.

The fabrication of the solar cells followed a previously described procedure [6]. 15 Ω/sq. Indium Tin Oxide (ITO) coated glass substrates patterned by photolithography (Kintec) were cleaned by sonicating in sequence with alconox (detergent), de-ionised

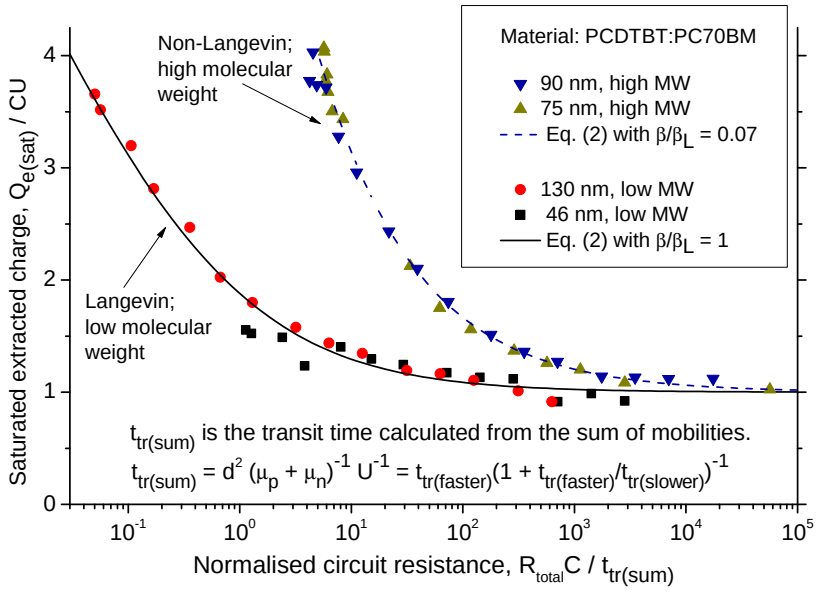

Figure 6.6: Experimentally measured extracted charge as a function of circuit resistance obtained using the HI-RPV technique. Films made with the low molecular weight polymer exhibit Langevin recombination, whereas films containing the high molecular weight polymer exhibit suppressed non-Langevin recombination. Non-Langevin recombination is beneficial to solar cell performance, indicating the importance of material quality in device fabrication.

water, acetone, and *iso*-propanol for 10 minutes. The cleaned substrates were coated with a 20 nm layer of poly(3,4-ethylenedioxythiophene):poly(styrene sulfonate) (PEDOT:PSS) by spin casting at 5000 rpm for 60 sec. The PEDOT:PSS layer was baked for 10 minutes at 170 °C. A solution of PCDTBT and commercially purchased PC70BM (Nano-C) with a mass ratio of 1:4 was prepared at a total concentration of 20 mg/mL in anhydrous 1,2-dichlorobenzene. This solution was deposited by spin coating on top of the PEDOT:PSS layer after filtration. Two substrates were prepared from the low molecular weight batch with active layer thicknesses of 46 nm and 130 nm, respectively. From the high molecular weight batch, two additional substrates were made with active layer thicknesses of 75 nm and 90 nm. Thicknesses were measured by a Veeco Dektak150 profilometer. Slow drying was performed after spin coating by placing the coated film in a partially opened petri dish for 2 hours. Finally, a 100 nm aluminium layer was deposited by thermal evaporation under a 10^{-6} mbar vacuum. The device areas were 0.035 cm^2 with three devices per substrate. The low molecular weight material produces solar cells with power conversion efficiencies (PCE) of approximately 4%; whereas optimised solar cells made from the high molecular weight material have PCEs in excess of 6% [256]. Transit times were measured using low light intensity resistance dependent photovoltage [3]; the mobilities were $\mu_{\text{low MW}} \approx 8\times10^{-5}\,\text{cm}^2\text{V}^{-1}\text{s}^{-1}$ and $\mu_{\text{high MW}} \approx 2\times10^{-3}\,\text{cm}^2\text{V}^{-1}\text{s}^{-1}$, demonstrating greatly improved charge transport in the latter devices.

HI-RPV measurements were performed using a pulsed third-harmonic Nd:YAG laser (Quantel Brio) working at a wavelength of 355 nm and pulse duration of 5 ns.

At 355 nm, the absorption coefficient of this blend [65] is 8×10^4 cm^{-1}, which gives αd values of 0.37 for the thinnest device (46 nm) and 1.0 for the thickest device (130 nm). The laser beam was attenuated using a neutral density filter set. No external voltage was applied; instead, the transients were driven by the solar cells' built-in field. The signal was recorded by a digital storage oscilloscope (LeCroy Waverunner A6200).

We performed HI-RPV with load resistances in the range from 1 Ω to 1 MΩ. The results are plotted in Figure 6.6. This graph demonstrates the application of the HI-RPV technique. It is important to note that the resistance value R on the horizontal axis is the *complete* circuit resistance, calculated as the sum of the load resistance and the solar cell series resistance. The experimental data is plotted together with the predicted curve from Eq. (6.2) with parameters (6.4)-(6.6). The measured extracted charge behaves as expected and as predicted by the simulations. The extracted charge decreases with increasing resistance until it saturates to $Q_{e(sat)}/CU = 1$. To determine the recombination strength, the coefficient β/β_L was adjusted until the predicted curves matched the experimental data.

Our results indicate that low molecular weight devices exhibit Langevin-type recombination, while the high molecular weight devices exhibit non-Langevin recombination with $\beta/\beta_L \approx 0.07$. Photo-CELIV measurements applied to the same devices demonstrated Langevin and non-Langevin recombination, respectively, supporting our results. However, photo-CELIV is subject to various limitations, as we discussed in the Introduction, and so we developed HI-RPV for the detailed study. The strong change in the recombination strength likely contributes to the improved power conversion efficiency of the high molecular weight blend. It has previously been reported that PCDTBT solar cell performance improves with increasing molecular weight [257]. Our results indicate that suppressed recombination may be the mechanism behind this performance trend, and hence the molecular weight is a parameter that should be considered when optimising solar cell performance. There may be further performance improvements to be gained by identifying the molecular weight at which the recombination is minimised.

A previous study of recombination in PCDTBT solar cells [75] reported reduction factors in the range of $\beta/\beta_L = 0.3$ to $\beta/\beta_L = 1$ depending upon the device thickness. Thinner devices were reported to exhibit more strongly reduced recombination. Thickness dependencies cannot be reliably studied using time-of-flight because variations in the thickness influence parameters such as the device capacitance, the RC time, the transit time, the optical absorption profile, and the amount of extracted charge. Consequently, with time-of-flight it is difficult to eliminate the dependence on the experimental parameters. In contrast, HI-RPV accounts for these effects. We did not observe any thickness dependence, although the range of thicknesses measured here is less than that in the previous study [75].

Further work is necessary in order to clarify the origin of this molecular weight dependence, as well as any dependence on other parameters such as polydispersity,

impurity density, and conjugation length. The novel HI-RPV technique will be beneficial for such future work.

6.7 Conclusion

We studied recombination in the organic photovoltaic system PCDTBT:PC70BM, and observed that devices made with a higher molecular weight polymer exhibit suppressed recombination relative to devices made with a lower molecular weight polymer. Our results highlight the importance of material quality for fabrication of high efficiency organic solar cells. We developed and implemented a theoretical framework for the novel High Intensity Resistance dependent PhotoVoltage (HI-RPV) technique, which allows recombination measurements that are independent of the experimental conditions, resolving a key weakness of previous time-of-flight based techniques. A key advantage of HI-RPV is its insensitivity to the light absorption profile in thin films, making it applicable to operational devices.

7

Intensity Dependent Photocurrent (IPC)

This chapter contains material that has been submitted for publication:

- Martin Stolterfoht, Ardalan Armin, Bronson Philippa, Ronald D. White, Paul L. Burn, Paul Meredith, Gytis Juška, and Almantas Pivrikas. Photocarrier drift distance in organic solar cells and photodetectors. *Scientific Reports* (submitted).

This chapter contains experimental data that was measured by Martin Stolterfoht, Ardalan Armin, and Almantas Pivrikas. Figure 7.9 was prepared by Martin Stolterfoht, and is reproduced here because it provides a validation of my theoretical work. The discussion here focusses on the simulation and theoretical aspects of the above paper, which were my contribution.

7.1 Introduction

The previous chapters reported experimental methods based on photoconduction *transients*, where current transients are measured after a nanosecond laser excitation. A solar cell spends the vast majority of its time under steady-state conditions, and so measurements conducted at steady-state would be the most representative of actual operational conditions. In this chapter, we study steady-state photocurrent. We examine the influence of the carrier mobilities, recombination coefficient, and trapping on the photocurrent that a solar cell can produce. We show that variation in the light intensity can be used to observe the onset of fast bimolecular recombination, and thereby

present "design rules" for achieving high transport efficiency without bimolecular recombination.

We will investigate the solar cell's photocurrent as a function of light intensity. Typically, this would be done under short circuit conditions, but it is also possible to apply a bias to test the device's response at the maximum power point. We call this measurement intensity dependent photocurrent (or IPC). This technique is very common in the literature [73, 242, 258–260], where it is often used as a test for bimolecular recombination. Many studies report a power law dependence, i.e. $j_{sc} \sim L^{\alpha}$ where j_{sc} is the short-circuit current, L is the light intensity, and α is the power law slope. A linear dependence ($\alpha = 1$) is known to indicate the absence of bimolecular recombination, whereas sublinear slopes ($\alpha < 1$) indicate bimolecular recombination losses [242, 261]. If this measurement is taken over a small range of light intensities [259], the true functional shape of α may be hidden, and so many orders of magnitude of light intensities are needed. Over a large range, one often observes a transition between linear behaviour at low light intensities, to sublinear behaviour at higher light intensities [242]. This indicates a transition from recombination-free to recombination-limited behaviour. Here, we will systematically examine this effect in order to understand the conditions under which bimolecular recombination is significant and the conditions under which it may be avoided or minimised.

7.1.1 Device fabrication and methods

Two different organic solar cell materials were used in this study. The first was poly[[4,8-bis[(2-ethylhexyl)oxy]benzo[1,2-b:4,5-b']dithiophene-2,6-diyl][3-fluoro-2-[(2-ethylhexyl)carbonyl]thieno[3,4-b]thiophenediyl]]:[6,6]-phenyl-C70-butyric acid methyl ester (PTB7:PC70BM) [262], while the second was poly[N-9"-hepta-decanyl-2,7-carbazole-*alt*-5,5-(4',7'-di-2-thienyl-2',1',3'-benzothiadiazole)] (PCDTBT):PC70BM [65]. To fabricate the devices, the substrates were prepared as described previously [263]. For the PTB7 devices, the active layer solution of PTB7 (purchased from 1-Material, Mw = 97.5 kDa, PDI = 2.1) and PC70BM (American Dye Source, Inc., Canada) was blended in a 1:1.5 ratio by weight in chlorobenzene with 3% 1,8-diiodoctane (DIO) by volume. Solar cells with three different junction thicknesses were prepared by using a total concentration of 31 mg/cm^3 for the 100 nm and 230 nm thick devices and a concentration of 45 mg/cm^3 for the 700 nm thick device. The solutions were spun cast at 2200 rpm, 400 rpm and 600 rpm for 120 seconds, respectively. The films were subsequently dried at 70 °C. For the PCDTBT devices, the solution of PCDTBT (SJPC, Canada, Mw = 122 200 g/mol, PDI=5.4) and PC70BM was blended in a 1:4 ratio by weight in 1,2-dichlorobenzene. Solar cells with three active layer thicknesses, 75 nm, 230 nm and 850 nm were fabricated by using a total concentration 25 mg/cm^3 for the 100 nm and 230 nm thick blends respectively, while a concentration of 40 mg/cm^3 was used to fabricate the 850 nm thick film. The solutions were spun cast at 2000 rpm, 500 rpm and 500 rpm for 90 seconds, respectively. The active layer thicknesses were measured with a DekTak 150 profilometer. All devices were completed by vacuum

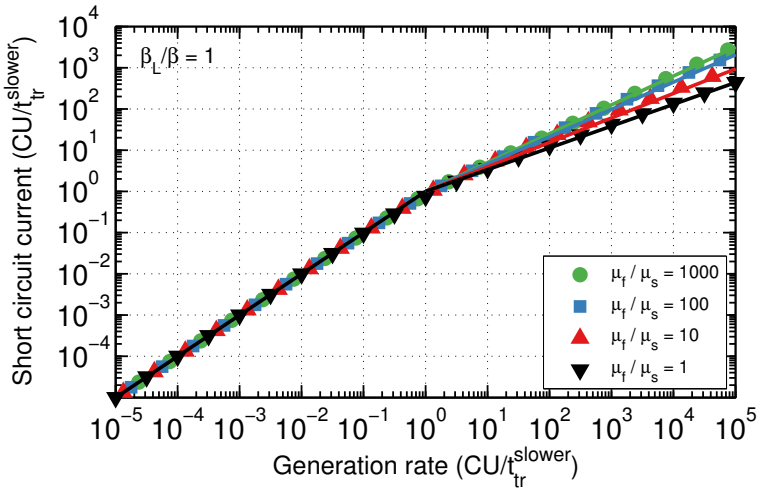

Figure 7.1: Simulated IPC data for various carrier mobility ratios. There is a universal shape that applies independently of the carrier mobility ratio, allowing general predictions to be made. For these simulations, the recombination coefficient was Langevin, i.e. $\beta_L/\beta = 1$. Simulation results are shown with points, and the lines are a guide to the eye.

evaporation of 1.2 nm of samarium followed by 75 nm of aluminum under a 10^{-6} mbar vacuum. The device areas were 0.2 cm^2 for current-voltage curves (JV), IPC and EQE measurements, and 3.5 mm^2 for RPV measurements (to characterise the mobility and calculate I_{sclc}). All device fabrication took place within a glove box with < 1 ppm oxygen and water. JV and EQE measurements were also performed inside a glove box. Subsequently the devices were encapsulated for the IPC measurements.

Simulations were conducted using the model described in Chapter 3. Of particular importance to this work is the normalisation scale that was described in that chapter. Notably, the light intensity is incorporated into the concomitant generation rate of free carriers. In other words, the efficiency of exciton separation is included in the generation rate. The objective of this work is to focus on charge transport, and so all the effects of light absorption, exciton separation, etc. are simply lumped together into an overall generation rate. This generation rate will itself be normalised with respect to $CU/t_{\text{tr}}^{\text{slower}}$, where C is the device's capacitance, U is the effective voltage (the built-in field plus any applied voltage), and $t_{\text{tr}}^{\text{slower}}$ is the transit time of slower carriers. The chosen charge scale (CU) is a natural choice because it indicates the approximate threshold at which space charge effects begin to appear. Similarly, the transport time $t_{\text{tr}}^{\text{slower}}$ is a natural time scale because it indicates the amount of time that a carrier would be expected to remain inside the device. Photocurrent is also normalised with respect to the same scale.

7.2 The Universal Functional Form

Initially considering the case of Langevin-type recombination, we simulated the IPC experiment over a very large range of light intensities. The results shown in Figure

7.1 display two notable features. Firstly, there is a universal functional form, and consequently variations in any of the parameters in the normalised generation rate (e.g. mobility, dielectric constant, thickness, ...) will simply move along the universal curve. The second notable feature is that the deviation point separating the linear and sublinear regimes always occurs at the same normalised light intensity, that being when the generation rate of free carriers is equal to $CU/t_{\mathrm{tr}}^{\mathrm{slower}}$.

There is much information encoded in the normalised axes. Increasing the light intensity has the impact of moving right and upward, following the universal shape of Figure 7.1. A more interesting result is that variations in any of the parameters contained within $CU/t_{\mathrm{tr}}^{\mathrm{slower}}$ would also move along the curve. For example, increasing the slower-carrier mobility while holding everything else constant moves to the left but also *down*. This is counter-intuitive: an improved mobility results in a *lower* photocurrent! However, a reduction in *normalised* photocurrent does not necessarily correspond to a reduction in *actual* photocurrent because the normalisation scale also changes. The interplay between normalised units and real units provides crucial insight that endows Figure 7.1 with much predictive power.

According to this simple model, variations in mobility have no impact on the photocurrent if the device remains in the linear regime. Physically, in this regime, there is negligible recombination, so charge transport is already sufficient to extract charges before they recombine, and improving the mobility provides no further benefit. A different situation arises in the sublinear regime, where an improvement in mobility would indeed improve the photocurrent. For example, consider a ten-fold improvement in slower-carrier mobility. The operating point moves one decade to the left in Figure 7.1, resulting in approximately a three-fold *decrease* in normalised current. However, the scaling factor to convert that normalised current back to real units increased by a factor of ten, resulting in a net gain of $\sim 10/3$ or approximately 3 times *improved* photocurrent. It is not just mobility that can be considered in this way, because $CU/t_{\mathrm{tr}}^{\mathrm{slower}}$ also contains the dielectric constant, active layer thickness, voltage, etc. This model allows predictions to be made with respect to any of these parameters.

In the discussion above, we assumed that non-geminate recombination caused the deviation from linearity, as has been previously reported [242]. To confirm this claim, we replotted the simulation of Figure 7.1 as internal quantum efficiency (IQE) and recombination losses, as shown in Figure 7.2. It is possible to plot recombination losses directly because the simulation allows access to such information that would not be observable in a real experiment. These results clearly show that the drop in IQE, and hence the sublinear behaviour at higher light intensities, is caused by non-geminate recombination.

7.3 Non-Langevin Recombination

The impact of non-Langevin recombination (i.e. $\beta_L/\beta > 1$) is to prolong the deviation from linearity until higher normalised generation rates, as shown in Figure 7.3. The

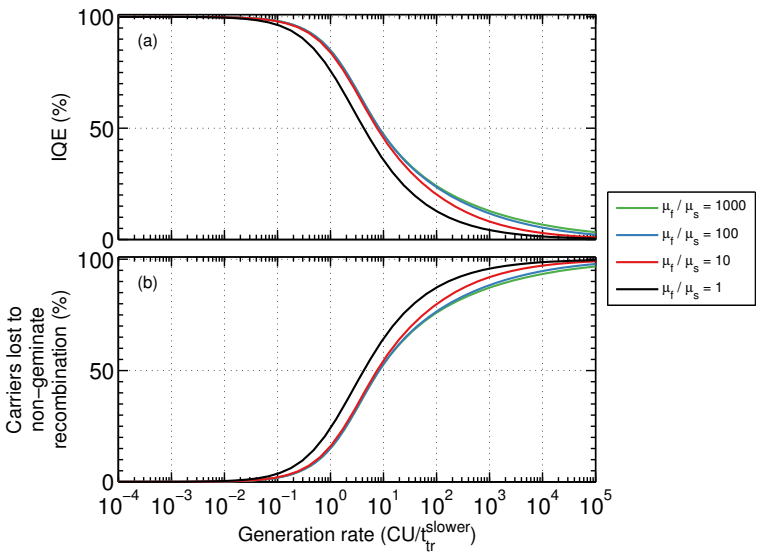

Figure 7.2: **(a)** Simulated internal quantum efficiency (IQE) as a function of light intensity for various carrier mobility ratios. The decline in IQE exactly coincides with the onset of non-geminate recombination as shown in panel **(b)**.

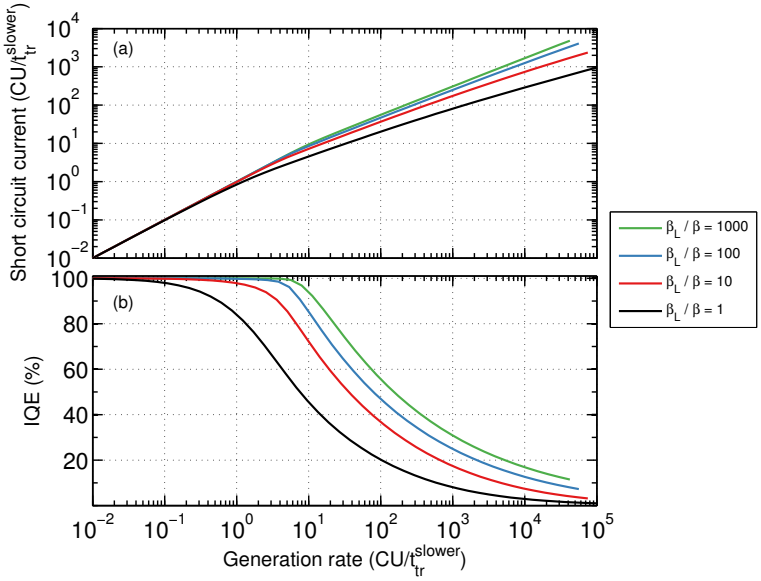

Figure 7.3: Simulated IPC data for various recombination coefficients. Panels **(a)** and **(b)** are from the same simulations. The impact of non-Langevin recombination is to allow higher light intensities without losses. It can be seen that the benefit is approximately proportional to the square root of β_L/β.

data are presented in two forms: as intensity-dependent photocurrent (Figure 7.3a) and also as internal quantum efficiency (Figure 7.3b). The advantage of the latter is that the onset of recombination is more clearly visible.

To make predictions about the amount of recombination that should occur, we desire a normalisation scale that will collapse all the data into the same universal curve, as was done above with Figure 7.1. Figure 7.3 (b) shows that a hundred-fold reduction in recombination results in approximately a ten-fold shift in the deviation point. This implies that the impact of non-Langevin recombination should be proportional

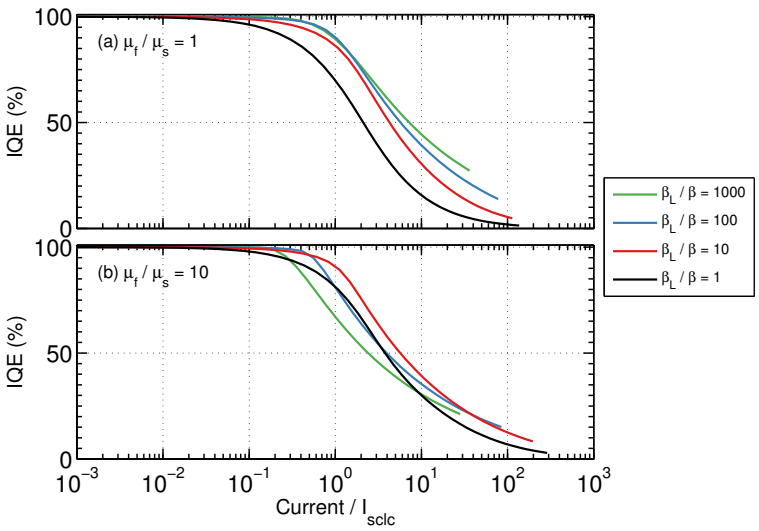

Figure 7.4: Simulated IPC data for various recombination coefficients. Recombination is seen to begin when the photocurrent reaches approximately the space-charge limited current (I_{sclc}).

to $\sqrt{\beta_L/\beta}$. Another transport problem that displays the same trend is the analytic solution for double injection into an undoped semiconductor [118]

$$I_{sclc} = \sqrt{\frac{9\pi}{4}}\sqrt{\frac{\beta_L}{\beta}} CU \left(\frac{\sqrt{\mu_p \mu_n} U}{d^2}\right), \tag{7.1}$$

where the sclc subscript stands for space charge limited current. Importantly, the impact of non-Langevin recombination is to enhance the injection current by a factor $\sqrt{\beta_L/\beta}$. Introducing that factor into the normalisation scale from above, we arrive at the simplified formula

$$I_{sclc} \sim \frac{CU}{t_{\mathrm{tr}}^{\mathrm{slower}}}\sqrt{\frac{\beta_L}{\beta}}. \tag{7.2}$$

It is demonstrated in Figure 7.4 that Eq. (7.2) is indeed an effective normalisation scale. The onset of recombination is approximated by Eq. (7.2) across three orders of magnitude of recombination coefficient. Therefore, the space-charge limited current indicates the approximate extraction capacity before recombination losses become significant.

7.4 Practical Issues

Before this theory can be applied to operational organic solar cells, several practical issues must first be considered. These are optical interference, circuit series resistance, and charge trapping.

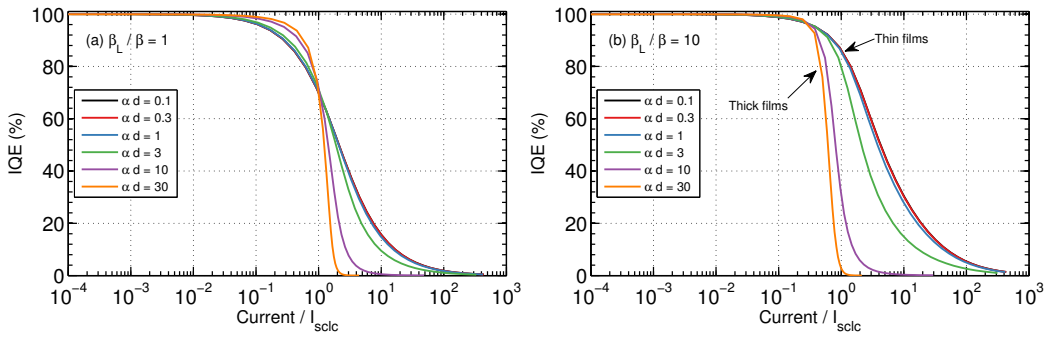

Figure 7.5: The impact of optical absorption patterns on IPC simulations for the case of **(a)** Langevin recombination and **(b)** non-Langevin recombination. In the case of thin films ($\alpha d \leq 3$), I_{sclc} gives an approximate indication of the onset of substantial recombination.

7.4.1 Optical interference

The light intensity profile inside a solar cell is non-uniform, because of absorption, reflection, and wave interference. It's important to test the impact of this absorption profile, because it can be an issue for other experiments such as photo-CELIV [133]. The simplest model for the light intensity profile is the Beer-Lambert law,

$$Q_{\text{ph}}(x) \propto e^{-\alpha x}, \tag{7.3}$$

where $Q_{\text{ph}}(x)$ is the spatial profile of charge photogeneration, α is the absorption coefficient, and x is the distance into the film. When normalised as described in Chapter 3, the absorption coefficient becomes the dimensionless quantity αd, where d is the film thickness.

Typical simulations for the case of varying αd values are shown in Figure 7.5. The absorption profile does cause some slight shifts, for example in the IQE that is predicted when the current equals I_{sclc}. Nevertheless, for the case of thin films, we find that I_{sclc} gives an approximate threshold for the onset of substantial recombination.

We also tested realistic absorption profiles as calculated using the transfer matrix approach [208]. The results are very similar to the thin film cases shown in Figure 7.5. As long as the photogeneration is substantially "in the volume" (as opposed to near the surface), then the impact of optical interference appears small.

7.4.2 Series resistance

Series resistances are expected in the circuit, which may arise for example due to the transparent electrode of the solar cell. The impact of the series resistance is shown in Figure 7.6. Resistances are expressed as the dimensionless ratio $RC/t_{\text{tr}}^{\text{faster}}$. The impact of the series resistance is to cause an earlier onset in recombination, with a notably sharp drop-off in IQE. This occurs when the voltage across the resistance becomes comparable with the solar cell's built-in voltage, for then charge accumulates on the electrodes and extraction is compromised.

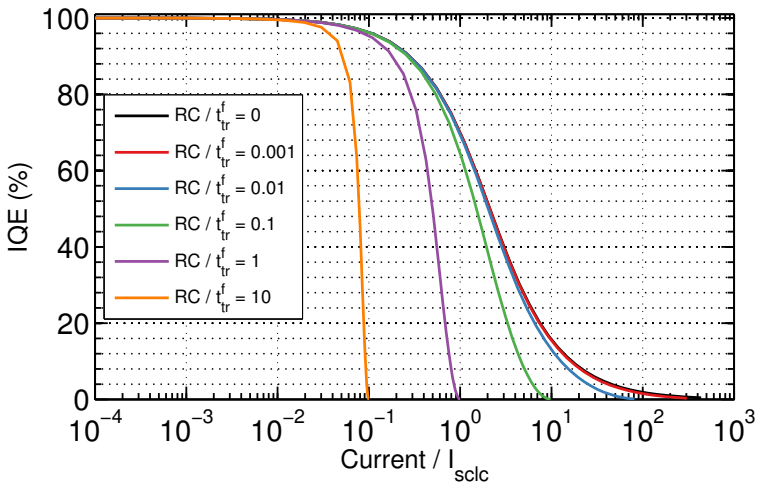

Figure 7.6: The impact of series resistances on IPC simulations. A large series resistance results in an earlier onset of recombination with a very sharp drop-off in IQE.

The results in Figure 7.6 indicate that series resistance might be an issue in some devices. The threshold at which R becomes limiting is approximately $RC/t_{\mathrm{tr}}^{\mathrm{faster}} \sim 1$. This is a large resistance, and the problem would be immediately obvious in a transient experiment such as photo-CELIV (Chapter 4) and RPV (Chapter 5). If $RC/t_{\mathrm{tr}}^{\mathrm{faster}} < 1$, then the series resistance should not affect the onset of recombination.

7.4.3 Charge trapping

To examine the impact of charge trapping, we applied the following model

$$\frac{\partial n_f}{\partial t} = -\frac{n_f}{\tau_c}\left(\frac{N_t - n_t}{N_t}\right) + \frac{n_t}{\tau_r} \tag{7.4}$$

$$\frac{\partial n_t}{\partial t} = \frac{n_f}{\tau_c}\left(\frac{N_t - n_t}{N_t}\right) - \frac{n_t}{\tau_r}, \tag{7.5}$$

where N_t is the number of available trap states, n_f is the free particle distribution, n_t is the trapped particle distribution, τ_c is the capture time, and τ_r is the release time.

The IPC experiment is conducted under steady-state conditions, so the most important characteristic is the quantity of charges that exist in trapped states; the temporal dynamics of their capture and release are insignificant once steady-state has been reached. There are two situations that we will consider:

1. The case where the number of available trap states is not limited, and therefore the quantity of trapped charges depends upon the equilibrium between capture, release, and recombination; and

2. The case where the number of available trap states is limited, and therefore the quantity of trapped charges is primarily determined by the density of *available* trap states. This could arise, for example, if the materials are of high quality and the traps are caused by rare defects.

The first situation will occur in the limit of large N_t, and equations (7.4) and (7.5) reduce to

$$\frac{\partial n_f}{\partial t} = -\frac{n_f}{\tau_c} + \frac{n_t}{\tau_r} \tag{7.6}$$

$$\frac{\partial n_t}{\partial t} = \frac{n_f}{\tau_c} - \frac{n_t}{\tau_r}. \tag{7.7}$$

Under steady-state conditions we find that

$$n_f = \frac{\tau_c}{\tau_r} n_t, \tag{7.8}$$

and it is the ratio between the capture and release rates that controls the equilibrium point. Equation (7.8) is a simplification because it neglects the other terms such as generation and recombination, but it is still a useful approximation to guide the modelling of trapping in the IPC experiment. Guided by this approximation, we will specify the trap parameters in terms of the proportion of charges available, $n_f/n_{\text{total}} = (1 + \tau_r/\tau_c)^{-1}$, where $n_{\text{total}} = n_f + n_t$.

The simulation results in Figure 7.7 (a) show that trapping causes an early onset of recombination. This is expected because each charge carrier must spend some time in traps, and therefore the average bulk mobility is reduced. A reduction in mobility compromises the ability of the system to extract charge carriers, and therefore the concentration increases until recombination sets in. We emphasise that the simulation incorporates both band-to-band recombination (between free carriers) as well as trap-assisted recombination.

If continual trapping and release causes an overall reduction in mobility from what it would be without traps, then all mobility measurements should be similarly affected. Indeed, the true mobility of the system is the one that incorporates this trapping effect. When I_{sclc} is adjusted accordingly, the impact of trapping vanishes (Figure 7.7 b). This is simply because the onset of recombination is driven by the overall concentration of charges (whether they are trapped or not).

Next, we turn to the second situation to be modelled, which was where the quantity of trapped charges is limited by the number of trap sites that exist. This case will occur when the release time is long ($\tau_r \gg t_{\text{tr}}$), such that all the traps eventually become filled. In practice, not every single trap site will be populated, because trap-assisted recombination will cause some to be empty. Nevertheless, if the capture time is fast ($\tau_c \ll t_{\text{tr}}$), recombined trapped charges will be quickly replaced, and the overall quantity of trapped charge will remain close to the physical limit. Simulations of this case are shown in Figure 7.8 for $\tau_c/t_{\text{tr}} = 0.1$, and $\tau_r = \infty$. In this situation, the amount of charges in the traps is largely independent of the light intensity, and consequently the trap-assisted recombination is first-order. This appears as a flat reduction in the internal quantum efficiency, as shown in Figure 7.8.

This type of trapping will only occur when the release time is long and/or the density of available trap sites is small. In the latter case, the effect is negligible, as

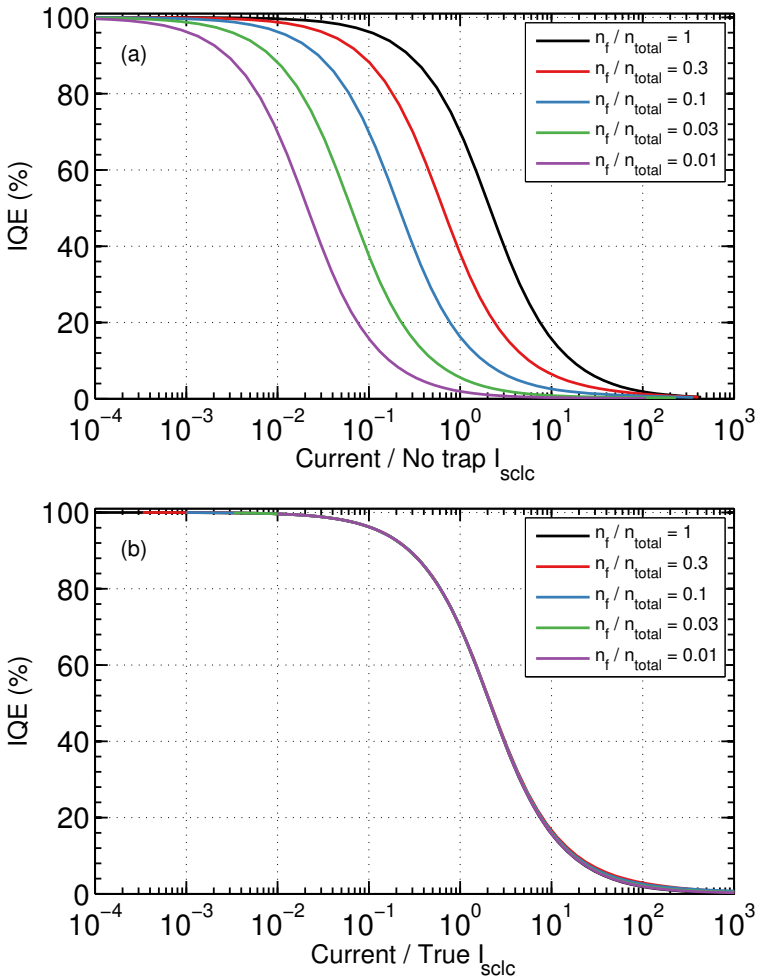

Figure 7.7: The impact of charge trapping, when the quantity of trapped charge is controlled by the equilibrium between the capture and release times. In panel **(a)**, the current is normalised to the space-charge limited current that is calculated using the mobility of free carriers, whereas in panel **(b)**, the normalisation scale is corrected for the reduction in bulk mobility that is caused by the trapping. Panel **(b)** is the realistic case because experiment will measure the "after trapping" mobility. Simulation settings were Langevin recombination, balanced mobilities, $\tau_c + \tau_r = 0.1t_{\mathrm{tr}}$, and both types of carriers trapped equally.

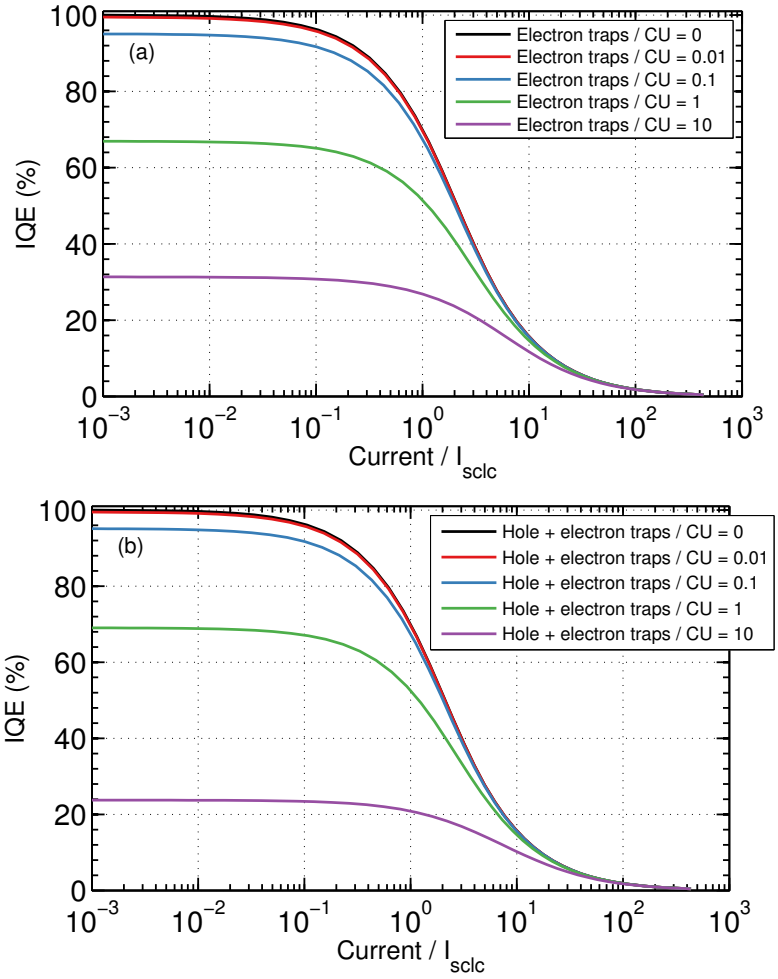

Figure 7.8: The impact of charge trapping, when the quantity of trapped charge is limited by the density of available trap sites. In panel **(a)**, only one type of charge carrier is trapped, whereas in panel **(b)** both types of carrier are trapped. In both situations, the quantity of trapped charge is independent of the light intensity, and therefore appears as first-order recombination and a flat reduction in IQE. Simulation settings were Langevin recombination, balanced carrier mobilities, $\tau_c/t_{\mathrm{tr}} = 0.1$, and $\tau_r = \infty$.

shown in Figure 7.8. Trap-assisted recombination is only significant when the density of (filled) traps approaches CU, which is a level that would be easily detected by charge extraction measurements [241]. Additionally, if the release time is long, then repetitive RPV experiments will reveal the presence of the trapped charge [3]. Consequently, it is experimentally possible to determine whether the observed first-order losses are determined by trapped charge or by geminate recombination.

In summary, our simulations indicate that trapping causes second-order recombination if the quantity of trapped charges increases with increasing light intensity (Figure 7.7), and it causes first-order recombination if the quantity of trapped charges is independent of light intensity and larger than $\sim CU$ (Figure 7.8).

7.5 Experimental Results and Discussion

The simulation results above indicate that substantial recombination should only occur when a solar cell's photocurrent reaches approximately

$$I_{\mathrm{sclc}} \sim \frac{CU}{t_{\mathrm{tr}}^{\mathrm{slower}}} \sqrt{\frac{\beta_L}{\beta}}, \tag{7.9}$$

provided that the device is not limited by series resistances.

This prediction was tested on a total of six different organic solar cells: three devices with PTB7:PC70BM as the active layer, and another three devices with PCDTBT:PC70BM as the active layer. The results are shown in Figure 7.9. The thinnest PTB7:PC70BM device (100 nm) is limited by the series resistance of the indium tin oxide (ITO) electrode, because in that device the very thin structure and the high mobility of PTB7 combine to produce a large I_{sclc}. Excluding that device, the remaining five demonstrate excellent agreement with the prediction that the onset of strong recombination coincides with the photocurrent reaching I_{sclc}.

To discuss the physical implications of this result, it is helpful to express I_{sclc} in terms of the fundamental device and material properties:

$$I_{\mathrm{sclc}} \sim \frac{S\epsilon\epsilon_0\mu_s U^2}{d^3} \sqrt{\frac{\beta_L}{\beta}}. \tag{7.10}$$

Notably, there is a very strong dependence of the device thickness (d). Optimising the device thickness is challenging, because increased thicknesses are desirable to maximise light harvesting, but at the same time an increased thickness has a very detrimental impact on charge transport. Other parameters such as the slower-carrier mobility (μ_s) or recombination coefficient (β_L/β) would need to improve dramatically in order to permit an increase in thickness. Additionally, inhomogeneities in the thickness (as might be caused by fabrication over large areas) would cause dramatic changes in the device's charge transport capacity. Another interesting observation is that a ten-fold improvement in mobility is equivalent to a hundred-fold improvement in the

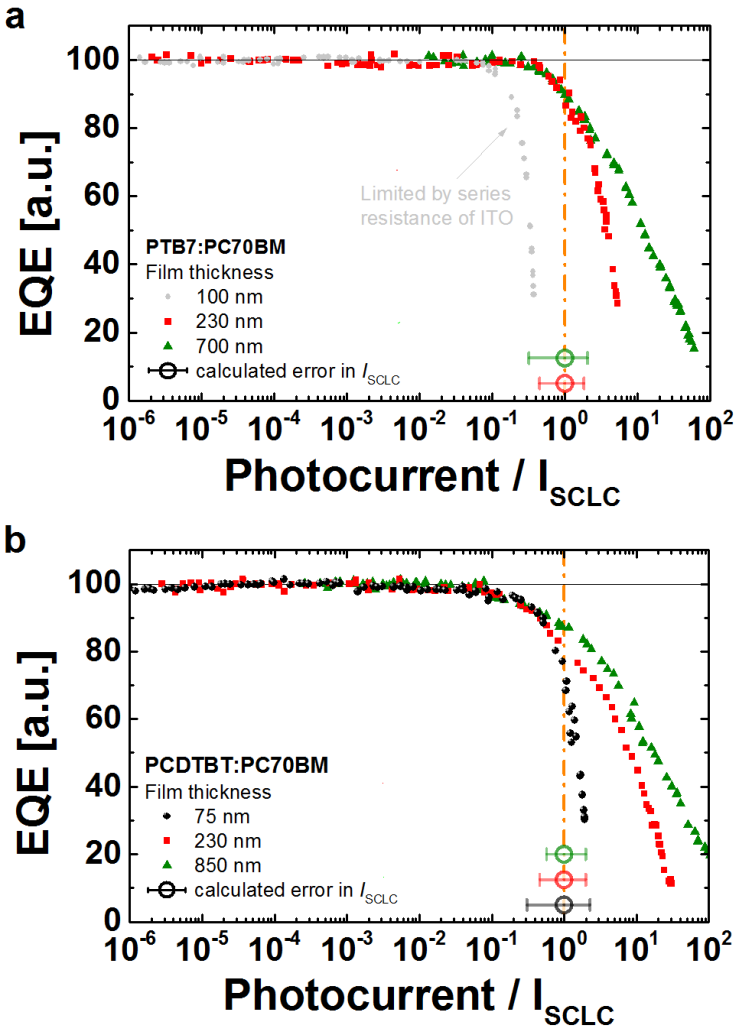

Figure 7.9: Experimental results confirming the prediction that non-geminate recombination begins when the photocurrent reaches the space charge limited current. This supports the conclusion from the modelling that I_{sclc} is the fundamental limit for charge extraction without losses.

recombination coefficient. It is clear that *strongly* suppressed recombination is needed in order to make substantial gains.

7.6 Conclusion

Normalised photocurrent as a function of normalised light intensity shows a universal shape (e.g. Figure 7.1), in which a linear regime transitions into sub-linear behaviour at higher generation rates. In the linear regime, non-geminate recombination is negligible, except in the case of large amounts of deep traps which could be detected experimentally through charge extraction measurements [241]. Consequently, non-geminate recombination is essentially negligible, and therefore losses that occur can be attributed to geminate recombination. However, substantial non-geminate recombination sets in once the photocurrent reaches the critical threshold of $I_{\text{sclc}} \sim \sqrt{\beta_L/\beta}\, CU/t_{\text{tr}}^{\text{slower}}$. In

this regime, the photocurrent is limited by charge transport. We emphasise that a given solar cell system can be switched from one regime to the other by changing the thickness or voltage, or if the device had a different permittivity, slower-carrier mobility, or recombination coefficient. Due to the universal shape of the IPC curve, this model can be used to estimate the rise in photocurrent that would occur given certain material improvements. The most important parameters to optimise are the mobility of slower carriers and the recombination coefficient.

8

The Fractional Advection-Diffusion Model

This chapter contains material that has been published in the following journal article:

[1] B. W. Philippa, R. D. White, and R. E. Robson. Analytic solution of the fractional advection-diffusion equation for the time-of-flight experiment in a finite geometry. *Physical Review E*, **84**, 041138 (2011). doi:10.1103/PhysRevE.84.041138.

8.1 Introduction

Dispersive transport occurs when photocurrent transients decay with time even before the transit time of the carriers [78, 264]. It can be modelled using a multiple trapping model—as in Chapter 3—but this does not incorporate dispersion directly into the transport model. Instead, that model creates dispersion by "partitioning" the number density into trapped and free distributions, and ensuring that the release times are subjected to a distribution.

An alternative mechanism is to specify a transport model that intrinsically implements dispersion. This can be achieved using a fractional diffusion equation. The advantage of this scheme is that only a single equation is needed; whereas the multiple trapping framework fundamentally requires a free distribution to be coupled to a trapped distribution. One such approach is that of *fractional diffusion* [185, 203, 265–269].

This chapter will apply a fractional diffusion model to the time-of-flight experiment. We begin by formulating the model. We consider a thin sample of disordered material confined between two plane-parallel electrodes, with all spatial variation confined to

the normal direction, which we take to be the z axis. In Chapter 2, we derived the following fractional diffusion equation that describes this system:

$$ {}_0^C D_t^\gamma n + W_\gamma \frac{\partial n}{\partial z} - D_{L,\gamma} \frac{\partial^2 n}{\partial z^2} = 0, \tag{8.1} $$

where W_γ and $D_{L,\gamma}$ are the fractional drift velocity and longitudinal diffusion coefficient, respectively. The fractional drift velocity has units $\mathrm{m/s}^\gamma$, while the fractional diffusion coefficient has units $\mathrm{m}^2/\mathrm{s}^\gamma$. We have assumed the small signal limit so that the transport coefficients W_γ and $D_{L,\gamma}$ are constant and uniform. The derivative operator ${}_0^C D_t^\gamma$ is the Caputo fractional partial derivative of order γ. We recall from Chapter 2 that the Caputo derivative is defined as

$$ {}_0^C D_t^\gamma f(t) \equiv \frac{1}{\Gamma(1-\gamma)} \int_0^t (t-\tau)^{-\gamma} f'(\tau) d\tau. \tag{8.2} $$

A simple and numerically efficient solution of Eq. (8.1) would be highly desirable. Previously reported solutions of fractional diffusive systems for bounded media have been expressed in terms of infinite series solutions [195, 200, 270]. Here, we show that the series solution to Eq. (8.1) with absorbing boundaries may be collapsed into a simple closed form solution in Laplace space by building upon the experience gained in solution of the *non-dispersive* diffusion equation in gaseous electronics [271].

The structure of this chapter is as follows. In Section 8.2, we model the time of flight experiment [112] and obtain a formal analytic solution of Eq. (8.1) as a series of Mittag-Leffler functions, which is cast into a tractable form, suitable for practical purposes, using the Poisson summation theorem. In Section 8.3, we express the current measured in a time-of-flight experiment in terms of this analytic solution, and show analytically that sums of the slopes in distinct time regimes add up to -2 on a log-log plot, as predicted by Scher and Montroll [77] and as observed in many experiments [78]. In Section 8.4, we explore the way that current varies with experimental parameters, and go on to fit selected experimental data. We show that our solution demonstrates the power-law decay characteristic of dispersive transport.

8.2 Time of Flight Solution

In this chapter, we will use Eq. (8.1) to model a disordered semiconductor in a time of flight experiment [112]. A one dimensional equation, such as (8.1), is appropriate for a thin sample of disordered material confined between two large plane parallel boundaries, which we shall take to be at $z = 0$ and L respectively.

In the idealized time-of-flight experiment, a sharp pulse of n_0 charge carriers is released from a source plane $z = z_0$ at time $t = t_0$, i.e.,

$$ n(z, t_0) = n_0 \delta(z - z_0), \tag{8.3} $$

and the fractional advection diffusion equation is solved using the methods and techniques described below. The solution for other experimental arrangements, e.g., for sources distributed in space and/or emitting for finite times, can be found by appropriate integration of this fundamental solution over z_0 and/or t_0 respectively. We assume absorbing boundary conditions at the electrodes, i.e.

$$n(0,t) = n(L,t) = 0. \tag{8.4}$$

The fractional partial differential equation (8.1) can be solved by separation of variables. The result is

$$n(z,t) = n_0 \sum_{m=1}^{\infty} \varphi_m(z) E_\gamma \left(-\omega_m \left(t - t_0\right)^\gamma\right), \tag{8.5}$$

where the spatial modes are

$$\varphi_m(z) \equiv \frac{e^{\lambda(z-z_0)}}{L} \left(\cos\left[k_m(z-z_0)\right] - \cos\left[k_m(z+z_0)\right]\right),$$

and where

$$\lambda \equiv \frac{W_\gamma}{2D_{L,\gamma}} \tag{8.6a}$$

$$\omega_m \equiv D_{L,\gamma}\left(\lambda^2 + k_m^2\right) \tag{8.6b}$$

$$k_m \equiv \frac{m\pi}{L}. \tag{8.6c}$$

In Eq. (8.5), $E_\gamma(z)$ is the Mittag-Leffler function [272] of order γ:

$$\begin{aligned} E_{\alpha,\beta}(z) &\equiv \sum_{k=0}^{\infty} \frac{z^k}{\Gamma(\alpha k + \beta)} \\ E_\alpha(z) &\equiv E_{\alpha,1}(z). \end{aligned} \tag{8.7}$$

Equation (8.5) gives an exact solution, however, this expression is somewhat difficult to manipulate due to the presence of the Mittag-Leffler function. Furthermore, a large number of terms are needed for this series to converge, and the numerical evaluation of the Mittag-Leffler to suitable precision is computationally difficult.

For inspiration as to how to resolve this challenge, we consider the correspondence principle between fractional and non-fractional systems. Starting with a fractional system, it must be possible to recover non-fractional behaviour in an appropriate limit. In this case, in the limit $\gamma \to 1$, the Mittag-Leffler function reduces to an exponential, i.e. $E_1(z) = e^z$, and (8.5) reduces to Eq. (3b) in Ref. [271]. In the classical, non-fractional limit [271], it was shown that the series convergence could be substantially improved through application of the Poisson summation theorem (PST):

$$\sum_{m=-\infty}^{\infty} f(mT) = \frac{1}{T} \sum_{m=-\infty}^{\infty} F\left(\frac{m}{T}\right), \tag{8.8}$$

where $F(k)$ is the Fourier transform of $f(x)$. Here, we show that the PST can also be applied to the fractional advection diffusion equation with similar benefits. Attempting to apply the PST directly to Eq. (8.5) results in an intractable Fourier transform involving the Mittag-Leffler function. On the other hand, the Mittag-Leffler function has a simple Laplace domain representation. Transformed into Laplace space, Eq. (8.5) becomes

$$n(z,s) = n_0 \sum_{m=1}^{\infty} \varphi_m(z) \frac{s^{\gamma-1}}{s^\gamma + \omega_m}, \tag{8.9}$$

where without loss of generality we have taken $t_0 = 0$.

Applying the Poisson summation theorem to Eq. (8.9) gives the equivalent form

$$n(z,s) = \alpha e^{\lambda z} \sum_{m=-\infty}^{\infty} \left[e^{-\beta|2Lm-(z-z_0)|} - e^{-\beta|2Lm-(z+z_0)|} \right], \tag{8.10}$$

where the space-independent parameters α and β are defined as

$$\alpha(s) \equiv \frac{n_0 s^{\gamma-1} e^{-\lambda z_0}}{2\sqrt{D_{L,\gamma}}\sqrt{s^\gamma + D_{L,\gamma}\lambda^2}} \tag{8.11}$$

$$\beta(s) \equiv \frac{\sqrt{s^\gamma + D_{L,\gamma}\lambda^2}}{\sqrt{D_{L,\gamma}}}. \tag{8.12}$$

Simplifying Eq. (8.10), we obtain the closed form expression

$$\bar{n}(z,s) = \alpha e^{\lambda z} \left[e^{-\beta|z-z_0|} - e^{-\beta|z+z_0|} - \frac{4\sinh(\beta z)\sinh(\beta z_0)}{e^{2\beta L} - 1} \right]. \tag{8.13}$$

A necessary condition for convergence to the closed form expression Eq. (8.13) is

$$|\exp(-2\beta L)| < 1, \tag{8.14}$$

which defines the region of convergence of the Laplace domain function Eq. (8.13).

It should be emphasized that Eq. (8.13) is a general result, valid for fractional and non-fractional cases. For normal (non-fractional) transport, $\gamma = 1$, and Eq. (8.10) has an analytic inverse Laplace transform that reduces to Eq. (7) of [271], where it was obtained using time domain methods. For dispersive (fractional) transport, $\gamma < 1$, and an analytical inverse Laplace transform is difficult to find, so the applications presented below required numerical inversion of the Laplace transform[1].

[1] Numerical inverse Laplace transformation was achieved using Matlab code published on the Mathworks File Exchange by W. Srigutomo (http://www.mathworks.com/matlabcentral/fileexchange/9987). For large values of the parameter β (defined in Eq. (8.12)), the Multiple Precision (MP) Toolbox for Matlab (http://www.mathworks.com/matlabcentral/fileexchange/6446) was required to obtain numerical convergence. The MP Toolbox uses the open-source GNU Multiple Precision Arithmetic Library (http://gmplib.org/).

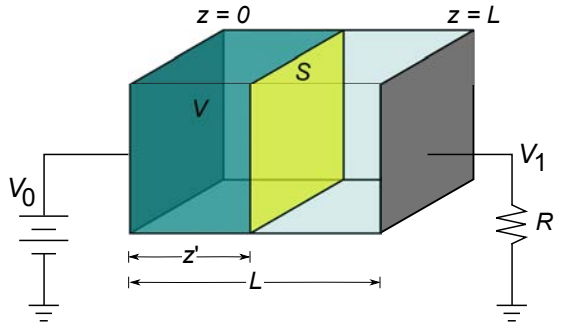

Figure 8.1: Simplified time of flight schematic used in current derivation. The two electrodes at $z = 0$ and $z = L$ have potentials V_0 and V_1, respectively. A surface $\mathcal{S}$ cuts through the sample at $z = z'$; the volume $\mathcal{V}$ is the space between the $z = 0$ electrode and the surface $\mathcal{S}$.

8.3 Currents and the Sum Rule

8.3.1 Current in the time-of-flight experiment

To calculate the current that would be measured in a time-of-flight experiment, we consider the measurement apparatus (Figure 8.1). An electrode at $z = 0$ is held at a potential V_0 by an external power supply, and the opposite electrode at $z = L$ has potential V_1 and is connected via a resistor R to the ground. We define a surface $\mathcal{S}$ which is normal to the electrodes at a position $z = z'$, and a volume $\mathcal{V}$ which is the entire area between the $z = 0$ electrode and the surface $\mathcal{S}$, as indicated in Figure 8.1.

The overall current will consist of a conduction current and a displacement current. Integrating across the width of the sample:

$$J = \frac{1}{L}\int_0^L j_n(z',t)dz' + \frac{\epsilon\epsilon_0}{L}\frac{d}{dt}\left(V_0 - V_1\right), \tag{8.15}$$

where J is the total current density, $j_n(z',t)$ is the conduction current density passing through the surface $\mathcal{S}$, and $\epsilon\epsilon_0$ is the permittivity of the semiconducting material.

If the time-of-flight experiment is conducted in differential mode ($RC \ll t_{tr}$), the voltage $V_0 - V_1$ is essentially constant, and the second term in Eq. (8.15) vanishes. Then the overall current density is simply the space-averaged conduction current:

$$J = \frac{1}{L}\int_0^L j_n(z',t)dz'. \tag{8.16}$$

Care must be taken to evaluate the current density j_n correctly. Some of the charge is trapped, so the current density is *not* proportional to the number density. The proper way to calculate j_n is by the rate of charge leaving the volume $\mathcal{V}$:

$$j_n(z',t) = -\frac{d}{dt}\int_0^{z'} en(z,t)dz.$$

Using Eq. (8.16):

$$J = -\frac{e}{L}\frac{d}{dt}\int_0^L \int_0^{z'} n(z,t)dzdz'.$$

Changing the order of integration:

$$\begin{aligned} J &= -\frac{e}{L}\frac{d}{dt}\int_0^L \int_z^L n(z,t)dz'dz \\ &= -\frac{e}{L}\frac{d}{dt}\int_0^L (L-z)\, n(z,t)dz \\ &= e\frac{d}{dt}\left\{\frac{1}{L}\int_0^L zndz - \int_0^L ndz\right\}. \end{aligned} \tag{8.17}$$

Substituting the time domain $n(z,t)$ solution Eq. (8.5) into Eq. (8.17), the current density is found to be

$$J(t) = \sum_{m=1}^{\infty} \kappa_m t^{-1} E_{\gamma,0}\left(-\omega_m t^{\gamma}\right), \tag{8.18}$$

with

$$\kappa_m = \frac{2en_0 e^{-\lambda z_0} k_m D_{L,\gamma}}{L^2\omega_m^2}\sin\left(k_m z_0\right)\left[2\lambda D_{L,\gamma}\left(e^{\lambda L}\left(-1\right)^m - 1\right) - L\omega_m\right].$$

The expression given in Eq. (8.18) can be slow to evaluate, because a large number of terms are required for the series to converge. A closed form solution can be found in Laplace space by applying Eq. (8.17) to Eq. (8.13):

$$\begin{aligned} \bar{J}(s) = en_0\left(1-\frac{z_0}{L}\right) + en_0 e^{-\lambda z_0}\Bigg\{&\left(1+\frac{2\lambda}{L\left(\lambda^2-\beta^2\right)}\right)\left(e^{-\beta z_0} - e^{\lambda z_0}\right) + \frac{z_0 e^{\lambda z_0}}{L} \\ &+ \sinh\left(\beta z_0\right)\left(\frac{e^{(\lambda-\beta)L}\left(\lambda+\beta\right)}{\beta}\left(\frac{1}{L\left(\lambda-\beta\right)}-1\right) - \frac{1}{\sinh\left(\beta L\right)}\Bigg[e^{-\beta L} - e^{\lambda L}\right. \\ &\left.+ \frac{2\lambda e^{-\beta L}}{L\left(\lambda^2-\beta^2\right)} + \frac{e^{\lambda L}}{2\beta L}\left\{\frac{\lambda-\beta}{\lambda+\beta} - L\left(\lambda-\beta\right) - e^{-2\beta L}\left[1-L\left(\lambda-\beta\right)\right]\right\}\Bigg]\right)\Bigg\}. \end{aligned} \tag{8.19}$$

8.3.2 Sum rule for asymptotic slopes

Experimental time of flight current traces plotted on double logarithmic axes often demonstrate two distinct straight line regimes (see, for example, Figure 8.5), a distinctive shape which has been described as the "signature" of dispersive transport [78]. In many materials, the sum of the slopes on logarithmic axes of these two regimes is very close to -2 (Refs. [78,273]), a prediction originally made for a continuous time random walk model by Scher and Montroll [77]. In what follows, we prove that our expression for the current, Eq. (8.18), demonstrates the same "sum of slopes" criterion.

The small argument asymptote of the Mittag-Leffler function can be written down from its power series definition, Eq. (8.7). The result is

$$E_{\gamma,0}(-\omega_m t^{\gamma}) \sim -\omega_m t^{\gamma},$$

where we have neglected terms of order $O\left(\left[\omega_m t^\gamma\right]^2\right)$ and higher. Substituting this into Eq. (8.18) we find the early time current to be

$$J_{\text{early}}(t) \approx \sum_{m=1}^{\infty} -\kappa_m t^{-1} \omega_m t^\gamma \sim t^{\gamma-1}.$$

Conversely, for the long time current, we use the large $|z|$ asymptote valid for negative real z [274]

$$E_{\alpha,\beta}(z) = -\sum_{k=1}^{p} \frac{z^{-k}}{\Gamma(\beta - \alpha k)} + O\left(|z|^{-1-p}\right).$$

If t is large, then by taking $p = 1$ we obtain the following form for the long time current

$$\begin{aligned} J_{\text{late}}(t) &\approx -\sum_{m=1}^{\infty} \kappa_m t^{-1} \frac{(-\omega_m t^\gamma)^{-1}}{\Gamma(-\gamma)} \\ &\sim t^{-(1+\gamma)}, \qquad \gamma \neq 1. \end{aligned}$$

In summary, the asymptotic forms of the current for $\gamma \neq 1$ are

$$J(t) \sim \begin{cases} t^{-(1-\gamma)}, & \text{early times} \\ t^{-(1+\gamma)}, & \text{late times,} \end{cases} \tag{8.20}$$

in agreement with the sums of slopes condition.

It is noteworthy that these asymptotes are *independent of the boundary conditions* imposed on the system. When solving the fractional diffusion equation $n(z,t)$ is factored as $n(z,t) = Z(z)T(t)$. The time-dependent function, $T(t)$ can be expressed in terms of Mittag-Leffler functions

$$n(z,t) = \sum_m Z_m(z) E_\gamma\left(c_m t^\gamma\right), \tag{8.21}$$

where c_m are the separation eigenvalues found by applying the boundary conditions to the differential equation for $Z(z)$. The asymptotes of the Mittag-Leffler functions [274] are such that physically acceptable solutions must have $c_m < 0$ so that $n(z,t)$ remains bounded as $t \to \infty$. Imposing only the requirement that the boundary conditions result in a negative separation constant, using Eq. (8.17) the current must take the form

$$J(t) = \sum_m \left\{ t^{-1} E_{\gamma,0}\left(c_m t^\gamma\right) \int_0^L \left(\frac{z}{L} - 1\right) Z_m(z) dz \right\}.$$

Using the asymptotic limits detailed above, the time dependence may be brought outside the summation, and the the same temporal asymptotes detailed above then follow. This result is independent of the spatial boundary conditions and hence independent of the specific form of $Z(z)$.

8.3.3 Transit Time

The transit time can be obtained from the expression for the total number of charge carriers within the medium. Defining

$$\bar{N}(s) \equiv \int_0^L \bar{n}(z,s)dz$$

we find in Laplace space

$$\bar{N} = \frac{n_0}{s}\left[1 - e^{-(\lambda+\beta)z_0} - \frac{\sinh(\beta z_0)}{\sinh(\beta L)}e^{-\lambda z_0}\left(e^{\lambda L} - e^{-\beta L}\right)\right]. \tag{8.22}$$

To simplify the mathematics and obtain an estimate for the transit time, we neglect diffusion by taking the limit $D_{L,\gamma} \to 0$:

$$\bar{N}_{D_{L,\gamma}=0} = \frac{n_0}{s}\left(1 - \exp\left[\frac{-s^\gamma (L - z_0)}{W_\gamma}\right]\right). \tag{8.23}$$

In the classical case with $\gamma = 1$, the above equation has the expected inverse Laplace transform

$$N_{D_L=0}^{(\text{classical})}(t) = n_0\left[1 - H\left(t - \frac{L - z_0}{W_\gamma}\right)\right],$$

where $H(t)$ is the Heaviside step function.

For the dispersive case, where $\gamma < 1$, Laplace inversion by complex contour integration gives

$$N_{D_{L,\gamma}=0}(t) = n_0 \sum_{m=1}^{\infty} \eta_{m,\gamma}\left(\frac{L - z_0}{W_\gamma t^\gamma}\right)^m, \tag{8.24}$$

where

$$\eta_{m,\gamma} \equiv \frac{(-1)^{m+1}\sin(m\pi\gamma)\,\Gamma(\gamma m)}{\pi m!}.$$

In the special case of $\gamma = 1/2$, the power series Eq. (8.24) is equivalent to the closed form expression

$$N_{D_{L,\gamma}=0}^{(\gamma=0.5)}(t) = n_0 \operatorname{erf}\left(\frac{L - z_0}{2W_\gamma\sqrt{t}}\right), \tag{8.25}$$

where erf is the Gaussian error function. It is interesting to note that Eq. (8.25) demonstrates great dispersion despite it being a zero diffusion limit of the true behavior of the system.

A clear transit time cannot be precisely defined because the packet of charge carriers becomes widely dispersed. Nevertheless, there exist two regimes of current transport behavior, and the boundary between these regimes can define a "transit time" for the material. It can be seen that two distinct regimes will emerge from Eq. (8.24), according to the magnitude of the term in parenthesis. The transit time, defining the

transition between regimes, is therefore approximately given by

$$\frac{L - z_0}{W_\gamma t_{tr}^\gamma} \sim 1.$$

Solving for the transit time t_{tr}

$$t_{tr} \sim \left(\frac{L - z_0}{W_\gamma}\right)^{1/\gamma}. \tag{8.26}$$

This is in agreement with the expected experimental length and field dependence [77, 78, 273].

8.4 Results

The model discussed above has five parameters: the fractional drift velocity W_γ, the fractional diffusion coefficient $D_{L,\gamma}$, the fractional order γ, the initial source location z_0, and the length of the sample L. These parameters are constrained such that $0 < \gamma \leq 1$, $0 < z_0 < L$ and $D_{L,\gamma} > 0$. The effects of varying the first three of these parameters will be discussed below. The remaining two, the initial location and length of the sample, have obvious implications for the number density profiles.

8.4.1 Impact of the fractional order

The fractional order γ is a dimensionless quantity which defines the degree of the trapping within the medium, with a smaller value corresponding to greater and longer lasting traps. The maximum value of $\gamma = 1$ corresponds to "normal transport," which is governed by the classical (non-fractional) diffusion advection equation.

The impact of γ on the current is demonstrated in Figure 8.2. For non-dispersive transport ($\gamma = 1$), the result is essentially a time independent (displacement) current until a sharp cutoff where the charged particles exit the system through the electrode. The finite drop off time is a reflection of the diffusion in the system. For dispersive transport, the departure of the current traces from the classical profiles is enhanced as the fractional order decreases. The fractional order γ defines the slopes of the two regimes, and hence, characterizes the fundamental *shape* of the current trace. The relevant relations are given in Eq. (8.20) above.

Number density profiles corresponding to the aforementioned current solutions are shown in Figure 8.3. Solutions for $\gamma = 1$ exhibit a moving Gaussian "pulse" of charge carriers, spreading according to $D_{L,\gamma}$ and drifting according to W_γ. This is shown in Figure 8.3a.

For $\gamma < 1$, the signature of fractional or dispersive behavior appears. In this mode, the number density profile retains a "memory" of the initial sharp spike at $z = z_0$. This peak in the density profile does not drift with W_γ, as it does in the non-dispersive case. This long persistence of the initial condition has previously been mentioned in the literature [77, 195, 268]. The smaller the value of γ, the more dispersive the transport.

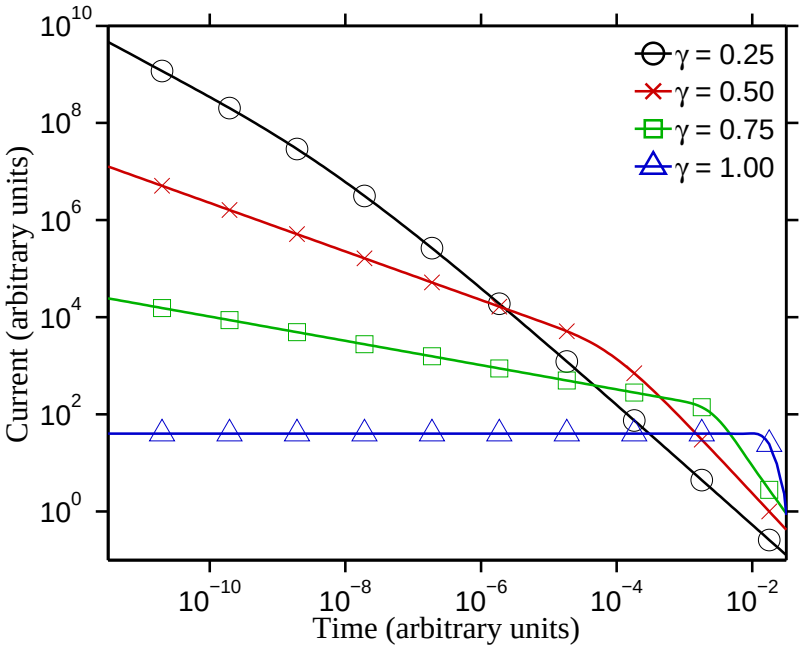

Figure 8.2: Impact of the fractional order γ on the time-of-flight transients. Each curve is the current resulting from the respective number density solution of Figure 8.3.

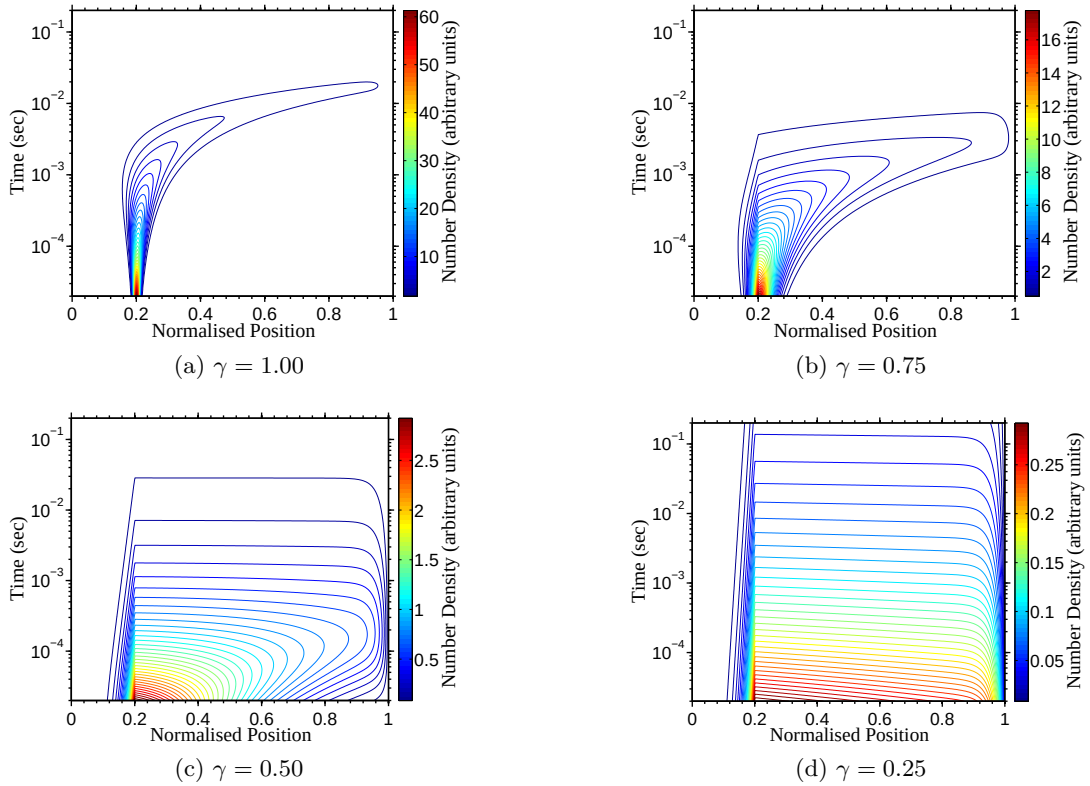

(a) $\gamma = 1.00$ (b) $\gamma = 0.75$

(c) $\gamma = 0.50$ (d) $\gamma = 0.25$

Figure 8.3: Impact of the fractional order γ on the space-time evolution of the number density. In these plots, $W_\gamma = 40/L$ and $D_{L,\gamma} = 1/L^2$.

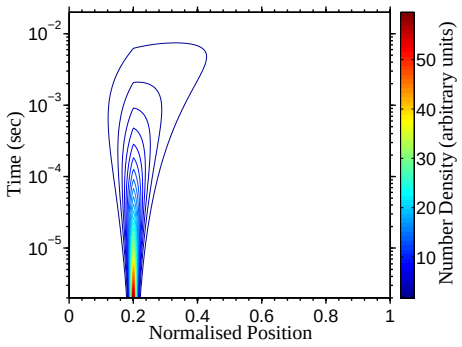

(a) $\gamma = 0.8$; $W_\gamma = 10.0$; $D_{L,\gamma} = 1.0$

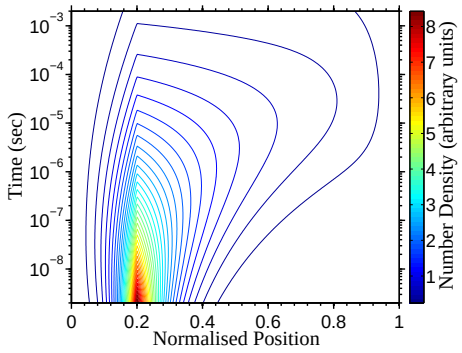

(b) $\gamma = 0.4$; $W_\gamma = 10.0$; $D_{L,\gamma} = 1.0$

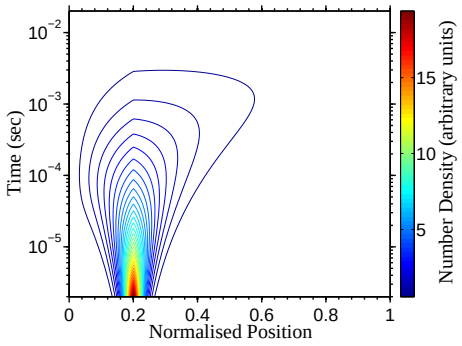

(c) $\gamma = 0.8$; $W_\gamma = 10.0$; $D_{L,\gamma} = 10.0$

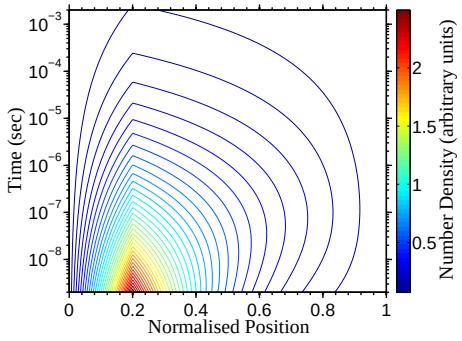

(d) $\gamma = 0.4$; $W_\gamma = 10.0$; $D_{L,\gamma} = 10.0$

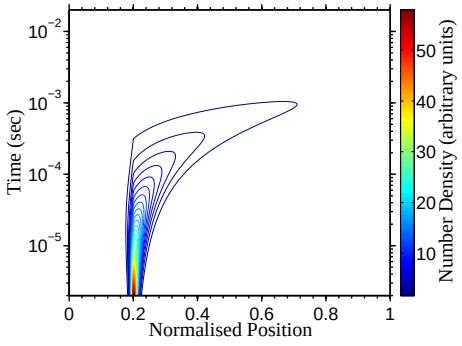

(e) $\gamma = 0.8$; $W_\gamma = 100.0$; $D_{L,\gamma} = 1.0$

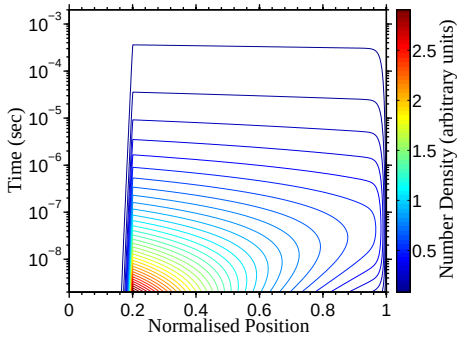

(f) $\gamma = 0.4$; $W_\gamma = 100.0$; $D_{L,\gamma} = 1.0$

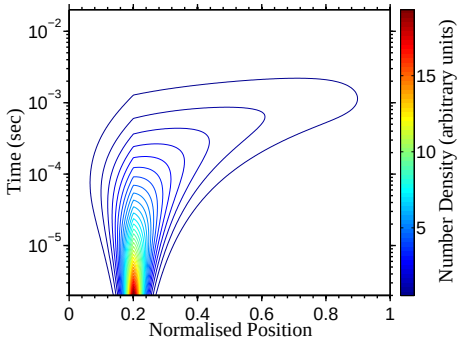

(g) $\gamma = 0.8$; $W_\gamma = 100.0$; $D_{L,\gamma} = 10.0$

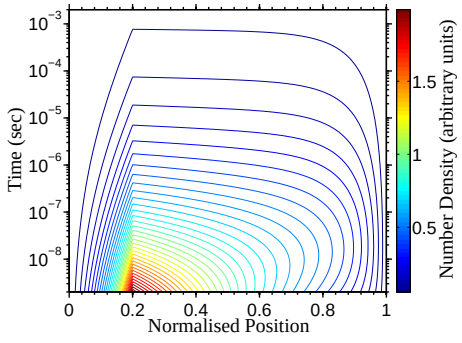

(h) $\gamma = 0.4$; $W_\gamma = 100.0$; $D_{L,\gamma} = 10.0$

Figure 8.4: Space-time evolution of the number density profile for $\gamma = 0.8$ (left column) and $\gamma = 0.4$ (right column). Here, W_γ and $D_{L,\gamma}$ are normalised to the length of the apparatus and are hence both specified in units of $\mathrm{s}^{-\gamma}$.

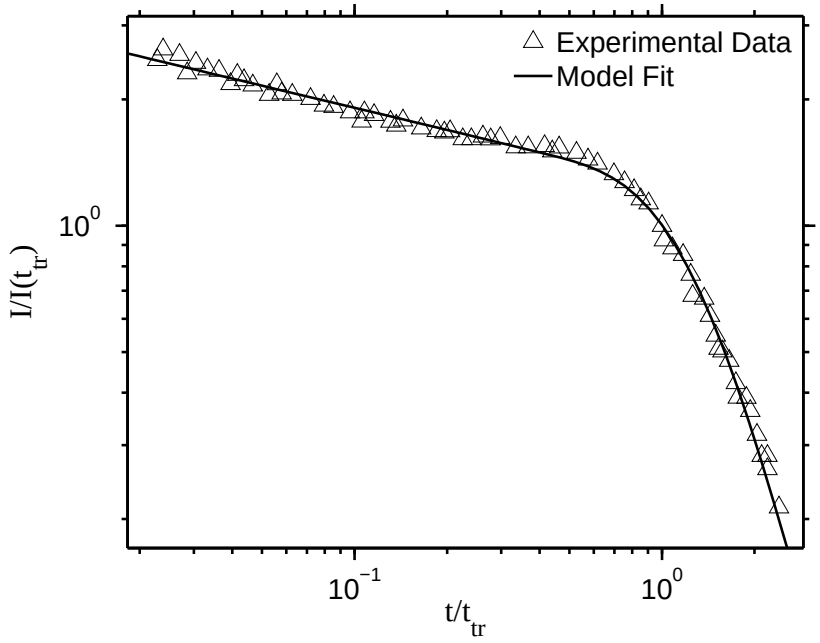

Figure 8.5: Comparison of the model with experimental transients for trinitrofluorenone-polyvinylcarbazole, digitised from Ref. [77]. There is an excellent agreement, demonstrating that the fractional diffusion equation can correctly describe charge transport in this system.

Indeed, for strongly dispersive systems, the spike at $z = z_0$ is the most prominent feature of the entire charge distribution for much of its lifetime. This sharp spike is most clearly illustrated in the contour plots of Figures 8.3c and 8.3d.

8.4.2 Impact of the drift velocity and diffusion coefficient

The fractional drift velocity has units of $\mathrm{m/s}^\gamma$, and describes the tendency of the charged particles to drift in the positive z direction. The fractional diffusion coefficient has units of $\mathrm{m}^2/\mathrm{s}^\gamma$, and describes the tendency of the charged particles to diffuse down the concentration gradient. The effects of varying W_γ and $D_{L,\gamma}$ are demonstrated in Figure 8.4, for a weakly dispersive system ($\gamma = 0.8$) and for a strongly dispersive system ($\gamma = 0.4$). The relevant parameters are indicated in the figure captions. For both systems, an increased W_γ sweeps the charge carriers further to the right, and an increased $D_{L,\gamma}$ spreads the charges over a wider area.

8.4.3 Comparison with time-of-flight data

To demonstrate the process by which this model may be fitted to time-of-flight experimental data, we consider the data for trinitrofluorenone and polyvinylcarbazole (TNF-PVK) presented as Figure 6 of [77]. The data were digitized from the scanned plot, and the slopes of the two regimes was used to furnish an estimate for γ. We used $L = 1$ to give a normalized length scale; and selected the initial source location z_0 to be 0.2, since the model is largely insensitive to the location of the source, provided it is sufficiently far from the electrodes to avoid substantial "back diffusion."

The intercept of the two straight lines was taken to be the transit time t_{tr}, and the following equation was used to furnish an estimate of W_γ, which provided a starting point for curve fitting:

$$t_{tr} \sim \frac{1}{2}\left(\frac{L - z_0}{W_\gamma}\right)^{\frac{1}{\gamma}}, \tag{8.27}$$

the factor of $1/2$ being an empirical correction that gives better results when compared with the order of magnitude estimate Eq. (8.26). There need not be a generalised Einstein relation linking W_γ and $D_{L,\gamma}$ for such systems. However, to give an initial starting point for the curve fitter, the diffusion coefficient was taken as $D_{L,\gamma} \approx W_\gamma/20$. We note that the measured current is insensitive to diffusion because of the strongly dispersive transport that is present, and so the precise value of $D_{L,\gamma}$ is insignificant.

The parameter estimates discussed above were used as the starting point for non-linear least squares curve fitting. The Matlab Curve Fitting Toolbox was used. The result of the model fitting is shown in Figure 8.5. The fitted γ parameter is 0.83.

8.5 Conclusion

We have demonstrated a fractional advection diffusion equation modelling the hopping transport observed in many disordered semiconductors. We have shown that the infinite series of Fourier modes [Eq. (8.5)] for the bounded solution can be collapsed into a closed form expression using the Poisson summation theorem [Eq. (8.13)]. It this closed form expression that then facilitates the extraction of model parameters from the experimental data using a simple curve fitting routine. We have modelled a time of flight experiment by assuming the initial condition $n(z, t_0) = n_0\delta(z - z_0)$. We have calculated the resultant electric current, and shown that the sum of slopes on logarithmic axes is -2, as predicted by other models and as verified by experiment. It is possible to extend this solution to sources of finite duration or finite width, by integrating with respect to t_0 or z_0, respectively.

9

Generalised Diffusion Equations and Fractional Kinetics

This chapter contains material that has been published in the following journal article:

[4] Bronson Philippa, R. E. Robson, and R. D. White. Generalized phase-space kinetic and diffusion equations for classical and dispersive transport. *New Journal of Physics*, **16**, 073040 (2014). doi:10.1088/1367-2630/16/7/073040.

Ron White and Rob Robson supervised the work, derived the phase-space model and its reduction to configuration space. It is simply stated here as the starting point of this chapter. The interested reader is referred to the above publication for further details. The configuration space analysis, which formed the second half of the above article, was performed by me and is presented here in greater detail than the above publication.

9.1 Introduction

The previous chapters applied advection-diffusion equations to various transport problems. The solution of these equations is a number density $n(\mathbf{r}, t)$. They are known as "configuration space" models, and are approximations of a more fundamental "phase space" description that also includes velocity space. Configuration space approximations are only valid in the hydrodynamic regime of smooth spatial gradients [207]. It is therefore fortunate that many physical systems, including ordered semiconductors, rapidly approach this regime. Consequently, configuration space models are often an excellent description of the dynamics of such materials.

A rapid approach to the hydrodynamic regime occurs when collisions dominate and memory of the initial condition is lost after only a few collisions. Any large gradients in the number density will be quickly smoothed. For such "classical" transport, the corresponding diffusion equation is a conventional partial differential equation of first order in t and second order in $\mathbf{r}$. Such systems are characterised by a diffusive regime wherein the mean square displacement grows linearly, i.e. $\langle x^2 \rangle - \langle x \rangle^2 \sim t$. In contrast, disordered semiconductors, such as those studied in this thesis, often demonstrate "anomalous" diffusion, wherein the mean square displacement is nonlinear, i.e. $\langle x^2 \rangle - \langle x \rangle^2 \sim t^\gamma$ where $\gamma \neq 1$ [77, 195, 268, 275].

Subdiffusion occurs when $\gamma < 1$. It arises from repeated trapping and de-trapping of the transported species, in which periods of "classical" transport are interrupted by (potentially long) periods of immobilisation. Consequently, the memory of the initial condition may persist for long times, and large gradients are not necessarily smoothed out. As in the previous chapter, such effects are often accounted for by replacing the conventional time derivative with a fractional derivative [266, 276–279]. The fractional derivative accounts for the memory effects. However, the spatial gradient terms are left intact, and thus the weak gradient assumption is therefore still implicit. This is an apparent contradiction that challenges the validity of the fractional diffusion equations. Until now, this issue has only been addressed in an *ad-hoc* manner, through solution of an exactly solvable model kinetic equation in phase space [280]. The phase space system does not require the assumption of weak gradients, so this questionable assumption is avoided. In that study [280], trapping effects were incorporated in the collision term, and even though the theory is consistent, it is nevertheless ad-hoc and warrants further scrutiny.

Recently, we resolved the ad-hoc nature of the previous approach by developing from first principles a new, physically-based, exactly solvable model kinetic equation [4]. A schematic of the fundamental processes is shown in Figure 9.1. Freely moving carriers may be captured by trap states, where they are held for some period of time drawn from a waiting time distribution $\phi(t)$. This distribution is defined such that the probability of being released after an time in the interval t to $t + dt$ is $\phi(t)dt$.

The resultant phase space model is [4]

$$\left(\partial_t + \mathbf{v} \cdot \nabla + \mathbf{a} \cdot \partial_{\mathbf{v}}\right) \; f = -\nu \left[f - \phi * f_{detrap} \right], \tag{9.1}$$

where f is the free particle distribution function, $\mathbf{a}$ is the external acceleration, ν is a rate constant for the trapping process, and f_{detrap} is the distribution function for the newly detrapped carriers. We assume that the velocity distribution of these carriers is a Maxwellian. This is an arguable assumption, in that it assumes that de-trapped carriers are effectively instantly thermalised with the medium temperature T. The resulting distribution function is

$$f_{detrap}(\mathbf{r}, \mathbf{v}, t) = n(\mathbf{r}, t) \left(\frac{m}{2\pi k_B T} \right)^{3/2} \exp\left(-\frac{m|\mathbf{v}|^2}{2k_B T} \right),$$

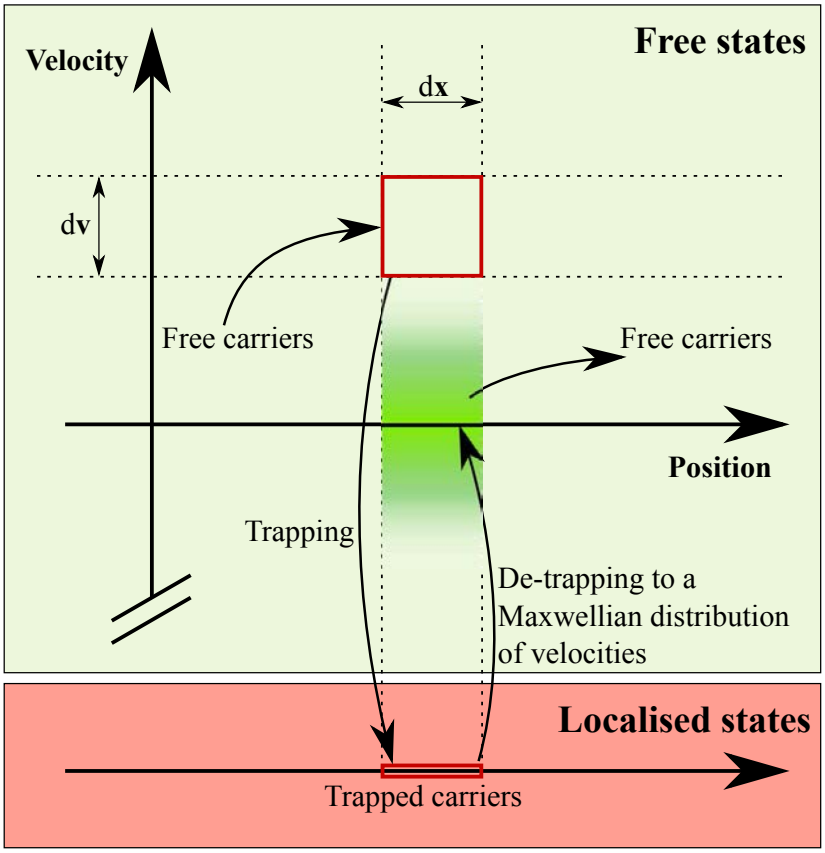

Figure 9.1: Key processes occurring in the kinetic model. Freely moving charges may be scattered into localised states. The newly detrapped charges emerge with a Maxwellian distribution of velocities at the medium temperature.

where $n(\mathbf{r},t) \equiv \int f(\mathbf{r},\mathbf{v},t)d^3\mathbf{v}$ is the number density, m is the carrier mass (or effective mass), k_B is the Boltzmann constant, and T is the medium temperature. Solving this model [4] for ideal time-of-flight conditions yields the "generalised diffusion equation" for the free charged particle density

$$\frac{\partial n}{\partial t} + \nu\left[1-\phi*\right]n + v_d\frac{\partial n}{\partial z} - D_L\frac{\partial^2 n}{\partial z^2} = 0, \tag{9.2}$$

where v_d is the drift velocity, and D_L is the longitudinal diffusion coefficient. Note that in contrast with the previous chapter, v_d and D_L are standard drift and diffusion coefficients and do not have fractional units.

In this chapter, we shall analyse the generalised diffusion equation (9.2). We find the analytic solution and then cast it into closed form by following the mathematical procedure that was developed in the previous chapter. Next, we analyse the role of the waiting time distribution ϕ, which is the key feature that differentiates Eq. (9.2) from other drift-diffusion models, including the fractional form from Chapter 8.

9.2 Formulation for Time-of-Flight

As in the previous chapter, we consider an ideal one-dimensional time-of-flight system. We introduce a slab of material of thickness L between two plane-parallel electrodes, the normal direction defining the z axis of the system of coordinates. We take absorbing boundary conditions, $n(0,t) = n(L,t) = 0$, and an impulse initial condition, $n(z,0) = n_0\delta(z - z_0)$.

9.2.1 Series solution

Equation (9.2) is solved by separation of variables. We write $n(z,t) = Z(z)T(t)$, and substitute into Eq. (9.2) to obtain:

$$\frac{\dot{T} + \nu[1 - \phi*]T}{T} = \frac{-\nu_d Z' + D_L Z''}{Z} = c, \tag{9.3}$$

where dots indicate time derivatives and primes indicate spatial derivatives, and c is an arbitrary separation constant. The spatial equation, i.e. the one involving Z, is identical to the ordinary diffusion equation (without any trapping effects). Its solution is

$$Z(z) = \sum_{m=1}^{\infty} A_m e^{\lambda z} \sin\left(\frac{m\pi z}{L}\right), \tag{9.4}$$

where $\lambda \equiv v_d/2D_L$ and A_m is an arbitrary constant of integration. The separation constant c is negative and multi-valued:

$$c_m = -\frac{m^2\pi^2 D_L}{L^2} - D_L\lambda^2. \tag{9.5}$$

The temporal equation, which is unique to this model, is

$$\dot{T} + \nu[1 - \phi*]T - c_m T = 0.$$

The convolution hints that a Laplace transform might be useful. Solving this equation in Laplace space yields

$$T(s) \quad = \quad \frac{T(0)}{s + \nu[1 - \phi(s)] - c_m}. \tag{9.6}$$

Combining these according to the separation ansatz $n = Z(z)T(t)$, the general solution is

$$n(z,s) = \sum_{m=1}^{\infty} A_m e^{\lambda z} \sin\left(\frac{m\pi z}{L}\right) \frac{1}{s + \nu[1 - \phi(s)] - c_m}, \tag{9.7}$$

where $T(0)$ has been merged into A_m.

The integration constants A_m will be specified by the initial condition. Using the initial value theorem,

$$n(z,0) = n_0\delta(z-z_0) = \sum_{m=1}^{\infty} A_m e^{\lambda z} \sin\left(\frac{m\pi z}{L}\right) \lim_{s\to\infty} \frac{1}{1+\nu[1-\phi(s)]s^{-1} - c_m s^{-1}}. \quad (9.8)$$

The limit must converge to unity for any probability distribution[1].

This is a Fourier series, from which we find the Fourier coefficients A_m to be

$$A_m = \frac{2n_0}{L} e^{-\lambda z_0} \sin\left(\frac{m\pi z_0}{L}\right). \quad (9.9)$$

Combining all the above, the solution is

$$n(z,s) = \sum_{m=0}^{\infty} \frac{n_0}{LD_L} e^{\lambda(z-z_0)} \frac{\cos\left[m\pi L^{-1}\left(z-z_0\right)\right] - \cos\left[m\pi L^{-1}\left(z+z_0\right)\right]}{\left(s+\nu[1-\phi(s)]\right) D_L^{-1} + \lambda^2 + m^2\pi^2 L^{-2}}. \quad (9.10)$$

The transformation from sin to cos was done to facilitate the use of the Poisson summation theorem.

9.2.2 Poisson Summation

As per the previous chapter, the Poisson summation theorem is useful in collapsing infinite series like Eq. (9.10) into closed form. Recall that the Poisson summation theorem is

$$\sum_{m=-\infty}^{\infty} f(mT) = \frac{1}{T} \sum_{m=-\infty}^{\infty} F\left(\frac{m}{T}\right), \quad (9.11)$$

where $F(k)$ is the Fourier transform of $f(mT)$. The first task is to write Eq. (9.10) in the form of the left hand side of Eq. (9.11). We introduce the parameters

$$\begin{aligned} \alpha &= \frac{n_0}{LD_L} e^{\lambda(z-z_0)} \\ \beta^2 &= \left(s+\nu[1-\phi(s)]\right)/D_L + \lambda^2 \\ T &= \frac{\pi}{L} \end{aligned}$$

to obtain

$$n(z,s) = \alpha \sum_{m=0}^{\infty} \frac{\cos\left[mT\left(z-z_0\right)\right] - \cos\left[mT\left(z+z_0\right)\right]}{\beta^2 + \left(mT\right)^2}.$$

[1]The non-trivial term in the denominator is

$$\lim_{s\to\infty} \frac{\phi(s)}{s}.$$

The numerator tends to zero in the limit of large s because the integrand vanishes exponentially

$$\lim_{s\to\infty} \phi(s) = \lim_{s\to\infty} \int_0^{\infty} e^{-st}\phi(t)dt \to 0,$$

and consequently,

$$\lim_{s\to\infty} \frac{\phi(s)}{s} = 0.$$

All other terms on the denominator in (9.8) have trivial limits as $s \to \infty$.

The limits of summation can be extended to $-\infty$ because each term is an even function of m:

$$n(z,s) = \frac{\alpha}{2} \sum_{m=-\infty}^{\infty} \frac{\cos\left[mT\left(z-z_0\right)\right] - \cos\left[mT\left(z+z_0\right)\right]}{\beta^2 + \left(mT\right)^2}.$$

Further, the cosine function can be replaced by the exponential representation

$$n(z,s) = \frac{\alpha}{2} \sum_{m=-\infty}^{\infty} \frac{e^{imT(z-z_0)} - e^{imT(z+z_0)}}{\beta^2 + \left(mT\right)^2},$$

which is a valid transformation because the imaginary component of each exponential is an odd function of m, and so all the imaginary components will cancel when the summation is taken. This equation now resembles the left hand side of Eq. (9.11).

The next task is to take the Fourier transformation. The necessary integral is

$$F(k) = \int_{-\infty}^{\infty} e^{-2\pi ik\tau} \frac{e^{i\tau(z-z_0)} - e^{i\tau(z+z_0)}}{\beta^2 + \tau^2} d\tau.$$

This integral can be evaluated using complex contours and the residue theorem. The result is

$$F(k) = \frac{\pi}{\beta}\left[e^{-\beta|2\pi k - (z-z_0)|} - e^{-\beta|2\pi k - (z+z_0)|}\right].$$

Finally, the Poisson summation theorem can be applied. We find

$$\begin{aligned} n(z,s) &= \frac{\alpha}{2T} \sum_{m=-\infty}^{\infty} F\left(\frac{m}{T}\right) \\ &= \frac{n_0}{2D_L\beta} e^{\lambda(z-z_0)} \sum_{m=-\infty}^{\infty} \left[\exp\left(-\beta\left|2mL - (z-z_0)\right|\right) - \exp\left(-\beta\left|2mL - (z+z_0)\right|\right)\right]. \end{aligned}$$

By separately considering the cases of $m < 0$, $m = 0$, and $m > 0$, with the cases of $z < z_0$ and $z > z_0$, this can be recognised as a geometric series with the closed form expression

$$n(z,s) = \frac{n_0 e^{\lambda(z-z_0)}}{2D_L\beta} \left\{ e^{-\beta|z-z_0|} - e^{-\beta|z+z_0|} - \frac{4\sinh\left(\beta z\right)\sinh\left(\beta z_0\right)}{e^{2\beta L} - 1} \right\}. \tag{9.12}$$

Equation (9.12) is the analytic solution to the time-of-flight problem.

9.2.3 Time-of-flight current

Since $n(z,s)$ represents free charge, rather than total charge as in the last chapter, the current expression is simply

$$\begin{aligned} j &= \frac{v_d}{L} \int_0^L n dz \\ &= \frac{v_d n_0}{2LD_L\beta} \int_0^L e^{\lambda(z-z_0)} \left\{ e^{-\beta|z-z_0|} - e^{-\beta|z+z_0|} - \frac{4\sinh\left(\beta z\right)\sinh\left(\beta z_0\right)}{e^{2\beta L} - 1} \right\} dz. \end{aligned}$$

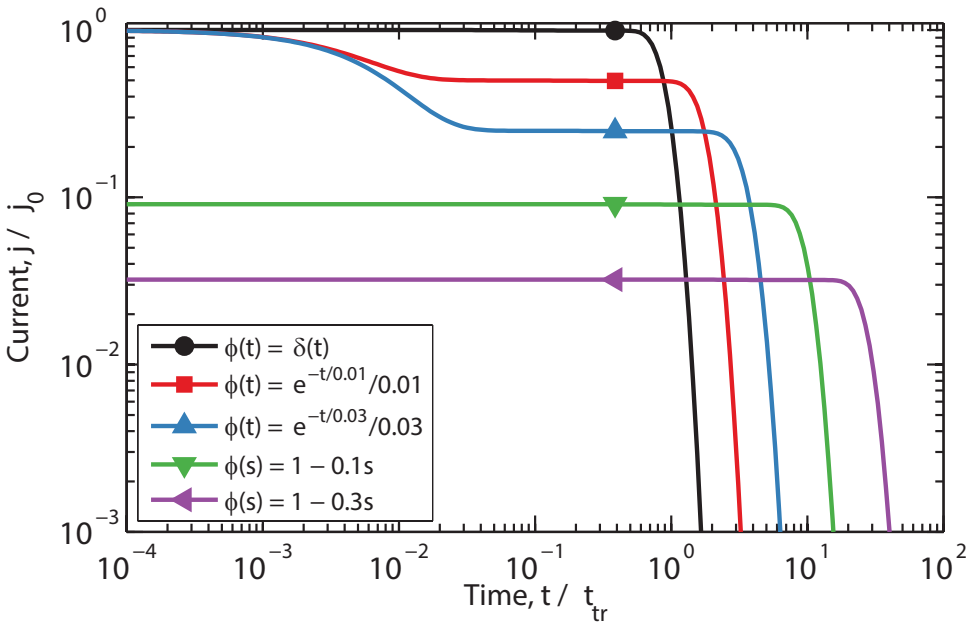

Figure 9.2: Modelled current transients for ideal time of flight experiments, showing the impact of various waiting time distributions ϕ. Results are plotted in normalised units, where j_0 is the initial current for the trap-free model, and $t_{tr} = L/v_d$ is the trap-free transit time. When $\phi(t) = \delta(t)$ (top line), no trapping occurs. In the other cases, the transients are influenced by trapping but the results exhibit "classical" transport with well-defined drift velocities and diffusion coefficients. The trapping rate is $\nu = 10^3/t_{tr}$, the reciprocal of which gives the timescale for the transition to trap-limited transport in the case of an exponential waiting time distribution. The first moments of the waiting time distribution functions from top to bottom are respectively 0, 0.01, 0.03, 0.1, 0.3, in units of t_{tr}. The dimensionless diffusion coefficient is $D_L t_{tr}/L^2 = 0.02$. The initial delta-function pulse is at $x_0/L = 0.1$. [In the legend, $\phi(s)$ is the Laplace transform of $\phi(t)$.]

Evaluating this integral and simplifying,

$$j(s) = \frac{v_d N(0)}{(s + \nu\,[1 - \phi(s)])\,L}\left(1 - e^{-\lambda z_0}\left[e^{-\beta z_0} + \frac{\sinh(\beta z_0)}{\sinh(\beta L)}\left(e^{\lambda L} - e^{-\beta L}\right)\right]\right). \quad (9.13)$$

To this point the discussion is quite general, but to go further, we must specify $\phi(t)$.

9.3 Role of the waiting time distribution

9.3.1 Waiting time distributions $\phi(t)$ with a finite first moment---'classical' transport

To study the impact of the waiting time distribution on the solution, we initially considered several simple $\phi(t)$ functions. Time of flight transients were calculated using Eq. (9.13), numerically inverting the Laplace transform. Dimensionless results are shown in Figure 9.2, where time is scaled to the transit time $t_{tr} = L/v_d$ through a

sample of thickness L, and concentration is scaled to the initial concentration $N(0)$. In this system of units, the normalised drift velocity is equal to 1. We set the normalised diffusion coefficient to $D_L t_{tr}/L^2 = 0.02$.

The simplest choice for the waiting time distribution is the Dirac delta, $\phi(t) = \delta(t)$. In this case, de-trapping occurs instantaneously and consequently has no impact. The system reduces to the standard advection-diffusion equation.

Another choice is an exponential distribution, $\phi(t) = e^{-t/\tau}/\tau$. Two examples with exponential distributions are shown in Figure 9.2, which different first moments, τ. The initial trap-free transport transitions into trap-limited transport on a timescale governed by the collision frequency ($\sim \nu^{-1}$). The trap-limited transport is characterised by an increased transit time (and hence decreased effective drift velocity) for increased τ because of the additional time spent in traps. For the same reason, the current density j falls with increased τ. Nevertheless, the transport is not dispersive, and there exists a clear time-of-flight arrival time.

A final option explored is a first-order truncation of the series expansion of the exponential waiting time distribution in Laplace space: $\widehat{\phi}(s) \sim 1 - \tau s$, where again τ is the first moment of the waiting time distribution function. As can be seen from Figure 9.2, the first moment of ϕ controls the long-time behaviour. Higher moments can only influence the behaviour at shorter times, as is demonstrated by the differences between the cases with an exponential distribution and those with the Laplace domain series expansion.

9.3.2 Relating the waiting time distribution to a density of trapped states

Rather than simply assuming an ad-hoc waiting time distribution, it may be useful to calculate it from a more fundamental physical model. In what follows, we give a specific example for how this might be achieved. We consider a semiconductor with traps that form a density of localized states below the band gap. The release times $\phi(t)$ are determined by the distribution of these traps in energy space.

To describe this semiconductor, we use a multiple trapping model with a uniform capture (trapping) cross-section [212] for charge carriers. We define the density of localised states to be $g(\epsilon)$, where $\epsilon < 0$ is the energy relative to the conduction band. If the rate of escape from a trap at energy ϵ is proportional to $\exp(\epsilon/k_B T)$ then

$$\phi(t) = \nu_0 \int_{-\infty}^{0} g(\epsilon) e^{\epsilon/k_B T} \exp\left\{-t\nu_0 e^{\epsilon/k_B T}\right\} d\epsilon, \tag{9.14}$$

where ν_0 is a frequency characterizing the rate of escape from traps. The density of states $g(\epsilon)$ can be measured experimentally [222, 281]. In this case we assume an exponential distribution, which occurs in certain organic and inorganic materials [12, 120]. Then $g(\epsilon) = e^{\epsilon/k_B T_c}/kT_c$, where T_c is a characteristic temperature that describes the width of the density of states. Eq. (9.14) yields

$$\phi(t) = \alpha\nu_0 \left(t\nu_0\right)^{-\alpha-1} \gamma\left(\alpha + 1,\, t\nu_0\right), \tag{9.15}$$

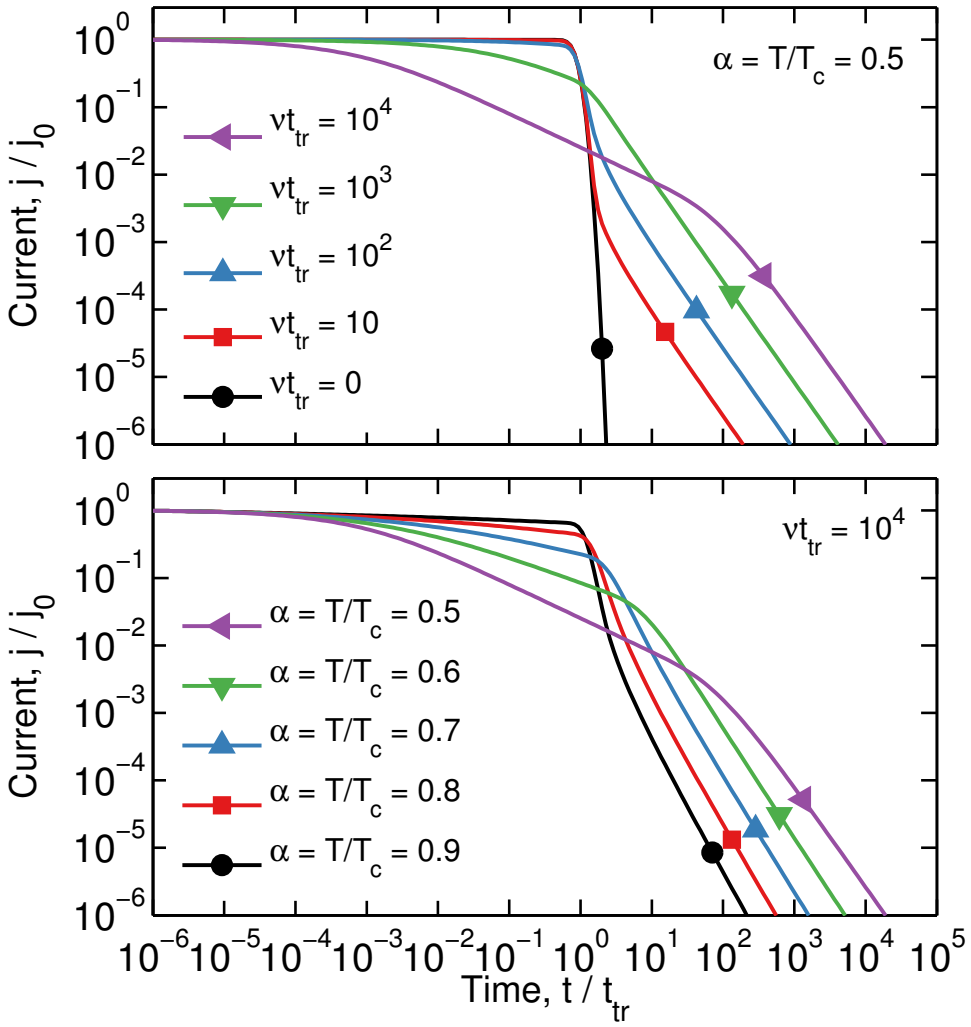

Figure 9.3: Modelled current transients for ideal time of flight experiments using the waiting time distribution (9.15), which was calculated for a semiconductor with an exponential distribution of localised states. An initial trap-free regime transitions into strongly-trap limited dispersive transport. Transport parameters are the same as Fig. 2, except for the alternative waiting time distribution. These plots were calculated for $\nu_0 t_{tr} = 5 \times 10^5$. The transition between "classical" and dispersive regimes occurs at $t/t_{tr} \sim (\nu t_{tr})^{-1}$.

where $\gamma(\cdot,\cdot)$ is the lower incomplete Gamma function[2], and $\alpha = T/T_c$. This distribution appears in the literature of the multiple trapping model, for example, Eqn (9) of Ref. [213]. This distribution is normalized, and it has a divergent first moment, sufficient to describe dispersive transport [192, 282, 283].

Figure 9.3 shows typical time of flight transients together the waiting time distribution Eq. (9.15). Initially, all carriers are assumed to be untrapped. At short times the profiles are classical, with a transition to dispersive behaviour at longer times as the carriers begin to enter the trap states. In the dispersive regime, the sum of slopes is -2, exactly as expected for an exponential density of states [77]. We note that a different form of dispersive transport may arise from a different density of states, and that our model can be readily adapted by evaluating Eq. (9.14) with the appropriate $g(\epsilon)$ function.

The parameters used for Figure 9.3 were chosen as follows. The attempt to escape frequency ν_0 is extremely fast (e.g. $\sim 10^{12}$ Hz for a realistic system [212]), so we consider only the situation where $\nu_0 t_{tr} \gg 1$. We selected $\nu_0 t_{tr} = 5 \times 10^5$ for Figure 9.3. The trapping frequency ν, which is a new feature of our model, must be large enough that $\nu t_{tr} > 1$, otherwise there will be negligible trapping events before the time of flight experiment has concluded. In Figure 9.3 (a), we demonstrate the influence of this parameter. It controls the time scale for the transition between classical and dispersive transport. Finally, if the transport is dispersive, the temperature T must be below the critical temperature T_c [212]. We examine the range $0.5 \leq T/T_c \leq 0.9$ in Figure 9.3 (b). It can be seen that the slope of the current transient is controlled by the temperature.

Our generalised diffusion equation (9.2) provides a framework for a unified analysis of transport, whether dispersive or classical. It is pertinent at this point to highlight that in the long time limit, one can make direct connection to the fractional diffusion equation literature [192, 282, 283]. If we consider the Laplace transform of the waiting time distribution Eq. (9.15)

$$\widehat{\phi}(s) = -\frac{\alpha\pi}{\sin\alpha\pi}\left(\frac{s}{\nu_0}\right)^{\alpha} + {}_2F_1\left(1, -\alpha; 1-\alpha; -\frac{s}{\nu_0}\right), \tag{9.16}$$

where ${}_2F_1$ is a hypergeometric function, then the small s (long time) representation of this is

$$\widehat{\phi}(s) \approx 1 - r_\alpha s^\alpha. \tag{9.17}$$

Here the coefficients of the s^α term have been collected into a single parameter $r_\alpha \equiv \nu_0^{-\alpha}\alpha\pi/\sin\alpha\pi$, which weights the relative importance of trapping effects. By substituting Eq. (9.17) into (9.2), and taking the limit of small s, one obtains a fractional diffusion equation, with a Riemann-Liouville or Caputo form of the fractional derivative depending upon whether one solves for untrapped charge or total charge. These fractional equations result from a waiting time distribution that was calculated using

[2]The lower incomplete gamma function is $\gamma(a,z) \equiv \int_0^z t^{a-1}e^{-t}dt$.

an exponential density of trap states. It remains to be seen whether alternative "fractional" equations could be formed by considering different distributions for the density of trapped states.

9.4 Concluding remarks

In this chapter we have studied a generalized diffusion equation (9.2) for transport in disordered materials. This equation is grounded in a phase-space kinetic model that accounts for both free particle transport and trapping/detrapping from localized states, described by a waiting time function $\phi(t)$. This model provides a unified framework for the analysis of transport, whether dispersive or not. The nature of the transport is strongly influenced by the waiting time distribution, and in particular, the first moment of this distribution plays a dominant role. By way of example, this model was applied to a disordered semiconductor, obtaining dispersive transport if the density of states is exponential. Other distributions (e.g. a Gaussian) might be expected to yield different detailed behaviour, which could be calculated using the generalized diffusion equation presented here.

10 Conclusion

10.1 Summary

Charge transport is a key contributor to the performance of any electronic device. In the specific case of organic solar cells, high power conversion efficiencies can only be achieved if charges are quickly extracted without significant recombination losses. The charge transport properties of current organic photovoltaics are inadequate, for example if device thicknesses are to be increased for optimal light harvesting, or because of inhomogeneities in large-scale fabrication. There is a need for better tools to quantify charge transport, which should lead to improved physical understanding and perhaps guide future performance gains. This thesis addressed these issues with the development of new experimental techniques that contributed physical insights into the charge transport mechanisms in a variety of OPV systems.

There is a huge design space of charge transport experiments that can be conceived using only a light source, arbitrary waveform generator, variable load resistor, and oscilloscope. Over the course of this project, many such experimental configurations were simulated. The simulations quickly identified those which were most promising in terms of robustness and accuracy, and also excluded many that were intuitively plausible but did not stand up to the rigorous analysis provided by the simulation software. The most promising techniques were further refined, using the simulations to learn how to recognise and work with non-ideal effects such as charge trapping and dispersive transport. Armed with the knowledge gained from the simulations, this thesis addressed questions of scientific importance regarding the impact of hot carriers, charge carrier thermalisation, and recombination.

Charge carrier thermalisation, in the form of a time-dependent mobility, was studied in three different polymer:fullerene blends using two different experimental techniques. The photo-CELIV technique was applied to poly[3,6-dithiophene-2-yl-2,5-di(2-octyldodecyl)-pyrrolo[3,4-c]pyrrole-1,4-dione-*alt*-naphthalene] (PDPP-TNT) : [6,6] phenyl-C71-butyric-acid-methyl-ester (PC70BM) [220] solar cells. A shift in the current maximum with increasing delay time was observed, as has previously been reported in other organic solar cell systems [137, 138]. However, numeric simulation with a drift-diffusion model demonstrated that this shift is induced by the measurement technique and does not necessarily indicate a genuine time-dependence in the mobility. Quantitative analysis of the observed data revealed that carrier mobility is *not* time-dependent in this system. This highlights a weakness of the photo-CELIV technique: variations in the experimental conditions might induce artificial trends into the apparent mobility. We also examined the impact of dispersion on photo-CELIV transients, and found that a systematic change in the apparent mobility occurs when the amount of dispersion is varied, even if the true mobility is held constant. This would be complicate temperature-dependent studies, since the amount of dispersion is often dependent upon temperature. It was concluded that care must be taken when examining trends in mobility obtained via photo-CELIV.

Next, carrier relaxation was studied in poly[N-9"-hepta-decanyl-2,7-carbazole-*alt*-5,5-(4',7'-di-2-thienyl-2',1',3'-benzothiadiazole)] (PCDTBT):PC70BM and poly[[4,8-bis-[(2-ethylhexyl)oxy]benzo[1,2-b:4,5-b']dithiophene-2,6-diyl][3-fluoro-2-[(2-ethylhexyl)carbonyl]thieno[3,4-b]thiophenediyl]] (PTB7):PC70BM. These experiments were performed using the novel technique of Resistance dependent PhotoVoltage (RPV), which was developed in order to address the limitations of photo-CELIV. There was no evidence of any time-dependent mobility as the transit time was varied by changing the bias voltage and device thickness. Similarly, there was no evidence of energetic relaxation extending to the timescale of charge transport when different wavelengths of laser pumping were used. This is in contrast to the prediction of the influential Gaussian Disorder Model that dispersive transport arises due to the energetic relaxation of charge carriers. Our observations are inconsistent with this hypothesis, and so we argue that dispersion in these systems is instead caused by charge trapping, and the reduction in photocurrent that is typically attributed to a time-dependent mobility is actually driven by the gradual loss of charges to deep trap states.

To study recombination, the RPV technique was extended to high light intensities (HI-RPV). It was shown that low molecular weight PCDTBT ($\overline{M}_n$ = 4.3 kDa, $\overline{M}_w$ = 12.1 kDa, PDI = 2.8) results in Langevin recombination, whereas high molecular weight PCDTBT ($\overline{M}_n$ = 22.7 kDa, $\overline{M}_w$ = 122.2 kDa, PDI = 5.4) results in non-Langevin recombination with a reduction factor $\beta/\beta_L \approx 0.07$. This highlights that molecular weight may need to be considered when optimising devices.

Next, we studied the steady-state short-circuit current as a function of light intensity, which we call IPC, or intensity-dependent photocurrent. Simulations identified that there is a critical threshold at which charge transport becomes inadequate and

substantial non-geminate recombination begins. This threshold is the space-charge limited current, $I_{\mathrm{sclc}} \sim \sqrt{\beta_L/\beta}\, CU/t_{\mathrm{tr}}^{\mathrm{slower}}$, from which the required mobility, recombination coefficient, device thickness, dielectric permittivity, and voltage can be calculated. We experimentally verified this prediction using solar cells of varying thickness made from PCDTBT:PC70BM and PTB7:PC70BM.

The second theme of this thesis was related to generalised (or "fractional") transport models. It was demonstrated that the Poisson summation theorem is applicable to the analytic solution of a fractional advection-diffusion equation. With the use of the Poisson summation theorem, the result can be expressed concisely in closed form in Laplace space. This is helpful in manipulating the analytic solution of such models. Finally, a new form of generalised kinetic model was proposed and analysed. This kinetic model introduces trapping and de-trapping into phase space, with the de-trapping mechanism specified via a waiting time probability density function. It was shown that differing choices of the waiting time distribution result in qualitatively different types of charge transport, and in particular, that the proposed kinetic model incorporates both normal and dispersive transport within the same common framework.

10.2 Recommendations for Future Work

This is a broad field and there are many opportunities, but we have identified several issues that directly arise from this work and can be addressed using the framework and tools that we have developed.

Analysis of recombination via photo-CELIV—In Chapter 4, we demonstrated that photo-CELIV measurements of the time-, field-, and temperature-dependence of mobility may be misleading due to variations in the shape of the photo-CELIV transient. The photo-CELIV technique is also used to study recombination, and it seems likely that similar artefacts would affect recombination studies too. It is recommended that simulations and experiments be performed in order to understand the impact of the delay time, charge trapping, and dispersive transport on recombination measurements.

Time-dependent mobility in pristine polymers—We have shown in Chapters 4 and 5 that three polymer:fullerene systems display no evidence of mobility relaxation on the timescales of charge transport, despite the fact that such dependencies have previously been reported (often with the photo-CELIV technique). An interesting test case that we have not yet explored is whether there is any energetic relaxation in pure polymer films, as opposed to polymer:fullerene blends. This would provide insight into the microscopic transport mechanism that applies in polymer domains and/or at the interface between polymers and fullerenes.

Impact of trapping on HI-RPV—The HI-RPV technique (Chapter 6) encounters difficulties in the presence of deep trapping. The extracted charge does not saturate to CU in the limit of large resistances, but instead to a value approximately 2-5 times higher than CU. We performed some preliminary simulations that demonstrated this effect when a substantial quantity of charge is trapped for long periods of time, but

due to the time constraints of this thesis, this work was not yet completed. Further analysis is needed in order to develop useful predictive tools.

Applying the Poisson summation theorem to other fractional equations—The Poisson summation theorem was shown to be useful in the analytic solution of a time-fractional Caputo diffusion equation (Chapter 8), and a generalised diffusion equation with a convolution term (Chapter 9). Given it was useful in these two distinct systems, it is likely that other types of fractional equation would benefit from a similar treatment. Many different fractional equations have been applied in the literature, and so it is likely that some of these would be amenable to the techniques presented here.

Dispersive transport with non-exponential density-of-states distributions—The generalised diffusion model in Chapter 9 produces standard Scher-Montroll dispersive transport when an exponential density-of-states (DOS) is used. However, some organic materials display different distributions, for example a Gaussian. To adapt the model for a different DOS, one evaluates the release time integral [Eq. (9.14)] for the new distribution. It would be interesting to examine whether other types of distribution can give rise to different types of dispersive transport, for example, whether the "sum of slopes" can be varied from the Scher-Montroll/exponential DOS value of -2.

Dispersive to non-dispersive transitions—Fractional models for subdiffusion exhibit instability in the presence of spatially varying fractional order [284, 285], as might be expected to arise in practice due to inhomogeneities in the material if the fractional order depends upon the material structure or properties. This is an important issue because spatial variations might be especially likely in disordered media, precisely where the existing (unstable) models are intended to be used! Preliminary analysis indicates that the model described in Chapter 9 can avoid this problem by an appropriate choice of waiting time distribution that triggers a transition to non-dispersive transport at long times. It is recommended that the transition to non-dispersion be investigated as a mechanism to prevent the structural instability in the fractional models.

Higher moments of the kinetic equation—In Chapter 9, the generalised kinetic model was integrated over all velocities to obtain a particle balance. Higher order moments in velocity space can be used to obtain, for example, a momentum balance and an energy balance. These are likely to contain information about relaxation effects that are associated with charge trapping, and possibly fields that are rapidly varying in time or space.

References

[1] B. W. Philippa, R. D. White, and R. E. Robson. Analytic solution of the fractional advection-diffusion equation for the time-of-flight experiment in a finite geometry. *Physical Review E*, **84**, 041138 (2011). doi:10.1103/PhysRevE.84.041138.

[2] Bronson Philippa, Martin Stolterfoht, Ronald D. White, Marrapan Velusamy, Paul L. Burn, Paul Meredith, and Almantas Pivrikas. Molecular weight dependent bimolecular recombination in organic solar cells. *The Journal of Chemical Physics*, **141**, 054903 (2014). doi:10.1063/1.4891369.

[3] Bronson Philippa, Martin Stolterfoht, Paul L Burn, Gytis Juška, Paul Meredith, Ronald D White, and Almantas Pivrikas. The impact of hot charge carrier mobility on photocurrent losses in polymer-based solar cells. *Scientific Reports*, **4**, 5695 (2014). doi:10.1038/srep05695.

[4] Bronson Philippa, R. E. Robson, and R. D. White. Generalized phase-space kinetic and diffusion equations for classical and dispersive transport. *New Journal of Physics*, **16**, 073040 (2014). doi:10.1088/1367-2630/16/7/073040.

[5] Bronson Philippa, Chellappan Vijila, Ronald D. White, Prashant Sonar, Paul L. Burn, Paul Meredith, and Almantas Pivrikas. Time-independent charge carrier mobility in a model polymer:fullerene organic solar cell. *Organic Electronics*, **16**, 205 (2015). doi:10.1016/j.orgel.2014.10.047.

[6] Ardalan Armin, Gytis Juška, Bronson W. Philippa, Paul L. Burn, Paul Meredith, Ronald D. White, and Almantas Pivrikas. Doping-induced screening of the built-in-field in organic solar cells: Effect on charge transport and recombination. *Advanced Energy Materials*, **3**, 321 (2013). doi:10.1002/aenm.201200581.

[7] Chellappan Vijila, Samarendra P Singh, Evan Williams, Prashant Sonar, Almantas Pivrikas, Bronson Philippa, Ronald White, Elumalai Naveen Kumar, S. Gomathy Sandhya, Sergey Gorelik, Jonathan Hobley, Akihiro Furube, Hiroyuki Matsuzaki, and Ryuzi Katoh. Relation between charge carrier mobility and lifetime in organic photovoltaics. *Journal of Applied Physics*, **114**, 184503 (2013). doi:10.1063/1.4829456.

[8] Martin Stolterfoht, Bronson Philippa, Ardalan Armin, Ajay K. Pandey, Ronald D. White, Paul L. Burn, Paul Meredith, and Almantas Pivrikas. Advantage

of suppressed non-Langevin recombination in low mobility organic solar cells. *Applied Physics Letters*, **105**, 013302 (2014). doi:10.1063/1.4887316.

[9] Peter W. Stokes, Bronson Philippa, Wayne Read, and Ronald D. White. Efficient numerical solution of the time fractional diffusion equation by mapping from its Brownian counterpart. *Journal of Computational Physics*, **282**, 334 (2015). doi:10.1016/j.jcp.2014.11.023.

[10] George Malliaras and Richard Friend. An Organic Electronics Primer. *Physics Today*, **58**, 53 (2005). doi:10.1063/1.1995748.

[11] Christoph J Brabec, Srinivas Gowrisanker, Jonathan J M Halls, Darin Laird, Shijun Jia, and Shawn P Williams. Polymer-fullerene bulk-heterojunction solar cells. *Advanced Materials*, **22**, 3839 (2010). doi:10.1002/adma.200903697.

[12] Carsten Deibel and Vladimir Dyakonov. Polymer-fullerene bulk heterojunction solar cells. *Reports on Progress in Physics*, **73**, 096401 (2010). doi:10.1088/0034-4885/73/9/096401.

[13] A. Mayer, S. Scully, B. Hardin, M. Rowell, and M. McGehee. Polymer-based solar cells. *Materials Today*, **10**, 28 (2007). doi:10.1016/S1369-7021(07)70276-6.

[14] Harald Hoppe and Niyazi Serdar Sariciftci. Organic solar cells: An overview. *Journal of Materials Research*, **19**, 1924 (2004). doi:10.1557/JMR.2004.0252.

[15] Stephen R. Forrest. The path to ubiquitous and low-cost organic electronic appliances on plastic. *Nature*, **428**, 911 (2004).

[16] John A. Rogers, Takao Someya, and Yonggang Huang. Materials and mechanics for stretchable electronics. *Science*, **327**, 1603 (2010). doi:10.1126/science.1182383.

[17] Matthew S. White, Martin Kaltenbrunner, Eric D. Glowacki, Kateryna Gutnichenko, Gerald Kettlgruber, Ingrid Graz, Safae Aazou, Christoph Ulbricht, Daniel A. M. Egbe, Matei C. Miron, Zoltan Major, Markus C. Scharber, Tsuyoshi Sekitani, Takao Someya, Siegfried Bauer, and Niyazi Serdar Sariciftci. Ultrathin, highly flexible and stretchable PLEDs. *Nature Photonics*, **7**, 811 (2013). doi:10.1038/nphoton.2013.188.

[18] Frederik C. Krebs. Fabrication and processing of polymer solar cells: A review of printing and coating techniques. *Solar Energy Materials and Solar Cells*, **93**, 394 (2009). doi:10.1016/j.solmat.2008.10.004.

[19] Martin A Green, Keith Emery, Yoshihiro Hishikawa, Wilhelm Warta, and Ewan D Dunlop. Solar cell efficiency tables (version 43). *Progress in Photovoltaics: Research and Applications*, **22**, 1 (2014). doi:10.1002/pip.2452.

[20] L. Koster, E. Smits, V. Mihailetchi, and P. Blom. Device model for the operation of polymer/fullerene bulk heterojunction solar cells. *Physical Review B*, **72**, 085205 (2005). doi:10.1103/PhysRevB.72.085205.

[21] M.T. Neukom, N.A. Reinke, and B. Ruhstaller. Charge extraction with linearly increasing voltage: A numerical model for parameter extraction. *Solar Energy*, **85**, 1250 (2011). doi:10.1016/j.solener.2011.02.028.

[22] M.T. Neukom, S. Züfle, and B. Ruhstaller. Reliable extraction of organic solar cell parameters by combining steady-state and transient techniques. *Organic Electronics*, **13**, 2910 (2012). doi:10.1016/j.orgel.2012.09.008.

[23] I M Sokolov and J Klafter. From diffusion to anomalous diffusion: a century after Einstein's Brownian motion. *Chaos (Woodbury, N.Y.)*, **15**, 26103 (2005). doi:10.1063/1.1860472.

[24] Eli Barkai. CTRW pathways to the fractional diffusion equation. *Chemical Physics*, **284**, 13 (2002). doi:10.1016/S0301-0104(02)00533-5.

[25] Benoît Robyns, Arnaud Davigny, Bruno François, Antoine Henneton, and Jonathan Sprooten. *Electricity Production from Renewables Energies*. Wiley (2012). ISBN 9781118563069.

[26] Wallace C.H. Choy (Editor). *Organic Solar Cells*. Green Energy and Technology. Springer, London (2013). ISBN 978-1-4471-4822-7. doi:10.1007/978-1-4471-4823-4.

[27] Stephen R Forrest. The Limits to Organic Photovoltaic Cell Efficiency. *MRS Bulletin*, **30**, 28 (2005). doi:10.1557/mrs2005.5.

[28] American Society for Testing and Materials. Reference Solar Spectral Irradiance: Air Mass 1.5.

[29] Ardalan Armin, Marappan Velusamy, Pascal Wolfer, Yuliang Zhang, Paul L Burn, Paul Meredith, and Almantas Pivrikas. Quantum Efficiency of Organic Solar Cells: Electro-Optical Cavity Considerations. *ACS Photonics*, **1**, 173 (2014). doi:10.1021/ph400044k.

[30] Yasuhiko Shirota and Hiroshi Kageyama. Charge carrier transporting molecular materials and their applications in devices. *Chemical reviews*, **107**, 953 (2007). doi:10.1021/cr050143+.

[31] Nieves Espinosa, Rafael García-Valverde, Antonio Urbina, and Frederik C. Krebs. A life cycle analysis of polymer solar cell modules prepared using roll-to-roll methods under ambient conditions. *Solar Energy Materials and Solar Cells*, **95**, 1293 (2010). doi:10.1016/j.solmat.2010.08.020.

[32] Martin Kaltenbrunner, Matthew S White, Eric D Glowacki, Tsuyoshi Sekitani, Takao Someya, Niyazi Serdar Sariciftci, and Siegfried Bauer. Ultrathin and lightweight organic solar cells with high flexibility. *Nature Communications*, **3**, 770 (2012). doi:10.1038/ncomms1772.

[33] Gilles Dennler, Niyazi Serdar Sariciftci, and Christoph J. Brabec. Conjugated Polymer-Based Organic Solar Cells. In *Semiconducting Polymers: Chemistry, Physics and Engineering*, edited by Georges Hadziioannou and George G. Malliaras, chapter 11, 455–530. WILEY-VCH Verlag GmbH & Co. KGaA, Weinheim, second edition (2007). ISBN 978-3-527-31271-9.

[34] Jenny Nelson. Polymer:fullerene bulk heterojunction solar cells. *Materials Today*, **14**, 462 (2011). doi:10.1016/S1369-7021(11)70210-3.

[35] Ian H Campbell, Brian K Crone, and Darryl L Smith. Physics of Organic Light-Emitting Diodes. In *Semiconducting Polymers: Chemistry, Physics and Engineering*, edited by Georges Hadziioannou and George G Malliaras, chapter 10, 421–454. WILEY-VCH Verlag GmbH & Co. KGaA, Weinheim, second edition (2007). ISBN 978-3-527-31271-9.

[36] Nir Tessler. Lasers Based on Semiconducting Organic Materials. *Advanced Materials*, **11**, 363 (1999). doi:10.1002/(SICI)1521-4095(199903)11:5<363::AID-ADMA363>3.0.CO;2-Y.

[37] I D W Samuel and G a Turnbull. Organic semiconductor lasers. *Chemical reviews*, **107**, 1272 (2007). doi:10.1021/cr050152i.

[38] Gilles Horowitz. Organic Field-Effect Transistors. *Advanced Materials*, **10**, 365 (1998). doi:10.1002/(SICI)1521-4095(199803)10:5<365::AID-ADMA365>3.0.CO;2-U.

[39] Giles Horowitz. Organic Thin-Film Transistors. In *Semiconducting Polymers: Chemistry, Physics and Engineering*, edited by Georges Hadziioannou and George G Malliaras, chapter 12, 531–566. WILEY-VCH Verlag GmbH & Co. KGaA, Weinheim, second edition (2007). ISBN 978-3-527-31271-9.

[40] Henning Sirringhaus. 25th anniversary article: organic field-effect transistors: the path beyond amorphous silicon. *Advanced Materials*, **26**, 1319 (2014). doi:10.1002/adma.201304346.

[41] Hee Taek Yi, Marcia M. Payne, John E. Anthony, and Vitaly Podzorov. Ultra-flexible solution-processed organic field-effect transistors. *Nature Communications*, **3**, 1259 (2012). doi:10.1038/ncomms2263.

[42] Yang Yang, Jianyong Ouyang, Liping Ma, Jia-Hung Tseng, and Chih-Wei Chu. Organic/Polymeric Thin-Film Memory Devices. In *Semiconducting Polymers: Chemistry, Physics and Engineering*, edited by Georges Hadziioannou and

George G Malliaras, chapter 15, 613–642. WILEY-VCH Verlag GmbH & Co. KGaA, Weinheim, second edition (2007). ISBN 978-3-527-31271-9.

[43] Hoang-Anh Ho and Mario Leclerc. Biosensors Based on Conjugated Polymers. In *Semiconducting Polymers: Chemistry, Physics and Engineering*, edited by Georges Hadziioannou and George G Malliaras, chapter 16, 643–666. WILEY-VCH Verlag GmbH & Co. KGaA, Weinheim, second edition (2007). ISBN 978-3-527-31271-9.

[44] Holger Spanggaard and Frederik C. Krebs. A brief history of the development of organic and polymeric photovoltaics. *Solar Energy Materials and Solar Cells*, **83**, 125 (2004). doi:10.1016/j.solmat.2004.02.021.

[45] C. W. Tang. Two-layer organic photovoltaic cell. *Applied Physics Letters*, **48**, 183 (1986). doi:10.1063/1.96937.

[46] N. S. Sariciftci, L. Smilowitz, A. J. Heeger, and F. Wudl. Photoinduced electron transfer from a conducting polymer to buckminsterfullerene. *Science*, **258**, 1474 (1992). doi:10.1126/science.258.5087.1474.

[47] S Matthew Menke, Wade a Luhman, and Russell J Holmes. Tailored exciton diffusion in organic photovoltaic cells for enhanced power conversion efficiency. *Nature Materials*, **12**, 152 (2012). doi:10.1038/nmat3467.

[48] Paul E. Shaw, Arvydas Ruseckas, and Ifor D. W. Samuel. Exciton Diffusion Measurements in Poly(3-hexylthiophene). *Advanced Materials*, **20**, 3516 (2008). doi:10.1002/adma.200800982.

[49] Tracey M Clarke and James R Durrant. Charge photogeneration in organic solar cells. *Chemical reviews*, **110**, 6736 (2010). doi:10.1021/cr900271s.

[50] G. Yu, J. Gao, J. C. Hummelen, F. Wudl, and A. J. Heeger. Polymer Photovoltaic Cells: Enhanced Efficiencies via a Network of Internal Donor-Acceptor Heterojunctions. *Science*, **270**, 1789 (1995). doi:10.1126/science.270.5243.1789.

[51] Jan C. Hummelen, Brian W Knight, F. LePeq, Fred Wudl, Jie Yao, and Charles L. Wilkins. Preparation and Characterization of Fulleroid and Methanofullerene Derivatives. *The Journal of Organic Chemistry*, **60**, 532 (1995). doi:10.1021/jo00108a012.

[52] Mikkel Jø rgensen, Jon E. Carlé, Roar R. Sø ndergaard, Marie Lauritzen, Nikolaj A. Dagnæ s Hansen, Sedi L. Byskov, Thomas R. Andersen, Thue T. Larsen-Olsen, Arvid P.L. Böttiger, Birgitta Andreasen, Lei Fu, Lijian Zuo, Yao Liu, Eva Bundgaard, Xiaowei Zhan, Hongzheng Chen, and Frederik C. Krebs. The state of organic solar cells—A meta analysis. *Solar Energy Materials and Solar Cells*, 1–10 (2013). doi:10.1016/j.solmat.2013.05.034.

[53] L. Jan Anton Koster, Sean E. Shaheen, and Jan C. Hummelen. Pathways to a New Efficiency Regime for Organic Solar Cells. *Advanced Energy Materials*, **2**, 1246 (2012). doi:10.1002/aenm.201200103.

[54] Brian A. Gregg. The Photoconversion Mechanism of Excitonic Solar Cells. *MRS Bulletin*, **30**, 20 (2005). doi:10.1557/mrs2005.3.

[55] V. I. Arkhipov, P. Heremans, and H. Bässler. Why is exciton dissociation so efficient at the interface between a conjugated polymer and an electron acceptor? *Applied Physics Letters*, **82**, 4605 (2003). doi:10.1063/1.1586456.

[56] Peter Peumans and Stephen R. Forrest. Separation of geminate charge-pairs at donor–acceptor interfaces in disordered solids. *Chemical Physics Letters*, **398**, 27 (2004). doi:10.1016/j.cplett.2004.09.030.

[57] Carsten Deibel, Thomas Strobel, and Vladimir Dyakonov. Origin of the Efficient Polaron-Pair Dissociation in Polymer-Fullerene Blends. *Physical Review Letters*, **103**, 036402 (2009). doi:10.1103/PhysRevLett.103.036402.

[58] G. Grancini, M. Maiuri, D. Fazzi, A. Petrozza, H-J. Egelhaaf, D. Brida, G. Cerullo, and G. Lanzani. Hot exciton dissociation in polymer solar cells. *Nature Materials*, **12**, 29 (2013). doi:10.1038/nmat3502.

[59] Koen Vandewal, Steve Albrecht, Eric T. Hoke, Kenneth R. Graham, Johannes Widmer, Jessica D. Douglas, Marcel Schubert, William R. Mateker, Jason T. Bloking, George F. Burkhard, Alan Sellinger, Jean M. J. Fréchet, Aram Amassian, Moritz K. Riede, Michael D. McGehee, Dieter Neher, and Alberto Salleo. Efficient charge generation by relaxed charge-transfer states at organic interfaces. *Nature materials*, **13**, 63 (2014). doi:10.1038/nmat3807.

[60] Simon Gélinas, Akshay Rao, Abhishek Kumar, Samuel L Smith, Alex W Chin, Jenny Clark, Tom S van der Poll, Guillermo C Bazan, and Richard H Friend. Ultrafast Long-Range Charge Separation in Organic Semiconductor Photovoltaic Diodes. *Science*, **512** (2013). doi:10.1126/science.1246249.

[61] Arun Aby Paraecattil and Natalie Banerji. Charge separation pathways in a highly efficient polymer:fullerene solar cell material. *Journal of the American Chemical Society*, **136**, 1472 (2014). doi:10.1021/ja410340g.

[62] Ardalan Armin, Yuliang Zhang, Paul L. Burn, Paul Meredith, and Almantas Pivrikas. Measuring internal quantum efficiency to demonstrate hot exciton dissociation. *Nature Materials*, **12**, 593 (2013). doi:10.1038/nmat3692.

[63] B Bernardo, D Cheyns, B Verreet, R D Schaller, B P Rand, and N C Giebink. Delocalization and dielectric screening of charge transfer states in organic photovoltaic cells. *Nature communications*, **5**, 3245 (2014). doi:10.1038/ncomms4245.

[64] Brian a. Gregg. Entropy of Charge Separation in Organic Photovoltaic Cells: The Benefit of Higher Dimensionality. *The Journal of Physical Chemistry Letters*, **2**, 3013 (2011). doi:10.1021/jz2012403.

[65] Sung Heum Park, Anshuman Roy, Serge Beaupré, Shinuk Cho, Nelson Coates, Ji Sun Moon, Daniel Moses, Mario Leclerc, Kwanghee Lee, and Alan J Heeger. Bulk heterojunction solar cells with internal quantum efficiency approaching 100%. *Nature Photonics*, **3**, 297 (2009). doi:10.1038/nphoton.2009.69.

[66] Charles Kittel. *Introduction to Solid State Physics*. John Wiley & Sons, New York, 7th edition (1996). ISBN 0471111813.

[67] S M Sze. *Semiconductor Devices: Physics and Technology*. John Wiley & Sons, second edition (2002). ISBN 9780470537947.

[68] Veaceslav Coropceanu, Jérôme Cornil, Demetrio A da Silva Filho, Yoann Olivier, Robert Silbey, and Jean-Luc Brédas. Charge transport in organic semiconductors. *Chemical reviews*, **107**, 926 (2007). doi:10.1021/cr050140x.

[69] Nir Tessler, Yevgeni Preezant, Noam Rappaport, and Yohai Roichman. Charge Transport in Disordered Organic Materials and Its Relevance to Thin-Film Devices: A Tutorial Review. *Advanced Materials*, **21**, 2741 (2009). doi:10.1002/adma.200803541.

[70] Anatoliy N. Sokolov, Sule Atahan-Evrenk, Rajib Mondal, Hylke B. Akkerman, Roel S. Sánchez-Carrera, Sergio Granados-Focil, Joshua Schrier, Stefan C.B. Mannsfeld, Arjan P. Zoombelt, Zhenan Bao, and Alán Aspuru-Guzik. From computational discovery to experimental characterization of a high hole mobility organic crystal. *Nature Communications*, **2**, 437 (2011). doi:10.1038/ncomms1451.

[71] Jenny Nelson. Diffusion-limited recombination in polymer-fullerene blends and its influence on photocurrent collection. *Physical Review B*, **67**, 1 (2003). doi:10.1103/PhysRevB.67.155209.

[72] A. Baumann, J. Lorrmann, D. Rauh, C. Deibel, and V. Dyakonov. A new approach for probing the mobility and lifetime of photogenerated charge carriers in organic solar cells under real operating conditions. *Advanced Materials*, **24**, 4381 (2012). doi:10.1002/adma.201200874.

[73] Christopher G. Shuttle, Richard Hamilton, Jenny Nelson, Brian C. O'Regan, and James R. Durrant. Measurement of charge-density dependence of carrier mobility in an organic semiconductor blend. *Advanced Functional Materials*, **20**, 698 (2010). doi:10.1002/adfm.200901734.

[74] G. Juška, N. Nekrašas, and K. Genevičius. Investigation of charge carriers transport from extraction current transients of injected charge carriers. *Journal of Non-Crystalline Solids*, **358**, 748 (2012). doi:10.1016/j.jnoncrysol.2011.12.016.

[75] Tracey M. Clarke, Jeff Peet, Andrew Nattestad, Nicolas Drolet, Gilles Dennler, Christoph Lungenschmied, Mario Leclerc, and Attila J. Mozer. Charge carrier mobility, bimolecular recombination and trapping in polycarbazole copolymer:fullerene (PCDTBT:PCBM) bulk heterojunction solar cells. *Organic Electronics*, **13**, 2639 (2012). doi:10.1016/j.orgel.2012.07.037.

[76] H. Bässler. Charge Transport in Disordered Organic Photoconductors a Monte Carlo Simulation Study. *Physica Status Solidi (B)*, **175**, 15 (1993). doi:10.1002/pssb.2221750102.

[77] Harvey Scher and Elliott Montroll. Anomalous transit-time dispersion in amorphous solids. *Physical Review B*, **12**, 2455 (1975). doi:10.1103/PhysRevB.12.2455.

[78] Harvey Scher, Michael F. Shlesinger, and John T. Bendler. Time-Scale Invariance in Transport and Relaxation. *Physics Today*, **44**, 26 (1991). doi:10.1063/1.881289.

[79] Tae-Jun Ha, Prashant Sonar, and Ananth Dodabalapur. Charge carrier velocity distributions in high mobility polymer field-effect transistors. *Applied Physics Letters*, **100**, 153302 (2012). doi:10.1063/1.3697994.

[80] Chen-Guan Lee, Brian Cobb, Laura Ferlauto, and Ananth Dodabalapur. Charge carrier velocity distributions in field-effect transistors. *Applied Physics Letters*, **98**, 092106 (2011). doi:10.1063/1.3558910.

[81] C. Deibel, A. Baumann, and V. Dyakonov. Polaron recombination in pristine and annealed bulk heterojunction solar cells. *Applied Physics Letters*, **93**, 163303 (2008). doi:10.1063/1.3005593.

[82] Almantas Pivrikas, Helmut Neugebauer, and Niyazi Serdar Sariciftci. Charge Carrier Lifetime and Recombination in Bulk Heterojunction Solar Cells. *IEEE Journal of Selected Topics in Quantum Electronics*, **16**, 1746 (2010). doi:10.1109/JSTQE.2010.2044978.

[83] Alexander Foertig, Juliane Kniepert, Markus Gluecker, Thomas Brenner, Vladimir Dyakonov, Dieter Neher, and Carsten Deibel. Nongeminate and Geminate Recombination in PTB7:PCBM Solar Cells. *Advanced Functional Materials*, **24**, 1306 (2014). doi:10.1002/adfm.201302134.

[84] R. Street, Sarah Cowan, and A. Heeger. Experimental test for geminate recombination applied to organic solar cells. *Physical Review B*, **82**, 11 (2010). doi:10.1103/PhysRevB.82.121301.

[85] L. J. A. Koster, V. D. Mihailetchi, and P. W. M. Blom. Bimolecular recombination in polymer/fullerene bulk heterojunction solar cells. *Applied Physics Letters*, **88**, 052104 (2006). doi:10.1063/1.2170424.

[86] Girish Lakhwani, Akshay Rao, and Richard H Friend. Bimolecular recombination in organic photovoltaics. *Annual review of physical chemistry*, **65**, 557 (2014). doi:10.1146/annurev-physchem-040513-103615.

[87] Daniel Rauh, Carsten Deibel, and Vladimir Dyakonov. Charge Density Dependent Nongeminate Recombination in Organic Bulk Heterojunction Solar Cells. *Advanced Functional Materials*, **22**, 3371 (2012). doi:10.1002/adfm.201103118.

[88] Tracey M. Clarke, Christoph Lungenschmied, Jeff Peet, Nicolas Drolet, and Attila J. Mozer. A Comparison of Five Experimental Techniques to Measure Charge Carrier Lifetime in Polymer/Fullerene Solar Cells. *Advanced Energy Materials* (2014). doi:10.1002/aenm.201401345.

[89] A. Pivrikas, G. Juška, A. J. Mozer, M. Scharber, K. Arlauskas, N. S. Sariciftci, H. Stubb, and R. Österbacka. Bimolecular Recombination Coefficient as a Sensitive Testing Parameter for Low-Mobility Solar-Cell Materials. *Physical Review Letters*, **94**, 176806 (2005). doi:10.1103/PhysRevLett.94.176806.

[90] Sarah Cowan, Anshuman Roy, and Alan Heeger. Recombination in polymer-fullerene bulk heterojunction solar cells. *Physical Review B*, **82**, 1 (2010). doi:10.1103/PhysRevB.82.245207.

[91] Christopher M. Proctor, Steve Albrecht, Martijn Kuik, Dieter Neher, and Thuc-Quyen Nguyen. Overcoming Geminate Recombination and Enhancing Extraction in Solution-Processed Small Molecule Solar Cells. *Advanced Energy Materials* (2014). doi:10.1002/aenm.201400230.

[92] A. Pivrikas, N. S. Sariciftci, G. Juška, and R. Österbacka. A review of charge transport and recombination in polymer/fullerene organic solar cells. *Progress in Photovoltaics: Research and Applications*, **15**, 677 (2007). doi:10.1002/pip.791.

[93] J. J. M. van der Holst, F. W. A. van Oost, R. Coehoorn, and P. A. Bobbert. Electron-hole recombination in disordered organic semiconductors: Validity of the Langevin formula. *Physical Review B*, **80**, 235202 (2009). doi:10.1103/PhysRevB.80.235202.

[94] G. Juška, K. Arlauskas, J. Stucklik, and R. Österbacka. Non-Langevin bimolecular recombination in low-mobility materials. *Journal of Non-Crystalline Solids*, **352**, 1167 (2006). doi:10.1016/j.jnoncrysol.2005.11.099.

[95] Tracey M. Clarke, Jeff Peet, Patrick Denk, Gilles Dennler, Christoph Lungenschmied, and Attila J. Mozer. Non-Langevin bimolecular recombination in a silole-based polymer:PCBM solar cell measured by time-resolved charge extraction and resistance-dependent time-of-flight techniques. *Energy & Environmental Science*, **5**, 5241 (2012). doi:10.1039/c1ee02434e.

[96] D. H. K. Murthy, Armantas Melianas, Zheng Tang, Gytis Juška, K stutis Arlauskas, Fengling Zhang, Laurens D. a. Siebbeles, Olle Inganäs, and Tom J. Savenije. Origin of Reduced Bimolecular Recombination in Blends of Conjugated Polymers and Fullerenes. *Advanced Functional Materials*, **23**, 4262 (2013). doi:10.1002/adfm.201203852.

[97] Xugang Guo, Nanjia Zhou, Sylvia J. Lou, Jeremy Smith, Daniel B. Tice, Jonathan W. Hennek, Rocío Ponce Ortiz, Juan T. López Navarrete, Shuyou Li, Joseph Strzalka, Lin X. Chen, Robert P. H. Chang, Antonio Facchetti, and Tobin J. Marks. Polymer solar cells with enhanced fill factors. *Nature Photonics*, **7**, 825 (2013). doi:10.1038/nphoton.2013.207.

[98] Martin Pope and Charles E. Swenberg. *Electronic processes in organic crystals and polymers*. Oxford University Press, second edition (1999).

[99] Jana Zaumseil, Chris Groves, Jessica M. Winfield, Neil C. Greenham, and Henning Sirringhaus. Electron-Hole Recombination in Uniaxially Aligned Semiconducting Polymers. *Advanced Functional Materials*, **18**, 3630 (2008). doi:10.1002/adfm.200800863.

[100] N. Nekrašas, K. Genevičius, M. Viliūnas, and G. Juška. Features of current transients of photogenerated charge carriers, extracted by linearly increased voltage. *Chemical Physics*, **404**, 56 (2012). doi:10.1016/j.chemphys.2012.01.008.

[101] Akshay Rao, Philip C. Y. Chow, Simon Gélinas, Cody W. Schlenker, Chang-Zhi Li, Hin-Lap Yip, Alex K.-Y. Jen, David S. Ginger, and Richard H. Friend. The role of spin in the kinetic control of recombination in organic photovoltaics. *Nature*, 6–11 (2013). doi:10.1038/nature12339.

[102] A. Pivrikas, G. Juška, R. Österbacka, M. Westerling, M. Viliunas, K. Arlauskas, and H. Stubb. Langevin recombination and space-charge-perturbed current transients in regiorandom poly(3-hexylthiophene). *Physical Review B*, **71**, 125205 (2005). doi:10.1103/PhysRevB.71.125205.

[103] Hamed Azimi, Thomas Heumüller, Andreas Gerl, Gebhard Matt, Peter Kubis, Monica Distaso, Rameez Ahmad, Tugce Akdas, Moses Richter, Wolfgang Peukert, and Christoph J. Brabec. Relation of Nanostructure and Recombination Dynamics in a Low-Temperature Solution-Processed CuInS 2 Nanocrystalline Solar Cell. *Advanced Energy Materials*, **3**, 1589 (2013). doi:10.1002/aenm.201300449.

[104] Gert-Jan A. H. Wetzelaer, Niels J. Van der Kaap, L. Jan Anton Koster, and Paul W. M. Blom. Quantifying Bimolecular Recombination in Organic Solar Cells in Steady State. *Advanced Energy Materials*, **3**, 1130 (2013). doi:10.1002/aenm.201300251.

[105] M. Kuik, L. Koster, G. Wetzelaer, and P. Blom. Trap-Assisted Recombination in Disordered Organic Semiconductors. *Physical Review Letters*, **107**, 1 (2011). doi:10.1103/PhysRevLett.107.256805.

[106] G. Juška, M. Viliunas, O. Klíma, E. Šípek, and J. Kočka. New features in space-charge-limited-photocurrent transients. *Philosophical Magazine Part B*, **69**, 277 (1994). doi:10.1080/01418639408240109.

[107] Jedrzej Szmytkowski. The influence of the thickness, recombination and space charge on the loss of photocurrent in organic semiconductors: an analytical model. *Journal of Physics D: Applied Physics*, **40**, 3352 (2007). doi:10.1088/0022-3727/40/11/015.

[108] W. Shockley and W. Read. Statistics of the Recombinations of Holes and Electrons. *Physical Review*, **87**, 835 (1952). doi:10.1103/PhysRev.87.835.

[109] R. Hall. Electron-Hole Recombination in Germanium. *Physical Review*, **87**, 387 (1952). doi:10.1103/PhysRev.87.387.

[110] Roderick C. I. MacKenzie, Thomas Kirchartz, George F. a. Dibb, and Jenny Nelson. Modeling Nongeminate Recombination in P3HT:PCBM Solar Cells. *The Journal of Physical Chemistry C*, **115**, 9806 (2011). doi:10.1021/jp200234m.

[111] Dirk Hertel and Heinz Bässler. Photoconduction in amorphous organic solids. *ChemPhysChem*, **9**, 666 (2008). doi:10.1002/cphc.200700575.

[112] Sanjay Tiwari and N. C. Greenham. Charge mobility measurement techniques in organic semiconductors. *Optical and Quantum Electronics*, **41**, 69 (2009). doi:10.1007/s11082-009-9323-0.

[113] Akshay Kokil, Ke Yang, and Jayant Kumar. Techniques for characterization of charge carrier mobility in organic semiconductors. *Journal of Polymer Science Part B: Polymer Physics*, **50**, 1130 (2012). doi:10.1002/polb.23103.

[114] Juliane Kniepert, Ilja Lange, Niels J. van der Kaap, L. Jan Anton Koster, and Dieter Neher. A Conclusive View on Charge Generation, Recombination, and Extraction in As-Prepared and Annealed P3HT:PCBM Blends: Combined Experimental and Simulation Work. *Advanced Energy Materials* (2014). doi:10.1002/aenm.201301401.

[115] Nico Christ, Siegfried W. Kettlitz, Jan Mescher, and Uli Lemmer. Extracting the charge carrier mobility from the nanosecond photocurrent response of organic solar cells and photodiodes. *Applied Physics Letters*, **104**, 053302 (2014). doi:10.1063/1.4863737.

[116] C. Tanase, E. J. Meijer, P. W. M. Blom, and D. M. de Leeuw. Unification of the Hole Transport in Polymeric Field-Effect Transistors and Light-Emitting Diodes. *Physical Review Letters*, **91**, 216601 (2003). doi:10.1103/PhysRevLett.91.216601.

[117] C. Tanase, P. Blom, and D. de Leeuw. Origin of the enhanced space-charge-limited current in poly(p-phenylene vinylene). *Physical Review B*, **70**, 193202 (2004). doi:10.1103/PhysRevB.70.193202.

[118] Murray A. Lampert and Peter Mark. *Current injection in solids*. Academic Press (1970).

[119] H. T. Nicolai, M. Kuik, G. A. H. Wetzelaer, B. de Boer, C. Campbell, C. Risko, J. L. Brédas, and P. W. M. Blom. Unification of trap-limited electron transport in semiconducting polymers. *Nature Materials*, **11**, 882 (2012). doi:10.1038/nmat3384.

[120] H. T. Nicolai, M. M. Mandoc, and P. W. M. Blom. Electron traps in semiconducting polymers: Exponential versus Gaussian trap distribution. *Physical Review B*, **83**, 1 (2011). doi:10.1103/PhysRevB.83.195204.

[121] S. van Mensfoort, S. Vulto, R. Janssen, and R. Coehoorn. Hole transport in polyfluorene-based sandwich-type devices: Quantitative analysis of the role of energetic disorder. *Physical Review B*, **78**, 1 (2008). doi:10.1103/PhysRevB.78.085208.

[122] G. Juška, M. Viliunas, K. Arlauskas, and J. Kočka. Space-charge-limited photocurrent transients: The influence of bimolecular recombination. *Physical Review B*, **51**, 16668 (1995). doi:10.1103/PhysRevB.51.16668.

[123] G. Juška, K. Genevičius, G. Sliaužys, a. Pivrikas, M. Scharber, and R. Österbacka. Double-injection current transients as a way of measuring transport in insulating organic films. *Journal of Applied Physics*, **101**, 114505 (2007). doi:10.1063/1.2736791.

[124] W.E. Spear. Drift mobility techniques for the study of electrical transport properties in insulating solids. *Journal of Non-Crystalline Solids*, **1**, 197 (1969). doi:10.1016/0022-3093(69)90001-5.

[125] WE Spear. Electronic transport and localization in low mobility solids and liquids. *Advances in Physics*, **23**, 523 (1974). doi:10.1080/00018737400101381.

[126] A. Pivrikas, Mujeeb Ullah, Th.B. Singh, C. Simbrunner, G. Matt, H. Sitter, and N.S. Sariciftci. Meyer-Neldel rule for charge carrier transport in fullerene devices: A comparative study. *Organic Electronics*, **12**, 161 (2011). doi:10.1016/j.orgel.2010.10.014.

[127] Gilles Dennler, Markus C. Scharber, and Christoph J. Brabec. Polymer-Fullerene Bulk-Heterojunction Solar Cells. *Advanced Materials*, **21**, 1323 (2009). doi:10.1002/adma.200801283.

[128] G. Juška, K. Arlauskas, M. Viliunas, and J. Kočka. Extraction Current Transients: New Method of Study of Charge Transport in Microcrystalline Silicon. *Physical Review Letters*, **84**, 4946 (2000). doi:10.1103/PhysRevLett.84.4946.

[129] A. J. Mozer, N. S. Sariciftci, L. Lutsen, D. Vanderzande, R. Österbacka, M. Westerling, and G. Juška. Charge transport and recombination in bulk

heterojunction solar cells studied by the photoinduced charge extraction in linearly increasing voltage technique. *Applied Physics Letters*, **86**, 112104 (2005). doi:10.1063/1.1882753.

[130] G. Juška, K Arlauskas, M. Viliūnas, K. Genevičius, R. Österbacka, and H Stubb. Charge transport in π-conjugated polymers from extraction current transients. *Physical Review B*, **62**, R16235 (2000). doi:10.1103/PhysRevB.62.R16235.

[131] J. Lorrmann, B. H. Badada, O. Inganäs, V. Dyakonov, and C. Deibel. Charge carrier extraction by linearly increasing voltage: Analytic framework and ambipolar transients. *Journal of Applied Physics*, **108**, 113705 (2010). doi:10.1063/1.3516392.

[132] Sebastian Bange, Marcel Schubert, and Dieter Neher. Charge mobility determination by current extraction under linear increasing voltages: Case of nonequilibrium charges and field-dependent mobilities. *Physical Review B*, **81**, 035209 (2010). doi:10.1103/PhysRevB.81.035209.

[133] G. Juška, N. Nekrašas, V. Valentinavičius, P. Meredith, and A. Pivrikas. Extraction of photogenerated charge carriers by linearly increasing voltage in the case of Langevin recombination. *Physical Review B*, **84**, 155202 (2011). doi:10.1103/PhysRevB.84.155202.

[134] Naveen Kumar Elumalai, Chellappan Vijila, Rajan Jose, Kam Zhi Ming, Amitaksha Saha, and Seeram Ramakrishna. Simultaneous improvements in power conversion efficiency and operational stability of polymer solar cells by interfacial engineering. *Physical chemistry chemical physics : PCCP*, **15**, 19057 (2013). doi:10.1039/c3cp53352b.

[135] Hui Joon Park, Jae Yong Lee, Taehwa Lee, and L. Jay Guo. Advanced Heterojunction Structure of Polymer Photovoltaic Cell Generating High Photocurrent with Internal Quantum Efficiency Approaching 100%. *Advanced Energy Materials*, **3**, 1135 (2013). doi:10.1002/aenm.201300245.

[136] Julia Schafferhans, Andreas Baumann, Alexander Wagenpfahl, Carsten Deibel, and Vladimir Dyakonov. Oxygen doping of P3HT:PCBM blends: Influence on trap states, charge carrier mobility and solar cell performance. *Organic Electronics*, **11**, 1693 (2010). doi:10.1016/j.orgel.2010.07.016.

[137] A. Mozer, G. Dennler, N. Sariciftci, M. Westerling, A. Pivrikas, R. Österbacka, and G. Juška. Time-dependent mobility and recombination of the photoinduced charge carriers in conjugated polymer/fullerene bulk heterojunction solar cells. *Physical Review B*, **72**, 1 (2005). doi:10.1103/PhysRevB.72.035217.

[138] A. Pivrikas, R. Österbacka, G. Juška, K. Arlauskas, and H. Stubb. Time-dependent Langevin-type bimolecular charge carrier recombination in regiorandom poly(3-hexylthiophene). *Synthetic Metals*, **155**, 242 (2005). doi:10.1016/j.synthmet.2005.01.042.

[139] Bekele Homa, Mattias Andersson, and Olle Inganäs. Photogenerated charge carrier transport and recombination in polyfluorene/fullerene bilayer and blend photovoltaic devices. *Organic Electronics*, **10**, 501 (2009). doi:10.1016/j.orgel.2008.11.010.

[140] Song Chen, Kaushik Roy Choudhury, Jegadesan Subbiah, Chad M. Amb, John R. Reynolds, and Franky So. Photo-Carrier Recombination in Polymer Solar Cells Based on P3HT and Silole-Based Copolymer. *Advanced Energy Materials*, **1**, 963 (2011). doi:10.1002/aenm.201100300.

[141] Marcel Schubert, Eduard Preis, James Blakesley, Patrick Pingel, Ullrich Scherf, and Dieter Neher. Mobility relaxation and electron trapping in a donor/acceptor copolymer. *Physical Review B*, **87**, 024203 (2013). doi:10.1103/PhysRevB.87.024203.

[142] Simon Sandén, Oskar Sandberg, Qian Xu, Jan-Henrik Små tt, Gytis Juška, Mika Lindén, and Ronald Österbacka. Effect of a large hole reservoir on the charge transport in TiO2/organic hybrid devices. *Physical chemistry chemical physics : PCCP*, **14**, 14186 (2012). doi:10.1039/c2cp41543g.

[143] Carsten Deibel. Charge carrier dissociation and recombination in polymer solar cells. *physica status solidi (a)*, **206**, 2731 (2009). doi:10.1002/pssa.200925282.

[144] Robert Hanfland, Martin A. Fischer, Wolfgang Brütting, Uli Würfel, and Roderick C. I. MacKenzie. The physical meaning of charge extraction by linearly increasing voltage transients from organic solar cells. *Applied Physics Letters*, **103**, 063904 (2013). doi:10.1063/1.4818267.

[145] G. Sliaužys, G. Juška, K. Arlauskas, A. Pivrikas, R. Österbacka, M. Scharber, A. Mozer, and N.S. Sariciftci. Recombination of photogenerated and injected charge carriers in π-conjugated polymer/fullerene blends. *Thin Solid Films*, **511-512**, 224 (2006). doi:10.1016/j.tsf.2005.12.103.

[146] Tracey M. Clarke, Christoph Lungenschmied, Jeff Peet, Nicolas Drolet, Kenji Sunahara, Akihiro Furube, and Attila J. Mozer. Photodegradation in Encapsulated Silole-Based Polymer: PCBM Solar Cells Investigated using Transient Absorption Spectroscopy and Charge Extraction Measurements. *Advanced Energy Materials*, **3**, 1473 (2013). doi:10.1002/aenm.201300337.

[147] C. G. Shuttle, B. O'Regan, A. M. Ballantyne, J. Nelson, D. D. C. Bradley, J. de Mello, and J. R. Durrant. Experimental determination of the rate law for charge carrier decay in a polythiophene: Fullerene solar cell. *Applied Physics Letters*, **92**, 093311 (2008). doi:10.1063/1.2891871.

[148] Arup K Rath, Maria Bernechea, Luis Martinez, F. Pelayo Garcia de Arquer, Johann Osmond, and Gerasimos Konstantatos. Solution-processed inorganic bulk

nano-heterojunctions and their application to solar cells. *Nature Photonics*, **6**, 529 (2012). doi:10.1038/nphoton.2012.139.

[149] C. Shuttle, B. O'Regan, A. Ballantyne, J. Nelson, D. Bradley, and J. Durrant. Bimolecular recombination losses in polythiophene: Fullerene solar cells. *Physical Review B*, **78**, 113201 (2008). doi:10.1103/PhysRevB.78.113201.

[150] Thomas Kirchartz and Jenny Nelson. Meaning of reaction orders in polymer:fullerene solar cells. *Physical Review B*, **86**, 165201 (2012). doi:10.1103/PhysRevB.86.165201.

[151] S. Novikov, D. Dunlap, V. Kenkre, P. Parris, and A. Vannikov. Essential role of correlations in governing charge transport in disordered organic materials. *Physical Review Letters*, **81**, 4472 (1998). doi:10.1103/PhysRevLett.81.4472.

[152] I. Fishchuk, V. Arkhipov, A Kadashchuk, P Heremans, and H. Bässler. Analytic model of hopping mobility at large charge carrier concentrations in disordered organic semiconductors: Polarons versus bare charge carriers. *Physical Review B*, **76**, 1 (2007). doi:10.1103/PhysRevB.76.045210.

[153] M. Bouhassoune, S. L. M. van Mensfoort, P. A. Bobbert, and R. Coehoorn. Carrier-density and field-dependent charge-carrier mobility in organic semiconductors with correlated Gaussian disorder. *Organic Electronics*, **10**, 437 (2009). doi:10.1016/j.orgel.2009.01.005.

[154] Michael C Heiber and Ali Dhinojwala. Dynamic Monte Carlo modeling of exciton dissociation in organic donor-acceptor solar cells. *The Journal of chemical physics*, **137**, 014903 (2012). doi:10.1063/1.4731698.

[155] Mattias Jakobsson, Mathieu Linares, and Sven Stafstrom. Monte Carlo simulations of charge transport in organic systems with true off-diagonal disorder. *The Journal of chemical physics*, **137**, 114901 (2012). doi:10.1063/1.4748796.

[156] I. Fishchuk, A. Kadashchuk, Mujeeb Ullah, H. Sitter, A. Pivrikas, J. Genoe, and H. Bässler. Electric field dependence of charge carrier hopping transport within the random energy landscape in an organic field effect transistor. *Physical Review B*, **86**, 1 (2012). doi:10.1103/PhysRevB.86.045207.

[157] Murat Mesta, Marco Carvelli, Rein J. de Vries, Harm van Eersel, Jeroen J. M. van der Holst, Matthias Schober, Mauro Furno, Björn Lüssem, Karl Leo, Peter Loebl, Reinder Coehoorn, and Peter A. Bobbert. Molecular-scale simulation of electroluminescence in a multilayer white organic light-emitting diode. *Nature Materials*, **12**, 1 (2013). doi:10.1038/nmat3622.

[158] B. Limketkai, P. Jadhav, and M. Baldo. Electric-field-dependent percolation model of charge-carrier mobility in amorphousorganic semiconductors. *Physical Review B*, **75**, 113203 (2007). doi:10.1103/PhysRevB.75.113203.

[159] E. Knapp, R. Häusermann, H. U. Schwarzenbach, and B. Ruhstaller. Numerical simulation of charge transport in disordered organic semiconductor devices. *Journal of Applied Physics*, **108**, 054504 (2010). doi:10.1063/1.3475505.

[160] V. Arkhipov, E. Emelianova, and G. Adriaenssens. Effective transport energy versus the energy of most probable jumps in disordered hopping systems. *Physical Review B*, **64**, 125125 (2001). doi:10.1103/PhysRevB.64.125125.

[161] S.D. Baranovskii, I.P. Zvyagin, H. Cordes, S. Yamasaki, and P. Thomas. Electronic transport in disordered organic and inorganic semiconductors. *Journal of Non-Crystalline Solids*, **299-302**, 416 (2002). doi:10.1016/S0022-3093(01)00956-5.

[162] Roland Schmechel. Gaussian disorder model for high carrier densities: Theoretical aspects and application to experiments. *Physical Review B*, **66**, 1 (2002). doi:10.1103/PhysRevB.66.235206.

[163] Allen Miller and Elihu Abrahams. Impurity Conduction at Low Concentrations. *Physical Review*, **120**, 745 (1960). doi:10.1103/PhysRev.120.745.

[164] Daniel T Gillespie. A general method for numerically simulating the stochastic time evolution of coupled chemical reactions. *Journal of Computational Physics*, **22**, 403 (1976). doi:10.1016/0021-9991(76)90041-3.

[165] H. Cordes, S. Baranovskii, K. Kohary, P. Thomas, S. Yamasaki, F. Hensel, and J.-H. Wendorff. One-dimensional hopping transport in disordered organic solids. I. Analytic calculations. *Physical Review B*, **63**, 1 (2001). doi:10.1103/PhysRevB.63.094201.

[166] J. J. M. van der Holst, F. W. A. van Oost, R. Coehoorn, and P. A. Bobbert. Monte Carlo study of charge transport in organic sandwich-type single-carrier devices: Effects of Coulomb interactions. *Physical Review B*, **83**, 085206 (2011). doi:10.1103/PhysRevB.83.085206.

[167] R. Coehoorn and S. van Mensfoort. Effects of disorder on the current density and recombination profile in organic light-emitting diodes. *Physical Review B*, **80**, 1 (2009). doi:10.1103/PhysRevB.80.085302.

[168] I. I. Fishchuk, A. K. Kadashchuk, J. Genoe, Mujeeb Ullah, H. Sitter, Th. B. Singh, N. S. Sariciftci, and H. Bässler. Temperature dependence of the charge carrier mobility in disordered organic semiconductors at large carrier concentrations. *Physical Review B*, **81**, 1 (2010). doi:10.1103/PhysRevB.81.045202.

[169] W. Pasveer, J. Cottaar, C. Tanase, R. Coehoorn, P. Bobbert, P. Blom, D. de Leeuw, and M. Michels. Unified description of charge-carrier mobilities in disordered semiconducting polymers. *Physical Review Letters*, **94**, 206601 (2005). doi:10.1103/PhysRevLett.94.206601.

[170] R. Coehoorn, W. F. Pasveer, P. A. Bobbert, and M. A. J. Michels. Charge-carrier concentration dependence of the hopping mobility in organic materials with Gaussian disorder. *Physical Review B*, **72**, 1 (2005). doi:10.1103/PhysRevB.72.155206.

[171] Ivan I Fishchuk, Andrey Kadashchuk, Volodymyr N. Poroshin, and Heinz Bässler. Charge-carrier and polaron hopping mobility in disordered organic solids: Carrier-concentration and electric-field effects. *Philosophical Magazine*, **90**, 1229 (2010). doi:10.1080/14786430903341394.

[172] R. Richert, L. Pautmeier, and H. Bässler. Diffusion and drift of charge carriers in a random potential: Deviation from Einstein's law. *Physical Review Letters*, **63**, 547 (1989). doi:10.1103/PhysRevLett.63.547.

[173] G. Wetzelaer, L. Koster, and P. Blom. Validity of the Einstein Relation in Disordered Organic Semiconductors. *Physical Review Letters*, **107**, 1 (2011). doi:10.1103/PhysRevLett.107.066605.

[174] J. Rogel-Salazar, D. D. C. Bradley, J. R. Cash, and J. C. Demello. An efficient method-of-lines simulation procedure for organic semiconductor devices. *Physical Chemistry Chemical Physics*, **11**, 1636 (2009). doi:10.1039/b813810a.

[175] B. Ruhstaller, S. A. Carter, S. Barth, H. Riel, W. Riess, and J. C. Scott. Transient and steady-state behavior of space charges in multilayer organic light-emitting diodes. *Journal of Applied Physics*, **89**, 4575 (2001). doi:10.1063/1.1352027.

[176] J. Barker, C. Ramsdale, and N. Greenham. Modeling the current-voltage characteristics of bilayer polymer photovoltaic devices. *Physical Review B*, **67**, 1 (2003). doi:10.1103/PhysRevB.67.075205.

[177] I Hwang and N C Greenham. Modeling photocurrent transients in organic solar cells. *Nanotechnology*, **19**, 424012 (2008). doi:10.1088/0957-4484/19/42/424012.

[178] Christof Pflumm, Christian Gartner, and Uli Lemmer. A Numerical Scheme to Model Current and Voltage Excitation of Organic Light-Emitting Diodes. *IEEE Journal of Quantum Electronics*, **44**, 790 (2008). doi:10.1109/JQE.2008.923557.

[179] R. Häusermann, E. Knapp, M. Moos, N. a. Reinke, T. Flatz, and B. Ruhstaller. Coupled optoelectronic simulation of organic bulk-heterojunction solar cells: Parameter extraction and sensitivity analysis. *Journal of Applied Physics*, **106**, 104507 (2009). doi:10.1063/1.3259367.

[180] J. C. Blakesley, H. S. Clubb, and N. C. Greenham. Temperature-dependent electron and hole transport in disordered semiconducting polymers: Analysis of energetic disorder. *Physical Review B*, **81**, 1 (2010). doi:10.1103/PhysRevB.81.045210.

[181] Salman M Arnab and M Z Kabir. An analytical model for analyzing the current-voltage characteristics of bulk heterojunction organic solar cells. *Journal of Applied Physics*, **115**, 034504 (2014). doi:10.1063/1.4861725.

[182] Davide Bartesaghi and L. Jan Anton Koster. The Effect of Large Compositional Inhomogeneities on the Performance of Organic Solar Cells: A Numerical Study. *Advanced Functional Materials* (2014). doi:10.1002/adfm.201402260.

[183] W. Tomaszewicz. On weakly dispersive multiple-trapping transport. *Journal of Non-Crystalline Solids*, **355**, 1414 (2009). doi:10.1016/j.jnoncrysol.2009.05.039.

[184] J. Noolandi. Multiple-trapping model of anomalous transit-time dispersion in a-Se. *Physical Review B*, **16**, 4466 (1977). doi:10.1103/PhysRevB.16.4466.

[185] Juan Bisquert. Fractional Diffusion in the Multiple-Trapping Regime and Revision of the Equivalence with the Continuous-Time Random Walk. *Physical Review Letters*, **91**, 1 (2003). doi:10.1103/PhysRevLett.91.010602.

[186] Vladimir I Arkhipov, Igor I Fishchuk, Andriy Kadashchuk, and Heinz Bassler. Charge Transport in Neat and Doped Random Organic Semiconductors. In *Semiconducting Polymers: Chemistry, Physics and Engineering*, edited by Georges Hadziioannou and George G Malliaras, chapter 8, 275–384. WILEY-VCH Verlag GmbH & Co. KGaA, Weinheim, second edition (2007). ISBN 978-3-527-31271-9.

[187] B. Hartenstein, H. Bässler, A. Jakobs, and K. W. Kehr. Comparison between multiple trapping and multiple hopping transport in a random medium. *Physical Review B*, **54**, 8574 (1996).

[188] Albert Compte, Ralf Metzler, and Juan Camacho. Biased continuous time random walks between parallel plates. *Physical Review E*, **56**, 1445 (1997). doi:10.1103/PhysRevE.56.1445.

[189] V. M. Kenkre, E. W. Montroll, and M. F. Shlesinger. Generalized master equations for continuous-time random walks. *Journal of Statistical Physics*, **9**, 45 (1973). doi:10.1007/BF01016796.

[190] Jenny Nelson. Continuous-time random-walk model of electron transport in nanocrystalline TiO2 electrodes. *Physical Review B*, **59**, 15374 (1999). doi:10.1103/PhysRevB.59.15374.

[191] J. Klafter, A. Blumen, and M. F. Shlesinger. Stochastic pathway to anomalous diffusion. *Physical Review A*, **35**, 3081 (1987).

[192] Ralf Metzler and Joseph Klafter. The restaurant at the end of the random walk: recent developments in the description of anomalous transport by fractional dynamics. *Journal of Physics A: Mathematical and General*, **37**, R161 (2004). doi:10.1088/0305-4470/37/31/R01.

[193] Elliott W. Montroll and Harvey Scher. Random walks on lattices. IV. Continuous-time walks and influence of absorbing boundaries. *Journal of Statistical Physics*, **9**, 101 (1973). doi:10.1007/BF01016843.

[194] J. Klafter and R. Silbey. Derivation of the Continuous-Time Random-Walk Equation. *Physical Review Letters*, **44**, 55 (1980). doi:10.1103/PhysRevLett.44.55.

[195] Ralf Metzler and Joseph Klafter. The random walk's guide to anomalous diffusion: a fractional dynamics approach. *Physics Reports*, **339**, 1 (2000).

[196] P. Butzer and U. Westphal. An Introduction to Fractional Calculus. In *Applications of Fractional Calculus in Physics*, edited by Rudolf Hilfer, chapter 1, 1–85. World Scientific, Singapore (2000). ISBN 9789810234577.

[197] C Li and W Deng. Remarks on fractional derivatives. *Applied Mathematics and Computation*, **187**, 777 (2007). doi:10.1016/j.amc.2006.08.163.

[198] Rudolf Gorenflo and Francesco Mainardi. Fractional Calculus: Integral and Differential Equations of Fractional Order. *arXiv preprint* (2008).

[199] Nicole Heymans and Igor Podlubny. Physical interpretation of initial conditions for fractional differential equations with Riemann-Liouville fractional derivatives. *Rheologica Acta*, **1**, 14 (2005). doi:10.1007/s00397-005-0043-5.

[200] O.P. Agrawal. Solution for a fractional diffusion-wave equation defined in a bounded domain. *Nonlinear Dynamics*, **29**, 145 (2002).

[201] F Mainardi, G Pagnini, and R Saxena. Fox functions in fractional diffusion. *Journal of Computational and Applied Mathematics*, **178**, 321 (2005). doi:10.1016/j.cam.2004.08.006.

[202] R. Hilfer. Fractional Diffusion Based on Riemann-Liouville Fractional Derivatives. *The Journal of Physical Chemistry B*, **104**, 3914 (2000). doi:10.1021/jp9936289.

[203] Juan Bisquert. Interpretation of a fractional diffusion equation with nonconserved probability density in terms of experimental systems with trapping or recombination. *Physical Review E*, **72**, 1 (2005). doi:10.1103/PhysRevE.72.011109.

[204] R Metzler and T Nonnenmacher. Space- and time-fractional diffusion and wave equations, fractional Fokker-Planck equations, and physical motivation. *Chemical Physics*, **284**, 67 (2002). doi:10.1016/S0301-0104(02)00537-2.

[205] Igor Podlubny. The Laplace transform method for linear differential equations of the fractional order. *Arxiv preprint funct-an/9710005* (1997).

[206] Igor Podlubny. *Fractional Differential Equations*. Mathematics in Science and Engineering. Academic Press, San Diego (1998). ISBN 9780080531984.

[207] Robert E. Robson. *Introductory Transport Theory for Charge Particles in Gases*. World Scientific Publishing Co. Pte. Ltd. (2006). ISBN 9812700110.

[208] Leif A. A. Pettersson, Lucimara S. Roman, and Olle Inganäs. Modeling photocurrent action spectra of photovoltaic devices based on organic thin films. *Journal of Applied Physics*, **86**, 487 (1999). doi:10.1063/1.370757.

[209] J. Campbell Scott. Metal–organic interface and charge injection in organic electronic devices. *Journal of Vacuum Science & Technology A: Vacuum, Surfaces, and Films*, **21**, 521 (2003). doi:10.1116/1.1559919.

[210] M. Baldo and S. Forrest. Interface-limited injection in amorphous organic semiconductors. *Physical Review B*, **64**, 1 (2001). doi:10.1103/PhysRevB.64.085201.

[211] Fred Schmidlin. Theory of trap-controlled transient photoconduction. *Physical Review B*, **16**, 2362 (1977). doi:10.1103/PhysRevB.16.2362.

[212] T. Tiedje and A. Rose. A physical interpretation of dispersive transport in disordered semiconductors. *Solid State Communications*, **37**, 49 (1980). doi:10.1016/0038-1098(81)90886-3.

[213] Andreas Jakobs and Klaus. W. Kehr. Theory and simulation of multiple-trapping transport through a finite slab. *Physical Review B*, **48**, 8780 (1993).

[214] Joseph Orenstein and Marc Kastner. Photocurrent Transient Spectroscopy: Measurement of the Density of Localized States in a-As2Se3. *Physical Review Letters*, **46**, 1421 (1981). doi:10.1103/PhysRevLett.46.1421.

[215] V. I. Arkhipov and A. I. Rudenko. Drift and diffusion in materials with traps II. Non-equilibrium transport regime. *Philosophical Magazine Part B*, **45**, 189 (1982). doi:10.1080/13642818208246327.

[216] Willem Hundsdorfer and Jan G. Verwer. *Numerical Solution of Time-Dependent Advection-Diffusion-Reaction Equations*. Springer, Berlin (2003). ISBN 9783540034407. doi:10.1007/978-3-662-09017-6.

[217] R. Street, K. Song, J. Northrup, and S. Cowan. Photoconductivity measurements of the electronic structure of organic solar cells. *Physical Review B*, **83**, 1 (2011). doi:10.1103/PhysRevB.83.165207.

[218] Attila Mozer, Niyazi Sariciftci, Almantas Pivrikas, Ronald Österbacka, Gytis Juška, Lutz Brassat, and Heinz Bässler. Charge carrier mobility in regioregular poly(3-hexylthiophene) probed by transient conductivity techniques: A comparative study. *Physical Review B*, **71**, 035214 (2005). doi:10.1103/PhysRevB.71.035214.

[219] Christopher R. McNeill and Neil C. Greenham. Charge transport dynamics of polymer solar cells under operating conditions: Influence of trap filling. *Applied Physics Letters*, **93**, 203310 (2008). doi:10.1063/1.3033372.

[220] Prashant Sonar, Samarendra P. Singh, Yuning Li, Zi-En Ooi, Tae-jun Ha, Ivy Wong, Mui Siang Soh, and Ananth Dodabalapur. High mobility organic thin film transistor and efficient photovoltaic devices using versatile donor–acceptor polymer semiconductor by molecular design. *Energy & Environmental Science*, **4**, 2288 (2011). doi:10.1039/c1ee01213d.

[221] Jon Ajuria, Sudam Chavhan, Ramón Tena-Zaera, Jihua Chen, Adam J. Rondinone, Prashant Sonar, Ananth Dodabalapur, and Roberto Pacios. Nanomorphology influence on the light conversion mechanisms in highly efficient diketopyrrolopyrrole based organic solar cells. *Organic Electronics*, **14**, 326 (2013). doi:10.1016/j.orgel.2012.11.010.

[222] Hiroyuki Tajima, Tomohiko Suzuki, and Motoi Kimata. Direct determination of trap density function based on the photoinduced charge carrier extraction technique. *Organic Electronics*, **13**, 2272 (2012). doi:10.1016/j.orgel.2012.07.017.

[223] C. Vijila, A. Pivrikas, H. Chun, C. Zhikuan, R. Osterbacka, and C. Jin. A study of charge transport in a novel electroluminescent poly(phenylene vinylene-co-fluorenylene vinylene) based π-conjugated polymer. *Organic Electronics*, **8**, 8 (2007). doi:10.1016/j.orgel.2006.10.002.

[224] Artem A. Bakulin, Akshay Rao, Vlad G. Pavelyev, Paul H. M. van Loosdrecht, Maxim S. Pshenichnikov, Dorota Niedzialek, Jérôme Cornil, David Beljonne, and Richard H. Friend. The role of driving energy and delocalized States for charge separation in organic semiconductors. *Science*, **335**, 1340 (2012). doi:10.1126/science.1217745.

[225] Askat E Jailaubekov, Adam P Willard, John R Tritsch, Wai-Lun Chan, Na Sai, Raluca Gearba, Loren G Kaake, Kenrick J Williams, Kevin Leung, Peter J Rossky, and X-Y Zhu. Hot charge-transfer excitons set the time limit for charge separation at donor/acceptor interfaces in organic photovoltaics. *Nature materials*, **12**, 66 (2013). doi:10.1038/nmat3500.

[226] Alan J Heeger. 25th anniversary article: Bulk heterojunction solar cells: understanding the mechanism of operation. *Advanced Materials*, **26**, 10 (2014). doi:10.1002/adma.201304373.

[227] P.W.M. Blom and M.C.J.M. Vissenberg. Charge transport in poly(p-phenylene vinylene) light-emitting diodes. *Materials Science and Engineering: R: Reports*, **27**, 53 (2000). doi:10.1016/S0927-796X(00)00009-7.

[228] Armantas Melianas, Vytenis Pranculis, Andrius Devižis, Vidmantas Gulbinas, Olle Inganäs, and Martijn Kemerink. Dispersion-Dominated Photocurrent in Polymer:Fullerene Solar Cells. *Advanced Functional Materials* (2014). doi:10.1002/adfm.201400404.

[229] Ian A. Howard, Fabian Etzold, Frédéric Laquai, and Martijn Kemerink. Nonequilibrium Charge Dynamics in Organic Solar Cells. *Advanced Energy Materials* (2014). doi:10.1002/aenm.201301743.

[230] Jason Seifter, Yanming Sun, and Alan J. Heeger. Transient photocurrent response of small-molecule bulk heterojunction solar cells. *Advanced Materials*, **26**, 2486 (2014). doi:10.1002/adma.201305160.

[231] S. Baranovskii, H. Cordes, F. Hensel, and G. Leising. Charge-carrier transport in disordered organic solids. *Physical Review B*, **62**, 7934 (2000). doi:10.1103/PhysRevB.62.7934.

[232] G Schönherr, H Bässler, and M Silver. Dispersive hopping transport via sites having a Gaussian distribution of energies. *Philosophical Magazine Part B*, **44**, 47 (1981). doi:10.1080/01418638108222366.

[233] R. Österbacka, A. Pivrikas, G. Juška, K. Genevičius, K. Arlauskas, and H. Stubb. Mobility and density relaxation of photogenerated charge carriers in organic materials. *Current Applied Physics*, **4**, 534 (2004). doi:10.1016/j.cap.2004.01.013.

[234] I. I. Fishchuk, A. Kadashchuk, S. T. Hoffmann, S. Athanasopoulos, J. Genoe, H. Bässler, and A. Köhler. Unified description for hopping transport in organic semiconductors including both energetic disorder and polaronic contributions. *Physical Review B*, **88**, 125202 (2013). doi:10.1103/PhysRevB.88.125202.

[235] Robert A. Street, Alexa Krakaris, and Sarah R. Cowan. Recombination through different types of localized states in organic solar cells. *Advanced Functional Materials*, **22**, 4608 (2012). doi:10.1002/adfm.201200031.

[236] Ardalan Armin, Gytis Juska, Mujeeb Ullah, Marappan Velusamy, Paul L Burn, Paul Meredith, and Almantas Pivrikas. Balanced carrier mobilities: Not a necessary condition for high-efficiency thin organic solar cells as determined by MIS-CELIV. *Advanced Energy Materials*, **4**, 1300954 (2014). doi:10.1002/aenm.201300954.

[237] Paul A. Staniec, Andrew J. Parnell, Alan D. F. Dunbar, Hunan Yi, Andrew J. Pearson, Tao Wang, Paul E. Hopkinson, Christy Kinane, Robert M. Dalgliesh, Athene M. Donald, Anthony J. Ryan, Ahmed Iraqi, Richard A. L. Jones, and David G. Lidzey. The Nanoscale Morphology of a PCDTBT:PCBM Photovoltaic Blend. *Advanced Energy Materials*, **1**, 499 (2011). doi:10.1002/aenm.201100144.

[238] Paul D. Cunningham and L. Michael Hayden. Carrier Dynamics Resulting from Above and Below Gap Excitation of P3HT and P3HT/PCBM Investigated by Optical-Pump Terahertz-Probe Spectroscopy †. *The Journal of Physical Chemistry C*, **112**, 7928 (2008). doi:10.1021/jp711827g.

[239] Kevin K.H. Chan, S.W. Tsang, Harrison K.H. Lee, Franky So, and S.K. So. Charge injection and transport studies of poly(2,7-carbazole) copolymer PCDTBT and their relationship to solar cell performance. *Organic Electronics*, **13**, 850 (2012). doi:10.1016/j.orgel.2012.01.030.

[240] P. W. M. Blom, V. D. Mihailetchi, L. J. A. Koster, and D. E. Markov. Device Physics of Polymer:Fullerene Bulk Heterojunction Solar Cells. *Advanced Materials*, **19**, 1551 (2007). doi:10.1002/adma.200601093.

[241] C. G. Shuttle, A. Maurano, R. Hamilton, B. O'Regan, J. C. de Mello, and J. R. Durrant. Charge extraction analysis of charge carrier densities in a polythiophene/fullerene solar cell: Analysis of the origin of the device dark current. *Applied Physics Letters*, **93**, 183501 (2008). doi:10.1063/1.3006316.

[242] L. Jan Anton Koster, Martijn Kemerink, Martijn M. Wienk, Klará Maturová, and René A. J. Janssen. Quantifying bimolecular recombination losses in organic bulk heterojunction solar cells. *Advanced Materials*, **23**, 1670 (2011). doi:10.1002/adma.201004311.

[243] Andrea Maurano, Rick Hamilton, Chris G Shuttle, Amy M Ballantyne, Jenny Nelson, Brian O'Regan, Weimin Zhang, Iain McCulloch, Hamed Azimi, Mauro Morana, Christoph J Brabec, and James R Durrant. Recombination dynamics as a key determinant of open circuit voltage in organic bulk heterojunction solar cells: a comparison of four different donor polymers. *Advanced Materials*, **22**, 4987 (2010). doi:10.1002/adma.201002360.

[244] A. Foertig, J. Rauh, V. Dyakonov, and C. Deibel. Shockley equation parameters of P3HT:PCBM solar cells determined by transient techniques. *Physical Review B*, **86**, 115302 (2012). doi:10.1103/PhysRevB.86.115302.

[245] Getachew Adam, Almantas Pivrikas, Alberto M. Ramil, Sisay Tadesse, Teketel Yohannes, Niyazi S. Sariciftci, and Daniel A. M. Egbe. Mobility and photovoltaic performance studies on polymer blends: effects of side chains volume fraction. *Journal of Materials Chemistry*, **21**, 2594 (2011). doi:10.1039/c0jm02668a.

[246] Daniel A M Egbe, Emine Tekin, Eckhard Birckner, Almantas Pivrikas, Niyazi S Sariciftci, and Ulrich S Schubert. Effect of Styryl Side Groups on the Photophysical Properties and Hole Mobility of PPE−PPV Systems. *Macromolecules*, **40**, 7786 (2007). doi:10.1021/ma071676i.

[247] Daniel A. M. Egbe, Getachew Adam, Almantas Pivrikas, Alberto M. Ramil, Eckhard Birckner, Vera Cimrova, Harald Hoppe, and Niyazi Serdar Sariciftci. Improvement in carrier mobility and photovoltaic performance through random distribution of segments of linear and branched side chains. *Journal of Materials Chemistry*, **20**, 9726 (2010). doi:10.1039/c0jm01482f.

[248] N. Yilmaz Canli, S. Günes, A. Pivrikas, A. Fuchsbauer, D. Sinwel, N.S. Sariciftci, Ö. Yasa, and B. Bilgin-Eran. Chiral (S)-5-octyloxy-2-[{4-(2-methylbuthoxy)-phenylimino}-methyl]-phenol liquid crystalline compound as additive into polymer solar cells. *Solar Energy Materials and Solar Cells*, **94**, 1089 (2010). doi:10.1016/j.solmat.2010.02.030.

[249] Serap Günes, Andreas Wild, Emel Cevik, Almantas Pivrikas, Ulrich S. Schubert, and Daniel A.M. Egbe. Effect of shifting of aromatic rings on charge carrier mobility and photovoltaic response of anthracene and thiophene-containing MEH-PPE-PPVs. *Solar Energy Materials and Solar Cells*, **94**, 484 (2010). doi:10.1016/j.solmat.2009.11.011.

[250] R. Österbacka, Gytis Juška, K. Arlauskas, A. J. Pal, K.-M. Källman, and H. Stubb. Electric field redistribution and electroluminescence response time in polymeric light-emitting diodes. *Journal of Applied Physics*, **84**, 3359 (1998). doi:10.1063/1.368493.

[251] Inchan Hwang, Christopher R. McNeill, and Neil C. Greenham. Drift-diffusion modeling of photocurrent transients in bulk heterojunction solar cells. *Journal of Applied Physics*, **106**, 094506 (2009). doi:10.1063/1.3247547.

[252] Roderick C. I. MacKenzie, Christopher G. Shuttle, Michael L. Chabinyc, and Jenny Nelson. Extracting Microscopic Device Parameters from Transient Photocurrent Measurements of P3HT:PCBM Solar Cells. *Advanced Energy Materials*, **2**, 662 (2012). doi:10.1002/aenm.201100709.

[253] G. Juška, K. Arlauskas, G. Sliaužys, A. Pivrikas, A. J. Mozer, N. S. Sariciftci, M. Scharber, and R. Österbacka. Double injection as a technique to study charge carrier transport and recombination in bulk-heterojunction solar cells. *Applied Physics Letters*, **87**, 222110 (2005). doi:10.1063/1.2137454.

[254] G. Juška, G. Sliaužys, K. Genevičius, K. Arlauskas, a. Pivrikas, M. Scharber, G. Dennler, N. Sariciftci, and R. Österbacka. Charge-carrier transport and recombination in thin insulating films studied via extraction of injected plasma. *Physical Review B*, **74**, 115314 (2006). doi:10.1103/PhysRevB.74.115314.

[255] Nicolas Blouin, Alexandre Michaud, David Gendron, Salem Wakim, Emily Blair, Rodica Neagu-Plesu, Michel Belletête, Gilles Durocher, Ye Tao, and Mario Leclerc. Toward a rational design of poly(2,7-carbazole) derivatives for solar cells. *Journal of the American Chemical Society*, **130**, 732 (2008). doi:10.1021/ja0771989.

[256] Ajay K Pandey, Muhsen Aljada, Marappan Velusamy, Paul L Burn, and Paul Meredith. Nanostructured, active organic-metal junctions for highly efficient charge generation and extraction in polymer-fullerene solar cells. *Advanced Materials*, **24**, 1055 (2012). doi:10.1002/adma.201103896.

[257] Salem Wakim, Serge Beaupré, Nicolas Blouin, Badrou-Réda Aich, Sheila Rodman, Russell Gaudiana, Ye Tao, and Mario Leclerc. Highly efficient organic solar cells based on a poly(2,7-carbazole) derivative. *Journal of Materials Chemistry*, **19**, 5351 (2009). doi:10.1039/b901302d.

[258] Zhe Li, Girish Lakhwani, Neil C. Greenham, and Christopher R. McNeill. Voltage-dependent photocurrent transients of PTB7:PC70BM solar cells: Experiment and numerical simulation. *Journal of Applied Physics*, **114**, 034502 (2013). doi:10.1063/1.4813612.

[259] Zhicai He, Chengmei Zhong, Xun Huang, Wai-Yeung Wong, Hongbin Wu, Liwei Chen, Shijian Su, and Yong Cao. Simultaneous enhancement of open-circuit voltage, short-circuit current density, and fill factor in polymer solar cells. *Advanced Materials*, **23**, 4636 (2011). doi:10.1002/adma.201103006.

[260] Martijn Lenes, Mauro Morana, Christoph J. Brabec, and Paul W. M. Blom. Recombination-Limited Photocurrents in Low Bandgap Polymer/Fullerene Solar Cells. *Advanced Functional Materials*, **19**, 1106 (2009). doi:10.1002/adfm.200801514.

[261] L. J. A. Koster, V. D. Mihailetchi, H. Xie, and P. W. M. Blom. Origin of the light intensity dependence of the short-circuit current of polymer/fullerene solar cells. *Applied Physics Letters*, **87**, 203502 (2005). doi:10.1063/1.2130396.

[262] Yongye Liang, Zheng Xu, Jiangbin Xia, Szu-Ting Tsai, Yue Wu, Gang Li, Claire Ray, and Luping Yu. For the bright future-bulk heterojunction polymer solar cells with power conversion efficiency of 7.4%. *Advanced materials (Deerfield Beach, Fla.)*, **22**, E135 (2010). doi:10.1002/adma.200903528.

[263] Ardalan Armin, Marrapan Velusamy, Paul L. Burn, Paul Meredith, and Almantas Pivrikas. Injected charge extraction by linearly increasing voltage for bimolecular recombination studies in organic solar cells. *Applied Physics Letters*, **101**, 083306 (2012). doi:10.1063/1.4747330.

[264] Igor M. Sokolov, Joseph Klafter, and Alexander Blumen. Fractional Kinetics. *Physics Today*, **55**, 48 (2002). doi:10.1063/1.1535007.

[265] V. V. Uchaikin. Subdiffusion and stable laws. *Journal of Experimental and Theoretical Physics*, **88**, 1155 (1999). doi:10.1134/1.558905.

[266] E. Barkai. Fractional Fokker-Planck equation, solution, and application. *Physical Review E*, **63**, 046118 (2001). doi:10.1103/PhysRevE.63.046118.

[267] V. V. Uchaikin and R. T. Sibatov. Fractional differential kinetics of dispersive transport as the consequence of its self-similarity. *JETP Letters*, **86**, 512 (2007). doi:10.1134/S0021364007200040.

[268] R. T. Sibatov and V. V. Uchaikin. Fractional differential kinetics of charge transport in unordered semiconductors. *Semiconductors*, **41**, 335 (2007). doi:10.1134/S1063782607030177.

[269] V. V. Uchaikin and R. T. Sibatov. Fractional theory for transport in disordered semiconductors. *Communications in Nonlinear Science and Numerical Simulation*, **13**, 715 (2008). doi:10.1016/j.cnsns.2006.07.008.

[270] R Metzler and J Klafter. Boundary value problems for fractional diffusion equations. *Physica A: Statistical Mechanics and its Applications*, **278**, 107 (2000). doi:10.1016/S0378-4371(99)00503-8.

[271] R. E. Robson. Diffusion corrections in electron conductance transients. *Physical Review A*, **31**, 3492 (1985). doi:10.1103/PhysRevA.31.3492.

[272] R. Hilfer and H. Seybold. Computation of the generalized Mittag-Leffler function and its inverse in the complex plane. *Integral Transforms and Special Functions*, **17**, 637 (2006). doi:10.1080/10652460600725341.

[273] Richard Zallen. The Physics of Amorphous Solids, Chapter 6. In *The Physics of Amorphous Solids*, chapter 6, 253–297. John Wiley & Sons (1983).

[274] Rudolf Gorenflo, Joulia Loutchko, and Yuri Luchko. Computation of the Mittag-Leffler function E(α, ß) and its derivatives. *Fractional Calculus and Applied Analysis*, **5**, 491 (2002).

[275] Gleb M Akselrod, Parag B Deotare, Nicholas J Thompson, Jiye Lee, William a Tisdale, Marc a Baldo, Vinod M Menon, and Vladimir Bulović. Visualization of exciton transport in ordered and disordered molecular solids. *Nature communications*, **5**, 3646 (2014). doi:10.1038/ncomms4646.

[276] Rudolf Hilfer (Editor). *Applications of Fractional Calculus in Physics*. Applications of Fractional Calculus in Physics. World Scientific, Singapore (2000). ISBN 9789810234577.

[277] Ralf Metzler, Eli Barkai, and Joseph Klafter. Anomalous Diffusion and Relaxation Close to Thermal Equilibrium: A Fractional Fokker-Planck Equation Approach. *Physical Review Letters*, **82**, 3563 (1999). doi:10.1103/PhysRevLett.82.3563.

[278] H. Jiang, F. Liu, I. Turner, and K. Burrage. Analytical solutions for the multi-term time–space Caputo–Riesz fractional advection–diffusion equations on a finite domain. *Journal of Mathematical Analysis and Applications*, **389**, 1117 (2012). doi:10.1016/j.jmaa.2011.12.055.

[279] B. I. Henry, T. A. M. Langlands, and P. Straka. Fractional Fokker-Planck Equations for Subdiffusion with Space- and Time-Dependent Forces. *Physical Review Letters*, **105**, 170602 (2010). doi:10.1103/PhysRevLett.105.170602.

[280] R. Robson and A. Blumen. Analytically solvable model in fractional kinetic theory. *Physical Review E*, **71**, 061104 (2005). doi:10.1103/PhysRevE.71.061104.

[281] I. Hulea, H. Brom, A. Houtepen, D. Vanmaekelbergh, J. Kelly, and E. Meulenkamp. Wide Energy-Window View on the Density of States and Hole Mobility in Poly(p-Phenylene Vinylene). *Physical Review Letters*, **93**, 166601 (2004). doi:10.1103/PhysRevLett.93.166601.

[282] R. Hilfer and L. Anton. Fractional master equations and fractal time random walks. *Physical Review E*, **51**, R848 (1995). doi:10.1103/PhysRevE.51.R848.

[283] Albert Compte. Stochastic foundations of fractional dynamics. *Physical Review E*, **53**, 4191 (1996). doi:10.1103/PhysRevE.53.4191.

[284] Sergei Fedotov and Steven Falconer. Subdiffusive master equation with space-dependent anomalous exponent and structural instability. *Physical Review E*, **85**, 031132 (2012). doi:10.1103/PhysRevE.85.031132.

[285] Sergei Fedotov. Nonlinear subdiffusive fractional equations and the aggregation phenomenon. *Physical Review E*, **88**, 032104 (2013). doi:10.1103/PhysRevE.88.032104.